

Generating and observing soliton dynamics in Bose Einstein Condensates

Paul B. Wigley

A thesis submitted in partial fulfillment of the requirements for the degree of
Doctor of Philosophy in Physics at the Australian National University

March, 2017



**Australian
National
University**

Generating and observing soliton dynamics in Bose Einstein Condensates

Paul B. Wigley

Department of Quantum Science,
Australian National University, Canberra, Australia.

Supervisory committee: Prof. J. J. Hope (Chair)
Assoc. Prof. N. P. Robins
Prof. C. M. Savage
Dr. A. R. R. Carvalho

Declaration

To the best of my knowledge and except where acknowledged in the customary manner, the material presented in this thesis is original and has not been submitted in whole or part for a degree in any university. Where work has been performed in collaboration with others, I have acknowledged the contributions of all authors.

Paul Wigley _____

Date _____

Abstract

Bose-Einstein condensates (BECs), a quantum state of matter formed when bosonic atoms are cooled close to absolute zero, have become the premier platform for investigating fundamental physics with atomic vapours. Experiments on Bose-Einstein condensates now achieve exquisite control over many aspects of the system, including interactions, trapping potential, and dynamics. This has precipitated a new wave of research into many-body quantum phenomena and, in particular, solitons. These structures are fundamental excitations of an interacting non-linear medium, of interest to a multitude of scientific disciplines from non-linear optics to financial markets. The highly controllable environment of BECs form an attractive playground for the study of solitons allowing the non-linearity to be dynamically tuned, facilitating deeper investigations into these structures.

Consistently generating and analysing solitons in BEC experiments continues to be problematic. In particular, the non-linear dynamics of BECs, though required for the generation of solitons, produce particularly challenging control and optimization problems. These control problems must be solved before further investigations into the fundamental physics of soliton dynamics can be answered. This thesis makes three important advances in the control and measurement of BECs that will lead to better generation and observation of solitons. (1) a theoretical model for a control scheme capable of highly precise wavefunction engineering, (2) the experimental implementation of a machine learning algorithm for online optimisation, and (3) a continuous non-destructive imaging system capable of directly observing soliton dynamics in real-time. Together, these advances provide a suite of tools for manipulating and exploiting solitons in Bose-Einstein condensates.

A novel technique was developed theoretically, offering control of the macroscopic wavefunction of a Bose-Einstein condensate with unprecedented spatial resolution and speed. The ability to control the atomic wavefunction at the fundamental length scale is key to the advancement of many quantum technologies such as quantum simulators. The magnetic resonance control scheme is demonstrated through simulation of a ^{87}Rb condensate with the exemplar model generating a single dark soliton with corresponding π phase kink. The soliton represents a structure at the fundamental length scale of

the system, and demonstrates the potential of the scheme for precision state engineering. The scheme is extended to generate higher-order soliton modes which are yet to be experimentally realised.

A machine learning algorithm based on Gaussian processes was developed and implemented on the evaporative cooling stage of the production of a ^{87}Rb Bose-Einstein condensate, successfully demonstrating fast optimisation to condensation. The Gaussian process develops a statistical model based on the data that enables the characterisation of the relationship between the experimental controls and resultant quality of the BEC. This relationship is often obfuscated through technical details of the apparatus, frustrating the use of theoretical models to design optimal evaporation ramps. These models often only consider ergodic dynamics with two-body s-wave interactions and no other loss rates with better ramps likely exploiting more complex interactions.

The internal model generated from the Gaussian process utilised uncertainty in measured data, making the optimisation more robust to experimental noise than alternate methods. The algorithm is shown to produce high quality Bose-Einstein condensates in 10 times fewer experimental iterations than previously used online optimisation techniques. By exploiting information on the sensitivity of each control, the model can be used to aid experimental design. The convergence of the optimisation is further improved by eliminating a superfluous parameter identified by the model. The general usefulness of machine learning compared with bespoke optimisation algorithms has seen machine learning approach ubiquity.

Finally, an experimentally straightforward technique for continuous non-destructive imaging of matter-wave solitons was developed and implemented, facilitating measurements of stochastic phenomena. The technique is readily practicable on any ultracold atom experiment with an existing absorption imaging system, simply requiring the probe laser be far-detuned from resonance. With a signal-to-noise of ~ 33 at 1.25 GHz detuning, the technique is capable of producing 100 images with no observable heating or atom loss. Coupled with a fast optical phase locked loop, the technique can be used in conjunction with absorption imaging to generate a series of non-destructive images followed by a final high signal-to-noise absorption image solely through moving the laser on resonance for the final image. The high performance and utility of this imaging setup make it a powerful tool for ultra-cold atom experiments.

Acknowledgements

I would like to acknowledge the Australian Government for their support in funding the majority of this research through the Australian Postgraduate Award.

It's a funny thing looking back on the last four years. The past always feels rosier, easier, and calmer in hindsight. Although this was never really the case, the kind people who have shared this journey with me have made it all that much better. To the many wonderful people I've shared an office with these last few years, Amir, Chris, Carlos, Chunhua, Ciaron, Ethan, Gordon, Jess, Johnny, Kyle, Mahasen, Manju, Patrick, Sam, thank you for always being there when it mattered, and never allowing a descent into monotony. To share this with all of you is undoubtedly my good fortune.

Nick, you have an innate trust in people without which I could never have made the switch to experiment, and without which I would not be here, now. I honestly can't thank you enough. Don't ever lose that belief in the people around you – it brings out the best in everyone, and we are all better for it. Joe, you've been steadfast throughout the years. Thank you for the support and particularly for supporting me in testing those experimental waters, I am truly grateful for the many years of supervision.

Michael, you have a genuinely wonderful spark of enthusiasm for all things. Thank you for providing that spark for me when I needed it most. I am profoundly grateful for it and for all you've taught me. Stuart, I never would have imagined eight years ago when I stepped into your tutorial that I would be here now. Your guidance, advice and good-humour have been a shining light on this journey.

To the folks from Monash; Lincoln, Lisa and in particular, Russell, thank you for the collaboration. Although that paper will likely haunt me for the rest of my days, I am glad to have had the opportunity and good-fortune to meet and work with you. Ethan, thank you for those final few edits, your keen eye and good judgement were very much appreciated. To Patrick and Carlos, thank you for taking me under your collective wings when I made the switch to experiment, your gentle patience meant a great deal to me. Kyle, thank you for keeping me sane in those last months. Sharing an office with you while we wrote, although provably less productive, was a pleasure and a joy and I am glad to have had your friendship through this.

To Madeleine. What can I say that is in any way adequate for the support and love that you've shown me these last three years. I think it is no stretch to say that being the partner of a physicist, particularly in this field, is wildly unenviable. The long hours, the frustration, the stress, throughout it you were there and brought joy to my life. I am forever grateful and forever glad that I met you.

To my family. You made me who I am. Distilled in all this is you made manifest in me. This is your achievement too.

All that is gold does not glitter,
Not all those who wander are lost;
The old that is strong does not wither,
Deep roots are not reached by the frost.

– J.R.R. Tolkein

Contents

Declaration	iii
Abstract	v
Acknowledgements	vii
List of Figures	xvii
List of Publications	xix
1 Introduction	1
1.1 Bose-Einstein condensation	1
1.2 Matter-wave solitons	3
1.3 Outline of this thesis	4
2 Background theory	7
2.1 Two-level atom	7
2.2 Adiabatic theorem	10
2.3 Hyperfine splitting in alkali atoms	13
2.3.1 Effect of an external magnetic field	13
2.4 Gross-Pitaevskii equation	18
2.5 Healing scales	20
2.6 Solitons	22
I Magnetic Resonance Control	25
3 Magnetic Resonance Control Theory	27
3.1 Model scheme	29
3.2 Adiabatic pulses	30
3.2.1 Landau-Zener pulse	31
3.2.2 Hyperbolic-secant pulse	34
3.2.3 Spatial selectivity using a magnetic-field gradient	37

3.3	Hyperbolic-secant pulse heuristics	38
3.3.1	Gradient optimisation and magnetically induced motion	42
4	Magnetic Resonance Control Simulation and Optimisation	45
4.1	Quasi-1D spin-1/2 Gross-Pitaevskii equation	45
4.2	Numerical simulations of MRC in a pseudospin-half system	48
4.2.1	Imaginary time propagation	48
4.2.2	Validation of numerical methods	50
4.2.3	Magnetic resonance control scheme with pseudospin half system using heuristics	50
4.2.4	Overlap fidelity	52
4.2.5	MRC scheme with pseudospin half system using fidelity optimisation	54
4.2.6	Experimental considerations	56
4.3	Extending to multiple solitons	56
II	Machine Learning	59
5	Theory of optimisation and machine learning	61
5.1	Optimisation	62
5.1.1	Notation	62
5.1.2	Local and global extrema	64
5.1.3	Continuous-time cost function	64
5.2	Numerical optimisation methods	66
5.2.1	Nelder-Mead	66
5.3	Optimisation using machine learning	70
5.3.1	Gaussian processes	70
5.3.2	Experimental algorithm	72
6	Experimental Machine Learning	77
6.1	Evaporative cooling of atoms	78
6.2	Experimental apparatus	79
6.3	Cost function	80
6.4	Parameterisations of evaporation ramps	83
6.5	Uncertainty handling	85
6.6	Results	86

III Imaging of Bose Einstein Condensates	91
7 Destructive Imaging of Bose Einstein Condensates	93
7.1 Absorption imaging	95
7.1.1 Experimental absorption imaging	100
7.2 Fluorescence imaging	101
7.3 Frequency modulation imaging	103
7.3.1 Experimental frequency modulation imaging	106
8 Dispersive Imaging of Bose Einstein Condensates	109
8.1 Scattered photons	110
8.2 Dual-species apparatus	111
8.3 Probe beam detuning with magnetic fields	112
8.4 Dark field imaging	114
8.5 Phase contrast imaging	116
8.5.1 Phase dot optimisation	119
8.5.2 Manufacture of dot	119
8.6 Polarisation phase contrast imaging	120
8.7 Shadowgraph imaging	124
8.7.1 Theoretical signal	125
8.7.2 Experimental details and camera plane	128
8.7.3 Experimental signal-to-noise and destruction	130
8.7.4 Applications	132
9 Conclusions and outlook	135
References	139

List of Figures

1.1	Combined images of relative velocity distribution of an ultracold gas down to condensation	2
2.1	Two-level atom level diagram	7
2.2	Avoided crossing diagram	11
2.3	Effect of an adiabatic sweep through resonance	12
2.4	Energy splittings in the low field regime	15
2.5	Energy splittings in the anomalous Zeeman regime	16
2.6	Illustration of a soliton in a 1D system	23
3.1	Schematic of the magnetic resonance control scheme	30
3.2	Effect of a Landau-Zener pulse	31
3.3	Landau-Zener adiabatic pulse optimisation analytics	33
3.4	Effect of a hyperbolic-secant pulse on a two-level system initially in the ground state	35
3.5	Adiabatic and asymptotic limits for the hyperbolic-secant pulse	36
3.6	Final population for hyperbolic-secant pulse	37
3.7	Analytic distribution after the first pulse	40
3.8	Relationship of the scheme resolution to pulse parameters	42
4.1	Change in ground-state shape as the non-linearity changes	49
4.2	Application of magnetic resonance control scheme using parameter heuristics	51
4.3	Optimisation of magnetic resonance protocol applied to a quasi one dimensional condensate	54
4.4	Model magnetic resonance control scheme applied to a pseudo-1D condensate	55
4.5	Double Solitons	57
4.6	Example of implementing the double soliton protocol twice in quick succession	58

5.1	Example of optimisation across a two-dimensional landscape	63
5.2	Illustration of the difference between local and global optima	64
5.3	Diagram of simplex in different dimensions	66
5.4	Example of the operations available to the Nelder-Mead algorithm	68
5.5	Flow diagram illustrating Nelder-Mead logic	69
5.6	Example of over-fitting	71
5.7	Example of a Gaussian process	72
5.8	Illustration of varying correlation lengths for a model	74
6.1	Expanded illustration of machine learning process	77
6.2	Illustration of evaporative cooling	78
6.3	Diagram of the dual-species experimental apparatus	80
6.4	Illustration of cost function calculation	81
6.5	Example of cost function calculation from real data	82
6.6	Basis functions describing the evaporation ramps	84
6.7	Analysis of variation in experiment over a week	85
6.8	Experimental optimisation of 16 ramps	86
6.9	History of evaporation ramps through optimisation procedure	87
6.10	Experimental optimisation of 6 and 7 parameters ramps	88
6.11	Example of the model building aspect of machine learning	89
7.1	Kramers-Kronig diagram showing signal for absorption and dispersion .	94
7.2	Schematic for absorption imaging system	96
7.3	Theoretical signal-to-noise ratio for absorption imaging	99
7.4	Absorption imaging applied to ^{87}Rb after a 550 ms time-of-flight	100
7.5	Schematic diagram of a fluorescence imaging system	101
7.6	Flow diagram of a frequency modulation imaging system	103
7.7	Frequency modulation imaging applied to ^{87}Rb condensate after a 550 ms time-of-flight	107
8.1	Non-destructive imaging of condensation in dual-species machine	112
8.2	Spectroscopy performed on ^{85}Rb	113
8.3	Schematic for dark field imaging	115
8.4	Schematic for phase contrast imaging using a phase dot	117
8.5	Diagram of change to signal as transmission changes	118
8.6	Signal at detector for various phase dot amounts	119
8.7	Schematic for Faraday rotation imaging system	121
8.8	Signal dependence for polarisation phase contrast imaging	123
8.9	Schematic for shadowgraph imaging	124

8.10 Comparison of the raw shadowgraph image with a background subtraction and Fourier inversion	128
8.11 Signal dependence on camera plane for shadowgraph imaging	129
8.12 Destruction dependence on detuning	130
8.13 Signal-to-noise ratio over a range of detunings	131
8.14 Demonstration of dispersive imaging for stochastic processes	132
8.15 Continuous imaging of a Bose-Einstein condensate falling	133
8.16 Shadowgraph imaging as applied to a measurement of trap oscillations .	134

List of Publications

The following publications are the result of research and collaborations undertaken during the course of this thesis:

- [1] P. B. Wigley, P. J. Everitt, A. v. d. Hengel, J. W. Bastian, M. A. Sooriyabandara, G. D. McDonald, K. S. Hardman, C. D. Quinlivan, P. Manju, C. C. N. Kuhn, I. R. Petersen, A. N. Luiten, J. J. Hope, N. P. Robins, and M. R. Hush. *Fast machine-learning online optimization of ultra-cold-atom experiments.* Scientific Reports **6**, 25890 (2016). ISSN 2045-2322. DOI: 10.1038/srep25890.
- [2] P. B. Wigley, P. J. Everitt, K. S. Hardman, M. R. Hush, C. H. Wei, M. A. Sooriyabandara, P. Manju, J. D. Close, N. P. Robins, and C. C. N. Kuhn. *Non-destructive shadowgraph imaging of ultra-cold atoms.* Optics Letters **41**, 4795 (2016). ISSN 1539-4794. DOI: 10.1364/OL.41.004795.
- [3] P. B. Wigley, L. M. Starkey, S. S. Szigeti, M. Jasperse, J. J. Hope, L. D. Turner, and R. P. Anderson. *Precise wave-function engineering with magnetic resonance.* Physical Review A **96**, 013612 (2017). DOI: 10.1103/PhysRevA.96.013612.
- [4] K. S. Hardman, P. B. Wigley, P. J. Everitt, P. Manju, C. C. N. Kuhn, and N. P. Robins. *Time-of-flight detection of ultra-cold atoms using resonant frequency modulation imaging.* Optics Letters **41**, 2505 (2016). ISSN 1539-4794. DOI: 10.1364/OL.41.002505. [p 103]
- [5] K. Hardman, P. Everitt, G. McDonald, P. Manju, P. Wigley, M. Sooriyabandara, C. Kuhn, J. Debs, J. Close, and N. Robins. *Simultaneous Precision Gravimetry and Magnetic Gradiometry with a Bose-Einstein Condensate: A High Precision, Quantum Sensor.* Physical Review Letters **117**, 138501 (2016). DOI: 10.1103/PhysRevLett.117.138501. [pp 2, 100, and 129]
- [6] P. J. Everitt, M. A. Sooriyabandara, M. Guasoni, P. B. Wigley, C. H. Wei, G. D. McDonald, K. S. Hardman, P. Manju, J. D. Close, C. C. N. Kuhn, S. S. Szigeti, Y. S. Kivshar, and N. P. Robins. *Observation of a modulational instability in Bose-Einstein condensates.* Physical Review A **96**, 041601 (2017). DOI: 10.1103/PhysRevA.96.041601.

Introduction

THE frontiers of human knowledge push persistently forward, ever driven by humanity's insatiable curiosity. As we delve deeper and deeper into the well of Nature, those last drops of knowledge become ever more difficult to obtain. To gather these drops requires the most subtle of tools and the most elegant of methods. The frigid realm of the Bose-Einstein condensate is one such well for which the frontier is ever harder to reach, and ever more difficult to expand. Without precise mastery and control of the system, without the efficient and thoughtful optimisation of current methods, without the ability to observe that which we create, the frontier will remain steadfast; the well withholding those last few revitalising drops.

1.1 Bose-Einstein condensation

Our frontier, the Bose-Einstein condensate (BEC), forms the archetypal quantum system enabling the unparalleled ability to investigate and manipulate quantum fields. Bose-Einstein condensation has a long and storied history, being theorised early in the twentieth century by Bose [1] and subsequently extended by Einstein [2]. The work described the statistics of identical integer spin particles called bosons for which the energy spectrum in thermal equilibrium is described by the Bose-Einstein distribution. This distribution exhibits a threshold temperature T_c , below which a macroscopic portion of the atoms will 'condense' into a single quantum state, the ground state. Despite the early theoretical work, it took a further seventy years for the clean experimental realisation of a Bose-Einstein condensate in dilute alkali gases, requiring elegant advances in laser cooling [3–7] and the development of the more brute force evaporative cooling techniques [8, 9]. This concerted scientific effort resulted in the 1997 Nobel prize for laser cooling [10] and the 2001 prize for the experimental realisation of Bose-Einstein condensation [11, 12], but perhaps most significantly it produced a new tool for studying quantum phenomena and a rich abundance of new physics to explore. Condensates have now been successfully generated in a diverse range of atomic species including alkali metals ^7Li , ^{23}Na , ^{39}K , ^{41}K , ^{85}Rb , ^{87}Rb , ^{133}Cs [13–19], alkaline earth metals ^{40}Ca , ^{84}Sr , ^{86}Sr , ^{88}Sr [20–23], lanthanide atoms ^{174}Yb , ^{164}Dy , ^{168}Er [24–26] as well as ^{52}Cr [27], atomic hydro-

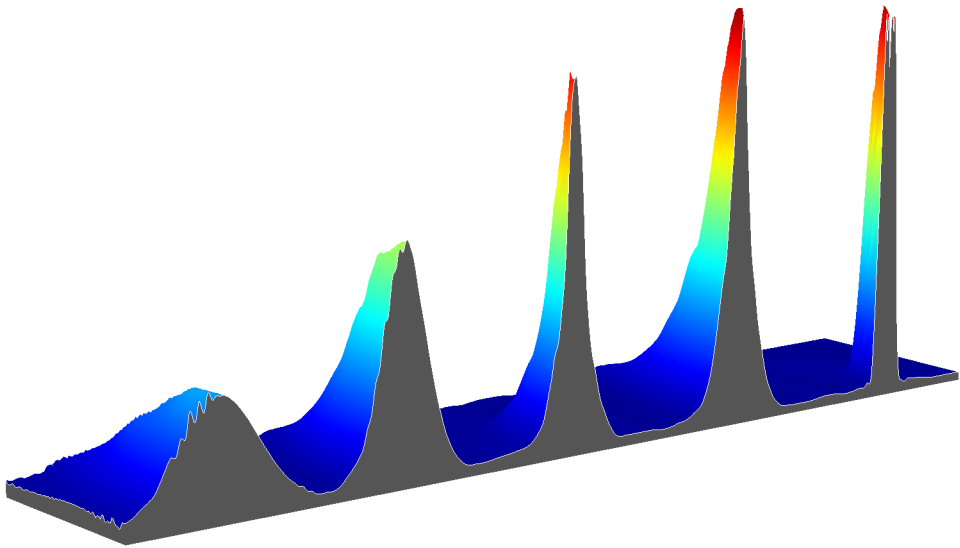


Figure 1.1: Combined experimental images of a dilute ultracold cloud showing the relative velocity distribution for a series of temperatures down to condensation. The velocity space representation is acquired through time-of-flight expansion after release from trap.

gen [28], and metastable helium [29]. This vast swathe of candidate condensate species provides a multitude of unique properties that can be exploited and studied.

Consisting of ultracold gases typically ranging from a few thousand to a few million atoms, Bose-Einstein condensates display properties over a range of spatio-temporal scales. Confined to harmonic traps characterised by a frequency ω_{HO} , with corresponding length scale $a_{\text{HO}} = [\hbar/m\omega_{\text{HO}}]^{1/2}$, typically on the order of Hz and μm respectively, condensates are enlarged by repulsive two-body interactions allowing them to be observed through optical techniques. This has been demonstrated using numerous methods, most commonly through the use of resonant probe light that is absorbed by the cloud, allowing a shadow of the cloud to be observed and the density quantified [18]. This process is inherently destructive, requiring dynamics be observed through repetition of experiments [30, 31]. In contrast, non-destructive imaging methods have been demonstrated [32], allowing condensates to be probed continuously through observation within the confining trap. Both momentum and coordinate space representations of the condensate can be observed through imaging in-trap or after ballistic expansion, allowing additional insight into the system and dynamics.

The wavelike nature of Bose-Einstein condensates has been demonstrated through the interference displayed by the overlap of two initially separated clouds [33]. Further, matter-wave interferometers using Bose-Einstein condensates make some of the best precision sensors [34], capable of simultaneous measurements of gravitational and magnetic signals [35]. By virtue of the unprecedented control over temperature, coherence, external potentials and interactions, Bose-Einstein condensates provide the ideal system for

studying quantum phenomena such as quantum tunnelling [36, 37] and form excellent tools for quantum simulation and emulation [38].

The experimental realisation of Bose-Einstein condensation spurred much theoretical work to explain condensates and their dynamics, as well as to predict new behaviour [39]. Mean-field approaches have proven successful, providing closed form equations of motion that describe the condensate dynamics in experimentally relevant regimes [40, 41]. These equations include a non-linear inter-particle interaction term that gives rise to many complex non-linear effects.

1.2 Matter-wave solitons

The presence of this non-linearity, arising from inter-particle interactions, results in many complex non-linear effects that can be studied in the highly controllable environment of a Bose-Einstein condensate. As a number of atomic species exhibit accessible Feshbach resonances, the strength of this inter-particle interaction can be precisely tuned using an external magnetic field [42]. Exploitation of this property provides a playground for the study of non-linear processes such as the collapse and explosion of condensates [43] as well as soliton collisions and interactions [44, 45]. In one-dimension, Bose-condensed systems exhibit repulsive interactions that support dark solitons consisting of a density minimum [46], while attractive interactions support bright solitons that instead display density maximums [47].

Matter-wave dark solitons exhibit a discontinuous jump in phase at their density minimum, making them interesting topological structures. Being ‘degenerate’ one-dimensional analogues to vortices, solitons are fundamental non-linear excitations of Bose-Einstein condensates. A large collection of theory has been developed describing solitons [48] with their unique properties enabling the investigation of quantum systems at the mesoscale [49]. More tangibly perhaps, matter-wave dark solitons provide a means of monitoring phase in an atom interferometer [50] with bright solitons shown to improve visibility in these interferometric measurements [51], potentially increasing the sensitivity of these measurement devices.

Dark solitons have been demonstrated experimentally, primarily through phase engineering techniques [52], with more nuanced approaches such as the adiabatic inversion of a trapping potential enabling generation of vortices [53] and skyrmions [54]. Bright solitons and soliton trains have been generated by changing the inter-particle interactions from repulsive to attractive [55, 56]. Dark-bright soliton pairs have also been simulated in a condensate with repulsive interactions, with the bright soliton supported by the non-linear coupling to the dark soliton component [57]. Indeed, the myriad of applications enabled by Bose-Einstein condensates and the non-linear physics of solitons compels

improvement of the way in which they are produced and harnessed. This thesis theoretically explores a method for robustly generating dark solitons, exploiting magnetic resonance techniques to alter the macroscopic wavefunction of a Bose-Einstein condensate. Through the use of generalisable machine learning methods, the evaporative cooling stage of Bose-Einstein condensate production is experimentally optimised. Finally a non-destructive imaging method is experimentally demonstrated, capable of imaging soliton dynamics continuously in real-time, allowing stochastic non-linear processes to be quantitatively analysed.

1.3 Outline of this thesis

This thesis has been divided into three distinct parts linked by the common thread of the application to ultracold atoms, Bose-Einstein condensates, and matter-wave solitons. Part I is centred around the development of the magnetic resonance control protocol developed in collaboration with the team of Russell Anderson, Lincoln Turner and Lisa Starkey of Monash University. Part II presents the basis and experimental implementation of a machine learning algorithm to a Bose-Einstein condensate apparatus. Part III comprises an overview of imaging techniques in the context of ultracold atoms. Theoretical details common to the three parts is delivered in Chapter 2.

Chapter 3 provides a detailed theoretical overview of the magnetic resonance control scheme in the context of static two-level atoms, developing a framework for optimal pulse parameters used for the protocol. Chapter 4 extends this work to the simulation of a ^{87}Rb condensate in the pseudo-1D regime under application of the scheme with successful engineering of a sub-diffraction limit structure written to the macroscopic wavefunction of the condensate.

Chapter 5 provides a background for optimal control theory, culminating in the development of a machine learning algorithm based on Gaussian processes. The result of this algorithm experimentally applied to the production of ^{87}Rb condensates is subsequently presented in Chapter 6, where it is used to optimise the evaporative cooling stage of condensate production. The results and utility of the algorithm and its internal model are demonstrated through experimental application, benchmarked against the commonly used Nelder-Mead algorithm.

Chapter 7 presents theoretical and experimental results pertaining to destructive imaging techniques as applied to Bose-Einstein condensates. The signal-to-noise of each technique is derived with experimental results providing key examples. Chapter 8 extends the previous chapter to include dispersive imaging techniques capable of continuously and non-destructively imaging Bose-Einstein condensates. A robust, technically simple method is presented with the technique applied experimentally and showcased through

a number of key applications. The thesis concludes with a summary of the work presented along with a discussion of future directions and extensions of the research.

Background theory

Though broad in scope, the topics of this thesis have many aspects related by a few fundamental principles and concepts. These concepts, such as the two-level atom and adiabatic passage, atom-light interactions and Bose-Einstein condensation are explored briefly in the following chapter. This theoretical overview provides a foundation for work presented in this thesis.

2.1 Two-level atom

The interaction of light with matter is one of the most powerful tools in atomic physics, providing a relatively simple means for cooling, trapping, imaging, and controlling the atomic system. Though theoretically simple, the coupling of a two-level atom to a classical electromagnetic field provides an elegant model for much of the physics encompassed by atom-light interactions. The two-level atom model characterises the system using a two-dimensional Hilbert space described by a Hamiltonian that yields two eigenstates. The two levels may be coupled in a number of ways, from optical frequency radiation coupling electronic states to radio-frequency radiation coupling magnetic sub-states. Being one of the most widely studied systems in physics, many undergraduate texts provide extensive analysis of the two-level system [58, 59] necessitating only a brief introduction provided here.

The two-level atom model considered below takes a semi-classical approach whereby the atom is considered quantum and the light field classical. This approach is valid when the driving field is large, as is the case for most applications in this thesis. Consider

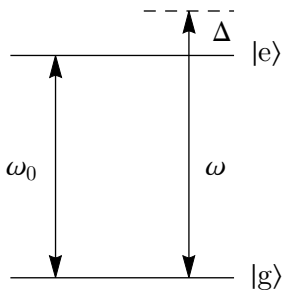


Figure 2.1: Illustration of a two-level atom energy level scheme. The ground state $|g\rangle$ and the excited state $|e\rangle$ are separated by a frequency of ω_0 . The two levels are coupled via a classical electromagnetic field of frequency $\omega = \omega_0 + \Delta$ where Δ is the detuning from resonance.

a two-level atom with eigenstates $|g\rangle$ and $|e\rangle$ corresponding to the ground and excited states respectively, as illustrated in Figure 2.1. Such a two-level system is valid if the field is on or near resonance with all other levels far enough detuned such as to be safely neglected. These two eigenstates are referred to as the ‘bare’ states and correspond to the eigenstates of the system without coupling. The two levels are separated by a frequency ω_0 and coupled via a classical electromagnetic field of frequency $\omega = \omega_0 + \Delta$ where Δ is the detuning from resonance. Each level is an eigenstate of the system with corresponding eigenvalues $\hbar\omega_g$ and $\hbar\omega_e$ for the ground and excited states respectively with the energy separation being $\hbar\omega_0$. The two levels are coupled by a linearly polarised classical electromagnetic field, expressed as

$$\mathbf{E}(t) = \mathbf{E}_0 \cos(\omega t + \phi), \quad (2.1)$$

where $|\mathbf{E}_0|$ is amplitude of the field, ω is the frequency of the light and ϕ is an arbitrary phase. The total Hamiltonian of such a system is $\hat{H} = \hat{H}_{\text{atom}} + \hat{H}_{\text{int}}$, where the atomic Hamiltonian is described by

$$\hat{H}_{\text{atom}} = \frac{1}{2}\hbar\omega_0 (|e\rangle\langle e| - |g\rangle\langle g|), \quad (2.2)$$

and the interaction Hamiltonian is given by

$$\hat{H}_{\text{int}} = \hat{\mathbf{d}} \cdot \mathbf{E}(t), \quad (2.3)$$

where $\hat{\mathbf{d}} = e\hat{\mathbf{r}}$ describes the electric dipole moment. Here we have invoked the dipole approximation, assuming that the wavelength of the light is large compared to the diameter of the atom, as is the case for much of the following work. The dipole operator is a matrix with elements $\mathbf{d}_{ij} = \langle i | \hat{\mathbf{d}} | j \rangle$. Assuming the atom has no permanent electric dipole moment, the interaction term of the Hamiltonian thus simplifies to

$$\hat{H}_{\text{int}} = \hbar\Omega (|g\rangle\langle e| + |e\rangle\langle g|) \cos(\omega t + \phi), \quad (2.4)$$

where we have defined the complex Rabi frequency as

$$\Omega = \frac{e\mathbf{d}_{ge} \cdot \mathbf{E}_0}{\hbar}. \quad (2.5)$$

The Rabi frequency describes the rate at which the population oscillates between the two states when the coupling is resonant with the transition. This is evident from the interaction Hamiltonian given by Equation (2.4) where the interaction is seen to couple the two states with coupling strength given with respect to Ω .

The total Hamiltonian, described in the Schrödinger picture and expressed using the basis $\{|g\rangle, |e\rangle\}$, is therefore given by

$$\hat{H} = \frac{\hbar}{2} \begin{pmatrix} \Delta - \omega & 2\Omega \cos(\omega t - \phi) \\ 2\Omega \cos(\omega t - \phi) & -(\Delta - \omega) \end{pmatrix}. \quad (2.6)$$

Given the time-dependent coupling, the interaction picture provides a simpler representation of the system for subsequent analysis. Transforming to the interaction picture involves separating the time-dependent and independent components of the Hamiltonian. Expressing the oscillating term using complex exponentials and performing the separation produces

$$\hat{H} = \underbrace{\frac{\hbar}{2} \begin{pmatrix} -\omega & 0 \\ 0 & \omega \end{pmatrix}}_{\hat{H}_0} + \underbrace{\frac{\hbar}{2} \begin{pmatrix} \Delta & \Omega(e^{i(\omega t - \phi)} + e^{-i(\omega t - \phi)}) \\ \Omega(e^{i(\omega t - \phi)} + e^{-i(\omega t - \phi)}) & -\Delta \end{pmatrix}}_{\hat{V}}, \quad (2.7)$$

where \hat{H}_0 and \hat{V} correspond to the time-independent and time-dependent terms respectively. The transformation to the interaction picture is then achieved using the unitary operator $\hat{U} = e^{-i\hat{H}_0 t/\hbar}$ such that

$$\hat{H}_{\text{I}} = \hat{U}^\dagger \hat{V} \hat{U} \quad (2.8)$$

$$= \frac{\hbar}{2} \begin{pmatrix} \Delta & \Omega e^{-i\phi} (1 + e^{-2i(\omega t - \phi)}) \\ \Omega e^{i\phi} (1 + e^{2i(\omega t - \phi)}) & -\Delta \end{pmatrix}. \quad (2.9)$$

The interaction picture essentially describes dynamics in the rotating frame. The terms that oscillate at twice the driving frequency effectively average to zero over any reasonable time scale of the system and mean the Hamiltonian simplifies to

$$H_{\text{I}} = \frac{\hbar}{2} \begin{pmatrix} \Delta & \Omega e^{-i\phi} \\ \Omega e^{i\phi} & -\Delta \end{pmatrix} \quad (2.10)$$

This approximation is termed the ‘rotating-wave approximation’ and for most purposes presented in this thesis, is acceptable. Care must be taken to avoid entering regimes where $\omega_0 \gg \Omega$ as this approximation is no longer valid.

Given the Hamiltonian found in Equation (2.10), the evolution of an arbitrary state, given by

$$|\psi(t)\rangle = c_g(t)|g\rangle + c_e(t)|e\rangle, \quad (2.11)$$

where $c_g(t)$ and $c_e(t)$ are the probability amplitudes of finding the atom in the ground

or excited state respectively. These probabilities evolve according to interaction picture form of the Schödinger equation, producing

$$2i\dot{c}_g(t) = \Delta c_g + \Omega e^{-i\phi} c_e, \quad (2.12)$$

$$2i\dot{c}_e(t) = \Omega e^{i\phi} c_g - \Delta c_e. \quad (2.13)$$

If the system is initially in the ground state at time $t = 0$, then the solution to these equations for a constant real Rabi frequency and detuning is given by

$$c_g(t) = \cos\left(\frac{\tilde{\Omega}t}{2}\right) - i\frac{\Delta}{\tilde{\Omega}} \sin\left(\frac{\tilde{\Omega}t}{2}\right), \quad (2.14)$$

$$c_e(t) = -i\frac{\Omega}{\tilde{\Omega}} \sin\left(\frac{\tilde{\Omega}t}{2}\right), \quad (2.15)$$

where the generalised Rabi frequency, $\tilde{\Omega} = \sqrt{\Omega^2 + \Delta^2}$, describes the frequency at which population oscillates between states for a particular coupling field [60]. The evolution of the populations is given by

$$|c_g(t)|^2 = \frac{\Delta^2}{\tilde{\Omega}^2} + \frac{\Omega^2}{\tilde{\Omega}^2} \cos^2\left(\frac{\tilde{\Omega}t}{2}\right) \quad (2.16)$$

$$|c_e(t)|^2 = \frac{\Omega^2}{\tilde{\Omega}^2} \sin^2\left(\frac{\tilde{\Omega}t}{2}\right). \quad (2.17)$$

At resonance, the system oscillates fully between the ground and excited states with frequency Ω . As the coupling field is detuned the frequency of oscillation increases to $\tilde{\Omega}$ and the amplitude of oscillation increases to $\Omega^2/\tilde{\Omega}^2$. The resonant oscillations give rise to two important pulses, the π -pulse and the $\pi/2$ -pulse. The π -pulse transfers all population, initially in the ground state, to the excited state and corresponds to a pulse duration such that $\Omega t = \pi$. This pulse is used in atom-interferometry in analogy to mirrors in optical interferometry. The $\pi/2$ -pulse, analogous to a beam splitter, corresponds to $\Omega t = \pi/2$ and results in population equally split between the two states. These pulses can be experimentally challenging to produce, as errors in timings or Rabi frequencies can produce lower fidelity pulses and imperfect population transfer. Adiabatic passage, discussed below, presents a means of transferring population robust to experimental imperfections albeit on a much slower time scale.

2.2 Adiabatic theorem

The adiabatic theorem applies across many different physical systems and describes the result of a Hamiltonian that changes at a sufficiently slow rate. Given a Hamiltonian

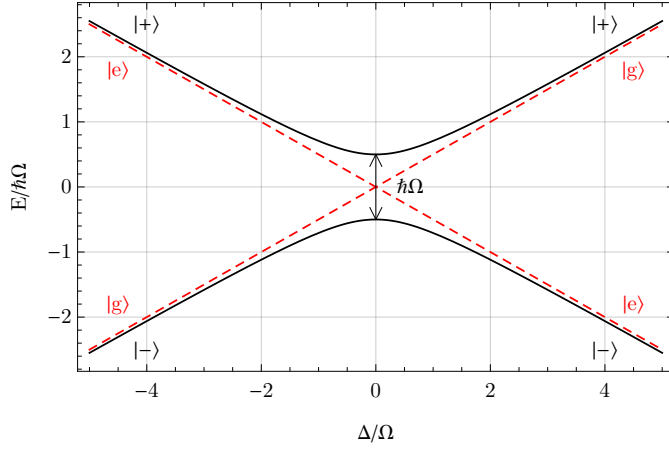


Figure 2.2: The energy eigenvalues of the two-level system described by the interaction picture Hamiltonian in Equation (2.10). Red dashed line corresponds to the bare states ($|g\rangle$ and $|e\rangle$) with the coupling turned off. The solid black lines correspond to the dressed states ($|+\rangle$ and $|-\rangle$). An avoided crossing is observed at resonance for the dressed states with an energy gap corresponding to $\hbar\tilde{\Omega}$. The avoided crossing can be exploited to efficiently transfer an atom from the ground to excited state by adiabatically sweeping Δ from $-\infty$ to $+\infty$ where the initial dressed state asymptotes to a different bare state.

slowly varying in time, a state initially in an eigenstate of the time-independent Hamiltonian will remain in an eigenstate of the new, time-dependent Hamiltonian for all time [61]. This so-called ‘adiabatic passage’ can be exploited to generate robust population transfer between atomic states. In the case of the two-level atom and the corresponding Hamiltonian, a slowly varying Rabi frequency and detuning can generate adiabatic passage. As a result of the slow time-dependent coupling, the $\{|g\rangle, |e\rangle\}$ basis no longer corresponds to a stationary solution of the Hamiltonian. The new eigenstates, the so-called ‘dressed’ states are given in the basis $\{|+\rangle, |-\rangle\}$ as

$$|+\rangle = e^{-i\phi/2} \cos\left(\frac{\theta}{2}\right) |g\rangle + e^{i\phi/2} \sin\left(\frac{\theta}{2}\right) |e\rangle , \quad (2.18)$$

$$|-\rangle = -e^{-i\phi/2} \sin\left(\frac{\theta}{2}\right) |g\rangle + e^{i\phi/2} \cos\left(\frac{\theta}{2}\right) |e\rangle , \quad (2.19)$$

where the so-called ‘mixing angle’, θ is defined by

$$\tan(\theta) = \frac{\Omega}{\Delta + \tilde{\Omega}} . \quad (2.20)$$

This new set of eigenstates has corresponding dressed-state eigenvalues given by

$$E_{\pm} = \pm \frac{\hbar\tilde{\Omega}}{2} . \quad (2.21)$$

As illustrated in Figure 2.2, for a large detuning from resonance, $\tan(\theta) \rightarrow 0$ and the dressed states asymptotically approach the bare states. Depending on the direction of

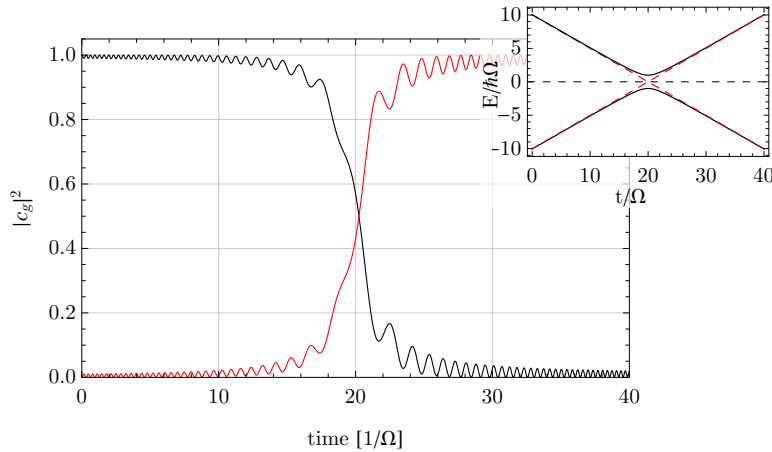


Figure 2.3: Example of the effect of an adiabatic sweep through resonance. Due to the finite duration of the sweep, small off-resonant Rabi oscillations remain at the culmination of the sweep. The adiabatic sweep is far longer than a resonant π pulse, but is more robust to experimental variations in the frequency and fields, and is capable of efficiently inverting the populations from the ground to excited state.

the detuning from resonance, the dressed states approach different bare states such that

$$\lim_{\Delta \rightarrow \pm\infty} \{|\pm\rangle, |\mp\rangle\} \rightarrow \{|g\rangle, |e\rangle\}. \quad (2.22)$$

Importantly, at resonance ($\Delta = 0$) the states produce an avoided crossing with an energy gap corresponding to $\hbar\Omega$. This convenient property gives rise to the possibility of adiabatic passage whereby highly efficient population transfer can occur by changing the Rabi frequency and detuning sufficiently slowly such that the state adiabatically follows the dressed state and thereby transfers to a different bare state. To illustrate this, consider a time varying coupling pulse initially negatively far-detuned from resonance such that the atom is in the dressed state $|-\rangle$ corresponding to the bare $|g\rangle$ eigenstate. By sweeping the detuning of the coupling pulse slowly through resonance and on, until far-detuned in the positive direction, the state will still be in the same dressed eigenstate $|-\rangle$, but this now corresponds to the excited bare eigenstate $|e\rangle$. If the coupling is subsequently extinguished, the atoms will be in the excited bare state with high probability. In the limit that the avoided crossing is traversed infinitely slowly, the population transfer will be perfect and the excited state will be completely populated. If, however, the sweep through the avoided crossing is too fast, some ground-state population will remain. Specifically, given a constant Rabi frequency with an accompanying detuning that is swept at a constant rate $\dot{\Delta}$, the probability of the atom being in the ground state at the end of an infinitely slow sweep is given by the Landau-Zener formula

$$P_{LZ} = \exp\left(-\frac{\pi\Omega^2}{2\dot{\Delta}}\right), \quad (2.23)$$

an expression simultaneously and independently derived by Landau, Zener, Majorana and Stückelberg [62–65]. The adiabatic limit is then given by $\Omega^2/\dot{\Delta} \gg 1$. This expression corresponds to the limit where the detuning is swept infinitely slowly. In practice this is not possible and the problem then becomes designing pulses to achieve some finite fidelity in a finite time. The particular form of the adiabatic pulse is crucial to the success of the adiabatic population transfer. Through optimisation of specific adiabatic pulses, the relative population of an ensemble of two-level atoms can be manipulated. This forms the basis for the magnetic resonance control scheme presented in Chapter 3 and Chapter 4 with adiabatic coupling pulses exploited to achieve precise wavefunction engineering.

2.3 Hyperfine splitting in alkali atoms

The energy structure of atoms is crucial to understanding their interaction with the environment and exploiting these levels is essential for experimental physics. In the context of this research, magnetic fields play a critical role in the magnetic resonance control scheme enabling the precise spatial selectivity necessary for wavefunction engineering. In addition, ^{85}Rb exhibits a Feshbach resonance allowing for the fine tuning of its scattering length in real-time by manipulation of an external magnetic field. The ability to image the resulting dynamics is highly desirable yet requires precise knowledge of the magnetically altered resonance in order to tune the imaging laser to correctly image a particular transition. The following section outlines the process of determining how the internal level structure of atoms is affected by an external magnetic field, particularly in the context of ^{85}Rb and ^{87}Rb .

2.3.1 Effect of an external magnetic field

The level structure of atoms is due to a complex relationship between various elements of the atom beginning with the interaction of the magnetic moment due to the electron spin and the electron orbital angular momentum, resulting in the fine structure. More complex hyperfine structure arises from the interaction of the nucleus with internally generated magnetic and electric fields with each hyperfine level (F) of an atom containing $2F + 1$ magnetic sub-levels which describe the angular distribution of the electronic wavefunction. When no external magnetic field is present these sub-levels are degenerate. As the magnetic field is increased this degeneracy is lifted and the magnetic sub-levels split as various elements couple to the field. This coupling arises from the electron spin, the electron orbital distribution and the nuclear magnetic moment, resulting in an interaction

Property	$^{85}\text{Rb } 5^2S_{1/2}$	$^{85}\text{Rb } 5^2P_{3/2}$	$^{87}\text{Rb } 5^2S_{1/2}$	$^{87}\text{Rb } 5^2P_{3/2}$
g_S			2.0023193043622(15)	
g_L		0.99999354		0.99999369
g_I		-0.00029364000(60)		-0.0009951414(10)
$h \cdot A_{\text{hfs}} [\text{MHz}]$	1.0119108130(20)	25.0020(99)	3417.341305452145(45)	84.7185(20)
$h \cdot B_{\text{hfs}}$		25.790(93)		12.4965(37)
$h \cdot \mu_B [\text{MHz/G}]$			1.399624604	

Table 2.1: Various values used for the calculation of the energy splitting due to an external magnetic field. Additional detail can be found in [66].

Hamiltonian given by

$$H_B = \frac{\mu_B}{\hbar} (g_S \mathbf{S} + g_L \mathbf{L} + g_I \mathbf{I}) \cdot \mathbf{B} \quad (2.24)$$

$$= \frac{\mu_B}{\hbar} (g_S S_z + g_L L_z + g_I I_z) B_z, \quad (2.25)$$

where the magnetic field \mathbf{B} is taken to be in the z -direction, g_S , g_L and g_I correspond to the electron spin, electron orbital and nuclear g -factors respectively and μ_B is the Bohr magneton. The values of these constants are provided for reference in Table 2.1. These factors enable the magnetic moment of the atom to be related to its quantum numbers, simplifying the expression. In the regime where the energy shift due to the external magnetic field is small compared to the fine splitting of the atom, the Hamiltonian is rewritten as

$$H_B = \frac{\mu_B}{\hbar} (g_J J_z + g_I I_z) B_z \quad (2.26)$$

where g_J is the Landé g factor describing the relationship of the magnetic moment to the total angular momentum. The Landé g -factor is related to the spin and orbital g -factors through

$$g_J = g_L \frac{J(J+1) - S(S+1) + L(L+1)}{2J(J+1)} + g_s \frac{J(J+1) + S(S+1) - L(L+1)}{2J(J+1)} \quad (2.27)$$

The relationship to the spin and orbital g -factors arises from a first-order perturbation to the energy of an atom under the influence of a weak external magnetic field [67]. If instead the energy shift due to the external magnetic field is small compared to the *hyperfine* splitting, F becomes the pertinent quantum number, with the Hamiltonian instead given by

$$H_B = \frac{\mu_B}{\hbar} g_F F_z B_z, \quad (2.28)$$

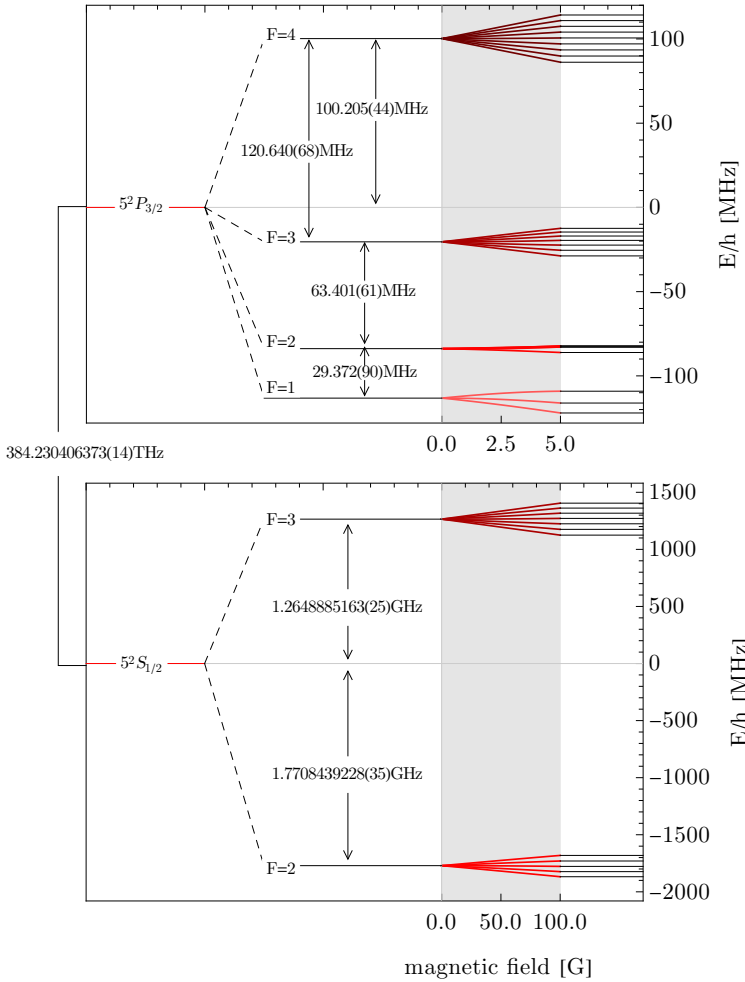


Figure 2.4: The D_2 level structure of ^{85}Rb illustrating the fine, hyperfine and magnetic splittings. Each two hyperfine manifolds and magnetic shift are shown to scale. The grey band indicates a magnetic field in the regime where the splitting is approximately linear with magnetic field and the energy is described by the Zeeman effect. The magnetic field splits the hyperfine levels into $2F + 1$ magnetic sub-levels. Note the different scales at which the Zeeman effect provides good representation of the magnetic splitting for the ground and excited-state manifolds.

where g_F is the *hyperfine* Landé g -factor defined as

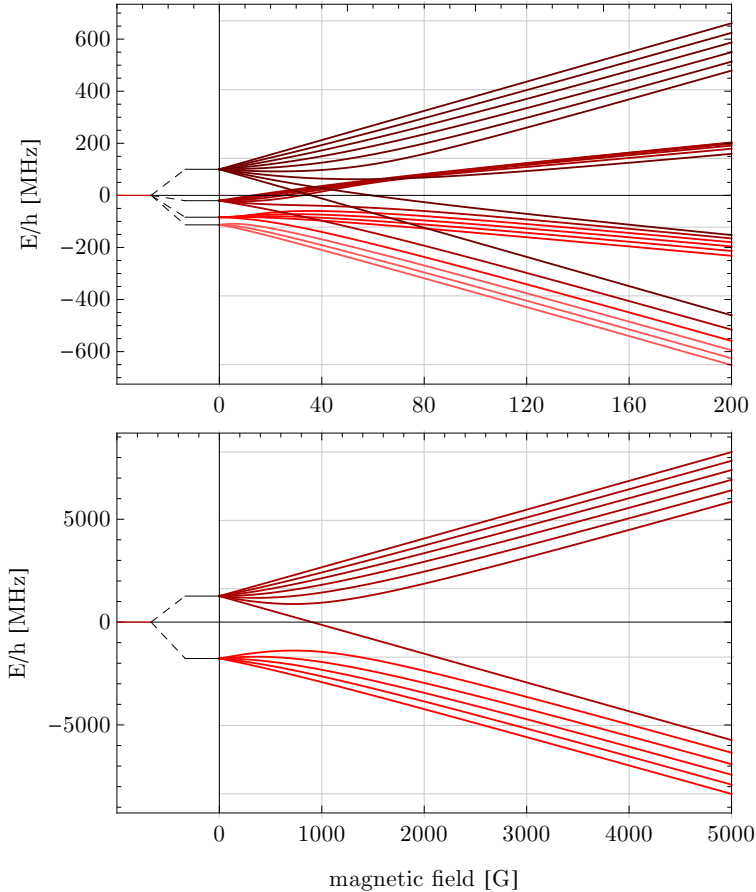
$$g_F = g_J \frac{F(F+1) - I(I+1) + J(J+1)}{2F(F+1)} + g_I \frac{F(F+1) + I(I+1) - J(J+1)}{2F(F+1)}. \quad (2.29)$$

In the low-field limit where the shift in energy of the atomic states is small compared to the hyperfine splitting the energy levels split linearly, giving rise to the Zeeman effect

$$\Delta E_{|F m_F\rangle} = \mu_B g_F m_F B_z. \quad (2.30)$$

This is illustrated in Figure 2.4, where the fine, hyperfine and magnetic sub-levels are shown to scale. The ground-state hyperfine manifold remains in the linear Zeeman regime for significantly higher magnetic fields than the excited-state manifold. As the magnetic field increases beyond this regime, the splitting of the energy levels becomes more complex, necessitating numerical diagonalisation of the interaction Hamiltonian,

Figure 2.5: Energy splittings in the anomalous Zeeman regime for the ^{85}Rb $5^2P_{3/2}$ (top) and $S_{1/2}$ (bottom) states under the influence of a strong external magnetic field. In this regime, the energy levels are no longer grouped according to their m_F quantum numbers, but instead according to m_J . The anomalous effects become evident at much lower magnetic fields for the $P_{3/2}$ level than the $S_{1/2}$ level. When operating at high magnetic field, it is important to take into account these nonlinear affects on the energy splitting.



$H = H_{\text{hfs}} + H_B$ where

$$H_{\text{hfs}} = A_{\text{hfs}} \mathbf{I} \cdot \mathbf{J} \quad (2.31)$$

$$+ B_{\text{hfs}} \frac{3(\mathbf{I} \cdot \mathbf{J})^2 + \frac{3}{2}(\mathbf{I} \cdot \mathbf{J}) - I(I+1)J(J+1)}{2I(2I-1)J(2J-1)} + H_B, \quad (2.32)$$

and

$$H_B = \frac{\mu_B}{\hbar} (g_J J + g_I I) B, \quad (2.33)$$

where A_{hfs} is the magnetic dipole constant, B_{hfs} is the electric quadrupole constant, provided in Table 2.1 and given in more detail in [66]. This high-field regime is known as the Paschen-Back regime [68] and describes the more complex response of the energy levels to a strong magnetic field.

Although the Hamiltonian given in Equation (2.32) typically requires numerical tools to calculate energy levels, a closed form analytic expression exists when either $J = \frac{1}{2}$, or $I = \frac{1}{2}$ as is the case in the ground-state D transition of ^{85}Rb and other species. Assuming that $J = \frac{1}{2}$, then the Hamiltonian reduces to a block diagonal matrix with analytic solution

given by the Breit-Rabi equation

$$E_{|F=I+1/2, m_F\rangle} = -\frac{\Delta E_{\text{hfs}}}{2(2I+1)} + g_I \mu_B m_F B \pm \frac{\Delta E_{\text{hfs}}}{2} \left(1 + \frac{4mx}{2I+1} + x^2 \right)^{1/2}, \quad (2.34)$$

where

$$\Delta E_{\text{hfs}} = A_{\text{hfs}} \left(I + \frac{1}{2} \right), \quad (2.35)$$

and

$$x = \frac{\mu_B(g_J - g_I)B}{\Delta E_{\text{hfs}}}. \quad (2.36)$$

Extreme care must be taken in the implementation of this solution as there is ambiguity in the sign of the final term where it must be determined by the sign of the specific m_J being calculated. Specifically, if we define our new quantum numbers as $m = m_I \pm m_J = m_I \pm \frac{1}{2}$, the sign in the Breit-Rabi formula is concomitant with this expression.

In the context of the two-level atom described in the previous sections, the magnetic field generates a modification to the resonant frequency such that

$$\Delta = \omega_{\text{rf}} - \omega_0, \quad (2.37)$$

where $\omega_0 = 2\pi \times B \times \gamma$ defines the splitting due to the magnetic field and $|\gamma| = \frac{g_F \mu_B}{\hbar}$ is the gyromagnetic ratio which defines a proportionality between the Larmor frequency and the strength of the external magnetic field. Relevant to the forthcoming chapter on magnetic resonance control, the magnetic sub-levels of the ground-state D_2 hyperfine manifold in ^{87}Rb in the low field regime split according to

$$\gamma_{F=1} = 2\pi \times 702.369 \text{ kHz/G} \quad (2.38)$$

$$\gamma_{F=2} = 2\pi \times 699.583 \text{ kHz/G}. \quad (2.39)$$

with the contribution due to non-linear effects being approximately

$$q = 2\pi \times B^2 \times 71.89 \text{ Hz}, \quad (2.40)$$

as determined through the Breit-Rabi equation.

The complex level structure arising from the application of external magnetic fields enables the precise spatial resolution of the magnetic resonance control scheme presented in Chapter 3 and Chapter 4. Through the use of a magnetic-field gradient a spatially-dependent resonance frequency is generated with adiabatic pulses used to generate spa-

tially-dependent population inversion. The relationship between internal energy levels and external magnetic fields is required in order to successfully and accurately model the scheme. Additionally, magnetic fields play a key role in the generation of soliton dynamics observed through non-destructive imaging methods in Chapter 8, with the specific operation of the probe laser requiring precise knowledge of the affect of a magnetic field on the imaging transition.

2.4 Gross-Pitaevskii equation

The Gross-Pitaevskii equation, independently derived by Gross [41, 69] and Pitaevskii [40], arises through a mean-field analysis for a distribution of atoms at zero temperature. In this regime, each atom is in the ground state and the evolution of the system can be found by describing the condensate using an order parameter, a complex scalar field defined as the expectation value of the many particle field operator.

This analysis begins by assuming the field operators describing the system can be written as a sum of single-particle wavefunctions and their respective annihilation operators such that

$$\hat{\Phi}(\mathbf{r}, t) = \sum_i \Phi_i(\mathbf{r}, t) \hat{a}_i, \quad (2.41)$$

where the annihilation operators lower the occupation of a particular mode, i , by 1. In this way, the field operators $\hat{\Phi}(\mathbf{r})$ and $\hat{\Phi}^\dagger(\mathbf{r})$ represent the creation and annihilation of a boson at position \mathbf{r} and obey the commutation relations

$$[\hat{\Phi}(\mathbf{r}'), \hat{\Phi}^\dagger(\mathbf{r})] = \delta(\mathbf{r}' - \mathbf{r}), \quad (2.42)$$

and

$$[\hat{\Phi}(\mathbf{r}'), \hat{\Phi}(\mathbf{r})] = [\hat{\Phi}^\dagger(\mathbf{r}'), \hat{\Phi}^\dagger(\mathbf{r})] = 0. \quad (2.43)$$

By definition, Bose-Einstein condensation occurs when a macroscopic number of atoms occupy the same single particle state, allowing the condensate component to be separated such that field operator is given by

$$\hat{\Phi}(\mathbf{r}, t) = \psi(\mathbf{r}, t) + \hat{\Phi}'(\mathbf{r}, t), \quad (2.44)$$

where $\hat{\Phi}(\mathbf{r}, t)$ represents the annihilation operator of the non-condensed fraction and

$$\psi(\mathbf{r}, t) \equiv \langle \hat{\Phi}(\mathbf{r}, t) \rangle, \quad (2.45)$$

represents an order parameter. The order parameter, often simply referred to as the condensate wavefunction, defines the density and phase through

$$\psi(\mathbf{r}, t) = \sqrt{n_0(\mathbf{r}, t)} e^{i\phi(\mathbf{r}, t)}, \quad (2.46)$$

with the density and phase given by $|\psi(\mathbf{r}, t)|^2$ and $\arg(\psi(\mathbf{r}, t))$, respectively. Given a cold, dilute gas, inter-particle interactions take the form of contact potentials [70] described using a Dirac delta function as

$$V(\mathbf{r}' - \mathbf{r}) = U_0 \delta(\mathbf{r}' - \mathbf{r}), \quad (2.47)$$

where \mathbf{r} and \mathbf{r}' correspond to the position of each particle and

$$U_0 = \frac{4\pi\hbar^2 a_s}{m} \quad (2.48)$$

defines the strength of interaction between the particles of mass m with s-wave scattering length a_s , generating repulsive interactions when $a_s > 0$ and attractive when $a_s < 0$. This framework leads to the closed form equation for the time-dependent evolution of the order parameter valid for describing macroscopic behaviour of low temperature bosonic systems dominated by variations at a scale larger than the mean distance between atoms. This, the so-called Gross-Pitaevskii equation, is given by

$$i\hbar \frac{\partial}{\partial t} \psi(\mathbf{r}, t) = \left[-\frac{\hbar^2 \nabla^2}{2m} + V_{\text{ext}}(\mathbf{r}) + U_0 |\psi(\mathbf{r}, t)|^2 \right] \psi(\mathbf{r}, t) \quad (2.49)$$

where V_{ext} describes the external trapping potential, typically taken to be that of the harmonic potential

$$V_{\text{ext}} = \frac{1}{2} m (\omega_x^2 x^2 + \omega_y^2 y^2 + \omega_z^2 z^2), \quad (2.50)$$

where ω_i is the trapping frequency in each dimension, with the potential defining the characteristic length scale of the harmonic oscillator

$$a_{\text{HO}} = \left(\frac{\hbar}{m\omega} \right)^{1/2}, \quad (2.51)$$

defined in each relevant dimension. The Gross-Pitaevskii equation is valid in the regime below the condensation transition temperature where the s-wave scattering length is much smaller than the average inter-particle spacing and when the number of atoms greatly exceeds unity. Typically the Gross-Pitaevskii equation is solved numerically to obtain the evolution of the condensate wavefunction, however an analytic ground state

exists in the regime where $Na_s/a \gg 1$, corresponding to a large number of atoms N with strongly repulsive interactions. This defines the Thomas-Fermi regime where the interaction energy is much larger than the kinetic energy, allowing the kinetic energy to be neglected in Equation (2.49). The Thomas-Fermi regime is a solution to the time-independent Gross-Pitaevskii equation, with the resulting analytic ground state given by

$$n(r) = |\psi(\mathbf{r})|^2 = \begin{cases} \frac{1}{U_0} [\mu - V_{\text{ext}}(\mathbf{r})] & \mu > V_{\text{ext}}(\mathbf{r}) \\ 0 & \text{otherwise} \end{cases} \quad (2.52)$$

where μ refers to the chemical potential, a Lagrange multiplier fixing the total particle number within the condensate and ensuring normalisation of the wavefunction to N particles. The chemical potential is given by

$$\mu = \frac{\hbar\bar{\omega}}{2} \left(\frac{15Na_s}{\bar{a}} \right)^{2/5} \quad (2.53)$$

where \bar{a} is a measure of the average harmonic oscillator length scale, given by

$$\bar{a} = \left(\frac{\hbar}{m\omega_{\text{ho}}} \right)^{1/2} \quad (2.54)$$

where $\bar{\omega} = (\omega_x\omega_y\omega_z)^{1/3}$. This analytic ground state is an inverted parabola, effectively a map of the potential within which the condensate resides. The parabola has a radius of

$$R_i = \frac{2\mu}{m\omega_i^2} \quad (2.55)$$

where $i \in \{x, y, z\}$ specifies the relevant spatial dimension. The Thomas-Fermi radius is typically larger than the harmonic oscillator length scale. The Thomas-Fermi approximation provides good agreement with numerical solutions in the appropriate regime, however relies on the order parameter varying sufficiently slowly across the cloud. This breaks down at the edges of the condensate, where a sharp discontinuity occurs and results in the kinetic energy diverging.

2.5 Healing scales

Various length scales are relevant to Bose-Einstein condensates and the mean-field Gross-Pitaevskii equation describing them. At the smallest scale is the s-wave scattering length a_s describing the length scale of inter-particle collisions, approximately 5 nm for ^{87}Rb and 20 nm for ^{85}Rb at zero magnetic field. At the larger scale is the Thomas-Fermi radius or

the trap dimensions given by the harmonic oscillator length scale a_{HO} , approximately $1.5 \mu\text{m}$ for a typical harmonic trap frequency of 50 Hz . In between exists the healing length [70, 71], a length scale extremely pertinent to the magnetic resonance control section of this thesis, and defined as

$$\xi_{\text{heal}} = \frac{\hbar}{\sqrt{2mn_0U_0}}, \quad (2.56)$$

where n_0 is the peak density. This length scale is a result of analytic solutions to the GPE in several regimes. One key example that elucidates this point is the classic box potential that confines a wavefunction $\psi(\mathbf{r})$ containing N particles to a volume V . When no interactions are present, this is the well-studied undergraduate problem resulting in sinusoidal basis functions. When interactions are present, the minimum energy state is more spread out, being optimal when the density of the condensate is almost constant across the entire volume. As the wavefunction nears a wall of the box it falls to zero density with functional form $\tanh(z/(\sqrt{2}\xi_{\text{heal}}))$. The length scale ξ_{heal} thus defines the length over which the perturbation generated by the wall of the box, is healed. For a ^{87}Rb condensate with peak number density of $10^{14} \text{ atoms/cm}^3$, the healing length is $\sim 270 \text{ nm}$.

An equivalent temporal scale is the healing time, which describes the time scale over which density fluctuations move a distance of the healing length given the relevant speed of sound in the condensate. The speed of sound in the uniform gas of the condensate is given by

$$s = \sqrt{\frac{n_0U_0}{m}}, \quad (2.57)$$

where n_0 is the peak density. The healing time is therefore given by

$$t_{\text{heal}} = \frac{\xi_{\text{heal}}}{s} = \frac{\sqrt{2m\xi_{\text{heal}}^2}}{\hbar}. \quad (2.58)$$

and represents the time over which density fluctuations occur. This gives an approximate bound on the time scale for which the magnetic resonance control scheme, detailed in Chapter 3, will efficiently operate. The scheme itself relies on the reversibility of the process, made more difficult by kinetic energy and inter-particle interactions present at time scales on the order of the healing time. By performing the control scheme faster than the healing time, typically on the order of $100 \mu\text{s}$, these effects are mitigated.

2.6 Solitons

Analytic solutions to equations of motion provide insight into behaviour of the system but are often only found for small excitations or under strict approximations. Perhaps surprisingly, the time-dependent non-linear Schrödinger equation has an exact solution in the form of solitary waves, or ‘solitons’. These solution arise from a balancing of the non-linear interaction term with the dispersion term and describe pulse-like waves that propagate without decaying or changing form. In the context of this research, these waves are often termed ‘solitonic’ owing to the fact that while the waves are soliton-like, they do not meet the strict theoretical criteria for a soliton. Having noted this, for simplicity, the term soliton and solitonic are used interchangeably henceforth.

Solitons are not solely restricted to the non-linear Schrödinger equation, having been observed in many other non-linear media and across numerous scientific fields, from the Korteweg-de Vries equation, describing the properties of shallow water waves [72] to modelling of financial markets [73]. Optical solitons have been observed in optical fiber as temporal pulses [74, 75] as well as spatial structures [76, 77], while experiments have produced excitations of non-propagating kinks in shallow water that is parametrically driven [78] and kinks in discrete mechanical systems [79]. Indeed, high-frequency dark solitons have been observed in magnetic films [80] as well as dissipative dark solitons in plasma [81]. In the context of Bose-Einstein condensates, solitons have a strong theoretical history with the exact solution to the Gross-Pitaevskii equation having been linked to that of the Korteweg-de Vries equation [82]. The theoretical results extend beyond the GPE to the non-linear Schrödinger equation (for which the GPE is a special case) with investigations into the collisions of solitons and the resulting dynamics [44]. Experimental work on solitons began soon after the realisation of Bose-Einstein condensates with matter-wave solitons being some of the first non-linear states observed [83–85]. In one-dimension, soliton solutions exist for attractive potentials, corresponding to density maximums. These so-called ‘bright’ solitons are self-bound states, localised to one-dimension. Higher order soliton modes also exist, including breathers [86, 87] and soliton trains [56] with solitons having been shown to be an extension to the Hermite-Gauss modes of the linear Schrödinger equation [88, 89], whereby the Hermite-Gauss modes smoothly transform to solitons as the non-linearity is increased. Non-stationary multiple dark solitons have been generated using phase imprinting methods [52, 90, 91] and matter-wave interferometry [92].

Unlike the soliton solutions found for shallow water waves, soliton solutions to the Gross-Pitaevskii equation with repulsive interactions exist as density depressions, with the difference being a result of the differing sign between their dispersion relations. These solitons, in analogy to their optical counterpart, are called ‘dark’ solitons. The functional

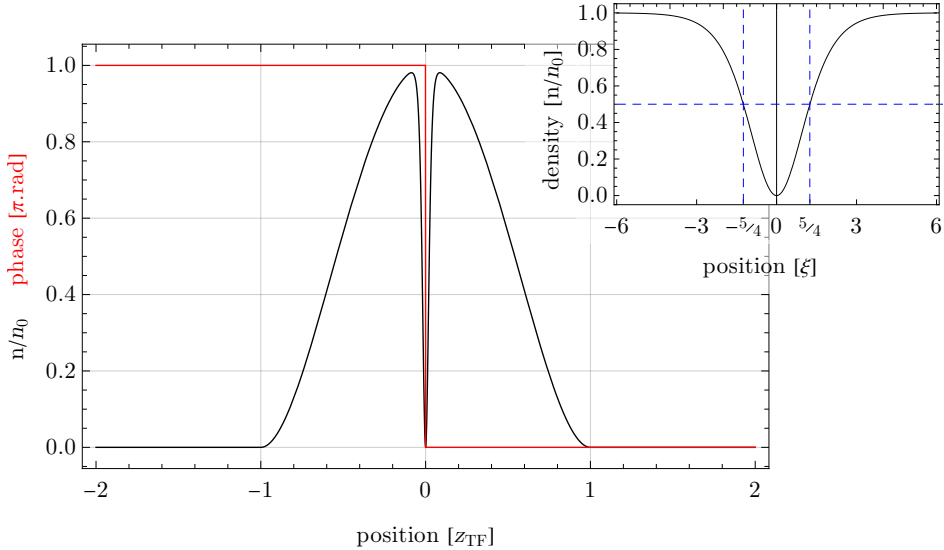


Figure 2.6: Example soliton in one dimension. The discontinuity in phase at the centre of the condensate causes a density hole to be carved out. For a π phase discontinuity the soliton is ‘dark’ and the density at the centre of the soliton is zero. For smaller phase discontinuities the depth of the soliton decreases and the soliton will oscillate in-trap. Inset shows a magnified view of the soliton and illustrates the width of the soliton being 2.5 times the healing length of the particular condensate.

form of these stationary solutions is found by extending the derivation of the healing length found in Section 2.5. This derivation considered a wavefunction confined to a box potential and found the solution near a wall. Extending this to the whole space, the form of the soliton is found to be

$$\psi(x) = \psi_0 \tanh\left(\frac{x - x_0}{\sqrt{2}\xi_{\text{heal}}}\right), \quad (2.59)$$

where x_0 describes the position of the centre of the soliton and

$$\xi_{\text{heal}} = \frac{\hbar}{\sqrt{2mn_0U_0}}, \quad (2.60)$$

is the healing length described in detail in Section 2.5. The density of a condensate with such a wavefunction is given by

$$|\psi(x)|^2 = |\psi_0|^2 \tanh^2\left(\frac{x - x_0}{\sqrt{2}\xi_{\text{heal}}}\right) \quad (2.61)$$

$$= |\psi_0|^2 \left[1 - \operatorname{sech}^2\left(\frac{x - x_0}{\sqrt{2}\xi_{\text{heal}}}\right)\right], \quad (2.62)$$

being the modulation of the original wavefunction with a sech shape corresponding to a density minimum and a discontinuity in the phase through the centre of the dip corresponding to exactly π radians. These so-called ‘black’ solitons correspond to a stationary

state of the GPE. The width of a dark soliton can be determined analytically, with the full-width at half-maximum (FWHM) given by

$$\text{FWHM} = 2\sqrt{2}\xi_{\text{heal}} \arctan\left(\frac{1}{\sqrt{2}}\right) \approx \frac{5\xi_{\text{heal}}}{2}, \quad (2.63)$$

being slightly larger than the healing length of the condensate. Matter-wave solitons have typically been experimentally generated using laser light as a ‘mask’ with an intensity that varies across the extent of the cloud. These methods rely on sharp boundaries in the pattern of the light in order to generate a phase kink on the condensate wavefunction, but are fundamentally limited by diffraction. This limitation arises from the finite resolvable spot size of a given optics system, with the diffraction limit being approximated by the size of the first order Airy disk and given by

$$x \approx 1.22 \frac{\lambda f}{D} \quad (2.64)$$

where light of wavelength λ , apertured to a diameter D passes through a lens of focal length f [93]. This fundamental limitation means that such optical methods generate imperfect dark solitons, typically being resolution limited to approximately half the wavelength (0.5 μm). These imperfect solitons are non-stationary solutions, where the density does not fall fully to zero at the centre on the condensate. These ‘grey’ solitons have a phase discontinuity diverging from π and a non-zero velocity causing them to oscillate back and forth within the trap. In order to surpass this limitation, a magnetic resonance technique is proposed in Chapter 3 and Chapter 4 whereby the dependence of the spatial resolution on the wavelength of light is removed, instead depending on the magnitude of a magnetic-field gradient and exploiting adiabatic transfer to generate sharp spatial structures in the condensate wavefunction.

Part I

Magnetic Resonance Control

Magnetic Resonance Control Theory

The following two chapters present theoretical work on magnetic resonance control and were developed in collaboration with Lincoln Turner, Russell Anderson and Lisa Starkey from Monash University and summarised in:

- **P. B. Wigley, L. M. Starkey, S. S. Szigeti, M. Jasperse, J. J. Hope, L. D. Turner, and R. P. Anderson.** Precise wave-function engineering with magnetic resonance. *Physical Review A* **96**, 013612 (2017). DOI: 10.1103/PhysRevA.96.013612.

The precise engineering of a quantum wavefunction at its most fundamental length scale is vital to the development of many quantum technologies including simulation and emulation [94–97], topological quantum computing [98, 99], spintronics [100, 101], and quantum metrology [34, 102–104]. Effective wavefunction engineering requires high spatial fidelity, ideally being finer than the fundamental length scale of the system. If this requirement is not met, any structure written to the wavefunction will only be approximated. For a Bose-Einstein condensate (BEC) the relevant length scale is the healing length and is typically shorter than the optical diffraction limit. For this reason, optical techniques are inferior for wavefunction engineering, requiring alternative methods to bypass the diffraction limit [105, 106]. The following two chapters outline a theoretical scheme, referred to as magnetic resonance control, that boasts a resolution uncoupled from the optical wavelength and therefore capable of sub-diffraction resolution. In addition, magnetic resonance control can be performed faster than the fundamental time scale, the healing time, allowing the target state to be written before the system can respond in any adverse way. Precise control can be achieved either through density engineering, phase engineering or a combination of the two. This scheme utilises phase engineering in order to create a spatially-dependent phase, with the exemplar system being a Bose-Einstein condensate. In doing so, the spatially-dependent wavefunction $\psi(z)$ describing the condensate is manipulated such that at a time T at the conclusion of the scheme

$$\psi(z, 0) \rightarrow \psi(z, T) = \psi(z) e^{i\phi(z)}, \quad (3.1)$$

where $\phi(z)$ is the arbitrary desired spatially-dependent phase written by the protocol.

The central advantage of the magnetic resonance control scheme is the spatial resolution being disconnected from the wavelength of light used for coupling, allowing the diffraction limit to be overcome. This feature arises from the combined mechanism of the adiabatic theorem discussed in Section 2.2 and the effect of an external magnetic-field gradient, discussed in Section 2.3. The adiabatic theorem shows that, given a constant Rabi frequency, a detuning swept slowly enough will allow an atom to transition from the ground to excited state with high probability. Providing a constant offset to this detuning sweep causes the probability of excitation to change. This offset can be achieved by application of an external magnetic field which, through the Zeeman effect, changes the energy of magnetic sublevels. Crucially, a magnetic-field *gradient* creates a spatially dependent detuning offset, resulting in a resonance ‘width’ for the adiabatic pulse. With such a gradient, the temporal sweep of the detuning now generates an inversion slice in a spatial ensemble of atoms, with excitation only occurring within the band where adiabatic transfer occurs with high probability. This mechanism allows the spatial selectivity to be entirely dependent on the strength of the magnetic-field gradient and not the wavelength of light, ensuring the scheme is not fundamentally limited by diffraction.

The capability of the magnetic resonance control scheme for precise wavefunction engineering is demonstrated in Chapter 4 through simulation of the scheme applied to a Bose-Einstein condensate with the goal of writing a stationary dark soliton to the condensate wavefunction. Optical techniques, despite being inherently diffraction limited, have used local phase shifts produced via off-resonant lasers to generate a soliton [52, 107] in a Bose-Einstein condensate. In two-dimensions, vortices have been created using Laguerre-Gaussian beams to transfer angular momentum, effectively ‘stirring’ the condensate [108]. Wavefunction engineering not limited by diffraction has been achieved using novel approaches such as inverting a trapping potential adiabatically, generating vortices [53] and skyrmions [54]. Despite better resolution, these techniques are inherently limited to producing symmetric structures and are required to be slow on the time scale of the system. Optically induced magnetic resonance has been used to create a vortex in a condensate [109], as well as an unstable soliton [85]. Since a soliton in a Bose-Einstein condensate has a width on the order of the healing length, this example provides a strict test of any wavefunction engineering scheme and is therefore a useful demonstration of the capability for precise quantum state engineering using magnetic resonance control.

The following chapter outlines the theoretical background for magnetic resonance control, outlining a model scheme for generating a density notch in a spatial ensemble of two-level atoms. The mechanics of adiabatic pulses are explored, with the required gradient found to be dependent on the particular adiabatic pulse parameters and the particular condensate the scheme is applied to. These parameters are discussed and op-

timised with the aim of generating an inversion slice with the sharpest edge while still encompassing the condensate. Given this constraint, the gradient required to produce a structure smaller than the diffraction limit is shown to be extremely experimentally challenging, being on the order of 10^3 G/cm (this is discussed in the context of experimental application in Subsection 4.2.6). Indeed, achieving the required parameters in an experimental setting would be an immense technical achievement. Despite this, the scheme does represent an alternative method for wavefunction engineering not fundamentally limited by diffraction.

3.1 Model scheme

While more complex methods are used to simulate the scheme in Chapter 4, this chapter illustrates the fundamental concepts through a simple two-level atom model. This model captures the salient features while keeping the analysis simple. The two-level macroscopic wavefunction $\psi(z)$ is used with the wavefunction described in the basis $\{\psi_{\downarrow}(z), \psi_{\uparrow}(z)\}^T$. The system is initially assumed to be entirely in the ground state ψ_{\downarrow} , while displaying uniform phase as shown in Figure 3.1(a). The scheme begins by transferring the left side of the condensate to the excited state. This is achieved by applying a linear magnetic-field gradient, exploiting the Zeeman effect to split the energy levels linearly across the condensate. In doing so, the cloud now has a spatially-dependent resonance that can be used to excite a specific band of the condensate using an adiabatic coupling pulse that sweeps through the cloud. Applying such a pulse transfers a slice of the condensate to the excited state. By adjusting the pulse appropriately, one edge of the slice may be positioned at the centre of the condensate ensuring that, after application of the pulse, half the condensate is in the ground state and half is in the excited state, as illustrated in Figure 3.1(b).

Once half the cloud has been excited, the radio-frequency coupling pulses and magnetic-field gradient are extinguished. The states are allowed to freely evolve, with the excited state evolving faster than the ground state. By allowing the free evolution to occur for a specific interval of time, a π phase difference will accrue between the two states, as illustrated in Figure 3.1(c). Equally the time taken to acquire the phase difference can be reduced by applying a magnetic-field bias which changes the splitting of the levels uniformly across the cloud, ensuring that the excited state evolves relative to the ground state at a tunable rate. Specifically, the bias field must be set to produce a detuning of

$$\Delta_{\phi} = \pi/T_{\phi}F \quad (3.2)$$

for a time of T_{ϕ} at which point a phase difference of exactly π will have accrued. Once

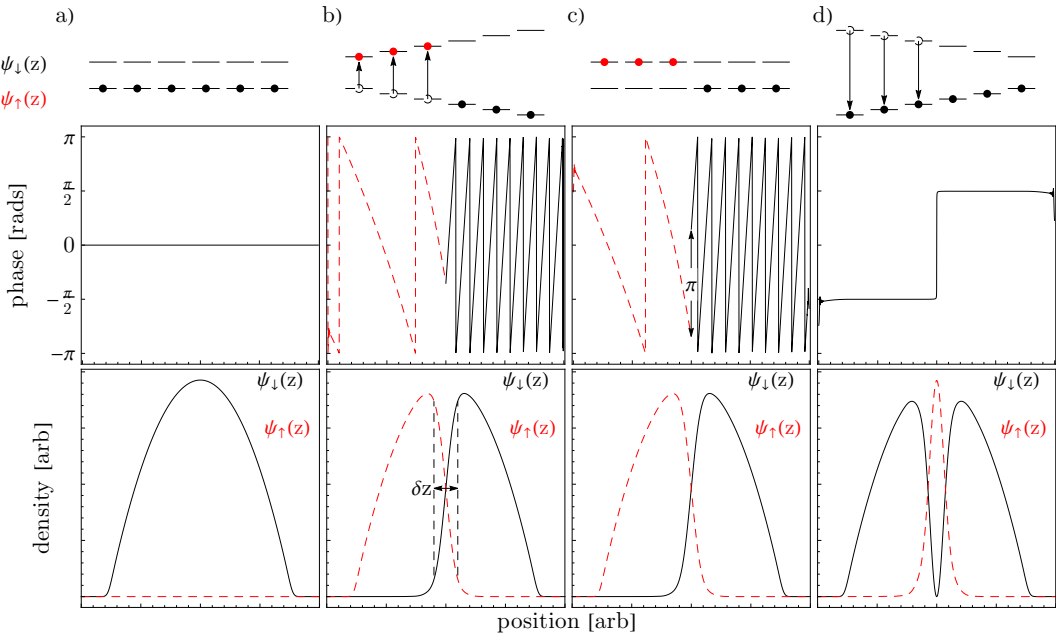


Figure 3.1: (a) Initially the system is in the ground state of the two-level system, $\psi_{\downarrow}(z)$, with uniform phase ($\arg \psi_{\downarrow}(z) = 0$). (b) A linear magnetic-field gradient is applied across the condensate, splitting the energy levels linearly in space. An adiabatic coupling pulse is applied, driving transitions between the two states. Since the magnetic-field gradient changes the resonant frequency of each atom according to the position in space, only a segment of the cloud is excited. By centring one edge of the slice at zero, exactly half the cloud may be transferred to the excited state, $\psi_{\uparrow}(z)$. (c) Upon completion of the coupling pulse, half the condensate has been transferred to the excited state. The magnetic field is then extinguished, and the system allowed to freely evolve until a π phase shift between the two states is acquired. At this point the magnetic-field gradient is reversed and reapplied along with time reversed coupling pulses. This causes the excited state to be driven back to the ground state as in (d). At the culmination of the pulse scheme, the system is returned to the ground state, now with a π phase kink and corresponding density minimum.

this relative phase difference exists, the original magnetic-field gradient is reversed and reapplied, splitting the energy levels in the opposite way. A time reversed version of the adiabatic coupling pulse is applied, causing the population in the excited state to return to the ground state. This leaves the condensate entirely in the ground state, but with a π phase kink and a notch in density at the centre of the cloud. By optimising the pulse parameters and magnetic-field gradient, the sharpness of the phase discontinuity and the density notch may be made such that the final state is a soliton of correct width, representing phase engineering at the healing length scale. The details of the magnetic-field gradient and adiabatic pulses are key to the success of the scheme.

3.2 Adiabatic pulses

The particular adiabatic pulse used plays an important role in the success of the magnetic resonance control scheme. These pulses are common to both nuclear magnetic resonance and magnetic resonance imaging. For the past half a century, these fields have optimised

radio-frequency pulses that obey the adiabatic theorem in order to produce a specific desired outcome such as inversion or refocussing [110]. Adiabatic pulses are valuable in this context as they are robust to field inhomogeneities and offsets in frequency. This improves the experimental viability of adiabatic pulses over methods like resonant π -pulses, as they are less susceptible to imperfections in an experimental apparatus.

3.2.1 Landau-Zener pulse

The simplest adiabatic pulse is the Landau-Zener pulse, consisting of a linear sweep of detuning with a constant coupling, as shown in the top right inset of Figure 3.2 and given by

$$\Omega(t) = \Omega_0, \quad (3.3)$$

$$\Delta(t) = \Delta_0 \left(t - \frac{t_{\text{pulse}}}{2} \right) + \Delta_1, \quad (3.4)$$

where Ω_0 is the peak amplitude of the Rabi frequency, Δ_0 is the magnitude of the detuning sweep, Δ_1 is some frequency offset and $t \in [0, t_{\text{pulse}}]$. This pulse is the archetypal scheme corresponding to adiabatic passage outlined in Section 2.2, and giving rise to the Landau-Zener probability given in Equation (2.23). Figure 3.2 illustrates the effect of the Landau-Zener pulse on a two-level system that is initially in the ground state, with the dynamics found by numerically solving the Hamiltonian in Equation (2.10). For short pulse lengths, Rabi oscillations dominate with the population seen to oscillate between the ground and excited state over the duration of the pulse at a frequency given by the

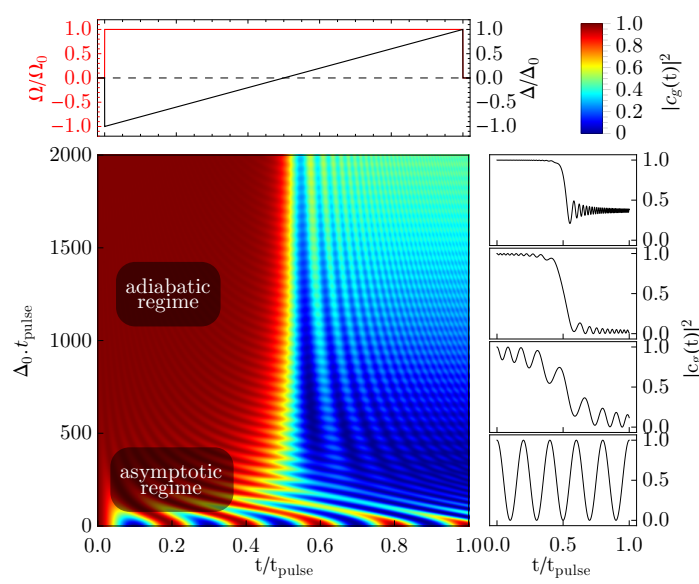


Figure 3.2: The effect of a Landau-Zener pulse on the ground-state population of a two-level system initially in the ground state. For small sweep rates, the system displays resonant Rabi oscillations (bottom right column). As the pulse length increases, the system begins to exhibit adiabatic population inversion mixed with off-resonant Rabi oscillations. For large pulse durations, the system displays efficient adiabatic population inversion with minor remnant oscillations. As the sweep rate is increased beyond this, the percent inversion decreases. The form of the Landau-Zener adiabatic pulse is shown at the top. The Rabi frequency (red) is constant in time while the detuning (black) linearly sweeps.

effective Rabi frequency. As the pulse length is increased, adiabatic dynamics begin to be displayed with efficient population inversion occurring with minor off-resonant Rabi oscillations present. As the duration is increased further, the efficiency of the adiabatic transfer begins to decrease. For a pulse where the magnitude of the detuning sweep is equal to the Rabi frequency, the pulse duration for full adiabatic transfer is approximately an order of magnitude slower than a resonant π -pulse. Although more efficient and faster adiabatic pulses exist and are key to the magnetic resonance control scheme presented in this chapter, the Landau-Zener pulse is theoretically simple, facilitating deeper analysis.

The regimes illustrated by Figure 3.2 can be quantified analytically, allowing the effective parameter space to be reduced. In general, and for any arbitrary pulse shape, the adiabaticity parameter, q is defined as

$$q = \frac{\tilde{\Omega}(t)}{|\dot{\theta}|}, \quad (3.5)$$

where $\tan \theta = \Delta(t)/\Omega(t)$ and $\tilde{\Omega}(t) = \sqrt{\Omega(t)^2 + \Delta(t)^2}$. Expanding and simplifying, it can be shown that

$$q = \frac{(\Delta(t)^2 + \Omega(t)^2)^{3/2}}{\Omega(t)\dot{\Delta}(t) - \Delta(t)\dot{\Omega}(t)}, \quad (3.6)$$

which, for the Landau-Zener pulse, reduces to

$$q = \frac{(t^2\Delta_0^2 + \Omega_0^2)^{3/2}}{\Delta_0\Omega_0}. \quad (3.7)$$

The adiabaticity varies over the duration of the pulse with the minimum adiabaticity occurring as the pulse sweeps through resonance. At this point the adiabaticity is given by $q_{\min}^{(LZ)} = \Omega_0^2/\Delta_0$ with the fraction of population left in the ground state given by

$$P_{LZ} = \exp\left(-\frac{\pi}{2}q_{\min}^{(LZ)}\right) = \exp\left(-\frac{\pi}{2}\frac{\Omega_0^2}{\Delta_0}\right). \quad (3.8)$$

If the pulse parameters are chosen such that the minimum adiabaticity, $q_{\min}^{(LZ)} \gg 1$, then the system is operating in the adiabatic limit and the excited state can be perfectly and efficiently populated through adiabatic passage. This expression corresponds to the limit that the pulse length goes to infinity and specifically that $|c_g(t \rightarrow -\infty)|^2 = 1$ and $|c_g(t \rightarrow \infty)|^2 = P_{LZ}$. For faster pulses, off-resonant Rabi oscillations become a significant factor in the evolution providing a second bound to the effective parameter space. In practice, both the adiabatic limit and off-resonant Rabi oscillations reduce the space of viable pulse parameters.

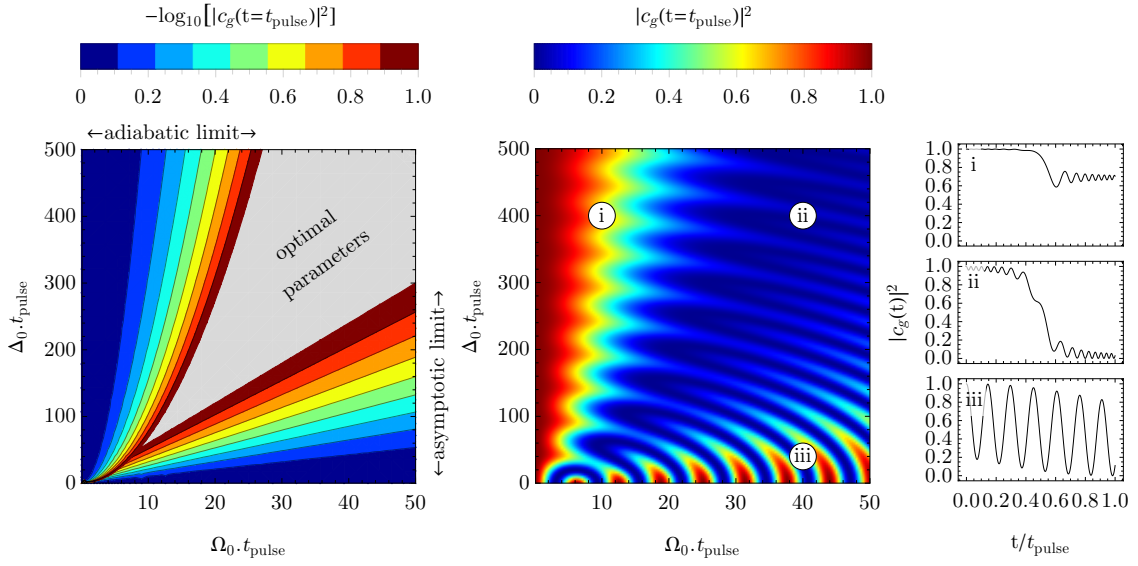


Figure 3.3: **Left:** Analytic regimes for the Landau-Zener pulse. The asymptotic limit corresponds to the off-resonant Rabi oscillations. The adiabatic limit corresponds to the Landau-Zener probability. Note the log scale. The red contour corresponds to 10% of the total population. **Middle:** Numerical results showing the final population in the ground state at the culmination of the pulse as found though numerically solving Equation (2.10). At the bottom of the plot the asymptotic limit can be seen corresponding to Rabi oscillations with full population inversion occurring every $\Omega t_{\text{pulse}} = \pi$ on resonance. On the left of the plot is the adiabatic limit whereby the efficiency of the adiabatic passage decreases. The blue band corresponds to regions where efficient adiabatic population inversion occurs.

The bound on effective parameters due to off-resonant Rabi oscillations can be found by considering the analytic solution to the two-level atom Hamiltonian in the presence of a constant Rabi frequency and constant detuning corresponding to the value at the limits of the Landau-Zener pulse. As evidenced in the solutions given by Equation (2.15), the Rabi oscillations have a magnitude of

$$\epsilon = \frac{\Omega^2}{\Omega^2 + \Delta^2}, \quad (3.9)$$

which in the case of the limits of the Landau-Zener pulse, corresponds to a magnitude of

$$\epsilon = \frac{\Omega_0^2}{\Omega_0^2 + \frac{\Delta_0^2}{2}}. \quad (3.10)$$

This parameter estimates the asymptotic limit which, along with the adiabatic limit, bound the problem space and constrain the set of viable parameters for efficient adiabatic population inversion. Both the adiabatic and asymptotic limit can be seen in the left of Figure 3.3 where magnitude of the population remaining in the ground state at the culmination of the pulse is shown on a log scale. By selecting an acceptable amount of remnant population, a bound on the parameter space can be obtained. These limits are seen in

middle of Figure 3.3 where the two-level Hamiltonian has been numerically solved with the populations at the end of the pulse shown as a function of the pulse area, defined as Ωt_{pulse} . Typically the Rabi frequency is limited by the particular experiment. Given this, and selecting an acceptable pulse fidelity, the pulse duration can be determined. In contrast to a resonant π -pulse, a Landau-Zener pulse of the same Rabi frequency requires approximately 30 times the pulse length to achieve a population inversion of $> 99\%$ with off-resonant Rabi oscillations limited to $< 1\%$. Whilst the Landau-Zener pulse is capable of adiabatic population inversion, more nuanced pulses exist that use the pulse shape to adjust the adiabaticity across the duration of the pulse to allow better efficiency and importantly, faster pulses.

3.2.2 Hyperbolic-secant pulse

One particular adiabatic pulse known for having higher adiabaticity at shorter times is the hyperbolic-secant pulse. This pulse is effectively a truncated and smoothed version of the Landau-Zener pulse. Whereas the Landau-Zener pulse contains a linear ramp in detuning, the hyperbolic-secant pulse has a smooth sweep with a tanh functional form. Further, where the Landau-Zener pulse maintains a constant coupling for the duration of the pulse, the hyperbolic-secant pulse ramps the Rabi frequency up and down in a ‘chirp’ with a sech functional form, as illustrated in the top of Figure 3.4. This ensures that the majority of the coupling corresponds to the steepest part of the detuning sweep. In addition the coupling goes to zero at the limits of the pulse, minimising off-resonant Rabi oscillations that were deleterious to the Landau-Zener pulse. The hyperbolic-secant pulse is given by a Rabi frequency and detuning of

$$\Omega(t) = \Omega_0 \operatorname{sech} \left[\beta \left(t - \frac{t_{\text{pulse}}}{2} \right) \right], \quad (3.11)$$

$$\Delta(t) = \Delta_0 \tanh \left[\beta \left(t - \frac{t_{\text{pulse}}}{2} \right) \right] + \Delta_1, \quad (3.12)$$

respectively, where Ω_0 is the peak coupling power, Δ_0 is the magnitude of the detuning sweep, β is the sweep rate, t_{pulse} is the length of the pulse such that $t \in [0, t_{\text{pulse}}]$ and Δ_1 represents a constant offset for the detuning sweep. The hyperbolic-secant pulse imitates the Landau-Zener pulse in the limit that $\beta t_{\text{pulse}} \rightarrow 0$ and the detuning is $\Delta_0 \rightarrow \Delta_0 / \beta$.

The hyperbolic-secant pulse enables faster adiabatic passage as a result of shifting the minimum adiabaticity away from the avoided crossing. This can be seen by evaluating Equation (3.6), with the adiabaticity parameter for the hyperbolic-secant pulse given by

$$q_{\text{HS}} = \frac{\Delta_0^2}{\Omega_0 \cosh^2(\beta t)} \left(\frac{\Omega_0^2}{\Delta_0^2} + \cosh^2(\beta t) - 1 \right)^{3/2}. \quad (3.13)$$

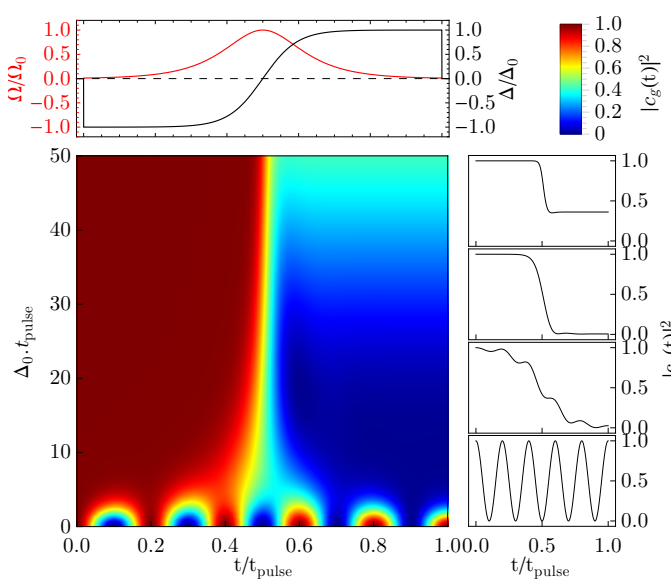


Figure 3.4: The effect of a hyperbolic-secant pulse on the ground-state population of a two-level system initially entirely in the ground state. The key difference to the equivalent plot in Figure 3.2 is the necessary time scale for efficient adiabatic population transfer, being approximately two orders of magnitude smaller for the hyperbolic-secant pulse for a given Rabi frequency. This is a result of the form of the hyperbolic-secant pulse scheme, where the majority of coupling occurs at the fastest part of the detuning sweep as indicated by the top figure. In addition, off-resonant Rabi oscillations are minimised as a result of the coupling asymptoting to zero at the culmination of the pulse.

Unlike the Landau-Zener pulse, the minimum adiabaticity across the duration of the pulse does not necessarily occur as the resonance is swept through. Whilst in the limit that the hyperbolic-secant pulse reflects the shape of the Landau-Zener pulse, the minimum adiabaticity is the same. Outside this limit the minimum adiabaticity deviates. For a general hyperbolic-secant pulse, the minimum adiabaticity is given by

$$\eta_{\min}^{(\text{HS})} = \begin{cases} \frac{3\sqrt{3}\Delta_0^2}{2\Omega_0} \sqrt{\frac{\Omega_0^2}{\Delta_0^2} - 1} & \frac{\Omega_0}{\Delta_0} > \sqrt{3}/2 \\ \frac{\Omega_0^2}{\Delta_0} & \frac{\Omega_0}{\Delta_0} \leq \sqrt{3}/2 \end{cases} \quad (3.14)$$

This is plotted as a function of the Rabi frequency and detuning in Figure 3.5 where it can be seen that above a value of $\mu = \Omega_0/\Delta_0 \approx 2$, the adiabaticity is approximately independent of μ . As in the Landau-Zener case, this provides a measure of the efficiency of the adiabatic passage assuming that the pulse duration is such that the system is already operating in the adiabatic regime. As such that pulse length and sweep rate are not present in the adiabaticity relationship. These parameters instead dictate the amount of off-resonant Rabi oscillations in the asymptotic regime. These oscillations can be estimated, as before, through the Rabi equations, given the value of the Rabi frequency and detuning at the culmination of the pulse. This produces an estimated amplitude of

$$\epsilon = \frac{\Omega^2}{\Delta^2 + \Omega^2} \quad (3.15)$$

$$= \frac{1}{1 + \mu^2 (\alpha^{-2} - 1)}, \quad (3.16)$$

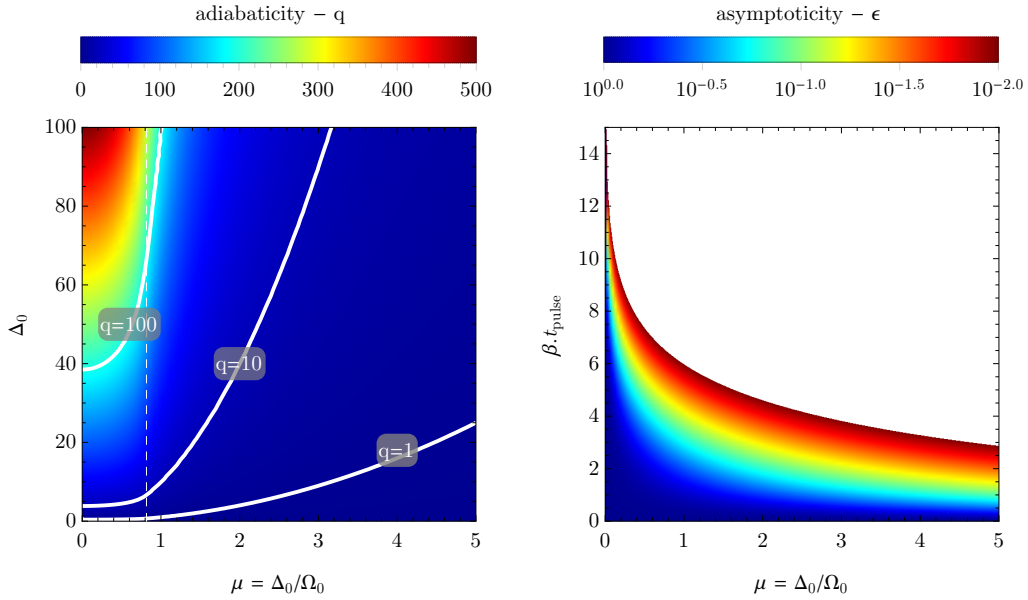


Figure 3.5: **Left:** the minimum hyperbolic-secant adiabaticity parameter, $q_{\min}^{(\text{HS})}$, as given by Equation (3.14). A value of $q \gg 1$ ensures the pulse is in the adiabatic limit assuming $t \rightarrow \infty$ and the system is already operating in the adiabatic regime. For values of $\mu = \Omega_0/\Delta_0 > 2$, q is approximately independent of μ . Given a particular μ , Δ_0 can be optimised for a required q . **Right:** the magnitude of off-resonant Rabi oscillations as given by the final value of the hyperbolic-secant pulse provides the asymptotic limit as described by Equation (3.16). The solution is only shown down to a value of $\epsilon = 10^{-2}$, with the white region representing off-resonant Rabi oscillations of lower magnitude than this cutoff tolerance. In general a $\beta t_{\text{pulse}} > 8$ will provide minimal off-resonant Rabi oscillations. In practice a set of parameters that lie in the adiabatic region with $q \gg 1$, while also below a set tolerance in the asymptotic limit will provide efficient adiabatic population inversion.

where $\alpha = \Omega_0 \operatorname{sech}(\beta/2)$ is the value of the Rabi frequency at the end of the pulse and $\mu = \Delta_0/\Omega_0$ is the normalised pulse bandwidth. The magnitude of the Rabi oscillations are shown in the right of Figure 3.5 down to one percent of the total amplitude. An ideal pulse operates with the βt_{pulse} lying above this regime and an adiabaticity $q \gg 1$. By numerically solving the two-level Hamiltonian using the hyperbolic-secant pulse, these regimes can be explicitly seen. This is shown in Figure 3.6 where the final population is given for a number of values of the pulse truncation α . For large values of α where the hyperbolic-secant pulse imitates the Landau-Zener pulse, the plot resembles that of Figure 3.3. For larger values of α , the off-resonant Rabi oscillations are decreased and the regime where efficient population inversion occurs increases. This also allows the pulse duration to decrease far beyond anything possible with the Landau-Zener scheme. Comparing once more to a resonant π -pulse, a hyperbolic-secant pulse of the same Rabi frequency requires approximately 5 times the pulse length to achieve a population inversion of $> 99\%$ with off-resonant Rabi oscillations limited to $< 1\%$ compared to 30 times for the Landau-Zener pulse. Since the system of choice for the magnetic resonance control scheme is a Bose-Einstein condensate where the relevant time scale is the healing

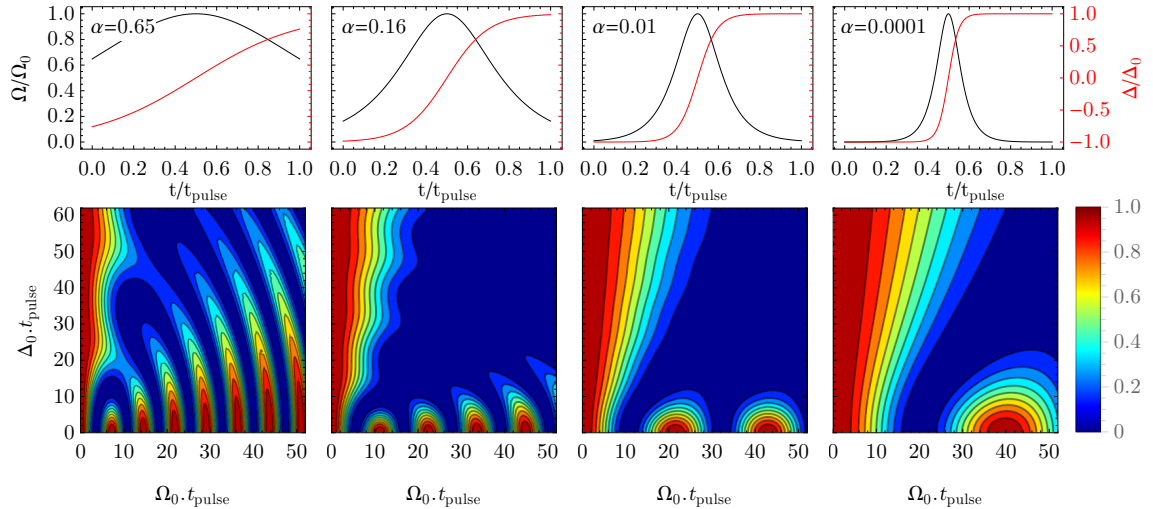


Figure 3.6: Population at end of hyperbolic-secant pulse sequence for a number of values of the truncation parameter, α . The blue region indicates the smallest residual ground-state population. Best parameters exist in this regime, bounded below in detuning and Rabi frequency by off-resonant Rabi oscillations and the adiabatic limit respectively.

length (on the order of $\sim 100 \mu\text{s}$ for a typical condensate), the hyperbolic-secant pulse provides a means of performing adiabatic population inversion fast enough that harmful dynamics are minimised.

3.2.3 Spatial selectivity using a magnetic-field gradient

In order to perform wavefunction engineering, the scheme requires a method of addressing different positions in space. This is enabled through a magnetic-field gradient which provides a spatially-dependent detuning offset to the system through the Zeeman effect. This offset shifts the position of the avoided crossing, and alters the amount of population transfer for a given adiabatic pulse as a function of the position in space. By using large magnetic-field gradients, the spatial selectivity of the adiabatic pulses is increased, allowing for precise manipulation of the macroscopic wavefunction. The mechanism for this process is given by the detuning offset, Δ_1 , as indicated in Equation (3.12). Specifically, the offset is given by

$$\Delta_1 = 2\pi \times B \times \gamma, \quad (3.17)$$

where

$$|\gamma| = \frac{g_F \mu_B}{\hbar} \quad (3.18)$$

is the gyromagnetic ratio describing the proportionality between the Larmor frequency and the strength of the magnetic field. Since the scheme exploits a magnetic-field *gradient*,

Δ_1 is in fact spatially dependent through B and results in a uniquely traversed avoided crossing for position in space. This results in a specific spatial slice of the condensate being inverted by the adiabatic pulse, with the width of the slice dictated by the strength of the gradient and the parameters of the adiabatic pulse. Choosing the correct gradient and parameters is crucial to the success of the scheme.

3.3 Hyperbolic-secant pulse heuristics

In order to codify the choice of parameters for the scheme, a set of heuristics is developed through analysis of the two-level atom model. This allows the problem to be recast to that of optimising only a single parameter. In the adiabatic limit there exists a solution for the population after application of the hyperbolic-secant pulse [111], given by

$$F_z = \operatorname{sech} \left[\pi \left(\frac{\Delta_0}{2\beta} + \frac{\Delta_z}{2\beta} \right) \right] \operatorname{sech} \left[\pi \left(\frac{\Delta_z}{2\beta} - \frac{\Delta_0}{2\beta} \right) \right] \cos \left[\pi \sqrt{\left(\frac{\Omega_0}{\beta} \right)^2 - \left(\frac{\Delta_0}{\beta} \right)^2} \right] \\ + \tanh \left[\pi \left(\frac{\Delta_0}{2\beta} + \frac{\Delta_z}{2\beta} \right) \right] \tanh \left[\pi \left(\frac{\Delta_z}{2\beta} - \frac{\Delta_0}{2\beta} \right) \right] \quad (3.19)$$

and $\Delta_z = \Delta_1$, altered to reflect the role of the detuning offset in the spatial selectivity and the mapping between position and detuning with Δ_1 effectively corresponding to a particular position in space. F_z corresponds to the longitudinal spin projection, which is related to the population in each level by

$$|c_{g,e}(t)|^2 = \frac{1 \pm F_z}{2}. \quad (3.20)$$

Applying this transformation, the final population in the ground state at the conclusion of the hyperbolic-secant pulse is given by

$$P_{HS} = \frac{\cosh \left(\frac{\pi}{\beta} \sqrt{\Omega_0^2 - \Delta_0^2} \right) + \cosh \left(\frac{\pi}{\beta} \Delta_z \right)}{\cosh \left(\frac{\pi}{\beta} \Delta_0 \right) + \cosh \left(\frac{\pi}{\beta} \Delta_z \right)}. \quad (3.21)$$

Equation (3.21) corresponds to the limit that the pulse length goes to infinity such that $|c_g(t \rightarrow 0)|^2 = 1$ and $|c_g(t \rightarrow \infty)|^2 = P_{HS}$, but nevertheless reflects the off-resonant Rabi oscillations, breaking down for large values of β . In the limit that $\beta \rightarrow 0$ and $\Delta_0 = \Delta_0/\beta$, the hyperbolic-secant pulse imitates the Landau-Zener pulse with probability given by

$$\lim_{\beta \rightarrow 0} P_{HS} = \exp \left(-\frac{\pi}{2} \frac{\Omega_0^2}{\Delta_0} \right) = P_{LZ}, \quad (3.22)$$

where P_{LZ} is the Landau-Zener probability given by Equation (2.23). It becomes useful to consider the problem using the following dimensionless parameters

$$\mu = \frac{\Delta_0}{\Omega_0} \quad (3.23)$$

$$\Gamma = \frac{\Omega_0}{\mu\beta} \quad (3.24)$$

$$\Delta_z = d\mu\Omega_0, \quad (3.25)$$

which simplifies the expression for the population such that

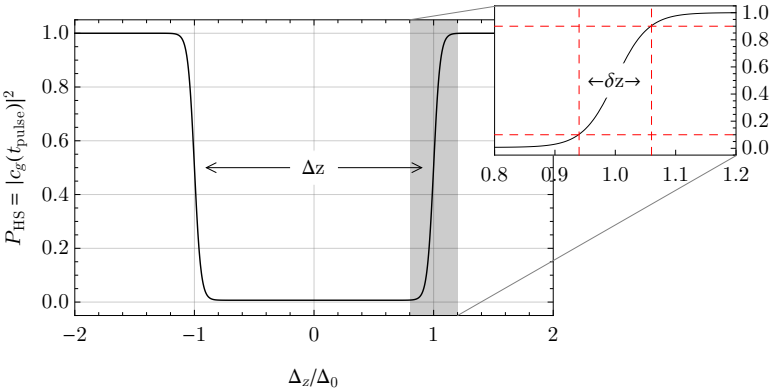
$$P_{HS} = \frac{\cosh(\pi\Gamma\mu^2) - \cosh(\pi\Gamma\mu\sqrt{\mu^2 - 1})}{\cosh(\pi\Gamma\mu^2) + \cosh(\pi\Gamma d\mu^2)}, \quad (3.26)$$

where $d = \frac{\Delta_z}{\Delta_0}$ corresponds to a position in space providing the mapping between magnetic-field gradient and detuning. Figure 3.7 shows, for a particular set of parameters, the excited-state population after the first pulse as a function of this effective position. Given the position-dependent bias, only a certain band of positions undergo population inversion resulting in an inversion slice across the profile. In the context of magnetic resonance control, this corresponds to the first half of the model scheme. If the π phase difference were to be acquired and the second half of the scheme implemented a soliton would be located at each of the two sharp edges. The width of the soliton is dependent of the size of these edges. In addition, the width of the inversion slice becomes important when applied to a Bose-Einstein condensate, as the thickness of the slice must be such that the condensate is encompassed by the whole inversion slice. Ideally only one soliton is required, being located at the centre of the condensate. This can be achieved by applying some constant offset to the magnetic field to move the position of the inversion slice. By centring one edge of the slice at the centre of the condensate, the inversion slice thickness is only required to be half the width of the condensate in order to successfully generate a single soliton in the centre of the cloud. These constraints provide a somewhat obvious figure of merit for the pulse scheme, the resolution, defined as

$$R = \frac{\Delta z}{\delta z}, \quad (3.27)$$

where Δz and δz are the slice thickness and slice sharpness respectively, as illustrated in Figure 3.7. The slice thickness is required to be $\Delta z = 5z_{TF}/2$, slightly larger than the Thomas-Fermi radius in order to ensure the outer edge of the slice is sufficiently removed from the condensate. The single-pulse slice sharpness is related to the final FWHM of the density notch through $\text{FWHM} = 4\delta z/5$, which when related to the analytic soliton FWHM given in Equation (2.63), requires a single-pulse slice sharpness of $\delta z \approx 3\xi$, where

Figure 3.7: Final excited state population over a range of normalised detunings as given by Equation (3.26), showcasing the slice thickness, Δz , and the single-pulse slice sharpness, δz used as metrics for the magnetic resonance control scheme.



ξ is the healing length of the condensate as defined in Equation (2.56). These conditions result in a target resolution of

$$R_{\text{target}} = \frac{2z_{\text{TF}}}{5\xi}, \quad (3.28)$$

where z_{TF} is the Thomas-Fermi radius and ξ is the healing length of the condensate, both of which are described in detail in Chapter 2. This target resolution is completely defined by the condensate parameters such as atom number, trap frequencies and scattering lengths. Once a particular condensate has been chosen, the target resolution is set and the scheme parameters can be optimised accordingly. In addition, the particular condensate sets a bound on the time scale of the scheme by way of the healing time

$$t_{\text{healing}} = \frac{\sqrt{2}M\xi^2}{\hbar} \quad (3.29)$$

where M is the atomic mass. The healing time dictates the time scale over which the healing length features evolve under the mean-field interaction of the condensate. Since the scheme relies on the reversibility of the inversion, it must be performed faster than the condensate can react to avoid adverse affects. Indeed if the scheme is performed faster than the healing time, the condensate can be approximated by a static system with only the internal dynamics being relevant. In this way, the two-level atom heuristics that follow provide an excellent approximation for use in parameter optimisation which may otherwise be intractable. The optimisation itself is also constrained by technical and experimental considerations, typically requiring the lowest peak Rabi frequency Ω_0 , and the shallowest magnetic-field gradient dB/dz still able to produce the desired soliton profile in a time scale short compared to t_{healing} .

In order to calculate an analytic expected resolution, Equation (3.26) can be solved for the position at which a particular ground-state population is generated. This inverse

equation is given by

$$d(P_{HS}) = \frac{1}{\pi\Gamma\mu^2} \cosh^{-1} \left[\left(P_{HS}^{-1} - 1 \right) \cosh(\pi\Gamma\mu^2) - P_{HS}^{-1} \cosh \left(\pi\Gamma\mu\sqrt{\mu^2 - 1} \right) \right], \quad (3.30)$$

and gives the normalised position d at which the population P_{HS} occurs. Given this, we can determine both the slice thickness and the slice sharpness analytically. Specifically, the slice thickness is given by the width between the two points at which $P_{HS} = 1/2$, or $2d(1/2)$. The slice sharpness is calculated as the 10% – 90% rise distance of the population transfer, given by $[d(0.9) - d(0.1)]$. As previously detailed, this expression corresponds to the adiabatic limit of an infinitely long pulse. As such, this defines our resolution in the adiabatic limit as

$$R_{\text{adiabatic}} = \frac{\Delta z}{\delta z} = \frac{2d(0.5)}{d(0.9) - d(0.1)}, \quad (3.31)$$

which is entirely dependent on the two parameters Γ and μ . Figure 3.8 illustrates how the resolution in the adiabatic limit increases with both μ and Γ . The expression generated by this relationship is complex and difficult to invert, necessitating the approximation

$$R_{\text{adiabatic}} \approx \sqrt{2}\Gamma\mu^2, \quad (3.32)$$

which provides an estimate to the resolution to within 1% for $\Gamma \geq 3$ and $\mu \geq 1$.

In practice, no pulse is infinitely long or purely adiabatic, with off-resonant Rabi oscillations contributing to imperfect population inversion through the asymptotic limit described in the previous section. The addition of Δ_z to the hyperbolic-secant pulse alters the asymptotic limit described in Equation (3.16) such that

$$\epsilon = \frac{\alpha^2}{\alpha^2 + \mu^2 \left(d + \sqrt{1 - \alpha^2} \right)^2}. \quad (3.33)$$

Ideally the resonant ($d = 0$) population is not severely limited by either the adiabatic limit or the asymptotic limit. Equation (3.33) defines a Lorentzian with a FWHM of $2\alpha/\mu$, centred at $d = -\sqrt{1 - \alpha^2}$. This generates an asymptotic resolution of $R_{\text{asymptotic}}$ which is adequately described by $R_{\text{adiabatic}}$ when

$$\alpha \leq \frac{\mu}{\eta} R, \quad (3.34)$$

where η is a design parameter that defines the tolerance. In general $\eta \approx 30$ produces a pulse truncation for which the asymptotic and adiabatic resolution agree to within 1%. The target resolution, approximate analytic adiabatic resolution, and the constraint on the

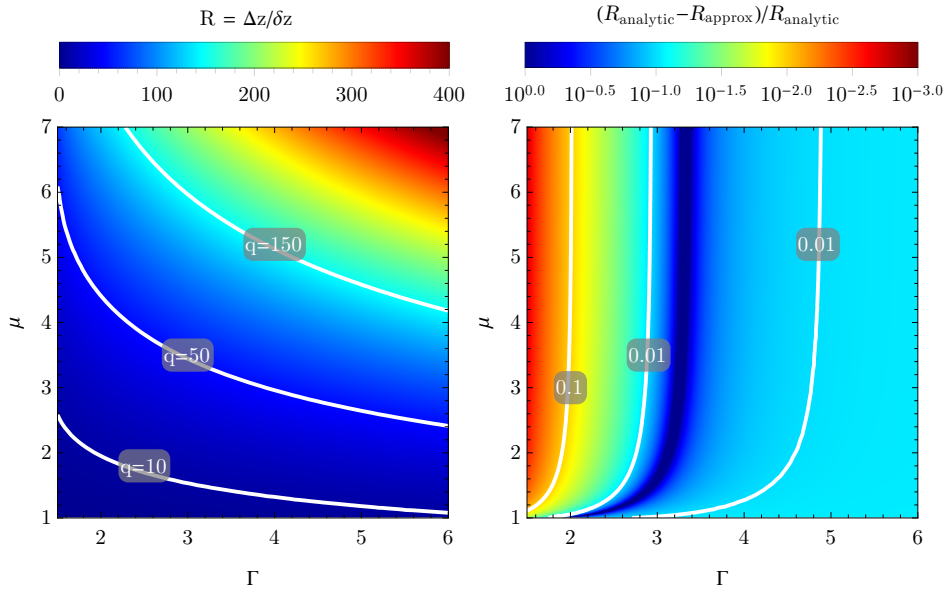


Figure 3.8: The slice thickness divided by the slice sharpness produces the resolution metric for the magnetic resonance scheme. In the adiabatic limit, this has an analytic solution that is a function of the two dimensionless parameters μ and Γ . The analytic expression for the resolution is complex, but in the regime that $\Gamma \geq 3$ and $\mu \geq 1$, the approximation $R \approx \sqrt{2}\Gamma\mu^2$ is accurate to within 1%. The fractional error between the analytic and approximate expressions for the resolution is shown in the right plot.

truncation parameter are sufficient to reduce the parameter space to a search on a single parameter, μ . That is, equating the target resolution (Equation (3.28)) with the analytic resolution (Equation (3.32)) and solving for Γ yields

$$\Gamma = \frac{\sqrt{2}z_{TF}}{4\mu^2}. \quad (3.35)$$

Choosing a design parameter of $\eta = 30$ and introducing the above expression for Γ into the constraint on the truncation parameter yields

$$\alpha = \frac{\mu}{12z_{TF}}. \quad (3.36)$$

Thus, choosing a value of μ will specify the remaining parameters. Given a particular target pulse area $(\Omega_0 t)_{\min} \rightarrow \Omega_0 t_\xi/4$, defined by experimental limitations and the condensate parameters the dimensionless parameters can then be returned to the real parameters.

3.3.1 Gradient optimisation and magnetically induced motion

Given the above heuristics the adiabatic pulse parameters can be chosen. All that remains is the choice of magnetic-field gradient. This is defined through the requirement that the

inversion slice has a thickness of $6z_{\text{TF}}/5$ in order to ensure one edge of the inversion slice is removed from the extent of the condensate. The magnitude of the magnetic-field gradient required to achieve this is

$$\left| \frac{dB}{dz} \right| = \frac{2\hbar\Delta_0}{\mu_B g_F \Delta z} = \frac{5\hbar\Delta_0}{3\mu_B g_F z_{\text{TF}}} \quad (3.37)$$

Whilst this magnetic field enables the high spatial precision of the magnetic resonance control scheme, it simultaneously causes a force on the atoms that can be detrimental to the efficiency. This is a result of the Stern-Gerlach force, given by

$$F_{\text{SG}} = \mu_B m_F g_F \frac{dB}{dz} \quad (3.38)$$

where μ_B is the Bohr magneton, m_F is the particular magnetic sub-level occupied by the atom and g_F is the hyperfine Landé g-factor defined in Equation (2.29). This force induces an acceleration of

$$a_{\text{SG}} = -\frac{\mu_B m_F g_F}{M} \frac{dB}{dz} = -\frac{\hbar\gamma m_F}{M} \frac{dB}{dz} \quad (3.39)$$

for the atom of mass M . The corresponding displacement due to the Stern-Gerlach force is then given by $x_{\text{SG}} = \frac{1}{2}a_{\text{SG}}t^2$. Ideally, the total displacement over the duration of the pulse is less than the healing length of the condensate. Since the pulse duration is taken to be $t_{\text{pulse}} = t_\xi/4$ and $t_\xi = \sqrt{2M\xi^2/\hbar}$, the bound on the size of the gradient is found to be

$$\left| \frac{dB}{dz} \right| < \frac{16\hbar}{\gamma m_F M \xi^3}. \quad (3.40)$$

For a typical ^{87}Rb condensate with healing length $\xi \approx 150 \text{ nm}$, the gradient must be below $\sim 8000 \text{ G/cm}$ in order to keep the displacement less than one healing length. Since the model magnetic resonance control scheme is spatially asymmetric in the inversion, the efficiency of the scheme is sensitive to this displacement. In particular, the choice of the sign of the gradient and detuning sweep alters the effectiveness of the protocol. By choosing a sign that results in both the ground and excited states moving away from the centre of the condensate (and therefore away from boundary of the slice), the second pulse is more effective, as atoms are less likely to have accelerated out of the resonant slice. This choice of sign depends on the particular transition used for the scheme as the product $m_F g_F$ will determine the direction of acceleration for each state. Importantly, the acceleration is exactly reversed by the second half of the protocol ensuring that the Stern-Gerlach force is not a limiting factor in the scheme.

The heuristics presented in this chapter correspond to the relatively simple case of

static atoms. In the regime where the pulse duration is small compared to the healing time, these heuristics provide excellent guidance for pulse optimisation. In practice, the magnetic resonance scheme must be numerically simulated using the full Gross-Pitaevskii equation, taking into account the more complex dynamics resulting from kinetic energy and inter-particle interactions. These additional dynamics manifest as a sub-optimal soliton that is non-stationary. This typically requires local optimisation on the static two-level atom heuristics and is covered in the next chapter.

Magnetic Resonance Control Simulation and Optimisation

The previous chapter outlined a model for generating a spatial population inversion slice using adiabatic pulses on an ensemble of two-level atoms under the effect of a magnetic-field gradient. In this chapter, the scheme is extended through simulation of a Bose-Einstein condensate, exemplifying the high spatial resolution capability of the scheme by writing a soliton to the condensate wavefunction. As outlined in Section 2.6, a soliton is a density notch with width on the order of the healing length, corresponding to a phase discontinuity of π radians. A soliton is a stationary state of the Gross-Pitaevskii equation, meaning that a condensate with a properly engineered soliton will not change shape as it freely evolves in time. Any faults in the wavefunction engineering will generate a state that is not stationary and thus provides an excellent measure scheme's success. The following chapter explores this goal of generating a soliton, using it to illustrate the key parts of the magnetic resonance scheme. Finally, the scheme is extended to generating more complex phase structures such as double solitons, both static and dynamically oscillating in-trap. Although the analysis is considered in the context of Bose-Einstein condensates, the scheme is not limited to this system. Any spatially-distributed quantum system containing internal states capable of spatially-dependent splitting and addressable through time-dependent coupling will permit such a scheme. Fermi gases [112], atoms confined to optical lattices [113–115] and ^3He films [116] have such properties.

4.1 Quasi-1D spin-1/2 Gross-Pitaevskii equation

In order to properly simulate the magnetic resonance control scheme as applied to a Bose-Einstein condensate, more complex dynamics must be accounted for. The Gross-Pitaevskii equation (GPE), presented in Chapter 2, provides a means for computing these dynamics. The 3D GPE accurately captures the dynamics of a Bose-Einstein condensate and reflects experiment, however the simulations are computationally expensive. The 3D GPE can be simplistically reduced to 1D through dimensional reduction that involves set-

ting the 1D chemical potential equal to that of the 3D GPE [117]. Although this produces more accurate results, especially at large scattering lengths, results still diverge from the 3D simulations. Currently the 1D non-polynomial Schrödinger equation (NPSE) most accurately reproduces ground states and dynamics of the full 3D GPE in a dimensionally reduced system [118]. The method relies on factorising the wavefunction into transverse and longitudinal components, with the transverse component described by an ansatz. This method operates under the assumption of weak temporal and z-dependence in the transverse mode of the condensate, assumptions that are only valid for weak excitations where the corresponding excitation in the transverse mode is negligible. In this regime, the transverse mode occupies the ground state, being Gaussian for weak interactions and Thomas-Fermi for strong interactions. Both Gaussian [118] and Thomas-Fermi [115] ansatz have been studied, providing superior results in high and low interaction systems respectively. The ansatz approach effectively requires the excitations to be larger than the transverse size of the condensate, a regime well suited to the model magnetic resonance control scheme which aims to produce a one-dimensional soliton using a magnetic-field gradient confined to a single dimension. This simulation technique, termed a quasi-1D non-polynomial Schrödinger equation, is used to reduce the number of simulated spatial dimensions. Bose-Einstein condensates in lower dimensions have been experimentally realised [119] with the following simulation corresponding to an elongated harmonic trap that produces a ‘cigar’ shape. The z direction will be taken to be the relevant dimension, and set to be that of the weakest confinement. The adiabatic coupling will occur between two states, making the system pseudospin half. Physically this might correspond to $|F = 1, m_F = -1\rangle$ and $|F = 2, m_F = -1\rangle$ coupled by a single microwave pulse or by an optical two-photon Raman transition.

To begin, consider a cylindrically symmetric two-component Bose-Einstein condensate described by the spinor order parameter

$$\Psi(r, z) = \begin{pmatrix} \psi_{\uparrow}(r, z) \\ \psi_{\downarrow}(r, z) \end{pmatrix}, \quad (4.1)$$

where r is the radial direction, and z represents the relevant dimension over which the important dynamics occur. The non-polynomial approach involves applying an ansatz for the radial component of the order parameter. Using the ansatz described in [120, 121], each component of the wavefunction may be represented by

$$\psi_i(r, z) = \Phi_{\perp, i}(r, \chi_i(z)) f_i(z), \quad (4.2)$$

where $\Phi_{\perp}(r, \chi_i(z))$ describes the radial dependence of the density for each component, assumed to be Gaussian in nature with the scale being dependent on the axial position

through scaling factors $\sigma_{\downarrow}(z)$ and $\sigma_{\uparrow}(z)$. This effectively produces a radial width dependent on the axial position z . The fields are normalised such that

$$\int |\psi_i(r, z)|^2 dV = \int_{-\infty}^{\infty} |f_i(z)|^2 dz = N_i, \quad (4.3)$$

where N_i is the number of atoms in each of the two states. The full three-dimensional atomic density can be calculated from $\psi_i(r, z)$ through

$$n_i(r, z) \equiv |\psi_i(r, z)|^2, \quad (4.4)$$

where $n_i(r, z)$ has units of atoms/m³. Similarly, the linear density along the axial direction is defined as

$$\rho_i(z) \equiv |f_i(z)|^2, \quad (4.5)$$

where $\rho_i(z)$ has units of atoms/m. Provided the factorisation in Equation (4.2), a Gaussian ansatz can be used for the radial component whereby

$$\Phi_{\perp,i}(r, \sigma_i(z)) = \frac{1}{\sqrt{\pi} a_r \sigma_i(z)} \exp\left(-\frac{r^2}{a_r \sigma_i(z)^2}\right), \quad (4.6)$$

where ω_r is the trapping frequency in the radial direction producing a harmonic oscillator length scale of

$$a_r = \sqrt{\frac{\hbar}{m \omega_r}}. \quad (4.7)$$

The axially-dependent scaling factors for the radial components, σ_{\downarrow} and σ_{\uparrow} , are found through a set of simultaneous equations,

$$\sigma_i^4 = 1 + 2a_{ii}\rho_i + 8a_{ij}\rho_j \frac{\sigma_i^4}{(\sigma_i^2 + \sigma_j^2)^2}; i \neq j, \quad (4.8)$$

which are solved at each point in time alongside the coupled quasi-1D non-polynomial Schrödinger equation for the components of the pseudo-spinor $\mathbf{f} = (f_{\downarrow}, f_{\uparrow})^T$,

$$i\hbar \frac{\partial f_{\downarrow}}{\partial t} = \left(-\frac{\hbar^2}{2m} \frac{\partial^2}{\partial z^2} + V + E_{\perp,\downarrow} + g_{\downarrow\downarrow} \eta_{\downarrow\downarrow} \rho_{\downarrow} + g_{\downarrow\uparrow} \eta_{\downarrow\uparrow} \rho_{\uparrow} - \frac{\Delta}{2} \right) f_{\downarrow} + \frac{\Omega}{2} f_{\uparrow}, \quad (4.9)$$

$$i\hbar \frac{\partial f_{\uparrow}}{\partial t} = \left(-\frac{\hbar^2}{2m} \frac{\partial^2}{\partial z^2} + V + E_{\perp,\uparrow} + g_{\uparrow\uparrow} \eta_{\uparrow\uparrow} \rho_{\uparrow} + g_{\downarrow\uparrow} \eta_{\downarrow\uparrow} \rho_{\downarrow} - \frac{\Delta}{2} \right) f_{\uparrow} + \frac{\Omega}{2} f_{\downarrow}, \quad (4.10)$$

where m is the atomic mass, $V = m\omega_z^2 z^2/2$ is the spin-independent external poten-

tial along the axial direction with angular trapping frequency ω_z , $g_{ij} = 4\pi\hbar^2 a_{ij}/m$ describes collisional interactions (with a_{ii} and $a_{i\neq j}$ the intra- and inter-state s -wave scattering lengths, respectively), $E_{\perp,i}(z)$ describes the transverse mode energy of each component, given by

$$E_{\perp,i}(z) = \frac{\hbar\omega_r(1 + \sigma_i^4)}{2\sigma_i^2}, \quad (4.11)$$

and $\eta_{ij}(z)$ are interaction scaling factors (with units of m^{-2}) given by

$$\eta_{ij}^{-1}(z) = \pi a_r^2 [\sigma_i(z)^2 + \sigma_j(z)^2]. \quad (4.12)$$

Finally, Δ and Ω are the time-dependent Rabi frequency and detuning coupling the two states and providing the mechanism for the magnetic resonance control scheme. This formalism is described in the instantaneous rotating frame of frequency ω , with the detuning described by $\Delta(z, t) = \Delta(t) - \gamma B(t)z$ where $\Delta(t) = \omega(t) - \gamma B(z = 0, t)$ is the detuning at $z = 0$, $B_q = dB/dz$ is the magnetic-field gradient, and $\gamma = \mu_B |g_F| / \hbar$ is the gyromagnetic ratio for the hyperfine ground state of ^{87}Rb .

4.2 Numerical simulations of MRC in a pseudospin-half system

All numerical simulations were conducted using XMDS2 [122], an open-source package for numerically integrating partial differential equations. The package allows the system to be coded as high-level XML script, with the package subsequently generating low level C++ code to perform the intensive calculations. The package supports parallelisation which was utilised through OpenMP, a compiler directive for threading. Simulations utilised a spatial grid of 4096 points ensuring sufficient points to resolve the soliton within the full spatial extent of the condensate and to ensure the simulations were grid independent. The equations were solved using a fourth-fifth order adaptive Runge-Kutta algorithm.

4.2.1 Imaginary time propagation

In order to perform the magnetic resonance control scheme, an initial ground state for the system must be found. Although approximate analytic ground states exist, numerical methods can be used to more accurately generate this initial condition. This can be achieved using imaginary time propagation, whereby the relevant equations of motion are evolved in imaginary time such that $t \rightarrow -it$ [123]. This causes the eigenstates of the system to decay at an exponential rate dictated by their eigenvalue, ensuring that the higher energy eigenstates decay faster than the ground state. By constantly renormalis-

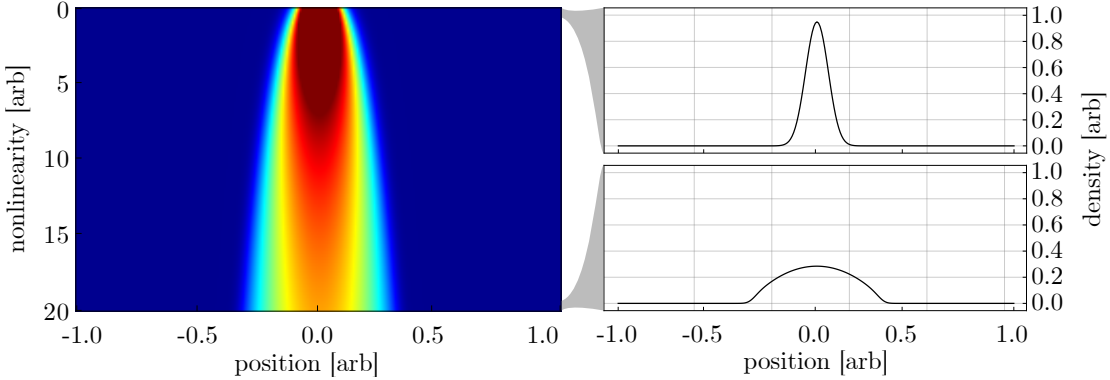


Figure 4.1: The result of imaginary time propagation for varying non-linearity strengths. For weak non-linearities, the profile of the ground-state density is Gaussian transitioning through to an inverted parabola with a broader width and lower peak density for strong non-linearities.

ing the field, the true ground state can be determined quickly and accurately. Though this is a local method, even with a rudimentary initial guess, it will rapidly converge to a solution. The acquired solution is not, however, guaranteed to be the global ground state. Indeed, the method preserves the symmetry of the initial condition. For harmonic traps this is typically acceptable, but care must be taken for more complex situations.

As an example, consider the extremely simple 1D-GPE for the field ϕ with harmonic potential V and non-linear interaction U_{int} . The corresponding equation of motion for this field is given by

$$i\hbar \frac{\partial \phi}{\partial t} = \left[-\frac{1}{2} \frac{\partial^2}{\partial x^2} + V(x) + U_{int}|\phi|^2 \right] \phi \quad (4.13)$$

Making the substitution $t \rightarrow -it$ gives the corresponding imaginary-time evolution equation

$$\hbar \frac{\partial \phi}{\partial t} = \left[\frac{1}{2} \frac{\partial^2}{\partial x^2} - V(x) - U_{int}|\phi|^2 \right] \phi \quad (4.14)$$

Figure 4.1 shows the result of imaginary time propagation on this system for a range of non-linearities, showcasing the transition between a Gaussian profile for small non-linearities towards the inverted parabola corresponding to the Thomas-Fermi regime with large non-linearities. The same imaginary time propagation method is performed on the more complex quasi-1D non-polynomial Schrödinger equation, detailed in Equation (4.10), in order to generate the correct ground-state initial condition for use with the magnetic resonance control scheme.

4.2.2 Validation of numerical methods

As with all theoretical investigations into physical systems, computational simulations require numerous checks throughout development to ensure good correspondence with reality. XMDS2, the package for numerically solving partial differential equations, has already undergone large-scale testing for validity of the underlying code and implementation of integration algorithms, with the remaining testing being that of the physicality of the resulting numeric solutions.

The ground state generated through imaginary time propagation was validated by allowing it to freely evolve over many trap period, with negligible changes observed. In addition, a large magnetic-field gradient applied for a short interval induced sloshing of the condensate within the trapping potential, with the oscillation frequency corresponding to the trap frequency. In the presence of a magnetic-field gradient, the different spin states of the condensate were observed to move in the appropriate direction, dictated by their corresponding g_f and m_F values. The coupling between states was tested in the absence of a magnetic-field gradient using both resonant π -pulses and adiabatic transfer, with the dynamics in agreement with the analytic results presented in Chapter 2 and Chapter 3. The magnetic resonance control scheme was developed in collaboration with the Lincoln Turner, Russell Anderson, and Lisa Starkey of Monash University, allowing a final comparison of the numeric results produced through entirely independent methods.

4.2.3 Magnetic resonance control scheme with pseudospin half system using heuristics

In order to showcase the capability and precision of the magnetic resonance control scheme, the quasi-1D pseudospin half non-polynomial Schrödinger equation presented in Equation (4.10) is used to simulate a condensate of 10^4 atoms of ^{87}Rb containing two spin states, $|\uparrow\rangle$ and $|\downarrow\rangle$. This condensate is confined within a harmonic potential with axial frequency $f_z = 20\text{ Hz}$ and radial frequency $f_r = 1200\text{ Hz}$. Such a trap is experimentally achievable using a 20 W 1064 nm optical dipole laser focused to a beam waist of $10.5\text{ }\mu\text{m}$ [124]. The specific condensate parameters were chosen such that the healing length would be sub-diffraction, highlighting the precise nature of the scheme. This particular set of condensate parameters produces a healing length of 150 nm and a Thomas-Fermi radius of $z_{\text{TF}} = 39.6\text{ }\mu\text{m}$ with a black soliton having a FWHM of 375 nm. In practice, any cigar-shaped condensate would suffice, albeit requiring different field strengths and pulse parameters.

Using a hyperbolic-secant pulse with parameters $\Omega_0/2\pi = 3.00\text{ MHz}$, $\mu = 3.5$, $\Gamma = 6.2$, and $\alpha = 0.0108$ in addition to a magnetic-field gradient of $|\text{dB}/\text{dz}| = 6319.61\text{ G/cm}$, a grey soliton was generated using the magnetic resonance control scheme as shown in

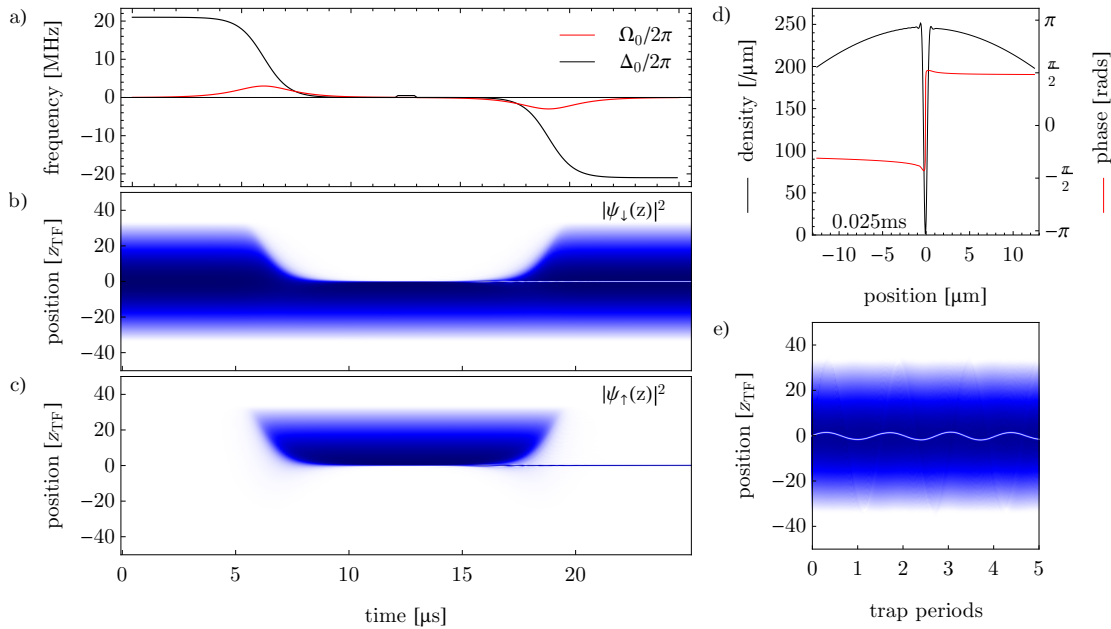


Figure 4.2: Applying the heuristic parameter optimisation of the previous chapter while providing a peak Rabi frequency of $\Omega_0 = 3.0$ MHz, a pulse duration of $t_{\text{heal}}/4$ and choosing $\mu = 3.5$ yields $\Gamma = 6.2$ and $\alpha = 0.0108$. These parameters produce the hyperbolic-secant pulse shown in a). The evolution of the ground and excited state, ψ_\downarrow and ψ_\uparrow , over the full magnetic resonance control scheme is shown in b) and c) with the final state d) allowed to freely evolve in e) for five trap periods. The resultant soliton is slightly mis-engineered resulting in a grey soliton that oscillates in the condensate.

Figure 4.2. The pulse parameters correspond to a single pulse duration of $t_p = 12.02$ μ s, $\sim 25\%$ of the condensate healing time of $t_\zeta = 42$ μ s. In order to position the correct edge of the inversion slice at the centre of the condensate, each pulse required a detuning offset of $|\Delta_1| = \mu\Omega_0$. With no detuning offset, the inversion slice would be symmetric about the centre of the condensate, with the full scheme resulting in two solitons where the edges of the slice were located. By setting the target slice thickness to be slightly larger than the condensate radius, $\Delta z \geq 1.2z_{\text{TF}}$, the second soliton is guaranteed to be outside the condensate. As previously mentioned, the particular choice of sign for the pulse scheme is tantamount to the success. A negative magnetic-field gradient is applied during the first pulse generating a Stern-Gerlach force that first accelerates the two states away from each other. The second half of the scheme swaps the sign of the gradient to positive pushing the populations back to the centre. Conversely, an initial gradient of opposite sign causes population to move toward each other, with some population crossing to the other side of the slice boundary thereby reducing the efficiency of the scheme, with higher amplitude sound waves being observed at the culmination.

The parameters were chosen to engineer a soliton with slice thickness of $\Delta z = 1.2z_{\text{TF}}$ and a slice sharpness of $\delta z = 3\xi_{\text{heal}}$, resulting in a target resolution of $R = 107.7$. The achieved resolution was only $R_{\text{achieved}} = 88.4$. This disparity is due to additional dynam-

ics resulting from the full simulation and the movement of the previously static atoms. Crucially, the choice of μ is not completely arbitrary and results in differing achieved resolutions when implemented using the full simulation. In addition, a non-negligible relative phase is acquired during each pulse, impairing the engineering process. By including a scaling parameter on the inter-pulse stage where the π phase difference is introduced, this additional deleterious phase can be mitigated. That is, the ideal inter-pulse detuning is altered such that

$$\Delta_\phi t_\phi = \pi \rightarrow \Delta_\phi t_\phi = c_\phi \pi, \quad (4.15)$$

where c_ϕ defines a scaling factor to minimise the unwanted phase acquired during the pulses. This inter-pulse detuning, Δ_ϕ , can be controlled by adjusting the spatially-uniform Zeeman splitting across the condensate with a magnetic field, or by adjusting the frequency of the coupling field between the pulses.

4.2.4 Overlap fidelity

The previous chapter outlined a heuristic method for determining optimal pulse parameters based on the resolution figure of merit. This enabled the parameter space to be reduced significantly, allowing faster convergence to optimal parameters. In the extension of the scheme to include the full condensate dynamics these heuristics must be augmented. This is achieved by introducing a metric called the overlap fidelity used in a ‘cost’ function to be minimised. This cost function elucidates the optimal control problem which seeks to determine a set of parameters \mathbf{X} , that cause the system to follow an ideal trajectory that minimises cost C .

The target soliton represents a stationary solution to the Gross-Pitaevskii equation that exhibits a π phase kink through the centre of the condensate. The analytic form of a dark soliton is given by

$$\psi(x) = \psi_0 \tanh\left(\frac{x}{\sqrt{2}\xi}\right), \quad (4.16)$$

with the magnetic resonance control scheme aiming to generate such a state in a condensate. By comparing the resultant wavefunction obtained through numerical simulation to the analytic solution, a measure of the success of the scheme can be generated. Consider a system initially in the ground state described by

$$|\psi_{\text{initial}}\rangle = \frac{1}{\sqrt{L}} \int_0^L dx |g_x\rangle, \quad (4.17)$$

where we have assumed a homogeneous condensate with L being the spatial extent and

$1/\sqrt{L}$ ensuring normalisation. The following analysis applies to any initial state, with the choice here taken for simplicity. Upon application of the pulse scheme the system is left in a new state given by

$$|\psi_{\text{final}}\rangle = \frac{1}{\sqrt{L}} \int_0^L dx (c_e(x)|e_x\rangle + c_g(x)|g_x\rangle), \quad (4.18)$$

where

$$c_j(x) = \sqrt{n_j(x)} e^{i\phi_j(x)}, \text{ for } j=g, e, \quad (4.19)$$

with $n_j(x)$ defining the density and $\phi_j(x)$ defining the spatially-dependent phase of the j th state. The desired target state is given by

$$|\psi_{\text{target}}\rangle = \frac{1}{\sqrt{L}} \int_0^L dx e^{i(\theta+\phi_{\text{target}}(x))} |g_x\rangle, \quad (4.20)$$

where θ is the absolute phase, $\phi_{\text{target}}(x)$ is the spatially-dependent relative phase that is desired, and the system resides once more in the ground state. By taking the inner product of the final state and the target state, the projection of ϕ_{target} onto ψ_{final} can be calculated

$$\begin{aligned} \langle \psi_{\text{final}} | \psi_{\text{target}} \rangle &= \frac{1}{L} e^{i\theta} \int_0^L dx \int dy \left(c_e^*(x) \langle e_x | + c_g^*(x) \langle g_x | \right) e^{\phi_{\text{target}}(y)} |g_y\rangle \\ &= \frac{1}{L} e^{i\theta} \int_0^L dx \left(c_g^*(x) e^{\phi_{\text{target}}(y)} \right). \end{aligned} \quad (4.21)$$

Finally, by taking the modulus squared of this inner product, changes to the absolute phase can be neglected with the resultant fidelity defined as

$$\begin{aligned} F &= |\langle \Psi_{\text{final}} | \Phi_{\text{target}} \rangle|^2 \\ &= \left| \frac{1}{L} \int_0^L dx \left(c_g^*(x) e^{\phi_{\text{target}}(x)} \right) \right|^2. \end{aligned} \quad (4.22)$$

Since the optimisation is a minimisation, the cost is defined as $(1 - F)$ resulting in an optimal value of zero corresponding to complete overlap between the target and final states. This cost function could be additionally augmented to include further requirements such as a penalty for long pulse durations, however in practice the temporal cost is redundant as the dynamics of the full simulation will inherently cause the fidelity to decrease for long pulse times. In the context of the magnetic resonance control scheme and the goal of generating a *stationary* black soliton, a more robust cost function is the fidelity averaged over a number of trap periods. This ensures that the engineered structure is a stationary state. In order to generate the desired final state, the cost must be minimised subject to

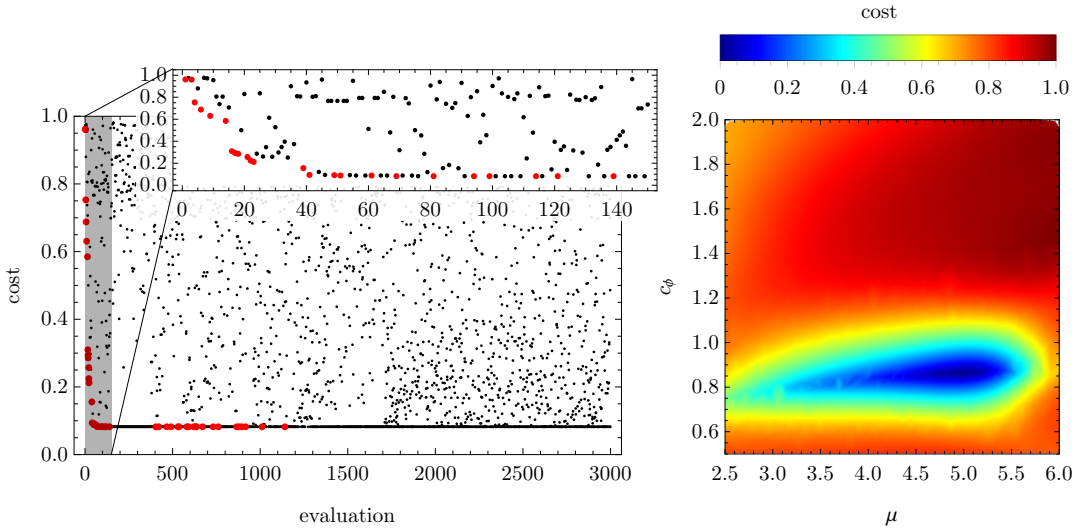


Figure 4.3: Using the heuristic optimisation method from the previous chapter, we require only optimisation of a single parameter μ from which we can obtain all other parameters through their relationship with the condensate parameters. In extending to the full simulation including dynamics, the inter-pulse detuning can be used as a parameter to finely tweak the result in order to optimise the soliton. The optimisation of these two parameters according to the cost function is shown in the left of the figure. An optimal set of parameters is found within the first 100 runs (red dots indicate new optima), with the optimiser allowed to continue as a rudimentary means of mapping the parameter space of cost landscape, shown on the right.

the relevant parameters describing the pulse scheme.

4.2.5 MRC scheme with pseudospin half system using fidelity optimisation

The static two-level atom heuristics developed in the previous chapter can now be augmented to include the inter-pulse detuning scaling factors c_ϕ , with both c_ϕ and μ optimised according to the overlap fidelity. This is shown in Figure 4.3 where a simple optimisation algorithm is applied, running many tests of parameters and calculating the resultant fidelity or cost. Although the optimisation converges to a solution within 100 evaluations, it is allowed to continue as a means of mapping out the parameter space, shown in the right of Figure 4.3. It can be seen that the fidelity is far less sensitive to μ than to c_ϕ , suggesting that the previous heuristics were suitable, but failed to account for the non-negligible phase acquired during the pulses.

The optimal fidelity averaged over two trap periods is 0.92 with the optimal parameters being $\mu = 4.97$ and $c_\phi = 0.861$. Provided a peak Rabi frequency of $\Omega_0 = 3.0$ MHz and pulse duration of $t_{\text{pulse}} = t_{\text{heal}}/4$, the heuristics result in $\Gamma = 3.08$ and $\alpha = 0.00154$ with the corresponding hyperbolic-secant pulse shown in Figure 4.4(a). The required magnetic-field gradient is $|\text{d}B/\text{d}z| = 8977.33$ G/cm, generating a single black soliton, as shown in Figure 4.4(d) and (e). The pulse parameters correspond to a single pulse duration of $t_p = 11.65$ μ s, $\sim 25\%$ of the condensate healing time of $t_\xi = 42$ μ s. The parameters

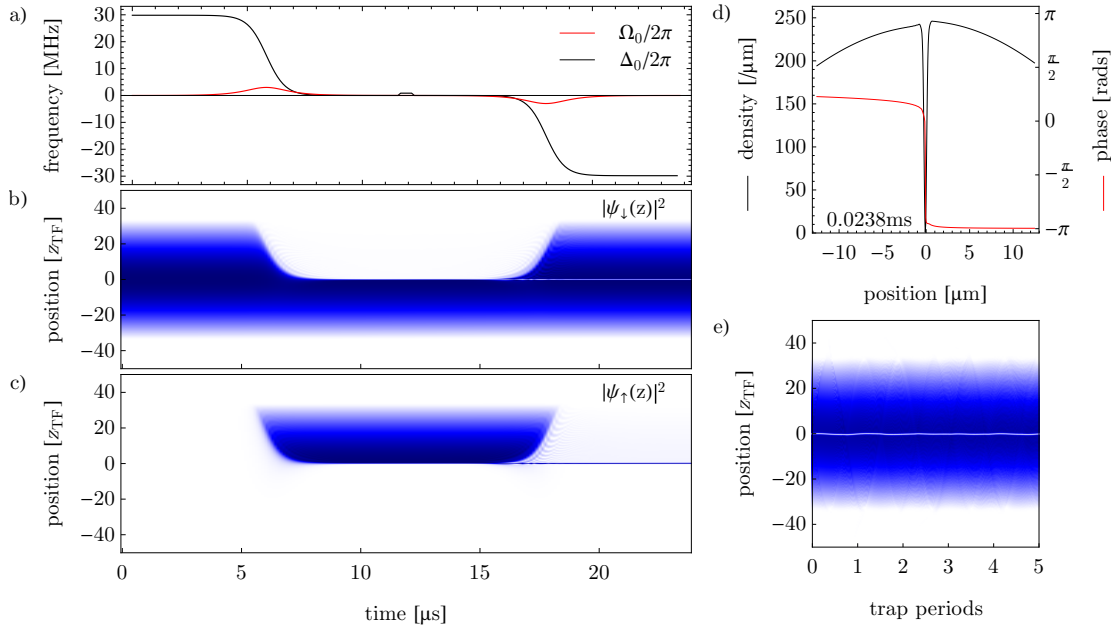


Figure 4.4: The evolution of the model magnetic resonance control scheme applied to a pseudo-1D Bose-Einstein condensate. a) the hyperbolic-secant pulse required to produce a single stationary soliton. The pulse required $\Omega_0/2\pi = 3.0 \text{ MHz}$, $\mu = 4.97$, $\Gamma = 3.08$ and $\alpha = 0.00154$, resulting in a single pulse duration of $t_p = 11.65 \mu\text{s}$, $\sim 25\%$ of the condensate healing time of $t_\xi = 42 \mu\text{s}$. The first hyperbolic-secant pulse is seen to form a spin domain wall [125, 126]. Not shown is a magnetic-field gradient of $|dB/dz| = 8977.33 \text{ G/cm}$, applied in coordination with the pulses. b) and c) show the evolution of the population of each state through the pulse scheme. d) shows the final ψ_\downarrow population (black) and phase (red) at the culmination of the protocol. The phase displays a π kink through the origin corresponding to the black soliton, formed by applying a detuning of $\Delta_\phi/2\pi = 861 \text{ kHz}$ during the wait time of $t_\phi = 0.5 \mu\text{s}$ between pulses. e) shows the free evolution of the soliton over five trap periods after the control scheme has finished. The soliton evolves without moving or changing shape, illustrating the success of the wavefunction engineering.

were chosen to engineer a soliton with slice thickness of $\Delta z = 1.2z_{\text{TF}}$ and a slice sharpness of $\delta z = 3\xi$, resulting in a target resolution of $R = 107.7$. The achieved resolution is $R_{\text{achieved}} = 107.3$, sufficient to produce a single black soliton that remains stationary for over five trap periods of free evolution post-scheme. As before, a detuning offset of $|\Delta_1| = \mu\Omega_0$ is implemented to position the correct edge of the inversion slice at the centre of the condensate. The magnetic resonance control scheme successfully generated both a π phase step and a narrow, dark notch in the density of the ground state, filled by residual population in the excited state $\sim 10^6$ times smaller. In order to create the desired single-component soliton, the excited-state population is set to zero at the culmination of the scheme. Experimentally this could be achieved using a final microwave or optical pulse intense enough to remove the excited-state population in a time scale short compared with the spin healing time.

The slight deviation from perfect overlap fidelity means the soliton is not quite that of the target soliton, with the scheme inducing a small slosh of the condensate in the trap

causing the overlap fidelity to oscillate at the trap frequency with a mean value of 0.92. Indeed, as a result of the imperfections in the soliton engineering, low-amplitude sound waves are emitted from the centre of the soliton as soon as the pulse scheme terminates. Despite this, the soliton remains effectively stationary over more than two trap periods (Figure 4.4(e)), demonstrating that the protocol indeed produces a single black soliton.

Variations of the hyperbolic-secant pulse [127, 128] exist, designed to achieve the same pulse resolution in a shorter time possibly further minimising sound wave generation. Additionally, the sound waves might be a result of the particular methods for simulating the system. It may be that higher order methods such as c-field techniques [129] see the sound waves dissipate faster with the scheme being more tolerant of imperfections in the soliton production.

4.2.6 Experimental considerations

The magnetic resonance control scheme as applied in the above context is experimentally challenging, requiring large magnetic-field gradients with fast switching times. The gradients are perhaps more suited to chip-trap experiments where the coils can be placed on the order of millimetres from the condensate with such magnitude gradients having been demonstrated [130]. However, such gradients are significantly more challenging for free-space apparatuses where coils and antennas are more than a centimetre away. Given this challenge, and the challenge of fast switching of the gradient, a spatially-varying splitting could be generated through a vector light shift from the edge of an off-resonant Gaussian laser beam [131], where a pure Zeeman shift can be generated by detuning the laser to a frequency between the D_1 and D_2 transitions such that the detuning from the D_2 is exactly twice that from the D_1 [132]. Such a technique is also much more readily able to be switched and modulated, with more complex field gradients possible through use of a spatial light modulator. The large radio-frequency coupling strengths also require an antenna situated close to the condensate. Given a large enough antenna with good impedance matching, the peak Rabi frequencies required by the scheme are achievable [133].

4.3 Extending to multiple solitons

As a final demonstration of the versatility and promise of magnetic resonance control, a number of non-trivial higher-order soliton modes are generated. Where the Hermite-Gauss polynomials form time-independent solutions to the linear Schrödinger equation with a harmonic potential, solitons form the equivalent solutions in the non-linear regime. It is possible to adiabatically sweep the non-linear term to a non-zero value and

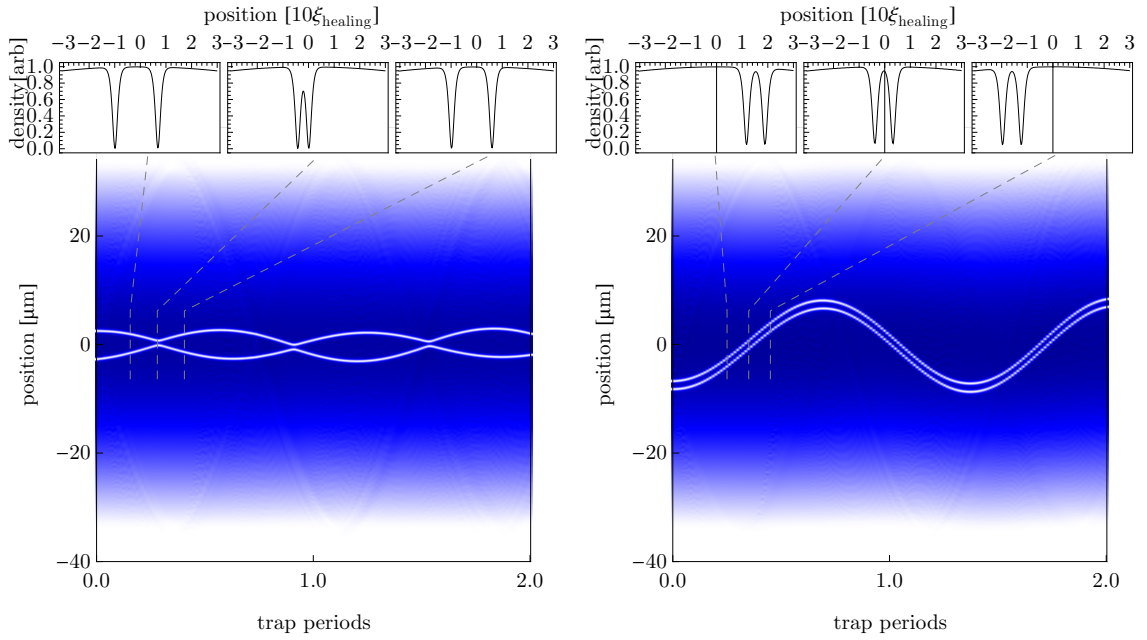


Figure 4.5: By decreasing the width of the inversion slice, the magnetic resonance control scheme is capable of creating two solitons. This is achieved by decreasing the range of the detuning Δ_0 , with the position of the solitons dictated by the offset $|\Delta_1|$. Left: Two solitons initially located at $z = \pm 2.6 \mu\text{m}$, formed using $\mu = 0.424$, $\Gamma = 35.31$, and an offset of $|\Delta_1| / (2\pi) = 0 \text{ Hz}$, oscillate out of phase. Right: If we instead use $\mu = 0.12$, $\Gamma = 32.31$ and $|\Delta_1| / (2\pi) = -3.60 \text{ MHz}$, the two solitons are formed at $z = 6.6 \mu\text{m}$ and $z = 8.05 \mu\text{m}$ and oscillate in phase. All other parameters are the same as that of the successful black soliton simulation.

remain in an eigenstate of the system. That is, one can begin in an excited state of the linear Schrödinger equation and adiabatically introduce a non-linear term moving to a multiple soliton state. [88, 134]. Non-stationary multiple dark solitons have been created using phase imprinting methods [52, 90, 91], and matter wave interference [92]. Magnetic resonance control provides the precision needed to create tightly bound or near-stationary double solitons. The modification to the scheme enabling the generation of two solitons is as follows. As previously stated, the pulse generates an inversion slice. In the single soliton case, one edge of the slice is positioned outside the extent of the condensate. By bringing this edge back within the condensate, a second soliton is formed. To ensure the slice sharpness of each soliton is preserved, the slice thickness is changed through modification to the range of the detuning sweep Δ_0 , rather than increasing the magnetic-field gradient. This corresponds to a decrease in the normalised pulse bandwidth μ , while proportionally increasing Γ with all other parameters remaining identical to the successful single soliton example. The detuning offset required to shift the edge of the slice by x is given by

$$\Delta_{\text{off}} = \frac{\mu_B g_F x B_{\text{grad}}}{2\hbar}. \quad (4.23)$$

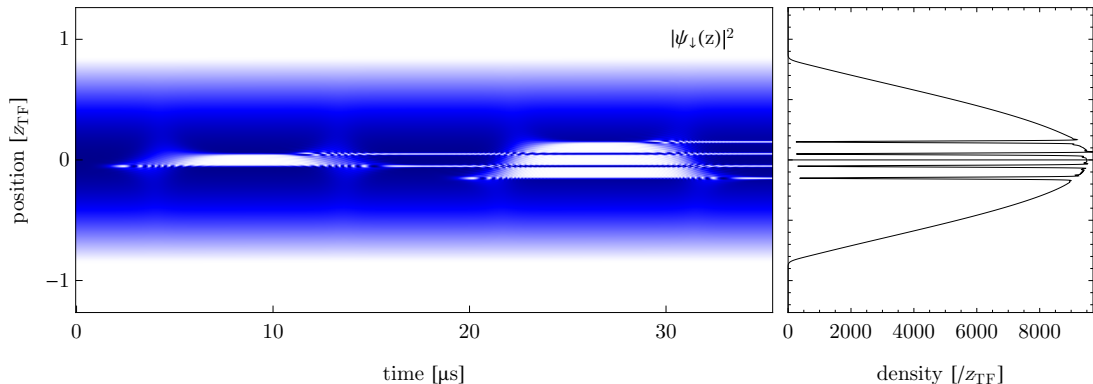


Figure 4.6: By implementing the double soliton magnetic resonance protocol twice in succession, four solitons can be generated. This highlights the possible extensions to the scheme whereby the step function in phase generated by a double soliton could be used to build an arbitrary structure in phase.

Adjusting this allows for the precise manipulation of initial position and trajectories.

Figure 4.5 shows the successful implementation of this, with two examples. In (a) the two solitons are generated symmetrically about the centre of the condensate and oscillate back and forth, reflecting off each other over the course of the oscillation. In contrast, Figure 4.5(b) the solitons are positioned on the same side of the condensate with the subsequent evolution occurring in phase with each other. This corresponds to the lowest anomalous mode of the double soliton state, having never been experimentally realised in a quantum fluid. The benefit of the extension to more than two solitons is immediate. With successive application of the scheme many pairs of solitons could be generated as illustrated in Figure 4.6. Since the phase of a double soliton forms a top-hat function, multiple pairs of double solitons could be used as a base unit for constructing more complex phase structures such as matter-wave analogues of lenses or mirrors.

The magnetic resonance control scheme presented over the previous two chapters represents a new method for generating dark solitons in Bose-Einstein condensates that is robust and highly tunable. The heuristics developed for optimisation of the scheme allow a reduction of the parameter space, but simulations demonstrate a need for further numerical optimisation. Ideally the scheme could be optimised on the experiment itself, allaying the need for time consuming feedback between experiment and theory. Traditional optimisation methods typically struggle with complex, noisy problems and fail at generalising to other situations. In the following two chapters, this concept will be explored and a new, generalisable method called machine learning introduced and applied to an experimental apparatus.

Part II

Machine Learning

Theory of optimisation and machine learning

The following two chapters present theoretical and experimental work on the development and implementation of a machine learning algorithm, summarised in:

- **P. B. Wigley, P. J. Everitt, A. v. d. Hengel, J. W. Bastian, M. A. Sooriyabandara, G. D. McDonald, K. S. Hardman, C. D. Quinlivan, P. Manju, C. C. N. Kuhn, I. R. Petersen, A. N. Luiten, J. J. Hope, N. P. Robins, and M. R. Hush.** *Fast machine-learning online optimization of ultra-cold-atom experiments.* *Scientific Reports* **6**, 25890 (2016). ISSN 2045-2322. DOI: 10.1038/srep25890.

Experiments in physics and particularly those involving ultracold quantum gases can be complex, with experimental controls that are often interrelated. Indeed, often the relationship to the actual physics is obfuscated by electronics between the control and the experiment, resulting in a difficulty translating theoretical optimisation to experimental optimisation. Optimisation of experimental systems often becomes a fine art, a heuristic process where the experimenter builds up an intuition on the response of the system to changes in input. This intuition forms a complex model developed over time and arising from experience. Machine learning provides a means of turning this heuristic process into an algorithm, creating a powerful and versatile tool for experimentalists. This becomes especially advantageous when the system gets sufficiently complex that simplified theoretical models begin to miss subtlety and detail that are essential to effective operation. In contrast, machine learning can automate the process of model building and of finding an optimal set of parameters.

Such machine learning algorithms allow computers to become generalists, solving problems without being specifically programmed for the task. Instead of bespoke algorithms designed solely for one task, machine learning provides a general algorithm that can be applied across many tasks with few adjustments. For a vast swathe of applications this becomes an invaluable tool for interfacing with complex systems. This chapter provides a theoretical basis for machine learning, beginning with a more general overview of

the framework of optimisation. In later chapters, this framework will be used for both the experimental optimisation of the evaporative cooling stage of Bose-Einstein condensate production (Chapter 6), as well as the theoretical optimisation of the magnetic resonance control scheme described in Chapter 3 and Chapter 4.

5.1 Optimisation

Broadly speaking, all life on Earth is derived from stochastic optimisation where the measure of success is the survival of the fittest [135]. Though often unnoticed, optimisation plays an essential role in everyday life. Workers will optimise their commute time given the cost of various modes of transport. Time or energy is optimised when walking from one place to another. The complexity of these everyday tasks is such that optimisation can be instinctive. Subtler problems such as the design of an engine optimised to yield the highest efficiency, or the strength of a bridge constrained to a certain weight, require a more rigorous approach. As is often the case, a mathematical framework allows a more powerful analysis and optimisation of the problem. In this case, the framework is optimal control theory, having a vast mathematical background, with applications throughout many sub-disciplines of physics, engineering and economics.

Any optimisation process involves some goal, such as efficiency or cost. Given all the possible configurations of controls, the idea is to find the configuration that achieves the best possible outcome. This often depends heavily on the form of the specific goal. As with the engine, high efficiency is vastly different from high power output, with the form of the goal often being extremely subtle. In addition, the space describing all control configurations is often not completely free, but contains some important constraints, limiting the domain of exploration and bounding the set of possible control values. Returning to the example of the bridge, a solution might be to use carbon fibre to construct the lightest, strongest bridge, however the construction project may be constrained by a certain budget that cannot afford such materials. As such, the space describing the possible control configurations is reduced to a set of ‘feasible’ controls. In experimental physics, the constraints might be the working range of a power supply or the limited range of movement of a translation stage.

5.1.1 Notation

To state the problem mathematically, optimisation involves finding an argument for which a given function is at an extremum. Formally, given a function $f : \mathbb{R}^n \rightarrow \mathbb{R}$ and a set of controls $S \subseteq \mathbb{R}^n$, we seek $\mathbf{x}^* \in S$ such that f attains a minimum on S at \mathbf{x}^* . That is, $f(\mathbf{x}^*) \leq f(\mathbf{x})$ for all $\mathbf{x} \in S$ [136]. We say that f is the cost function, which may be linear

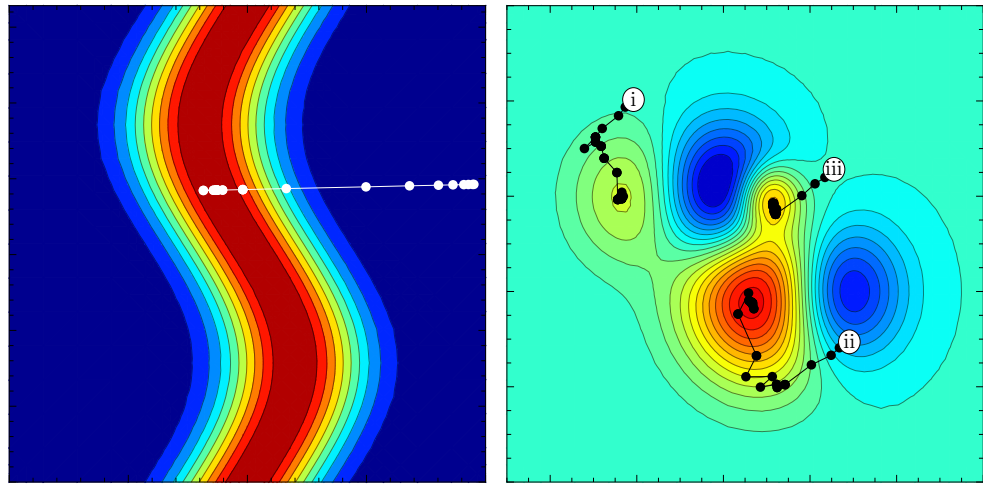


Figure 5.1: Illustration of optimisation on two dimensional landscapes. Optimisation works to change parameters in order to locate a minimum (or maximum) of a cost function. Left: an example of a landscape with a single maximum on a plateau. Such a landscape contains no traps for optimisation algorithms. Right: an example of a landscape containing multiple local maxima (and minima) and a single global maximum (and minimum). Such a landscape is difficult for optimisation algorithms and especially gradient-based solvers which tend to get trapped in local optima, exemplified by three optima returned by a gradient optimisation method beginning at three different initial conditions.

or non-linear. S is the set of linear, or non-linear constraints, that are formed by equations or inequalities. In general, continuous optimal control problems are of the form

$$\min_{\mathbf{x}} f(\mathbf{x}), \text{ subject to } \mathbf{g}(\mathbf{x}) = \mathbf{0} \text{ and } \mathbf{h}(\mathbf{x}) \leq \mathbf{0}. \quad (5.1)$$

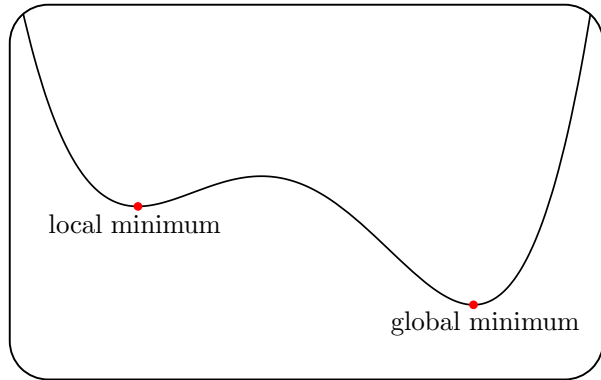
If f , \mathbf{g} and \mathbf{h} are all linear, the problem is said to be a linear programming problem. Similarly, if any of these functions are non-linear, it is termed a non-linear programming problem.

For example, consider the problem of minimising the surface area of a cylinder given a required volume. In this case, we have two variables and one constraint. The variables describe the radius x_1 and height x_2 , with the constraint describing the required volume V . Under the optimal control framework, this problem would be written as

$$\min_{x_1, x_2} f(x_1, x_2) = 2\pi x_1 (x_1 + x_2) \text{ subject to } \pi x_1^2 x_2 - V = 0. \quad (5.2)$$

This problem contains both a non-linear cost function and constraint. Physically, this might be used to generate the ideal shape for a container, using the least amount of materials.

Figure 5.2: Global and local minima in one-dimension. Given higher dimensions and complexity, it can be very difficult to find, or even confirm, that a solution is a global, and not simply a local, optimum. Often optimisation algorithms can get stuck in local optima.



5.1.2 Local and global extrema

It is necessary to elaborate on the definition of optimisation solutions. It was previously stated that a solution is defined as \mathbf{x}^* such that $f(\mathbf{x}^*) \leq f(\mathbf{x})$ for all feasible values of \mathbf{x} . In fact, this is the definition of a global minimum and is illustrated in Figure 5.2. Finding these points for a complex cost function is very difficult unless the problem has properties such as convexity. Indeed, even confirming that a given solution is a global minimum is difficult. Most simple optimisation methods are designed to use information that is local to the point, such as derivatives or Taylor expansions. These local optimisation methods find solutions \mathbf{x}^* such that $f(\mathbf{x}^*) \leq f(\mathbf{x})$ in some neighbourhood of \mathbf{x} , and have great difficulty in finding a global minimum. Generally, it is not possible to guarantee that a global minima may be found using typical numerical methods. Given a poor initial guess, even local minima are not guaranteed.

The complexity of the cost function plays a key role in optimisation. Consider a cost function that is dependent on two parameters. Mapping out this cost as a function of the two parameters will form a ‘landscape’ as illustrated in Figure 5.1. Simpler landscapes may have only a single optimum or a plateau and are said to be ‘trap-free’ meaning that algorithms are less likely to fail and be trapped by a local optimum. More complex landscapes may have multiple optima that have the possibility of trapping optimisation algorithms. This is illustrated in the right of Figure 5.1, where three optima have been returned by an optimisation algorithm given three different initial starting points. Such landscapes make global optimisation vastly more difficult.

5.1.3 Continuous-time cost function

Certain cost functions can be developed from a model of the system that adequately predicts the behaviour given a set of inputs or controls. The optimisation of the magnetic resonance control scheme is one such problem requiring this formalism. Consider a sys-

tem that is described at time t by a set of variables

$$\mathbf{x}(t) = \{x_1(t), x_2(t), \dots, x_n(t)\}, \quad (5.3)$$

with controls at time t given by

$$\mathbf{u}(t) = \{u_1(t), u_2(t), \dots, u_n(t)\}. \quad (5.4)$$

The corresponding equations of motion for the system can then be described by

$$\dot{\mathbf{x}}(t) = \mathbf{f}(\mathbf{x}(t), \mathbf{u}(t), t), \quad (5.5)$$

where \mathbf{f} is some vector of functions. Given this, the general optimal control problem on the interval $[t_i, t_f]$ is defined as

$$\min J(\mathbf{x}, \mathbf{u}) = \varphi(\mathbf{x}(t_f)) + \int_{t_i}^{t_f} \mathcal{L}(\mathbf{x}(t), \mathbf{u}(t), t) dt \quad (5.6)$$

$$\text{s.t. } \dot{\mathbf{x}}(t) = \mathbf{f}(\mathbf{x}(t), \mathbf{u}(t)), \quad (5.7)$$

$$\mathbf{e}(\mathbf{x}(t_i), \mathbf{x}(t_i)) = 0 \quad (5.8)$$

$$\mathbf{g}(\mathbf{x}(t), \mathbf{u}(t)) \geq 0 \quad (5.9)$$

where φ is the terminal cost, and \mathcal{L} describes the running cost. \mathbf{e} and \mathbf{g} are the initial and path constraints respectively. In the case of the magnetic resonance control optimisation, the state variables \mathbf{x} might be the ground and excited states $\psi_g(t)$ and $\psi_e(t)$, with the equations of motion given by the coupled GPE equations.

Since many optimal-control problems are non-linear, and do not have analytic solutions, numerical methods for optimisation become essential. At the time of the mid-twentieth century, when numerical methods for optimal control were in their infancy, indirect approaches were used to solve these optimisation problems. These methods primarily involved the application of calculus of variations to the problem. Unfortunately, this method leads to two-point boundary value problems that are generally non-linear. These must be solved in order to find an expression for the optimal control; a very difficult task. In general, even with linear, time-invariant systems, these are impossible to solve for $n \geq 3$ [137]. More recently, direct methods have been developed for solving optimal-control problems. In this case, the state and controls can be approximated using methods such as polynomial approximation [138]. In addition, the cost functional is approximated as a cost function. In this way, the coefficients used in the function approximation become the optimisation parameters, and the continuous time optimal control problem is translated to a non-linear programming problem with algebraic, rather than

differential, constraints. Despite the large number of parameters that this method generally yields, it is in fact easier to solve than the boundary value problems that arise from the indirect method. For this reason, many algorithms have been written to solve these problems.

5.2 Numerical optimisation methods

As the complexity and dimensionality of optimisation problems increase, it becomes necessary to use numerical methods for optimisation. Prior to the development of machine learning many, often bespoke, algorithms were developed for the optimisation of various tasks. The last half century has seen extensive development of these numerical optimisation methods. Genetic algorithms have found recent success, having been employed to optimise a number of experiments [139–152]. The numerous variations and types of genetic algorithms make them problematic as a benchmark for other algorithms. For this reason, and by virtue of its simple and effective implementation, the Nelder-Mead algorithm was chosen as a benchmark for the machine-learning algorithm. The following section will explore the properties and use of the Nelder-Mead algorithm, before focusing on the development of a machine-learning algorithm based on Gaussian processes.

5.2.1 Nelder-Mead

Simplex methods have been shown to be powerful, yet computationally compact, optimisation algorithms. The Nelder-Mead algorithm is one such method, developed in the early 60's as an extension to earlier work by Spendley, *et al.* [153, 154]. In the context of this thesis, the Nelder-Mead algorithm provides a benchmark used in later chapters, allowing the success or failure of the machine-learning algorithm to be assessed. The choice of Nelder-Mead as a benchmark stems from the general method it provides in addition to being an extremely well-characterised optimisation algorithm. Indeed, in the

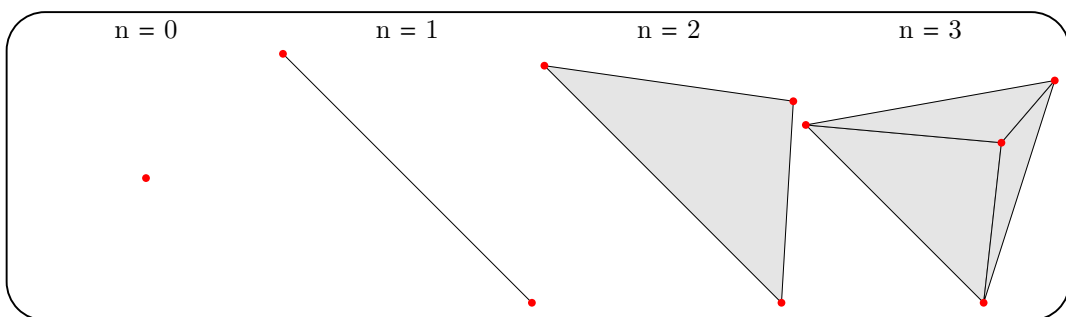


Figure 5.3: In n -dimensions the simplex is generated from $n + 1$ connected points and represents the simplest closed shape in an n -dimensional space.

context of experimental quantum physics, Nelder-Mead has been successfully used as a method for optimising quantum gates [155].

Given an optimisation problem with n input parameters, a closed shape is formed from $n + 1$ points. This shape is a simplex, a general object that represents the smallest closed region in the n -dimensional space. In 0-dimensions, this is simply a point; in 1 dimension a line; in 2-dimensions a triangle. Figure 5.3 illustrates this idea up to $n = 3$. The Nelder-Mead algorithm generates a set of $n + 1$ points that it maintains throughout the optimisation with each iteration determining a new test point to replace the worst vertex of the simplex. Using these points and a set of rules, the simplex ‘walks’ across the landscape towards the lowest point. Where the original work by Spendley *et al.* was more rigid in the way the simplex traversed the optimisation landscape, the Nelder-Mead approach introduced a more general set of operations and conditions describing the simplex movement.

To outline the procedure, consider a two-dimensional cost function $f(\mathbf{x})$, with $\mathbf{x} = \{x, y\}$. A simplex is generated from $n + 1$ points in the two-dimensional space with vertices represented by $\mathbf{P}_i = (x_i, y_i)$ where $i \in \{1, 2, 3\}$. The value of the optimisation function is determined for each \mathbf{P}_i and written as $z_i = f(x_i, y_i)$. The order of the subscripts are then changed to ensure that $z_1 \leq z_2 \leq z_3$, assuming here that the goal of the optimization is one of minimization and therefore that \mathbf{P}_1 is the optimal point on the current simplex corresponding to z_1 and \mathbf{P}_3 corresponding to z_3 is the least optimal. Also calculated are the centroids of each of the points, given by

$$\bar{\mathbf{P}}_{ij} = \left(\frac{x_i + x_j}{2}, \frac{y_i + y_j}{2} \right), i \neq j \quad (5.10)$$

with the distance between points \mathbf{P}_i and \mathbf{P}_j written as $[\mathbf{P}_i \mathbf{P}_j]$. At each iteration of the algorithm, the least optimal point z_3 is replaced by a new point, found using three operations; reflection, contraction and expansion with the choice of operation determined by a set of conditions and logical steps defined as follows:

Reflection: Since the value of the cost function decreases from the worst point (\mathbf{P}_3) to the two best points (\mathbf{P}_1 and \mathbf{P}_2) it is sensible to consider that a point \mathbf{r} reflected through $\bar{\mathbf{P}}_{12}$ may have a lower value still. The reflected point is constructed by drawing a line segment from \mathbf{P}_3 through the centroid $\bar{\mathbf{P}}_{12}$ to a point a set distance from $\bar{\mathbf{P}}_{12}$. The reflected point is given by

$$\mathbf{r} = (1 + \alpha) \bar{\mathbf{P}}_{12} - \alpha \mathbf{P}_3, \quad (5.11)$$

where α is the reflection coefficient, determining the distance along the line segment to which the reflection occurs. Typically this is set to one, and the reflection is

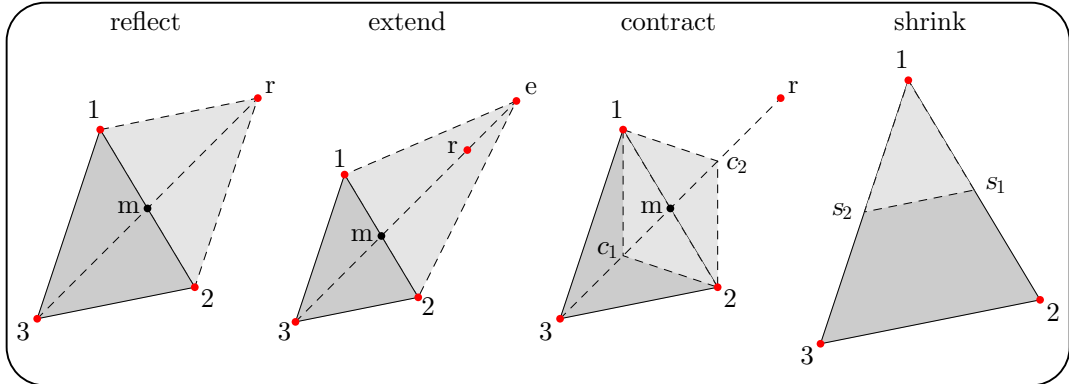


Figure 5.4: Illustration of the various operations available to the Nelder-Mead algorithm. Each example begins with the sample two-dimensional simplex with vertices 1, 2, 3. The vertices are ordered by their value with 1 having the lowest and best value. The simplex can *reflect*, replacing the worst point 3 with the new vertex r . The simplex can *extend*, replacing 3 with e . The simplex can *contract*, replacing 3 with points c_1 or c_2 placed along the line formed by z and r . The simplex can *shrink*, replacing 3 and 2 with s_1 and s_2 lying along the previous edge of the simplex.

symmetric.

If the new point $z_1 < z_r < z_3$, then z_3 is replaced by the reflected point and the process restarted. If the new point is lower than the optimum such that $z_r < z_1$, then the algorithm moves to the next step, expansion.

Expansion: Since the reflected value is the new minimum, it is feasible that moving further along the line segment will improve the cost further. This results in an expansion of the simplex given by

$$\mathbf{e} = \gamma \mathbf{r} + (1 - \gamma) \bar{\mathbf{P}}_{12}, \quad (5.12)$$

where $\gamma > 1$ is the expansion coefficient defining the amount of expansion along the line segment from $\bar{\mathbf{P}}_{12}$ to \mathbf{r} .

If the new optimum is found such that $z_e < z_1$, then the process is restarted with the worst point \mathbf{P}_3 replaced by \mathbf{e} . If the expansion has failed to find a better point, then \mathbf{P}_3 is replaced by \mathbf{r} and the process is also restarted. If instead, upon performing the reflection operation, $z_r > z_i \forall i \neq 3$ such that replacing the worst point by \mathbf{P}_r leaves the new point as the worst point then the contraction operation is performed.

Contraction: The new point due to contraction is computed as

$$\mathbf{c} = \beta \mathbf{P}_3 + (1 - \beta) \bar{\mathbf{P}} \quad (5.13)$$

where \mathbf{P}_3 is either the original value or the reflected value depending on which

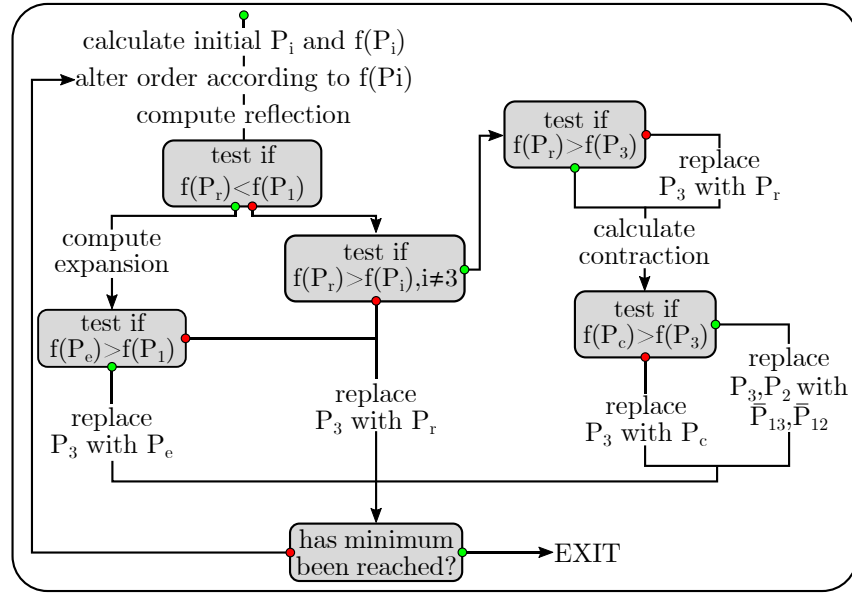


Figure 5.5: Flow diagram illustrating the logic of Nelder-Mead. Grey boxes represent IF statements. Green circles represent the paths taken when the result is true, red circles represent that of false. Flow always goes towards an arrowhead.

is lower and $0 < \beta < 1$ is the contraction coefficient, typically set to leave the contracted point at the midpoint of \mathbf{P}_3 and $\bar{\mathbf{P}}_{12}$ or $\bar{\mathbf{P}}_{12}$ and \mathbf{r} .

If the new contracted point yields a larger value than that of the reflected point or the original \mathbf{P}_3 , then a final operation is performed.

Shrink: If the value of the function at \mathbf{P}_c is not smaller than the least optimal point then the simplex must be shrunk. This involves replacing \mathbf{P}_2 and \mathbf{P}_3 with the centroids $\bar{\mathbf{P}}_{12}$ and $\bar{\mathbf{P}}_{12}$.

The four operations and corresponding logic define the Nelder-Mead algorithm. Typically the expansion operation fails when it spans a valley such that the new point is further up the opposite side. Contraction fails when the simplex straddles a valley asymmetrically such that the contraction causes the point to move away from the bottom. Generally, the four operations together will allow the algorithm to find the bottom of a valley. The Nelder-Mead method typically has the possibility of getting stuck in local optima however, given the nature of the operations, there is a chance for it to escape.

Ideally an optimisation algorithm would better explore an unknown cost landscape in order to avoid local traps. Perhaps the algorithm would preferentially explore locations where it has the highest uncertainty or would be capable of building a simplified model of the system as it runs. Machine learning provides these features in a fashion capable of extension to many applications with little change.

5.3 Optimisation using machine learning

Whilst methods like Nelder-Mead have proven surprisingly effective despite their inherently local-search behaviour, more robust and general methods are desirable. Machine learning has recently proved itself to be a candidate for such optimisation, receiving much attention over the last decade. Already machine learning has revolutionised the way computers tackle image recognition [156, 157], now even being implemented for self-driving cars to recognise the world around them [158]. More recently, machine learning algorithms have been used to best the world champion player of the board game ‘Go’ [159], as well as successfully matching expert cardiologists in the detection of heart disease indicators [160] and determining patient outcomes [161].

Machine learning can be split into three broad categories, *supervised learning*, *unsupervised learning*, and *reinforcement learning*. The work presented in this thesis is primarily related to supervised learning, whereby the computer is directed as to whether an output is good or bad. The computer is then required to learn the mapping from inputs to outputs, seeking the best output. Within these categories, machine learning is split into two forms, classification and regression, dependent of the form of the output. Classification involves discrete data and, in the context of ultracold atom experiments, might entail classifying absorption images into condensate or thermal cloud. Regression involves continuous outputs such as the fraction of condensate in an absorption image with the goal being to maximise the fraction. Here the task requires mapping the experimental inputs to the corresponding output absorption image. This model allows the experimental parameters required to maximise the condensate to be computed. In general then, machine learning involves providing an algorithm with examples to learn from and requiring it to generalise this experience to regimes it has never encountered.

In a more formal sense, suppose we have a set of inputs $\mathbf{x} = \{x_1, \dots, x_N\}$, typically a large set of parameters. These inputs produce an output y . The output can be either discrete when performing classification or continuous when doing regression. Given a dataset $\mathcal{D} = \{(\mathbf{x}_i, y_i) | i = 1, \dots, n\}$ of n observations, the goal is to make predictions for a new set of inputs \mathbf{x}_* . This involves taking a finite set of ‘training’ data and creating a continuous function f that successfully models the data and is capable of predicting outputs for all inputs. The way in which we choose how to produce this model is subtle and whilst many methods exist, this thesis focusses on one particular approach; a Gaussian process.

5.3.1 Gaussian processes

Two common approaches exist for determining the model for the dataset using Gaussian processes. The first involves restricting the available classes of functions. This approach

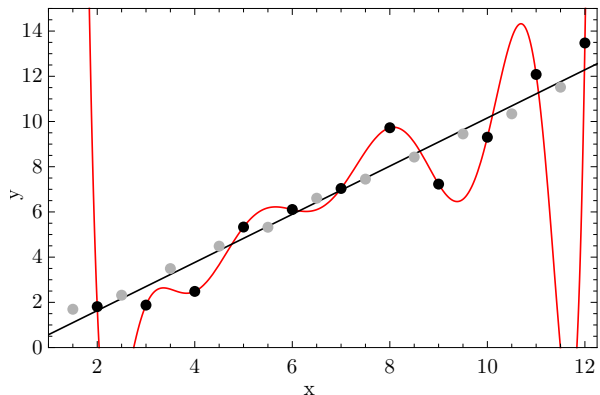


Figure 5.6: An example of over-fitted data. The training data (black dots) is over-fitted by the algorithm (red line). When applied to a broader range of inputs, the over-fitted model fails to accurately predict the output (grey dots) which are actually better fit by a far less complex model (black line).

can fail when the class of functions poorly models the data or conversely is prone to over-fitting when too large a class of functions is made available. Over-fitting results in a model that poorly predicts the output, as the model is too highly tuned to the training data, as illustrated by the red fitted function in Figure 5.6, fit to the training black points. In this example the linear fit is likely a far more robust fit to the data as indicated by the future results shown in grey.

An alternate approach, often termed Bayesian modelling, involves providing a prior probability to all possible functions, biased such that more likely functions have a higher probability. Among other possible criteria, a bias might be towards functions that are smooth or functions that are linear, representing the probability of predicted functions that describe the data. This is shown in the left of Figure 5.7 where, provided no observations, a set of functions describe the space with the mean function shown in red. The shaded region represents the variance of all values of $f(x)$ given by each function. When observations are added, as in the right of Figure 5.7, the prior is refined to only consider functions that pass through the data with the new mean of the distribution of functions (red) passing through these points. The variance on the functions is now minimised at values where data exists, indicating the knowledge passed to the Gaussian process. This now represents the posterior distribution of functions, defined by the prior and the data. As observations are made, the posterior will change and the mean of the functions will adapt and reflect the new data.

The mean and variance of the functions, along with other possible properties, define the covariance function for the Gaussian process. The choice of covariance function is crucial, with the properties of the covariance function being ‘learned’ in order to better satisfy the prior and the data. The covariance function often defines the characteristic length scale of the controls, a measure of the sensitivity of $f(x)$ to x . By allowing the covariance to be optimised, the Gaussian process learns to better model the observations. Finally, Gaussian processes can utilise uncertainty in observations to generate a better posterior, making the optimisation and learning process robust to noisy data. For ex-

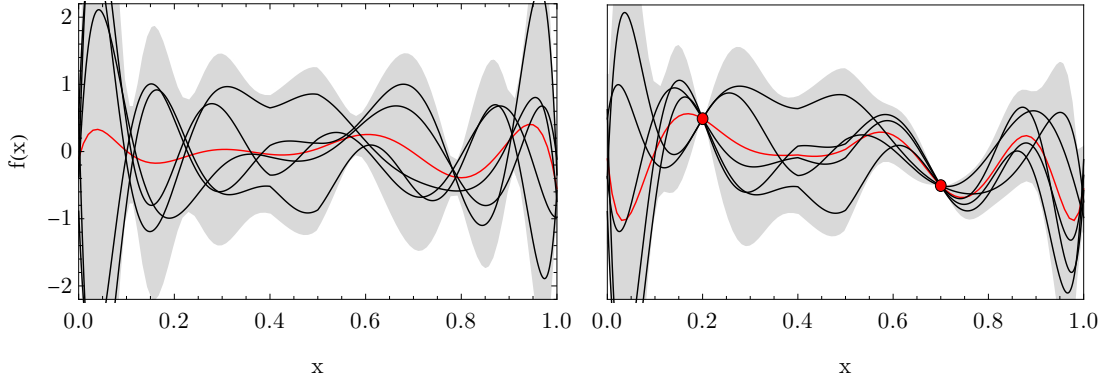


Figure 5.7: Illustration of a Gaussian process. The system begins with no data and a space specified by large uncertainty. Various models fit this space, and the mean (red) of these models is taken. Data is acquired (red dots in right figure) which allow the models to be refined. Now the uncertainty at these points is significantly reduced and the mean of the models better reflects the space. As more data is acquired, the uncertainty in the space decreases and the optimisation of the model is more effective.

perimental applications, this is extremely valuable as noise is generally inherent to all real-world systems.

5.3.2 Experimental algorithm

Since the experiment is noisy and sensitive to external variables that are often uncontrollable, the same parameters often produce different results. As such, the experiment is modelled as a stochastic process $\mathcal{C}(\mathbf{X})$ dependent on the input parameters

$$\mathbf{X} = (x_1, \dots, x_M). \quad (5.14)$$

Any measurement and resulting cost can be interpreted as a sample of this process $C(\mathbf{X})$ with some associated uncertainty $U(\mathbf{X})$, taking into account the variability and noise of the experiments. Given this, the set of all parameters, costs and uncertainty previously measured are given by

$$\mathcal{X} = (\mathbf{X}_1, \dots, \mathbf{X}_N), \quad (5.15)$$

$$\mathcal{C} = (C_1, \dots, C_N), \quad (5.16)$$

$$\mathcal{U} = (U_1, \dots, U_N), \quad (5.17)$$

respectively, with the set collectively referred to as the observations

$$\mathcal{O} = (\mathcal{X}, \mathcal{C}, \mathcal{U}). \quad (5.18)$$

The online optimisation of the experiment aims to use the previous observations \mathcal{O} as a basis for planning future experiments, with the goal being to determine a set of parame-

ters that minimise the mean cost of the stochastic process $M_{\mathcal{C}}(\mathbf{X})$.

This is achieved by estimating the stochastic process given the observations $\mathcal{C}(\mathbf{X}|\mathcal{O})$ and using this to determine what subsequent parameters should be used. This scheme utilises a Gaussian process to model $\mathcal{C}(X)$. As outlined in Subsection 5.3.1, a Gaussian process describes a distribution over *functions*. This Gaussian process is implemented with a constant mean function and covariance defined by a squared exponential correlation function

$$K(\mathbf{X}, \mathbf{X}', \mathbf{H}) = \exp \left[- \sum_{j=1}^M \frac{(x_j - x'_j)^2}{h_j^2} \right], \quad (5.19)$$

where

$$\mathbf{H} = (h_1, \dots, h_M) \quad (5.20)$$

is a set of correlations lengths for each of the parameters. The mean function, evaluated through a set of matrix operations [162] and conditional on the observations \mathcal{O} and correlations lengths \mathbf{H} of the Gaussian process is given by

$$\mu_{\mathcal{C}}(\mathbf{X}|\mathcal{O}, \mathbf{H}). \quad (5.21)$$

Additionally, the variance of the functions, conditioned on \mathcal{O} and \mathbf{H} is represented by

$$\sigma_{\mathcal{C}}(\mathbf{X}|\mathcal{O}, \mathbf{H}). \quad (5.22)$$

Both of these estimates depend on the correlation lengths \mathbf{H} , normally referred to as the hyper-parameters of the estimate. \mathbf{H} is assumed to be unknown a-priori, thus requiring fitting be performed online.

The correlation lengths \mathbf{H} control the sensitivity of the model to each of the parameters, relating to how much a parameter needs to change before significantly affecting the cost. A standard approach is to fit the hyper-parameters through a maximum likelihood estimation [162]. Here, the hyper-parameters are globally optimised over the likelihood of the parameters \mathbf{H} given the observations \mathcal{O} , or equivalently $L(\mathbf{H}|\mathcal{O})$ [162]. However, when the dataset is small there will often be multiple local optima for the hyper-parameters whose likelihoods are comparable to the maximum. We term these hyper-parameters the hypothesis set

$$\mathbf{H} = (H_1, \dots, H_p), \quad (5.23)$$

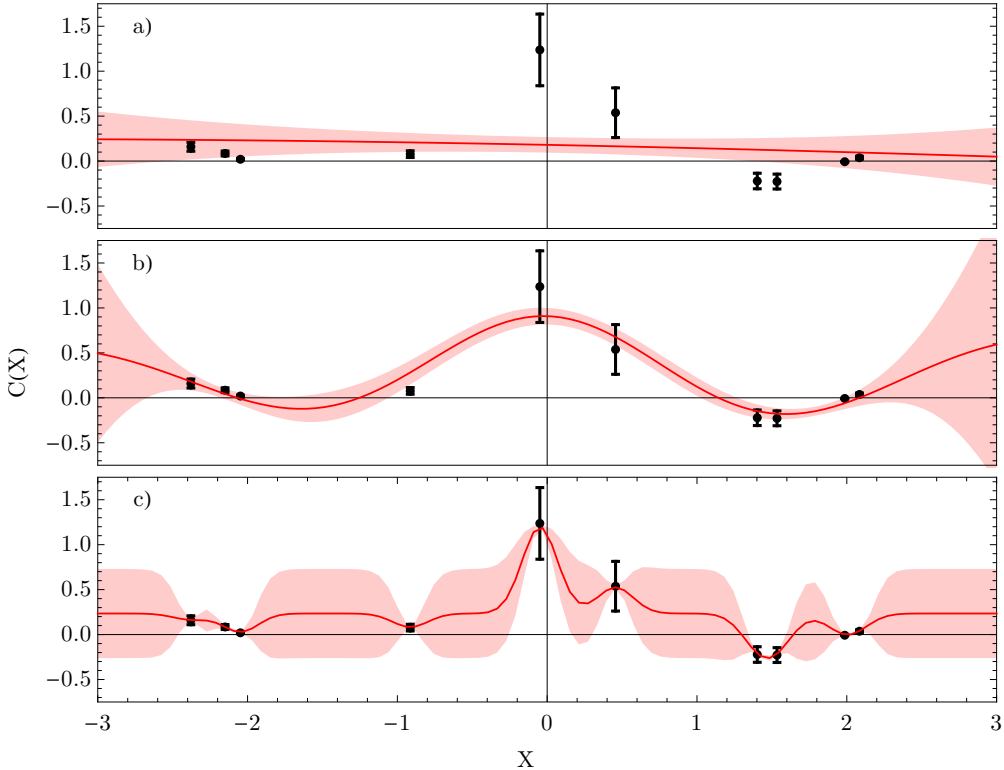


Figure 5.8: Illustration of the effect of different correlation lengths on the Gaussian process model. The machine learning algorithm models the relationship between the input parameters, X , and the resulting cost function, $C(X)$, using a Gaussian process. The model depends on a set of correlation lengths for each parameter. Illustration shows a set of data (black) with corresponding uncertainties (black error bars) along with three possible Gaussian process models that fit the data. Part a) shows a long correlation length, b) a medium correlation length and c) and short correlation length. The model produces a mean cost function (solid red line) along with uncertainty in the model (red shading representing ± 1 standard deviation from mean). The correlation length essentially relates to the amount of structure in the model and affects both the mean and the uncertainty. Note also that the uncertainty decreases close to the experimental data. The final cost function produced by the model is produced via a weighted average over all the correlation lengths. The learner uses this final model to recommend the next set of parameters for the experiment.

with corresponding likelihood set

$$\mathbf{L} = (L_1, \dots, L_P). \quad (5.24)$$

To produce the final estimates for the mean function and variance, each hypothesis set is treated as a ‘particle’ [163], with a weighted average generated over \mathbf{H} . The weighted mean function is now defined as

$$M_{\hat{\mathcal{C}}}(\mathbf{X}|\mathcal{O}, \mathbf{H}) \equiv \sum_{i=1}^P w_i \mu_{\hat{\mathcal{C}}}(\mathbf{X}|\mathcal{O}, H_i), \quad (5.25)$$

with the weighted variance of the functions given by

$$\Sigma_{\hat{\mathcal{C}}}^2(X|\mathcal{O}, \mathbf{H}) \equiv \sum_{i=1}^P w_i (\sigma_{\hat{\mathcal{C}}}^2(\mathbf{X}|\mathcal{O}, H_i) + \mu_{\hat{\mathcal{C}}}^2(\mathbf{X}|\mathcal{O}, H_i)) - M_{\hat{\mathcal{C}}}^2(\mathbf{X}|\mathcal{O}, \mathbf{H}), \quad (5.26)$$

where

$$w_i = \frac{L_i}{\sum_{i=1}^P L_i} \quad (5.27)$$

are the relative weights for the hyper-parameters. Given the final estimate for $\mathcal{C}(\mathbf{X}|\mathcal{O}, \mathbf{H})$, an optimisation strategy must be chosen for selecting the next set of parameters to test.

The solution is two competing strategies, each selected for a different specific goal. The first aims to test parameters that are predicted to minimise $M_{\hat{\mathcal{C}}}(\mathbf{X})$, ensuring the learner acts as an ‘optimiser’. This alone would likely result in the learner getting trapped in local minima, resulting in the reinforcement of ignorance. Conversely a strategy might be designed to test parameters that maximise $\Sigma_{\hat{\mathcal{C}}}^2(X)$ and test points where the model is least certain. This would provide the learner with experimental data that allows it to refine the internal model and better discriminate between the hypotheses. In this respect the learner would be acting as a ‘scientist’. With this strategy alone, the learner would require an inordinately large number of trials to map the space effectively and would not prioritise refinement of the global minima. Instead, consider a balanced strategy that repeatedly sweeps between both extreme strategies through minimising a biased cost function

$$B_{\hat{\mathcal{C}}}(\mathbf{X}) \equiv bM_{\hat{\mathcal{C}}}(\mathbf{X}) - (1-b)\Sigma_{\hat{\mathcal{C}}}^2(\mathbf{X}), \quad (5.28)$$

where b represents the bias that describes the weighting of each strategy. By linearly increasing the bias from 0 to 1 in a cycle of length Q the learner can be swept from acting completely as an ‘optimiser’ ($b = 1$) to acting completely as a ‘scientist’ ($b = 0$). This process was found to be significantly more robust and efficient than fixing the learner to a single strategy.

Finally, the minimisation of $B_{\hat{\mathcal{C}}}(\mathbf{X})$ is somewhat constrained by implementing bounds on the possible values of new test points. These bounds are defined as 20% of the maximum-minimum values of the parameters, relative to the last best measured \mathbf{X} . Called a ‘leash’ these bounds restrict how fast the learner changes the parameters while still allowing the full space to be explored, similar to trust-regions [164, 165]. The use of parameter bounds stems from technical considerations outlined in the following chapter. Specifically, a set of parameters vastly different from the previous set typically resulted in a failed cost function. This required a default cost to be assigned eventuating in little

meaningful gradient information being returned to the learner.

Once the next set of parameters is determined they are sent to the experiment to be tested. After the resultant cost is measured this is then added to the observation set \mathcal{O} with $N \rightarrow N + 1$ and the entire process is repeated. Crucially, the fitting of H , the estimation of $M_{\mathcal{C}}(\mathbf{X})$ and the minimisation of $B_{\mathcal{C}}(\mathbf{X})$ is all done online while the experiment is being performed.

The algorithm outlined above is the basis for the machine learning algorithm implemented experimentally to the optimisation of the evaporation stage of the production of ^{87}Rb Bose-Einstein condensate, the results of which are shown in the following chapter. Through comparison with the Nelder-Mead algorithm, the machine learning algorithm is benchmarked.

Experimental Machine Learning

The optimisation of complex physical processes is often achievable with theoretical models, however, these models typically include approximations to the system and certainly do not include the nuances and subtleties of a particular experiment. As such, it becomes enticing to perform the actual optimisation on the experiment itself with all the intricacies, by definition, accounted for. Such optimisation is called ‘online’ optimisation. Online optimisation of experimental physics has the potential to be a powerful tool. As experiments become more and more complex with increasing inputs, machine learning provides a tool for generating fast optimisation with additional insight into the input-output relationship. Online optimisation using genetic algorithms has been used extensively to optimise experiments [139–152], as well as simpler gradient based algorithms [166] and more subtle hybrid optimisation algorithms [155, 167]. Online optimisation using Gaussian processes [162, 163, 168–170] have been used in robotics [171, 172], vision [173], industrial chemistry [174, 175] and biochemistry [176]. The following chapter describes the process of applying the Gaussian process machine learning algorithm described in the previous chapter for the purpose of online optimisation of the evaporative cooling stage of Bose-Einstein condensate production.

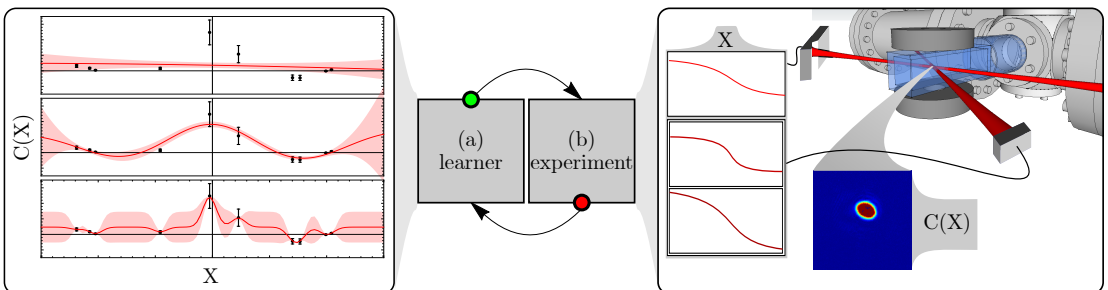


Figure 6.1: Diagram of a closed-loop control system. (a) and (b) appear to each other as ‘black boxes’, providing only outputs and inputs in the form of a performance measure $C(X)$ and parameters to test X . In this context the learner, (a), provides a set of parameters, X which are fed to the experiment (b). The evaporation ramps are produced from these parameters and used in the experiment. An image is taken of the resultant cloud of atoms and a function $C(X)$ applied to produce a quantitative value for the success of the experiment. This value is returned to the learner with a corresponding uncertainty. The learner uses the data to refine a model based on Gaussian processes before optimising the model and returning a new set of parameters to test.

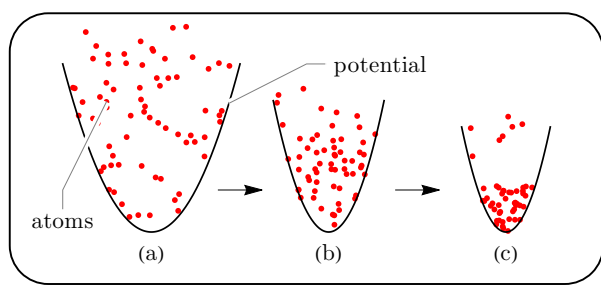
The online optimisation outlined in this chapter is a closed-loop control system. The basis of closed loop control is illustrated in Figure 6.1. Here (a) and (b) are simple ‘black boxes’, only interacting with each other through an input and an output. The learning algorithm (a in Figure 6.1) provides the experiment (b in Figure 6.1) with parameters \mathbf{X} to test. The experiment runs using these values and evaluates the result. The performance is characterised by a single value $C(\mathbf{X})$ and returned to the learner. The learning algorithm assesses the result before refining the internal model and producing more parameters to test, continuing the cycle. The ultimate goal of the learner is to produce a set of parameters that produce the best cost along with a model of the system.

6.1 Evaporative cooling of atoms

The development of evaporative cooling using both magnetic and optical confinement was a key to the experimental realisation of Bose-Einstein condensation [177]. Forced evaporation of neutral atoms trapped in such potentials occur as the trap depth is slowly lowered allowing the hotter atoms with higher kinetic energy, to escape. The remaining atoms undergo elastic collisions, rethermalising to a lower temperature, while ideally retaining high densities. Optimisation of evaporation, and the process by which the trap depth is decreased, leads to larger, colder samples. Numerous theoretical models have been developed to determine optimal evaporation schemes [178, 179], however the system is treated under conditions of ergodic dynamics with two-body s-wave interactions and no other loss rates which is likely sub-optimal for real experiments. Microscopic semi-classical theory exists to describe the process [180], but oversimplifies the dynamics and overlooks more complex methods for achieving evaporation. Shobu *et al.* found that using higher order inelastic scattering processes could achieve better evaporation [181]. It is likely that similar methods exist for other atomic species with complicated scattering properties [182], but currently very little theory exists modelling such schemes.

The problem is further complicated by the disconnect between the experimental controls and the potentials experienced by the sample. Often the relationships between input voltage and output laser intensity is not clear and often not even linear. This means

Figure 6.2: Illustration of the evaporative cooling process. By lowering trap depth, higher energy atoms are allowed to escape, with the remaining atoms rethermalising to a lower temperature producing a higher phase-space density. The evaporative cooling process continues until the critical temperature is reached and condensation occurs.



that formulating optimal methods for lowering trap depth does not equate to an optimal scheme for changing the experimental controls and complicates the application of theoretical models to experiments.

6.2 Experimental apparatus

The experimental apparatus is described in detail in [183]. A 2D magneto-optical trap (MOT) is initially used to cool a sample of ^{87}Rb atoms. A pair of co-propagating push beams loads the primary 3D MOT system with the full load taking approximately 10 s and resulting in $\sim 5 \times 10^8$ trapped ^{87}Rb atoms. This process is limited by the size of the MOT beams and the flux of the 2DMOT. Polarisation gradient cooling is then used to reduce the temperature of the cloud to $\sim 15 \mu\text{K}$. After $\sim 25 \mu\text{s}$ of polarisation gradient cooling the sample is pumped to its magnetic ground state ($|F = 1, m_F = -1\rangle$). Immediately following this, the magnetic coils are switched to a quadrupole configuration and the magnetic field steadily increased as two crossed dipole lasers are also initialised and their intensity increased. The resultant hybrid magnetic and optical dipole trap holds the sample of atoms. The cloud is further cooled by 3 seconds of radio-frequency (rf) evaporation before the magnetic field is slowly extinguished and the cloud fully loaded into the crossed dipole trap. At this point, the sample contains 4×10^7 atoms at a temperature of $\sim 5 \mu\text{K}$ with a phase space density of ~ 0.05 . A final evaporation stage is performed using the dipole trap, with the intensity of each beam slowly reduced, cooling and increasing the phase-space density until condensation occurs. This final stage of evaporation is where the optimisation occurs with control of the crossed-dipole beam intensity surrendered to the machine learning algorithm. Typically the evaporation stage occurs over a period of 3.5 s, however, the period of the evaporation stage is provided to the learner as an input. The cross dipole trap is formed from two intersecting 1090 nm and 1064 nm lasers with approximate waists of 350 μm and 300 μm respectively producing a trap with frequencies $185 \times 185 \times 40 \text{ Hz}$. The depth of the cross trap is determined by the intensity of the two beams and is found to be approximately 70 μK . The 1064 nm beam is controlled by varying the current to the laser, while the 1090 nm beam is controlled using the current and a wave plate rotation stage combined with a polarising beam splitter to provide additional power attenuation while maintaining mode stability. The final sample is imaged using an absorption imaging system set up to capture after a set time-of-flight after the dipole trap is extinguished. As the condensate falls through the imaging region (typically after a $\sim 25 \text{ ms}$ time-of-flight), it is repumped into the $|F = 2\rangle$ ground state. Following this, the atoms are imaged using a 100 μs pulse from a probe beam resonant with the $|F = 2\rangle \rightarrow |F' = 3\rangle, D_2$ transition. The atoms absorb part of the beam generating a shadow proportional to the optical column density of the

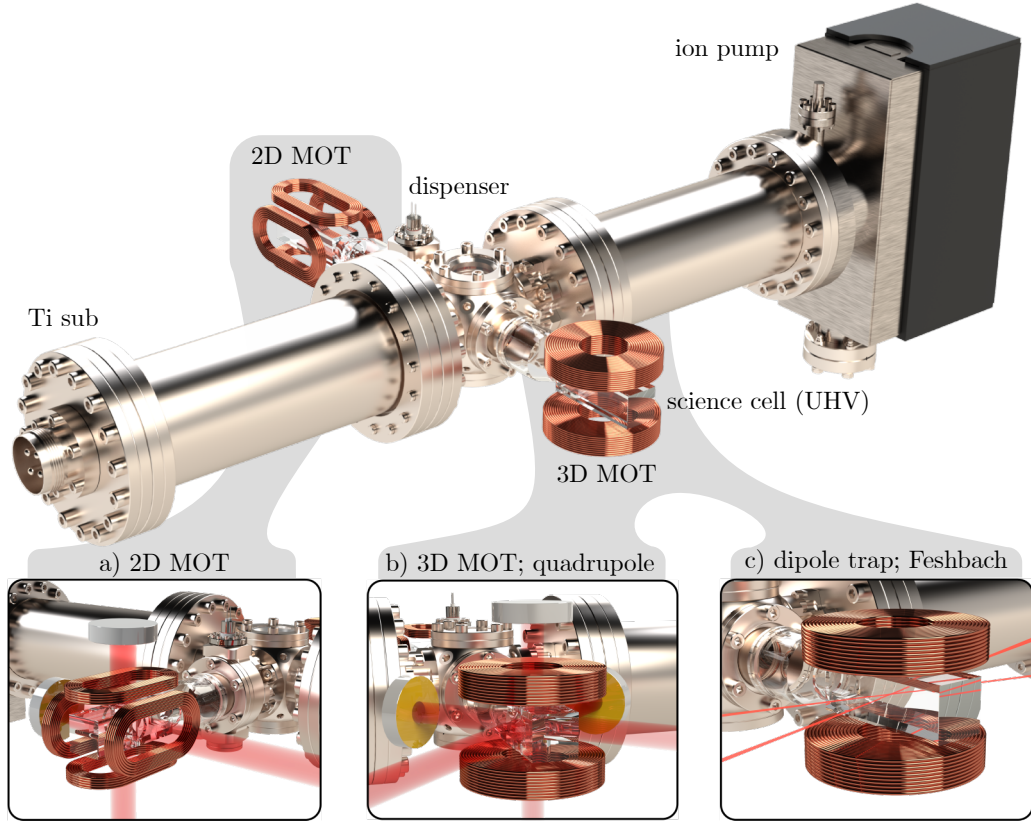


Figure 6.3: Diagram of the dual-species vacuum system and various key components. A rubidium vapour dispenser provides the atomic source for both isotopes, ^{85}Rb and ^{87}Rb . (a) the 2D MOT collects these atoms in a line through the centre of the glass cell. A push-beam is used to move atoms from the 2D MOT through a high impedance line to the ultra-high vacuum (UHV) science cell. (b) the atoms are collected and cooled by a 3D MOT with subsequent polarisation gradient cooling reducing the temperature further. Radio-frequency evaporative cooling is then performed using a quadrupole configuration for the magnetic coils. (c) The atoms are then transferred to a dipole trap formed by two crossed dipole laser beams with the temperature further reduced through lowering the dipole trap intensity, driving a final stage of evaporative cooling. One of the dipole beams can be extinguished for experiments using a waveguide. The direction of current in one of the coils can be flipped to produce a uniform magnetic field across the atoms allowing experiments exploiting the ^{85}Rb Feshbach resonance.

sample. This shadow is then imaged using a standard $2f$ lens system and recorded using a charge-coupled-device (CCD). A second image without the sample is also obtained as a background reference and used to calculate the optical density (see Section 7.1). This image provides spatial density information and allows for the calculation of the measure of success which is subsequently provided to the machine learning algorithm.

6.3 Cost function

Key to any optimisation process is the quantification of success. Often this performance measure is termed the ‘cost’ or ‘cost function’. Developing a robust cost function is im-

perative to optimisation, especially if the process being optimised passes through many different regimes. For the optimisation of the evaporative cooling stage of a Bose-Einstein condensate experiment, the cost function must always point towards a denser, cooler sample.

A number of cost functions were investigated with varying success. In a preliminary test, the cost function was defined as the total number of atoms after the evaporation stage. Optimisation using this cost function resulted in the machine learning algorithm holding the inputs constant and effectively removing the evaporation stage from the experiment. Although this did maximise the total number of atoms (as none were lost to evaporation), the resultant cloud was not any cooler or denser. This result is, perhaps, an obvious side-effect of such a cost function and demonstrates the importance of a well chosen and characterised cost function.

Alternatively it was thought that the phase-space density, a measure of the number of atoms per cubic de Broglie wavelength, may provide a good measure of success. The phase space density, defined as

$$\rho = n\Lambda^3 \propto \frac{n}{T^3} \quad (6.1)$$

where Λ is the de Broglie wavelength, scales as N/T^3 [184]. Calculating this cost function for each absorption image therefore requires a robust measurement of temperature. Typically a precise measurement of temperature requires multiple images of the cloud undergoing ballistic expansion. This was not possible given the constraints of the exper-

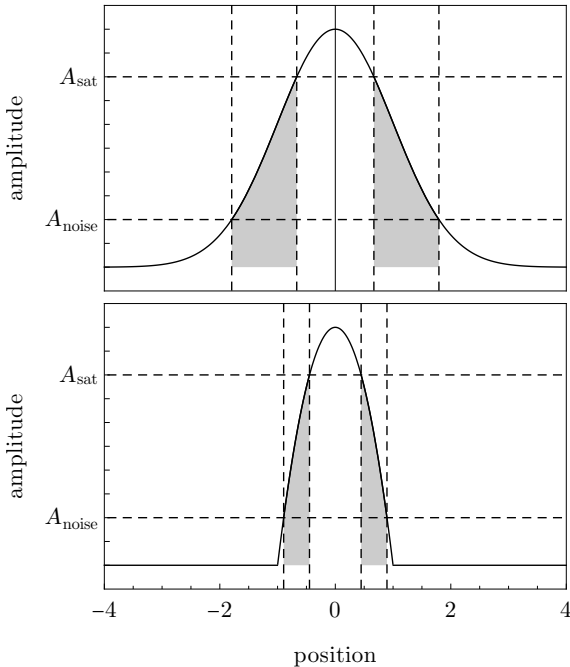


Figure 6.4: Final method for calculating the cost function, showcasing the different regimes the machine operates in. The top figure shows a Gaussian distribution, highlighting the broader thermal case. The bottom figure shows an inverted parabola indicating the operation of the cost function in the condensed regime. In practice the experiment varies smoothly between these two distributions, often with a clear ‘bi-modal’ shape. A_{sat} is set by the saturation level on the camera. This prevents noise above the saturation point contributing to the cost. A_{noise} is set by the dark noise on the camera and similarly prevents noise from contributing to the cost.

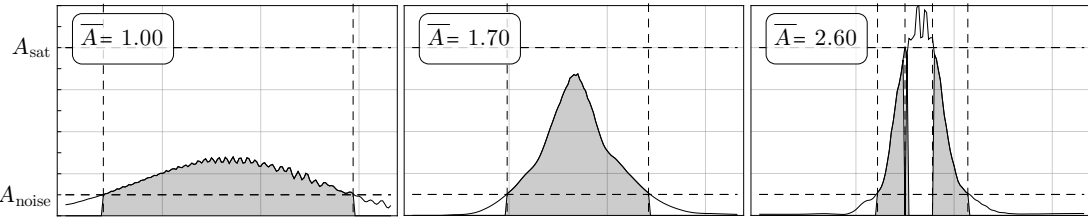


Figure 6.5: An example set of one dimensional data, outlining the utility of the designed cost function. A noise floor, A_{noise} , ensures that dark noise on the camera affects the value of the cost function less. Likewise a ceiling A_{sat} ensures that the effect of saturation on the cost function is diminished. These two thresholds work in unison to make the cost calculation more robust. The calculation essentially works to determine the sharpness of the ‘wings’ of the cloud. For a more thermal distribution (top), the entirety of the signal lies below saturation and so the wings essentially extend across the whole cloud resulting in a low cost. For condensed samples the density is high and only the sharp edges of the cloud contribute to the cost. The centre image shows a set of example data that is bi-modal. \bar{A} defines the mean cost of the area between the cutoffs.

iment and so an estimate was used instead. This estimated temperature was calculated using width of a Gaussian fit to the absorption image. Unfortunately this proved to be extremely temperamental, especially when the cloud reached a regime close to condensation where the temperature becomes poorly defined. Although not implemented at the time of this research, a non-destructive imaging system was later built for this experiment (see Chapter 8 for further details). It is possible that this system could be used to more precisely and robustly measure temperature (in a single experimental run) thereby improving the cost function.

Given the constraints of the system, a more successful cost function was found using a more heuristic method. By imaging fully on-resonance, the peak of the sample is saturated, but importantly the ‘wings’ are well characterised. Given the saturation of the absorption images, an upper threshold level (A_{sat}) is set, with all data above this value being set to zero. This ensures that the cost function is not overly affected by the noise on the saturation. Similarly, a lower threshold (A_{noise}) is set, with all data below this value set to zero. This ensures that any contribution of background noise is minimal. What remains after these thresholds have been applied is only data at the edges of the cloud. The cost is calculated by averaging the value of these edges. This process is illustrated in the toy examples shown in Figure 6.4 where the cost function has been applied to both a Gaussian distribution (top) and an inverted parabola (bottom).

Crucially, hotter thermal clouds with a Gaussian distribution result in a large edge width, which decreases as the temperature decreases. Eventually the phase transition is reached and a significant portion of the cloud is represented by a Thomas-Fermi distribution indicated by an inverted parabola. This distribution has a much sharper and narrower edge and therefore a lower cost. These two regimes are smoothly connected by this cost function, with the cloud generally transitioning between the two via a ‘bi-

modal' distribution. An illustration of the method is shown in Figure 6.5, where the cost function has been applied to experimental data (shown as a 1D slice for simplicity). The left image shows a hotter, thermal cloud where the majority of the cloud lies between the thresholds resulting in a poor cost. The right image shows a cloud that is much closer to condensation with only part of the cloud (the edges) lying between the thresholds. This results in a much better value for the cost. The middle image illustrates the regime between thermal and condensate with the bi-modal distribution evident. It should be noted that this cost function does not specifically optimise the condensate number, but could be altered to achieve this goal.

6.4 Parameterisations of evaporation ramps

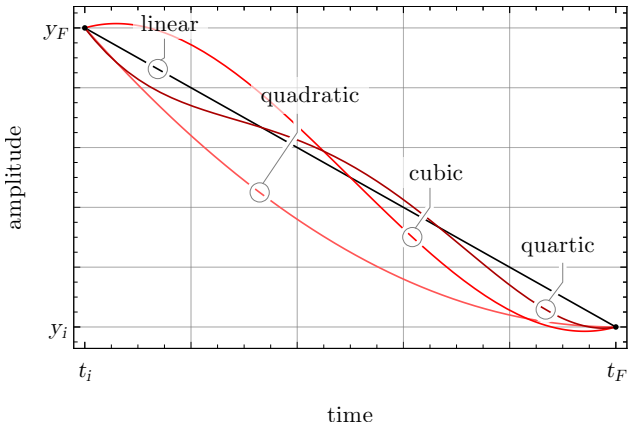
Any optimisation process requires inputs that are altered to improve the outcome. In this case, the laser powers input at the evaporation stage directly affect the quality of the condensate produced. In principle, the entire evaporation ramp could be parameterised by n points linearly sampling the interval. However, this produces a prohibitively large parameter space resulting in a problem that is extremely difficult to optimise. To allay this problem, a set of basis functions define the shape of the ramps, with the weight of the basis functions then being the input parameters to be optimised. In theory the basis should be infinite, allowing any arbitrary curve to be built. In practice, however, the basis set is truncated to a more manageable size. This truncation is less problematic if the lower order basis states reflect the optimal solution, therefore allowing a smaller set of parameters. The naïve approach for experimental evaporation ramps is to use exponentially decreasing functions, as the optimal theoretical ramps given ergodic dynamics and two-body s-wave interactions is a potential that decreases exponentially. To enable more freedom in the shape of the ramps, yet still allow the lower order basis states to provide a decreasing ramp, a polynomial basis was chosen.

Two levels of truncation were chosen to test; one, the 'simple' parameterisation, requiring only 3 parameters and the other 'complex' parameterisation consisting of 5 parameters. The simple parameterisation of the evaporation ramps is

$$\mathcal{R}_s(y_i, y_f, t_f) = y_i + (y_f - y_i) \frac{t}{t_f}, \quad (6.2)$$

where y_i and y_f specify the start and end amplitudes of the ramps and t_f specifies the length in time, given the beginning of the ramp is at t_i . The complex parameterisation

Figure 6.6: The curves representing each of the basis functions of the evaporation parameterisation. The beginning time is set by the previous experimental procedure. The final time, initial and final height act as input parameters with the full set of parameters being $\mathbf{X} = \{t_f, y_i, y_f, A_1, A_2, A_3\}$. Each of the basis functions attempts to encode a more complex part of the curve. Experimentally, the amplitude cannot be negative, so the final curve is automatically truncated at zero before being sent to the experiment.



forms an extension of the simple version, with the evaporation ramp defined by

$$\mathcal{R}_c(y_i, y_f, A_1, A_2, A_3, t_f) = y_i + (y_f - y_i) \frac{t}{t_f} + A_2 t (t - t_f) \quad (6.3)$$

$$+ A_3 t (t - t_f) \left(t + \frac{1}{2} t_f \right) \quad (6.4)$$

$$+ A_4 t (t - t_f) \left(t + \frac{2}{3} t_f \right) \left(t + \frac{1}{3} t_f \right), \quad (6.5)$$

where A_1 , A_2 and A_3 correspond to the 3rd, 4th and 5th order polynomial terms respectively, with each polynomial having evenly spaced roots between $t = t_i$ and $t = t_f$. As with the simple parametrisation t_f specifies the end of the ramps in time.

The ramps dictate the power of the crossed dipole trap formed by two intersecting 1090 nm and 1064 nm lasers. The depth of the cross trap is determined by the intensity of the two beams. As previously detailed, the 1064 nm beam is controlled directly by varying the current to the laser. The 1090 nm beam has a slightly more complicated control, consisting of both current control and the use of a wave plate rotation stage combined with a polarising beam splitter. This additional control allows for precise attenuation while maintaining mode stability of the laser. The additional control for the 1090 nm laser is a technical choice rather than any fundamental reason. A simplified diagram of the experimental set up is shown in the right of Figure 6.1. Each of the three controls require a separate ramp, each being optimised. Five of the six parameters, y_i , y_f , A_1 , A_2 , and A_3 are independent with the final time, t_f , being common to all three. For technical reasons, the amplitude of the ramps cannot be negative, so the final curve is automatically truncated at zero before being sent to the experiment. We hand over control of these ramps to the machine learning algorithm.

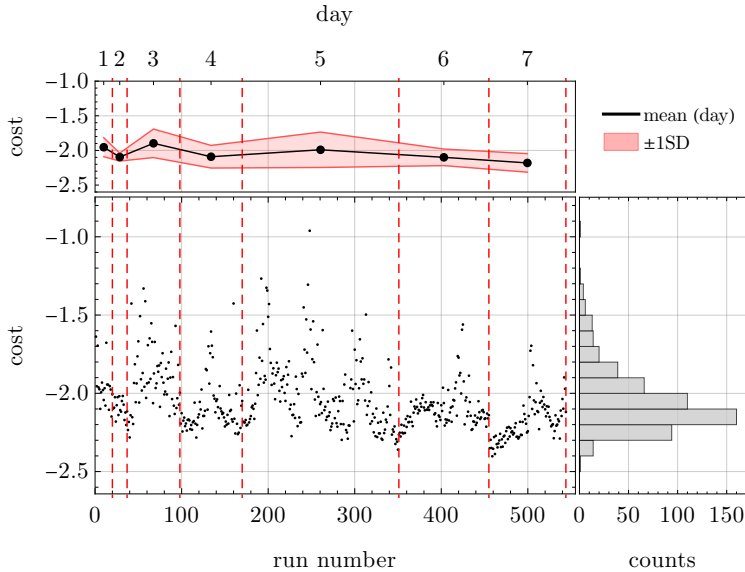


Figure 6.7: The variation in outcome for an experimental run that produces Bose-Einstein condensates. The experiment was run many times using the same parameters over the course of a week. The results generate a skewed Gaussian shape with the skew being towards lower cost results. The experiment appears to have some low frequency sweeps, possibly due to thermal cycles in the room.

6.5 Uncertainty handling

Since the experiment is sensitive to many external factors that are unable to be controlled, a set of parameters will produce a different outcome run-to-run. The machine learning algorithm is able to account for this by associating an uncertainty with each calculated cost. Ideally this uncertainty would be determined by evaluating a single set of parameters numerous times and applying statistics to calculate a standard deviation in the result. Given the experimental cycle is ~ 25 s, this becomes infeasible and certain approximations must be implemented.

In order to characterise the stability of the experiment, a set of data was obtained, sampled once a day across a week with the results shown in Figure 6.7. This simple characterisation suggests that the experiment roughly obeys Gaussian statistics. This enables us to estimate an uncertainty in the calculated cost for a given set of parameters which is then provided to the machine learning algorithm. To achieve this, the experiment is run twice for each set of parameters, with the average of the calculated costs being recorded. If two random variables are sampled from a Gaussian distribution with width σ_X to get a value $Y = X_1 - X_2$, then Y will also be Gaussian with a mean $\bar{Y} = 0$ and standard deviation $\sigma_Y = \sqrt{2}\sigma_X$. The probability that σ_Y will be subsequently be less than σ_X is: 52%. But if $Y = 2(X_1 - X_2)$ is instead used, the probability of underestimating the uncertainty will be reduced to 27%. The uncertainty is therefore taken to be twice the range of the two costs, with this value and the mean of the two costs given to the algorithm. As an added safety measure, the uncertainty is constrained; too small an uncertainty and a default lower value is used, too high and a default upper value is used.

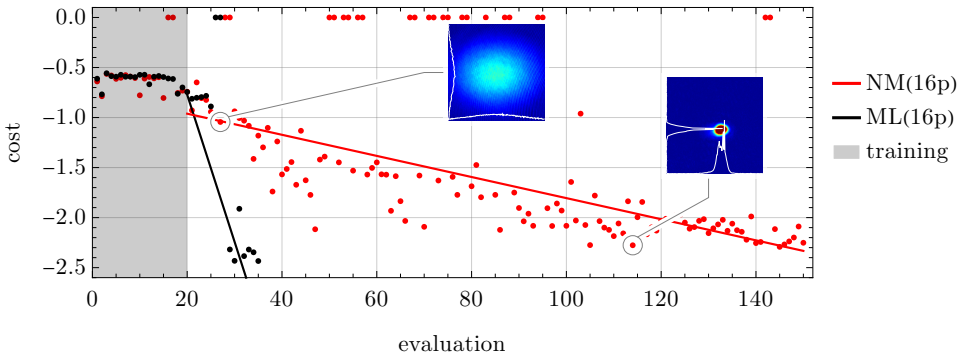


Figure 6.8: The optimisation of the evaporation stage of the production of a Bose-Einstein condensate using the complex 16 parameter scheme. The first 20 evaluations are an initial training run using a simple Nelder-Mead algorithm. The machine learning algorithm (black) then quickly optimises to a Bose-Einstein condensate. The insets show the different regimes experienced by the experiment, from a completely Gaussian thermal distribution, through the bimodal distribution containing a thermal background to the sharp edged condensate. The included cross-section illustrates how the cost decreases as the edges of the cloud get sharper.

6.6 Results

In order to characterise and demonstrate the performance of the machine learning algorithm, a set of optimisation runs were performed and compared to a standard Nelder-Mead algorithm (as outline in Subsection 5.2.1). Initially, the complex parameterisation described in Section 6.4 was used for all three evaporation ramps. This amounted to 16 parameters with the total time of the ramp also controlled. For context, a simple brute force search and optimisation of this number of parameters to within 10% accuracy of their maximum-minimum bounds would require approximately 10^{16} runs which, given the duration of a single experimental run, would take longer than the age of the universe to complete. Despite this complexity, even the simple Nelder-Mead algorithm was able to find a set of parameters producing a Bose-Einstein condensate in only 145 runs. In contrast, the machine learning algorithm required only 10 additional runs after the initial 20 training runs common to both algorithms. This is shown in Figure 6.8 where the machine learning algorithm (black) quickly finds an optimum, whereas the Nelder-Mead algorithm requires more runs to obtain this optimum. Figure 6.9 shows the history of the evaporation ramps attempted by both algorithms. The machine learning algorithm is seen to produce ramps that were shorter in time. Although not targeted specifically, this could be added to the cost function to generate faster evaporation ramps. It is also worth noting that though both algorithms converged to ramps that decrease over the course of the evaporation, they produce slightly different optimal parameters, suggesting there might be multiple minima present. Furthermore, the optimal ramps differ quite significantly from exponential ramps typically used. This may reflect the complexity inherent in experimental systems that mean an exponential ramp in the control does not equate to

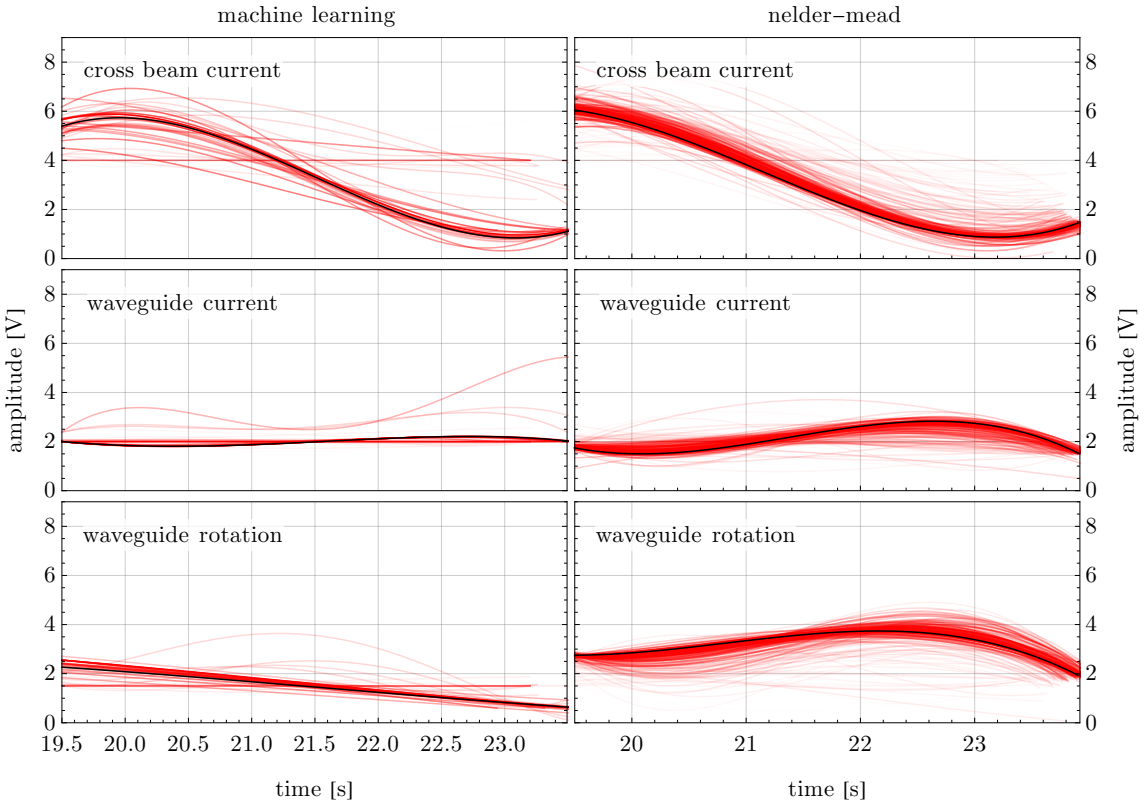


Figure 6.9: Evaporation ramps through the optimisation procedure. Left figure shows the machine learning history with the ramp quickly converging to the optimal parameters. Right figure shows the equivalent Nelder-Mead optimisation illustrating the slow approach where the algorithm slowly walks down the cost landscape towards the minimum. Although the optimal ramps are similar, they are not equal indicating that the landscape may be complex and contain multiple minima. Note also that the Nelder-Mead algorithm converged to a longer evaporation ramp than the machine learning. Although time was not explicitly optimised it would be possible to include this in the cost function as a means of decreasing the time spent performing evaporation. The time axis begins at 19.5s reflecting the duration of the experimental run prior to the evaporation.

an exponential ramp in the potential height highlighting the power of a machine learning algorithm for experimental physics.

Since the parameter-space was so large, the 16 parameter optimisation was restricted to only consider the best hypothesis set when picking the next set of parameters. This restriction is a result of the computational complexity of evaluating multiple Gaussian processes. When allowing multiple hypothesis sets, the evaluation was unable to produce a new parameter set faster than the duty cycle of the experiment. Despite this restriction however, the machine learner was able to determine an optimum set of parameters in few iterations of the experiment. The reason for the success was likely due to the choice of parameterisation, with the endpoints of the ramps seemingly the most important parameters. The correlation lengths corresponding to these parameters were consistently well-estimated, unlike the correlation lengths for the other parameters which were poorly estimated and failed to converge despite the success of the optimisation. As a result, any

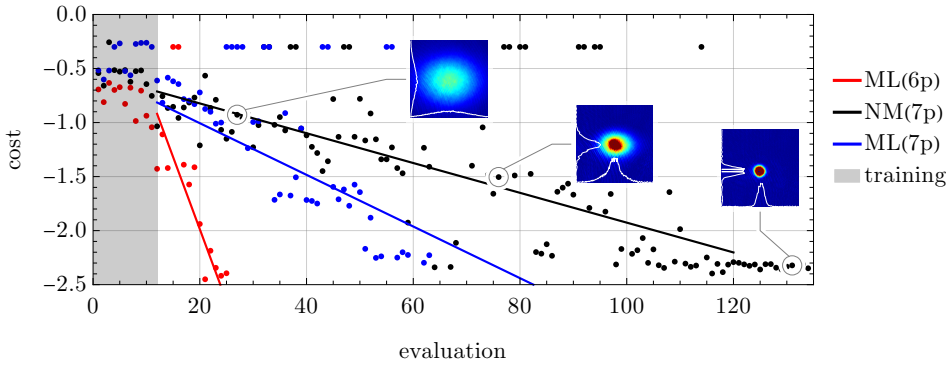


Figure 6.10: Experimental optimisation of evaporation curves to produce a Bose-Einstein condensate. The first $2N$ evaluations use a simple Nelder-Mead algorithm as training to learn about the cost space. The machine learning algorithm (red and blue) optimises to a condensate faster than the Nelder-Mead (black). By utilising the machine learning model a parameter is eliminated and the convergence improves (red).

prediction of the cost landscape is less reliable and using the model to determine the least important parameters is not possible.

Although the algorithm was able to determine a set of successful parameters, it would be desirable to obtain a reliable model of the cost landscape. It has been suggested that using multiple particles enables better online estimation of the Gaussian process correlation lengths [163]. With this in mind, the number of hypothesis sets used by the learning algorithm was increased with the number of particles set to 16. Since the computational expense also increases with this addition, the simple parameterisation was implemented reducing the number of parameters to a total of 7. As shown in Figure 6.10, the machine learning algorithm (blue) is able to produce a successful set of parameters faster than the corresponding Nelder-Mead algorithm (black), albeit with a less pronounced difference. The addition of more particles has reduced the speed of convergence compared to the case with the complex parameterisation. Despite this, the calculated correlation lengths are now more reliable and the resultant model better able to predict the cost landscape. This enables analysis of the model to guide experimental design and implementation.

By increasing the number of particles, the correlation lengths used to produce the Gaussian process model converge and can be more reliably trusted. Figure 6.11(a) shows a 1D cross-section of the cost landscape as taken through the best measured point with the two most sensitive (black, red) shown along with the least sensitive (blue). The least sensitive parameter is seen to have little bearing on the outcome of the experiment and whether or not the evaporation ramps produce a condensate or not. This parameter actually corresponds to an intentionally added 7th parameter that does not correspond to any physical input on the apparatus. The learner correctly identifies this, despite only performing a limited number of experiments and having such a small data set. Once this parameter has been identified the design and implementation of the experiment can be

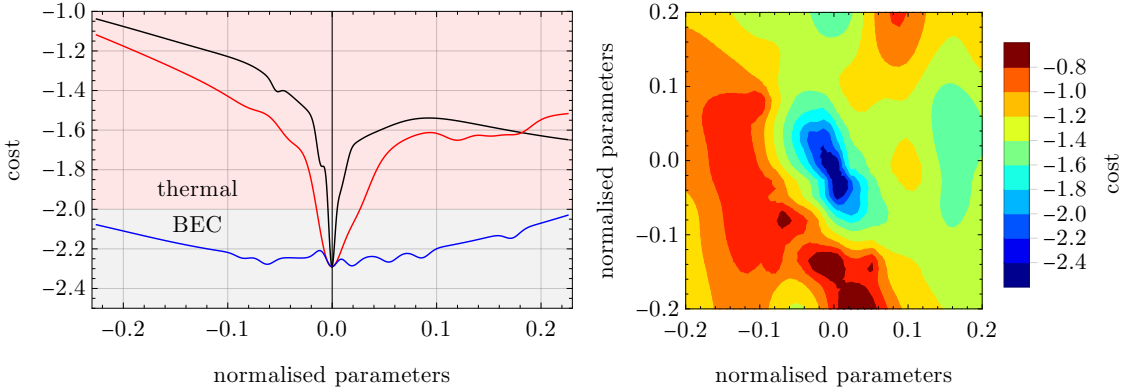


Figure 6.11: Plots of the cross sections through the minima of the cost landscape as predicted by the learner. In (a) the predicted cost is shown as a function of the end of the polarisation ramp (red), the end of the dipole beam ramp (black) and the unconnected parameter (blue). The learner correctly identifies that the unconnected parameter does not have a significant effect on the production of a Bose-Einstein condensate. In (b) a cross section of the 2 most sensitive parameters are plotted against cost.

altered and the optimisation process continued without the redundant parameter. Although this parameter was intentionally added, it provides a proof-of-concept for using the model to obtain beneficial insight into the system.

By applying this insight the least sensitive parameter can be removed and the optimisation restarted with only 6 parameters. The result of this is shown in red in figure Figure 6.10 where the optimisation is seen to converge more rapidly than the previous 7 parameter case and still successfully produces a condensate. The machine learning algorithm no longer needs to waste experimental runs to determine the importance of the intentionally added and useless 7th parameter, allowing it to achieve condensation more rapidly. A 2D cross-section of the cost landscape for the two most sensitive parameters from the 6 parameter optimisation is shown in Figure 6.11(b). The landscape displays a very sharp transition to Bose-Einstein condensate consisting of a very deep valley.

The number of experiments required for online optimisation, even for the simpler Nelder-Mead algorithm, are seen to vastly differ from that of a brute force search. It has been suggested that this profound discrepancy is a result of the topology of the optimisation landscapes in quantum experiments. It has been proven, under the assumption of controllability, that laser-aided quantum chemistry has optimisation landscapes that are ‘trap-free’ [185]. This theory has been refined [186–190], with the generality of the results being heavily debated [191–193]. The results presented in this thesis add to this discussion, with observations that the Nelder-Mead algorithm repeatedly succeeded in producing a Bose-Einstein condensate despite being a simple local optimisation algorithm heavily susceptible to being trapped by local minima in the landscape. This suggests that the optimisation landscape corresponding to this experiment is also ‘trap-free’ adding to the hypothesis that this is a universal principle for *all* quantum online optimisation

systems.

The machine learning algorithm, subsequently called M-LOOP (machine-learning online optimisation), has been made available online [194]. The algorithm is written in python and utilises the ski-kit package to evaluate the Gaussian processes [195]. M-LOOP can be immediately applied to experiments that have previously used online optimisation, such as quantum chemistry [139], femtosecond physics [143], and quantum computing [155]. The program is designed specifically to ensure that meshing with many different programs is simple. This is a result of the varied computing environment often found in the lab. In this research, the experiment is controlled by LabView with the absorption images analysed and cost calculated by Matlab. The machine learning algorithm simply outputs a text file with new parameters to test and waits for a new file with the resultant cost and uncertainty. This versatile communication method means that it can be implemented on any automated experiment with a resource of measurable quality.

Part III

Imaging of Bose Einstein Condensates

Destructive Imaging of Bose Einstein Condensates

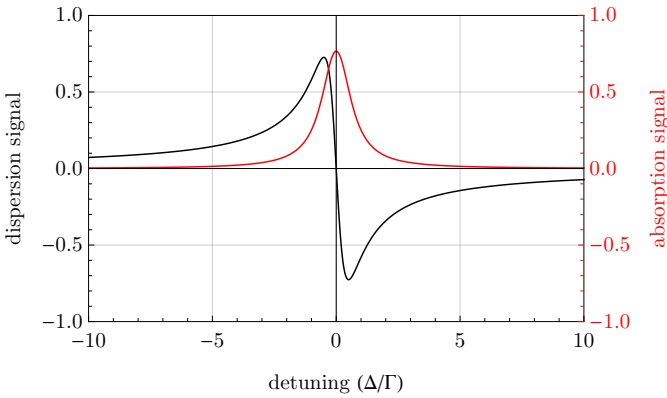
The following chapter presents work summarised in:

- *K. S. Hardman, P. B. Wigley, P. J. Everitt, P. Manju, C. C. N. Kuhn, and N. P. Robins.*
Time-of-flight detection of ultra-cold atoms using resonant frequency modulation imaging.
Optics Letters **41**, 2505 (2016). ISSN 1539-4794. DOI: 10.1364/OL.41.002505.

The detection of Bose-Einstein condensates is key to our ability to perform science and better understand the physics of the system. Due to the fragile nature of the sample this detection process can be very difficult. A single resonant photon can cause heating which can lead to destruction of the condensate. For many purposes this destruction is tolerable in that an image of the condensate may be acquired before the cloud is fully destroyed. Although time consuming, dynamics can be observed by performing the same experiment numerous time with an image captured at differing time-steps. Despite experimental variation, large datasets can be built up allowing quantitative analysis with statistical significance. Alternatively one may use less destructive techniques at the expense of signal-to-noise in order to observe dynamics in real-time. In addition to efficiency, this allows for the observation of dynamics where statistical averaging is difficult, such as stochastic processes. The following two chapters provide a theoretical basis for destructive and dispersive imaging techniques along with experimental results for a number of key methods. The benefits and failings of each technique is discussed in the context of experimental design and application. The following chapter begins with an outline of atom-light interaction in the context of imaging before concentrating on destructive imaging techniques such as absorption imaging (Section 7.1), fluorescence imaging (Section 7.2) and frequency modulation imaging (Section 7.3).

Both destructive and non-destructive techniques rely on the atom-light interaction of the sample with a probe laser. Fundamentally this interaction is described by the refractive index of the sample being probed. The refractive index is due to the polarisability of

Figure 7.1: The refractive index of a two-level atom, well approximating an experimental system, includes a real and imaginary component. Each corresponds to a different experimental signal with the imaginary component being observed as the destructive absorption signal and the real being a dispersive, less destructive signal. Importantly, the dispersive signal scales as $1/\Delta$ while absorption scales as $1/\Delta^2$ meaning that the level of destruction falls off faster than the dispersive signal. It should be noted that the dispersive signal is taken relative to vacuum.



the atoms,

$$n_{\text{ref}} = \sqrt{1 + 4\pi n\alpha}, \quad (7.1)$$

where n is the density of atoms and α is the atomic polarisability. Provided the system only consists of two levels, as is typically applicable in this context, $n_{\text{ref}} - 1 \ll 1$ and therefore under the rotating wave approximation, the refractive index is given by

$$n(\mathbf{x}, z) = 1 + \frac{\sigma_0 \lambda \rho(\mathbf{x}, z)}{4\pi} \left(\frac{i}{1 + \delta^2} - \frac{\delta}{1 + \delta^2} \right), \quad (7.2)$$

where

$$\sigma_0 = \frac{3\lambda^2}{2\pi} \quad (7.3)$$

is the cross-section, λ is the wavelength, $\rho(\mathbf{x}, z)$ is the atomic density, $\delta = \Delta/(\Gamma/2)$ is the detuning (Δ) in half linewidths ($\Gamma/2$) and $\mathbf{x} = \{x, y\}$ is the spatial coordinates of the plane perpendicular to the direction of propagation, z . Key to this expression are the distinct real and imaginary components which manifest as different physical effects. The imaginary term corresponds to an attenuation or absorption of the input light by the atoms. This results in recoil heating leading to destruction of the sample. The real component corresponds to dispersion and results in a phase shift of the input probe light. In general, both terms contribute to the overall effect, however the amount of contribution depends on the detuning from resonance. This is illustrated in Figure 7.1 where both components are plotted separately as a function of the detuning from resonance. The destructive term (red) peaks at resonance before falling off sharply as the probe is detuned. The dispersive term peaks half a linewidth from resonance and falls off much slower. This different scaling in signal means that there are regimes where the destruction is low enough to probe

the sample multiple times while still generating a dispersive signal.

In general, any probe beam passing through the atoms will be attenuated and phase-shifted with the resultant electric field written as

$$E(\mathbf{x}) = E_0 \exp \left(\frac{2\pi}{\lambda} \int (n(\mathbf{x}, z) - 1) dz \right) = E_0 t(\mathbf{x}) e^{i\phi(\mathbf{x})}, \quad (7.4)$$

where the refractive index has been taken relative to vacuum. At resonance the real part of the refractive index is zero, resulting in no dispersion or phase shift ($\phi = 0$), and the imaginary part of the refractive index solely contributing to the signal in the form of absorption. As the probe beam is detuned, the real part of the refractive index becomes non-zero generating a phase shift in the light with the two signals described by

$$t(\mathbf{r}) = \exp \left(-\frac{\sigma_0 \tilde{\rho}(\mathbf{x})}{2} \frac{1}{1 + \delta^2} \right) \quad (7.5)$$

$$\phi(\mathbf{r}) = \frac{\sigma_0 \tilde{\rho}(\mathbf{x})}{2} \frac{\delta}{1 + \delta^2}, \quad (7.6)$$

where $t(\mathbf{r})$ and $\phi(\mathbf{r})$ correspond to the absorption and phase shift respectively, and

$$\tilde{\rho}(\mathbf{x}) = \int n \cdot dz \quad (7.7)$$

is the column density corresponding to the density integrated along the direction of propagation.

With few exceptions, all imaging techniques measure signals resulting from either of these two terms. Depending on the objective, different techniques are more successful or more experimentally prudent. Absorption imaging is technically robust and gives excellent signal-to-noise for the atomic densities typically encountered. Dispersive imaging allows for continuous, non destructive probing of a sample. The following sections describe some of the more common imaging techniques in detail and compares their use and utility, beginning with destructive imaging techniques.

7.1 Absorption imaging

Absorption imaging is the most common imaging technique for ultracold atom experiments, being robust and providing high signal-to-noise measurements. Absorption imaging is schematically simple, as shown in Figure 7.2 where a sample is seen to be illuminated by resonant or near-resonant light. Photons from the probe beam are absorbed, generating a shadow of the sample which may then be imaged onto a sensor. Typically the sensor is a charge coupled device (CCD) capable of measuring spatial variation in the light, but a photodetector can also be used. A one-to-one image can be created using a $2f$

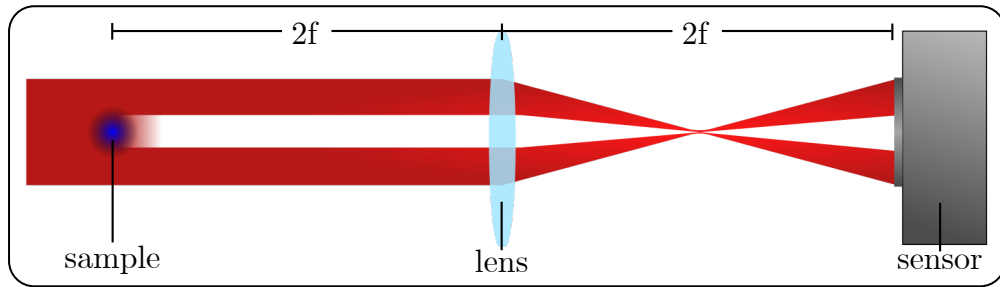


Figure 7.2: Diagram for a one-to-one magnification absorption imaging system. Resonant probe light is incident on the condensate with that light absorbed by the cloud. A shadow of the sample is then imaged onto a sensor (typically a charge coupled device or photodetector) using a single lens. This lens allows for magnification of the image.

optics setup as shown in Figure 7.2, or alternative optics setups can be used to magnify the image.

Often times the density and size of condensates becomes prohibitive for optic systems used in imaging. One method of overcoming this limitation is to turn off the trapping potential, allowing the condensate to expand after the conversion of mean-field energy to kinetic energy. This time-of-flight (TOF) method allows for large, optically dense condensates to be imaged and properties to be extracted. This is especially useful in absorption imaging as optically thick clouds cause saturation whereby all the light from the probe beam has been absorbed. This complicates any quantitative analysis, necessitating TOF imaging.

Ideally, with no bandwidth limitation, light can be input to the sample at a rate that minimises stimulated emission ensuring that the signal is optimal and the technique is shot noise limited. In practice, however, a bandwidth limitation exists requiring an amount of stimulated emission to be accepted, adding noise to the signal. In ultracold atom experiments, this bandwidth is dictated by the amount of recoil heating from spontaneous emission that is deemed acceptable. As resonant light is used for absorption imaging, each photon input generates spontaneous emission resulting in recoil heating. Given the fragile nature of condensates, this can only be tolerated so much before the sample is destroyed. Similarly, spontaneous emission can be removed from the signal by imaging at ‘infinity’. Since spontaneous emission results in photons emitted spherically, this additional noise source decreases as the solid angle to the imaging system decreases. Both stimulated and spontaneous emission produce positive signals, adding noise to the absorption signal (which is a lack of photons). In the following section, the theoretical signal-to-noise ratio for absorption imaging is outlined given the above limitations. Experimentally it is seen that the probe time and intensity are key parameters for operating at peak signal-to-noise.

The refractive index, given in Equation (7.2), can be used to determine the transmis-

sion coefficient of the sample. This specifies the amount of incident light that is transmitted through the sample, and therefore the amount of light absorbed. Assuming resonant operation with no dispersive component to the signal, the intensity of light after passing through the atoms is given by

$$I = I_0(1 - t) = I_0 \left[1 - \exp \left(-\frac{\sigma \bar{\rho}(\mathbf{x})}{2} \right) \right] \quad (7.8)$$

Here we have replaced the on-resonance small sample cross section with the total scattering cross section given by

$$\sigma = \frac{\sigma_0}{1 + 4\Delta^2/\Gamma^2 + I_0/I_{\text{sat}}}, \quad (7.9)$$

where

$$I_{\text{sat}} = \frac{\hbar\omega_0^3\Gamma}{4\pi c^2} \quad (7.10)$$

is the saturation intensity and accounts for stimulated emission. The cross-section goes to zero for large detuning from resonance in addition to intensities large compared to the saturation intensity.

For a sample containing N_{atoms} total atoms with corresponding area perpendicular to the beam given by A , the intensity of the light after passing through the atoms becomes

$$I = I_0 \left[1 - \exp \left(-\frac{N_{\text{atoms}}A}{2} \frac{\sigma_0}{1 + 4\Delta^2/\Gamma^2 + I_0/I_{\text{sat}}} \right) \right]. \quad (7.11)$$

This is directly related to the number of photons hitting the detector after passing through the sample and is what produces a signal, given by

$$\text{signal} = \eta N_\lambda \left[1 - \exp \left(-\frac{\sigma N_{\text{total}}}{2 A_{\text{BEC}}} \right) \right] = \frac{\eta I}{\hbar\omega} \left[1 - \exp \left(-\frac{\sigma N_{\text{total}}}{2 A_{\text{BEC}}} \right) \right] \quad (7.12)$$

where η is the quantum efficiency of the detector, dictating how well the collected photons can be converted to electrons. For this research a complementary metal-oxide-semiconductor (CMOS) camera supplied by Point Grey (model number GS3-U3-41C6NIR-C) with a quantum efficiency of 45% at 780 nm was used.

Finally, the noise is simply given by the shot noise of the total number of photons hitting the camera,

$$\text{noise} = \sqrt{2\eta N_\lambda} = \sqrt{\frac{2\eta I}{\hbar\omega}}, \quad (7.13)$$

with the factor of two accounting for both the noise on the signal and the noise on zero

signal. Combining the expressions for signal and noise, the signal-to-noise ratio for absorption imaging is therefore given by

$$\text{SNR} = \frac{\text{signal}}{\text{noise}} = \sqrt{\frac{\eta I}{2\hbar\omega}} \left[1 - \exp \left(-\frac{\sigma N_{\text{total}}}{2 A_{\text{BEC}}} \right) \right]. \quad (7.14)$$

In practice, the signal-to-noise ratio is more complex than the expression above. Since the system is not perfectly two-level, illumination generates a non-zero chance of an off resonant transition occurring with the atom subsequently decaying to a state that is removed from the imaging cycle. For ^{87}Rb , imaging typically occurs between the $F = 2 \rightarrow F' = 3$ levels. Problematically, the $F' = 2$ transition is only 260 MHz detuned from $F' = 3$ meaning that there is a likelihood of an atom being excited to $F' = 2$ and subsequently decaying to $F = 1$ and therefore being lost from the imaging scheme. In order to account for this in the SNR calculation, the number of atoms, N_{atoms} is altered to include a time dependence based on the probability of decaying out of the imaging cycle. That is

$$N_{\text{atoms}} = N_0 \left[1 + r_{\text{loss}} \left(1 - \frac{1}{1 + I_0/I_{\text{sat}}} \right) \right]^{-\gamma t}, \quad (7.15)$$

where N_0 is the total number of atoms initially and r_{loss} is the rate of loss from the imaging transition cycle. The value for r_{loss} is a result of a number key factors, specifically

1. the ratio of the scattering rate between the resonant $F = 2 \rightarrow F' = 3$ level and the off-resonant $F' = 2$ level 260 MHz away;
2. the ratio of the transition strength of $F = 2 \rightarrow F' = 2$ and $F' = 3$;
3. the ratio of the transition strengths between $F' = 2 \rightarrow F = 2$ and $F = 1$.

Metcalf [196] provides the Clebsch-Gordon coefficients for a range of alkali atoms including ^{87}Rb facilitating the calculation of a loss rate.

Incorporating the time-dependent atom number into the signal-to-noise expression allows a more complete analysis of the imaging technique. The final signal is found by integrating the instantaneous signal over the total probe duration. The noise is also integrated over the same period, with the signal-to-noise subsequently found. The result of this calculation with resonance probe light is shown in 7.3. Importantly, the instantaneous noise is constant, but the signal decreases as the probe time increases and atoms are lost from the cycle. This means that there is an optimum probe time that produces the largest signal-to-noise ratio for a given intensity. As the intensity changes, so too the optimum probe time changes. CCD cameras are easily saturated however, placing another limitation on the probe time. Typically the probe time used for this research is 100 μs with the intensity being approximately one-tenth the saturation intensity.

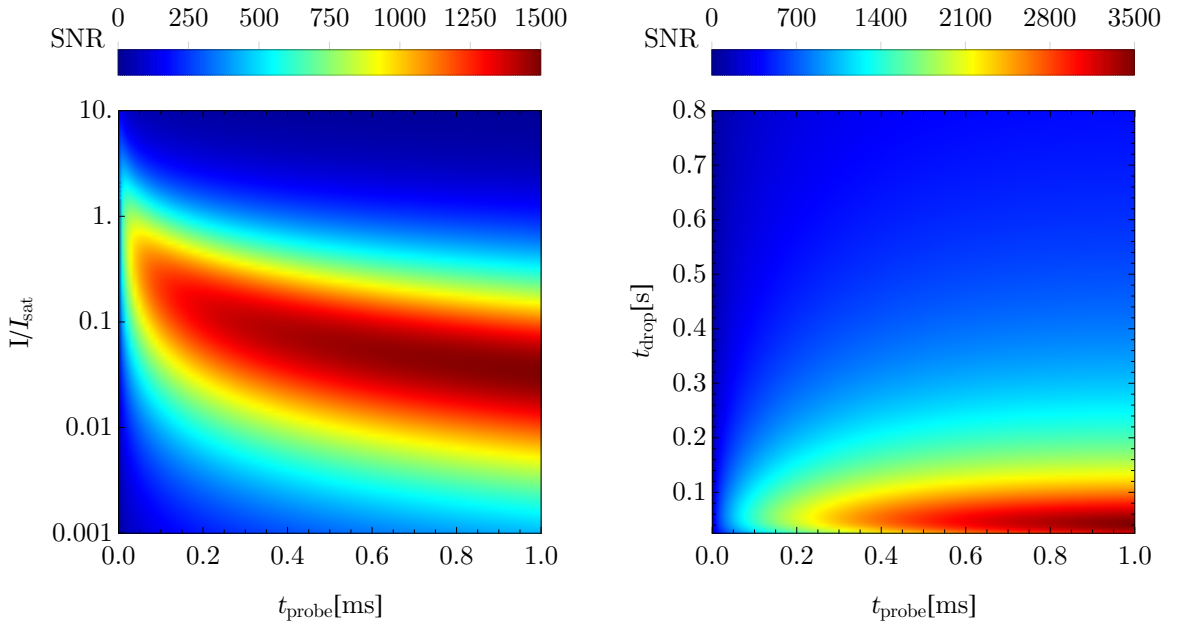


Figure 7.3: Left: Theoretical signal-to-noise ratio for absorption imaging. As the probe intensity is increased, the optimum amount of probe time decreases. Right: The dependence of the signal-to-noise ratio on the size of the cloud, given a particular intensity of light, is illustrated. As the cloud falls, it expands according to its temperature and presents a larger area perpendicular to the probe beam. As this area increases, the SNR is seen to decrease. Typically the probe time used in this research is 100 μ s with an intensity approximately one-tenth the saturation intensity.

Finally, as the perpendicular area of the cloud increases and the sample becomes less dense, the signal weakens. This occurs as the time-of-flight increases when the cloud is released from trap. To account for this, the perpendicular area of the cloud is parametrised as a function of the time-of-flight drop time. For a Bose-Einstein condensate consisting of a cloud of atoms of mass m with temperature T , the radius of the cloud after drop time t_{drop} is given by

$$r = t_{\text{drop}} \sqrt{\frac{3k_B T}{m}} + r_0, \quad (7.16)$$

with the area calculated as usual. The area of the probe beam is assumed to be that of the perpendicular area of the sample. The affect on the signal-to-noise ratio for absorption imaging of changing cloud size is shown in the right of Figure 7.3 where the signal-to-noise is shown for a given intensity over a range of probe and drop times. The optimum probe time is seen to be dependent on the size of the cloud.

Two images are typically used to characterise a sample using absorption imaging, being a background image with no sample (I_0) and one with the sample present (I). The

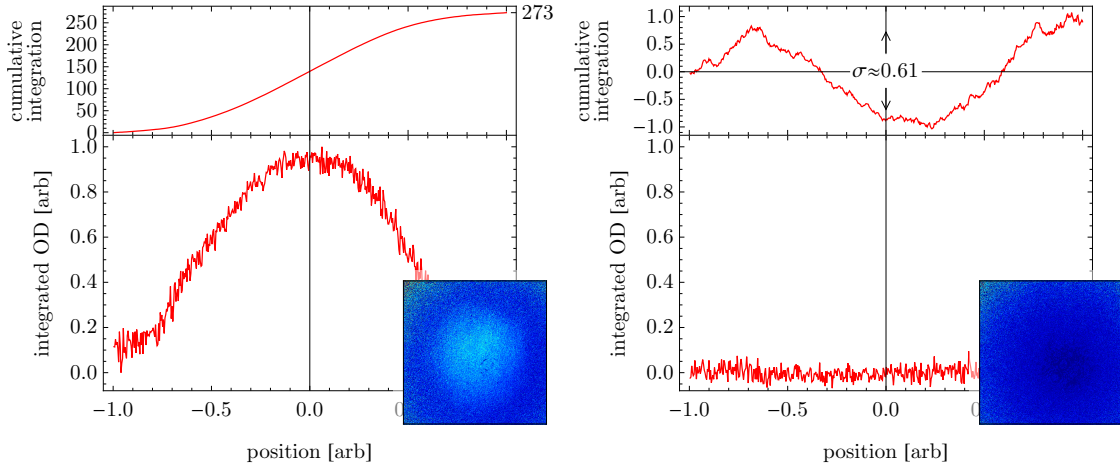


Figure 7.4: Example experimental absorption imaging data showing a Bose-Einstein condensate after a 550 ms time-of-flight expansion observed as a bump (left) in a uniform background (right). Since the condensate occupies the majority of the sensor, two separate runs are used to characterise the signal and the noise. Within each run, two images are acquired with the atoms present and without. The background is subtracted and the optical depth calculated as in Equation (7.17). The image (inset) is integrated along one dimension as indicated and shown in the bottom plots. A second, cumulative integration is performed with the signal taken to be the final value of this integration (~ 273). The noise is shown in the right of the figure with the cumulative integral shown above. The noise is taken to be the standard deviation of the cumulative integration (~ 0.61). Computing the signal to noise yields a value of ~ 450 .

integrated atom density, or column density, can be found by computing at each pixel

$$n = \frac{1}{\sigma} \ln \frac{I_0}{I}, \quad (7.17)$$

with the optical depth (OD) given by $n\sigma$. With its high signal-to-noise and technical simplicity, absorption imaging is ubiquitous for ultracold physics.

7.1.1 Experimental absorption imaging

A characterisation of absorption imaging was performed on the ANU Gravimeter [35], an apparatus enabling a direct comparison between absorption and frequency modulation imaging at large time scale time-of-flight expansion. On this machine absorption imaging provides strong signal-to-noise with simple experimental setup for condensate drop times of up to ~ 600 ms before being dominated by classical noise. Frequency modulation imaging, detailed in Section 7.3 is more technically involved, but is capable of producing high signal-to-noise images for much longer condensate expansion times. Both techniques are demonstrated with application to a ^{87}Rb condensate at a 550 ms time-of-flight. The condensate, consisting of $\sim 2 \times 10^6$ atoms is optically pumped from the D_2 ground-state manifold $F = 1$ hyperfine level to the $F = 2$ level where a probe beam,

resonant with $F = 2 \rightarrow F' = 3$ images the cloud through a $100\text{ }\mu\text{s}$ exposure. The probe beam, partially absorbed by the condensate is then imaged using a one-to-one lens system focussed onto a charge-coupled device (CCD) (Point Grey GS3-U3-14S5M) capable of a quantum efficiency of $\eta = 15\%$ at 780 nm .

A second image is taken after the atoms have exited the imaging region and is used for a background subtraction. The optical depth is calculated as in Equation (7.17) with the resulting image show in the left of Figure 7.4. Since the condensate has expanded to encompass the entire sensor area, a second experimental run with no condensate is used to generate a corresponding image of the noise in the optical depth, shown in the right of the Figure 7.4. The images are integrated along a single dimension as indicated with the result shown in the bottom of each plot. A second cumulative integration is then performed and shown in the top of each plot. The signal is given by the final value of this cumulative integration with the noise given by the variance. The signal-to-noise for this implementation of absorption imaging at 550 ms time-of-flight is found to be ~ 450 , approximately 30% of the fundamental shot noise limit given by $\sqrt{N_{\text{atoms}}}$ and in good agreement with the theoretical signal-to-noise calculated in the previous section.

7.2 Fluorescence imaging

Fluorescence imaging provides an alternative means of imaging with high signal-to-noise without the reliance on easily saturated detectors such as CCDs, instead using a photodetector. The technique again relies on resonant probe light and is therefore destructive. The light is input on the sample and absorbed as described in the previous section. Each photon that is absorbed results in a photon spontaneously emitted in a random direction with the time scale dictated by the spontaneous emission rate. When averaged over a large homogeneous sample of atoms this results in a spherical radiation mode. By capturing the emitted photons, or a subset of these photons, on a photodetector it is possible

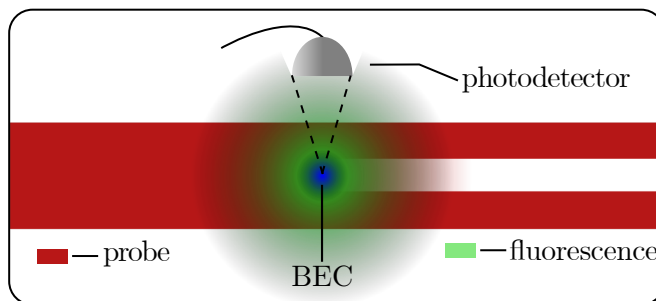


Figure 7.5: Schematic diagram of a fluorescence imaging system. Resonant probe light is incident on the sample and is absorbed. As a result the sample spontaneously emits in all directions with spherical symmetry. By collecting these photons, or a subset of these photons, it is possible to infer characteristics of the cloud.

to infer properties of the sample. Specifically it is possible to relate the number of photons in a given solid angle to the number of atoms in the fluorescing sample. Given γ photons scattered per atoms per second, the number of photons collected by a detector of area A at distance r from the atomic sample is given by

$$N_\lambda = \frac{\gamma N_{\text{atoms}} A}{4\pi r^2}. \quad (7.18)$$

The detector response is altered by both quantum efficiency and gain profile for a given intensity, encompassed by η . The signal is then given by integrating over the total probe time, t_{probe} , and scaled by the bandwidth of the detector, B , such that

$$\text{signal} = \int_0^{t_{\text{probe}}} \frac{\gamma \eta N_{\text{atoms}} A}{4\pi r^2 B} dt = \frac{\gamma \eta N_{\text{atoms}} A t_{\text{probe}}}{4\pi r^2 B}. \quad (7.19)$$

Given the dark background nature of fluorescence imaging, the noise is simply the square-root of the signal. The theoretical signal-to-noise ratio of fluorescence imaging is therefore given by

$$\text{SNR}_{FI} = \sqrt{\frac{\gamma \eta N_{\text{atoms}} A t_{\text{probe}}}{4\pi r^2 B}}. \quad (7.20)$$

The signal-to-noise can be improved by increasing the size of the detection area, although this is difficult to achieve in practice as it involves detecting around a full sphere of emitted photons. Given the noise on photodetectors it would be preferential to surround the sample with an optical setup capable of redirecting the signal to a single photodetector. Another note is that γ represents the spontaneous emission rate, here taken to be the high intensity value as there is little advantage operating fluorescence at low intensity.

As with the theoretical analysis of absorption imaging in the previous section, non-cycling transitions lead to a decrease in atom number over time, lowering the signal. The same treatment can be made to account for this, however, typically fluorescence imaging operates with a repump beam continually pumping those lost atoms back into the imaging cycle. The routine approach for ^{87}Rb is to image using the $F = 2 \rightarrow F' = 3$ whilst repumping on the $F = 1 \rightarrow F' = 2, D_2$ transitions. Although this improves the signal, it also generates additional heating, thereby lowering the acceptable probe time.

In practice fluorescence imaging provides a relatively simple technique that yields lower noise than absorption imaging as a result of being a dark-ground imaging system. The technique typically has very low collection efficiency and is difficult to setup in a way that gains spatial information about the sample. Such information requires a falling cloud passing through a light sheet. This limits the atom-light interaction time and reduces the signal strength.

7.3 Frequency modulation imaging

Frequency modulation imaging, originally developed as an off-resonant imaging technique can be used on-resonance to great effect. The technique amounts to detecting the distortion on a frequency modulated probe beam caused by the sample. Bjorklund, et al. provide an excellent explanation of the technique as applied detuned from resonance [197]. The following section outlines the signal-to-noise ratio for the technique when operated at resonance as applied in the ANU gravimeter [198].

The technique involves applying a strong carrier probe at frequency ω_c with two weak sidebands at $\omega_c \pm \omega_m$. One of the sidebands is specifically constructed to be resonant with a particular transition of the atomic sample. The beam is then passed through the sample with this sideband completely absorbed for the duration that the atoms are overlapped with the beam. The light is collected on a photodetector with the electrical signal at frequency ω_m detected. By tracking the phase and amplitude of the beat signal, the absorption and dispersion components of the sample can be determined. By creating a light sheet for the atoms to fall through, a spatial profile of the sample can be generated.

The signal-to-noise calculation for frequency modulation begins by considering the electric field of the probe light after the addition of sidebands by an electro-optic mod-

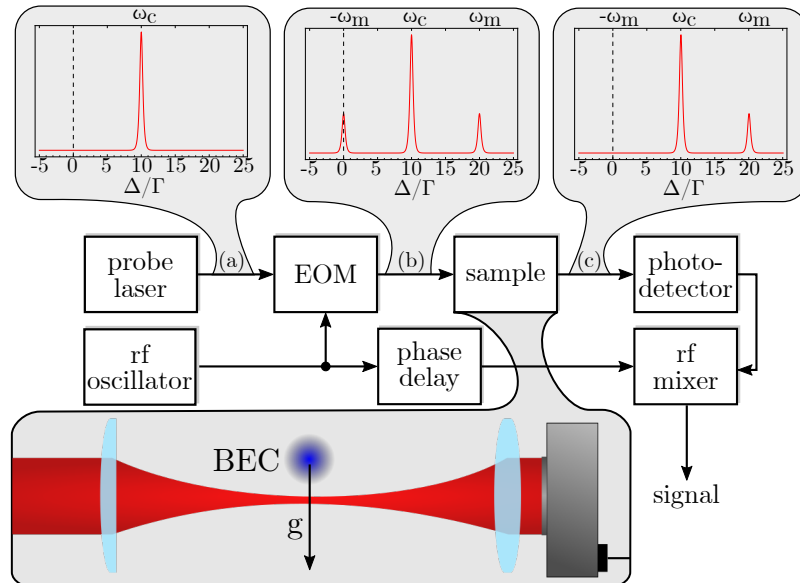


Figure 7.6: Flow diagram for frequency modulation imaging as applied to imaging a falling Bose-Einstein condensate. A narrow linewidth probe laser of frequency ω_c is input to an electro-optic modulator (EOM) where an rf oscillator generates sidebands at $\omega_c \pm \omega_m$. The frequency is set such that one of the sidebands lies on resonance for a particular atomic transition. The other sideband and original carrier are far enough from resonance that any absorption or phase shift is negligible. The output of the EOM passes through a cylindrical lens, generating a sheet of probe light that the atomic sample falls through. The light is then collected on a fast photodetector. This signal is mixed with the original (phase adjusted) rf oscillator signal, providing a signal that effectively images the sample.

ulator (EOM). These sidebands (ω_m) are added to the carrier (ω_c) such that one of the sidebands lies at the resonance frequency of a particular transition of the atoms. The electric field prior to interaction with the sample is then given by

$$E_{\text{in}} = E_0 \left[\underbrace{-\frac{M}{2} e^{i(\omega_c - \omega_m)t}}_{-1 \text{ sideband}} + \underbrace{e^{i\omega_c t}}_{\text{carrier}} + \underbrace{\frac{M}{2} e^{i(\omega_c + \omega_m)t}}_{+1 \text{ sideband}} \right], \quad (7.21)$$

where M is the modulation index, a measure of the ratio of the power in the carrier compared to the sidebands, here assumed to be much less than one. This electric field represents a pure frequency modulated optical spectrum where the sidebands have been added at $\omega_c \pm \omega_m$.

Once modulated, the probe is then passed through the atomic sample where it is absorbed and phase shifted according to the refractive index as described in Equation (7.4). After this interaction the electric field is modified such that

$$E = E_0 \left[-\frac{M}{2} e^{-\delta_{-1} - i\phi_{-1}} e^{i(\omega_c - \omega_m)t} + e^{-\delta_0 - i\phi_0} e^{i\omega_c t} + \frac{M}{2} e^{-\delta_1 - i\phi_1} e^{i(\omega_c + \omega_m)t} \right], \quad (7.22)$$

where t_i and $\phi_i, i \in \{-1, 0, 1\}$, represents the absorption and phase shift in the negative sideband, carrier and positive sideband frequencies respectively. The corresponding intensity is given by $I = c\epsilon_0 |E|^2 / 2$. Under the assumption that the sidebands are of much lower power than the carrier, $M \ll 1$ and all terms of order M^2 are dropped. In addition, assuming that the sample is imaged in the regime where it is considered optically thin, such as large time-of-flight expansion, the assumption may be made that $|\delta_0 - \delta_1|$, $|\delta_0 - \delta_{-1}|$, $|\phi_0 - \phi_1|$ and $|\phi_0 - \phi_{-1}|$ are $\ll 0$ allowing the exponential to be approximated, resulting in the following intensity signal

$$I = \frac{c\epsilon_0}{2} |E_0|^2 e^{-2\delta_0} [1 + (\delta_{-1} - \delta_1) M \cos \omega_m t + (\phi_1 + \phi_{-1} - 2\phi_0) M \sin \omega_m t]. \quad (7.23)$$

The probe light described above is collected by a photodetector with the signal being converted to an electrical signal. When the absorption in each sideband is not equal ($\delta_{-1} - \delta_1 \neq 0$), or the addition of the phase accumulation in the two sidebands is not equal to twice that in the carrier ($\phi_1 + \phi_{-1} - 2\phi_0 \neq 0$), then there will be a beat signal at the rf frequency ω_m due to the sine and cosine components. By phase-shifting the original modulation and mixing this with the photodetector signal, this beat can be detected.

In practice it is also critical to apply a bandpass filter and amplification to the signal. The technique lends itself to use of a bandpass filter as the signal is caused by the condensate falling through a thin sheet of probe light and will therefore always be of low frequency. In the case where the modulation frequency is large compared to the natural linewidth of the atomic transition then the signal is directly proportional to the absorp-

tion or dispersion. When performing this technique on resonance, this is the optimal regime for operation.

Finally, assuming that the absorption and phase shift experienced by the carrier and non-resonant sideband (+1 for the following analysis) are negligible such that

$$\delta_1 = \delta_0 = \bar{\delta}, \quad (7.24)$$

$$\phi_1 = \phi_0 = \bar{\phi}, \quad (7.25)$$

where $\bar{\delta}$ and $\bar{\phi}$ are the background absorption and phase shift. Critically, the signal is now a deviation from these background losses and phase shifts, such that our signal is

$$I = \frac{c\epsilon_0}{2} |E_0|^2 e^{-2\bar{\delta}} [1 + \Delta\delta M \cos \omega_m t + \Delta\phi M \sin \omega_m t]. \quad (7.26)$$

The two oscillating terms are therefore proportional to the absorption and phase shift caused by the sample.

In order to calculate the theoretical signal-to-noise ratio for frequency modulation imaging, let us begin with the above equation, assuming operation at resonance with zero phase shift and with setup such that there is negligible background on the carrier or non-interacting sideband, such that $\Delta\phi = \bar{\delta} = 0$. In this regime, the optical power captured by the photodetector is given by

$$P(t) = P_0(1 + \Delta\delta M \cos \omega_m t), \quad (7.27)$$

where the intensity signal at the detector has been multiplied by the area of the photodetector to obtain power. In terms of the number of photons hitting the detector per unit time, this is

$$P(t) = \frac{N\hbar\omega_c}{t}(1 + \Delta\delta M \cos \omega_m t). \quad (7.28)$$

This power includes both the background term and the signal term. The photodetector converts the optical power to a current according to

$$i = S_P g \eta P(t), \quad (7.29)$$

where S_P is the sensitivity of the photodetector, g is the gain and η is the photodetector efficiency. The beat signal photocurrent is therefore

$$i_{\text{sig}} = \eta \frac{P_0}{\hbar\omega_c} \Delta\delta M \cos \omega_m t. \quad (7.30)$$

The root-mean square power of the signal is given as

$$\bar{i}_{\text{sig}}^2 = \frac{1}{2}\eta^2 \left(\frac{P_0}{\hbar\omega_c} \right)^2 \Delta\delta^2 M^2, \quad (7.31)$$

and specifies the signal for frequency modulation imaging.

The noise is simply the shot noise on the counting of background electrons. This is obtained by considering the background term in Equation 7.28

$$i_{\text{SN}} = \frac{S_P g \hbar \omega_c}{t} \sqrt{N\eta}, \quad (7.32)$$

with the corresponding root-mean square current for the noise being

$$\bar{i}_{\text{SN}}^2 = \frac{S_P^2 g^2 \hbar^2 \omega_c^2}{t^2} N\eta. \quad (7.33)$$

The signal-to-noise is then given by

$$\text{SNR}_{FMI} = \frac{\bar{i}_{\text{sig}}^2}{\bar{i}_{\text{SN}}^2} = \frac{P_0 \eta \delta^2 M^2 t}{2 \hbar \omega_c B}, \quad (7.34)$$

where P_0 is the total laser power, η is the photodiode efficiency, δ is the sideband absorption ratio, M is the modulation index, \hbar is Planck's constant, ω_c is the carrier frequency of the light, and B is the bandwidth of the detector, detecting for time t . The signal-to-noise ratio is seen to scale with input probe power allowing relatively easy scaling of the signal. The technique provides a powerful alternative to fluorescence imaging for low optical depth clouds making it a useful tool for large time-of-flight detection.

Much like fluorescence imaging, frequency modulation imaging is a zero background detection system as there is little to no background in the rf range. In contrast, however, FMI has significantly higher detection efficiency. Whereas in fluorescence imaging the detection efficiency is typically on the order of one percent, frequency modulation imaging allows collection of all probe light.

7.3.1 Experimental frequency modulation imaging

As with the previously detailed absorption imaging, the experimental signal-to-noise analysis for frequency modulation imaging utilises the ANU Gravimeter. The system is used to image a ^{87}Rb Bose-Einstein condensate consisting of $\sim 2 \times 10^6$ atoms at an effective temperature of $\sim 50\text{ nK}$ after 550 ms of time-of-flight expansion. 100 μs prior to imaging, the condensate is pumped from the D_2 ground-state manifold $F = 1$ hyperfine level to the $F = 2$ level. The probe beam, modulated via an electro-optic modulator such that the $\omega_c + \omega_s$ sideband is resonant with the $F = 2 \rightarrow F' = 3$ transition. The condensate

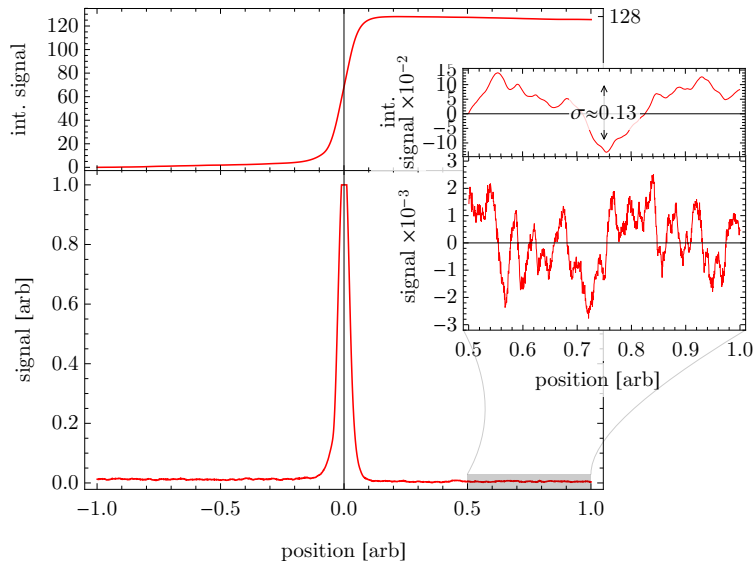


Figure 7.7: Example experimental frequency modulation imaging data showing a Bose-Einstein condensate after a 550 ms time-of-flight expansion observed as a high-signal to noise peak (bottom). The signal acquired at the photodetector is analogous to the initial integration along one axis shown in Figure 7.4. The integrated signal is shown at the top, with the final value of the cumulative integration taken to be the signal. The noise is magnified in the inset with the cumulative integral shown above. The noise is taken to be the standard deviation of the cumulative integration. Computing the signal to noise yields a value of ~ 880 . A key limitation to the demonstrated implementation is spatial resolution. Whereas the 550 ms absorption image generated a signal that has ~ 500 data points across the region of interest, the frequency modulation imaging displays only ~ 150 . This could be improved by increasing the detection rate and laser power to enable more data points to be taken in the time the cloud falls through the probe light sheet.

falls through the horizontal light sheet, absorbing this sideband and altering the probe light. This light is subsequently detected on an ac-coupled photodiode with the output mixed with the modulation signal. This demodulates the output which is then amplified and filtered using a bandpass filter. The filter is qualified by the disparity between the frequency of the cloud falling (Hz) and the natural linewidth of the atomic transition, allowing additional suppression of noise.

The resulting demodulated signal corresponds to the condensate falling through the light sheet which allows a mapping from time to space. In effect, an integration along one dimension has already been applied as a result of the detection method. This is shown in the bottom of the main plot in Figure 7.7 where the condensate is seen as a high signal-to-noise peak on a very flat background. A cumulative integration of the signal is shown in the top of Figure 7.7 with the signal given by the final value of ~ 128 . The noise is calculated variance of the cumulative integration of an atom-free region of the signal giving a value of ~ 0.13 and resulting in a signal-to-noise of ~ 880 , approximately 50% of the fundamental shot noise limit.

As a result of the detection rate, the temporal resolution of the cloud (and correspond-

ing spatial resolution) is significantly lower than the spatial resolution of absorption imaging. By increasing the temporal resolution, the signal-to-noise could be increased dramatically.

The imaging methods discussed in this chapter are capable of high signal-to-noise images with varying degrees of technical difficulty and optimal for different situations. Though resulting in excellent signals, the reliance of these techniques on resonant light to generate a signal inherently means they are destructive. For most applications this is acceptable as reliable statistics can be generated by performing the same experiment numerous times. However, the ability to continuously image in a single experiment without destroying the sample would enable faster data acquisition and unlock new dynamical regimes unable to be statistically probed.

Dispersive Imaging of Bose Einstein Condensates

The following chapter presents work summarised in:

- **P. B. Wigley, P. J. Everitt, K. S. Hardman, M. R. Hush, C. H. Wei, M. A. Sooriyabandara, P. Manju, J. D. Close, N. P. Robins, and C. C. N. Kuhn.** *Non-destructive shadowgraph imaging of ultra-cold atoms.* *Optics Letters* **41**, 4795 (2016). ISSN 1539-4794.
DOI: 10.1364/OL.41.004795.

Whilst techniques relying on the imaginary part of the refractive index are well characterised and understood they are inherently destructive and therefore limit the situations in which they can be used. From a technical perspective, absorption imaging with resonant probe light can lead to saturation of the detector. Whilst this can be reduced by detuning, doing so generates a non-zero real component to the refractive index, resulting in lensing and non-ideal behaviour of the imaging system. Similarly, fluorescence imaging has a strong dependence on intensity which can cause a spatially-varying interaction between the centre of a cloud and the edges. More fundamentally, destructive imaging restricts the data acquisition to a single image per experiment. In addition to making data acquisition more time consuming and prone to experimental drift, this rules out any informative observation of random stochastic processes. Without the ability to image in real-time, these regimes cannot be probed in any particularly meaningful way. Dispersive imaging can provide a way of probing the system without causing heating or destruction and can extend the probing regime to suit situations not covered by traditional destructive techniques. Such methods have been used extensively to observe thermal clouds and Bose-Einstein condensate alike [199–201], taking advantage of the real part of the refractive index which generally results in a phase shift on the light. Methods for imaging using the real part of the refractive index were investigated as early as Hooke, who noticed the effect of a transparent media on light [202]. More recently, the 1953 Nobel prize in physics was awarded to Zernike for his work on phase contrast imaging in the field of microscopy [203]. This work allowed cells to be probed without the need for the lethal technique of staining. These powerful imaging methods provide a means for

probing physical regimes not accessible to destructive imaging. The following section will investigate a number of dispersive imaging techniques, outlining various theoretical and experimental results as well as their advantages and disadvantages in the context of experimental ultracold physics.

8.1 Scattered photons

An important consideration in dispersive imaging is the amount of spontaneous emission generated for a given interaction time and a specific detuning from resonance. Each absorbed photon imparts momentum to the atom, kicking it in the opposite direction whilst generating a spontaneously emitted photon in a random direction. The recoil energy of a single resonant photon $\hbar k$ for ^{87}Rb corresponds to an energy of $\sim 400 \text{ nK}$ [66], typically greater than the trap depth and enough energy to kick the atom out of the trap and deplete the condensate. Depending on the optical thickness of the cloud, the scattered photon may be reabsorbed and emitted, adding to the depletion of the condensate. The number of events is dictated by the mean-free path and can lead to many atoms being removed from the condensate resulting in destruction of the fragile sample. This destruction must be minimised in order to facilitate continuous imaging. As the probe light is detuned further from resonance the cloud becomes optically thin and multiple scattering events become less common.

The amount of scattering is dictated by the scattering rate, Γ_{scatt} , determined by considering the polarisability of an atomic oscillator given the limit of large detunings [204]. This analysis results in a scattering rate given by

$$\Gamma_{\text{scatt}}(\mathbf{r}) = \frac{3\pi c^2}{2\hbar\omega_0^3} \left(\frac{\Gamma}{\Delta} \right)^2 I(\mathbf{r}), \quad (8.1)$$

where c is the speed of light, \hbar is Planck's reduced constant, ω_0 is the frequency of resonance, Γ is the linewidth of the transition, $\Delta = \omega - \omega_0$ is the detuning of the laser from resonance and $I(\mathbf{r})$ is the intensity of the light. The total number of scattering events across an area of beam is given by integrating this expression over the relevant area. In this context, a probe laser of intensity of 10 W m^{-2} illuminating an area of 0.1 mm^2 (the approximate spatial area of a condensate in-trap), detuned by 1 GHz from a 6 MHz linewidth resonance, and exposed for $100 \mu\text{s}$ a total of 100 times, will result in approximately ~ 10 scattering events. Such a level of destruction, even after probing the system 100 times would be extremely desirable, even for a relatively small 10^4 atom condensate that is typical of the ^{85}Rb condensates produced for this research.

8.2 Dual-species apparatus

^{85}Rb provides an attractive playground for any non-destructive continuous imaging system due to the Feshbach resonance at 155G. This resonance allows for direct manipulation of the non-linearity of the Gross-Pitaevskii equation and provides access to experiments such as solitonic propagation and collisions [51, 205], and the bosenova [43, 182, 206, 207]. In addition the system exhibits a stochastic process called modulational instability which is dependent on the scattering length. The ability to continuously image the system in-situ and in a single experimental run is key to gaining any quantitative insight into this or any other stochastic process.

The experimental apparatus used to produce the dual-species $^{85}\text{Rb}/^{87}\text{Rb}$ Bose-Einstein condensates has been described in detail in [183] with the ^{87}Rb production described in Section 6.2. Whilst the majority of the experimental procedure is identical, a number of crucial steps required for ^{85}Rb production require explanation. Figure 6.3 shows a simplified diagram of the experimental apparatus including the features required for exploiting the ^{85}Rb Feshbach resonance.

Briefly, a 2D magneto-optical trap (MOT) is used for an initial stage of cooling for both atomic species. This 2D MOT is used to load a 3D MOT via a pair of co-propagating push beams, taking approximately 10 s and resulting in approximately 5×10^8 and 3×10^6 ^{87}Rb and ^{85}Rb atoms respectively. 25ms of polarisation gradient cooling is subsequently applied, resulting in a $\sim 15 \mu\text{K}$ sample and both isotopes pumped to their respective magnetic ground states. Using a hybrid magnetic and optical trap, the ^{85}Rb atoms are then sympathetically cooled using the ^{87}Rb atoms. The remaining cloud, cooled to around $1 \mu\text{K}$, is transferred to an optical crossed dipole trap where it is cooled further by reducing the dipole beam intensity, driving further sympathetic evaporative cooling until the Bose-Einstein condensate phase transition is reached, as indicated in Figure 8.1. The cloud may be loaded into an optical wave-guide beam by extinguishing one of the dipole beams.

The ^{85}Rb atomic interactions are manipulated using a magnetic bias field through exploiting a Feshbach resonance present in the isotope. The field is jumped through the resonance at 155 G to 165.74 G [208], minimising inelastic collisional losses. During the last 0.5 s of evaporation, the bias field is tuned such that the scattering length of the ^{85}Rb atoms is $254a_0$, increasing the physical size in order to maximise atom number. By changing the ratio of the two species in the MOT loading stage, various final ratios can be produced from pure ^{85}Rb to pure ^{87}Rb .

The experiments benefiting from a non-destructive continuous imaging system with ^{85}Rb stem from the ability to dynamically manipulate the scattering length of the species, achieved using a magnetic field. This magnetic field imposes constraints on the imaging

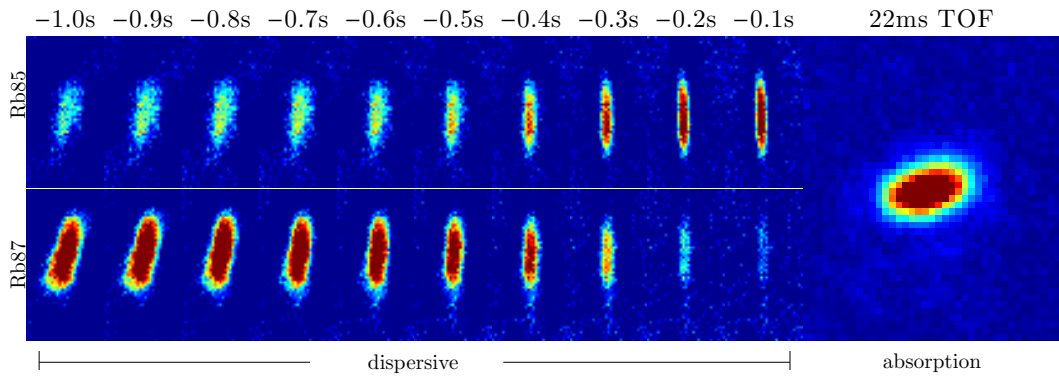


Figure 8.1: The sympathetic evaporation process forming Bose-Einstein condensate in ^{85}Rb . The top row shows 10 in-trap images of ^{85}Rb captured 100 ms apart with the final image taken 100 ms before condensation. The lower set shows 10 in-trap images of the same process, instead imaging ^{87}Rb . Sympathetic evaporation cools the sample, with the ^{87}Rb content reducing to zero as the ^{85}Rb atoms become cooler and denser with no observed atom losses. The rightmost picture shows an absorption image taken after a 22 ms time of flight in order to confirm the phase transition and to accurately count the number of atoms, 3×10^4 .

system.

8.3 Probe beam detuning with magnetic fields

A magnetic field applied across the atomic cloud results in a shift of the magnetic sub-levels causing the resonance frequency of any particular transition to change. Since the destructiveness of the imaging system is dependent on the detuning from resonance, it is critically important to understand the effect of the magnetic field on the atomic transitions and to understand which transitions are being used to image.

The theoretical effect of a magnetic field on atomic level structure is explored in detail in Section 2.3. In summary, in the absence of a magnetic field, the magnetic sub-levels of each hyperfine state are degenerate. As the magnetic field is increased the degeneracy is lifted and the magnetic sub-levels split. In the low field limit where the shift in energy of the atomic states is small compared the hyperfine splitting, the Zeeman effect is sufficient to calculate this change, and the states may be described the quantum numbers F and m_F . As the magnetic field increases beyond this regime, as is the case in most experimental applications, the splittings become more complex and it becomes necessary to numerically diagonalise the interaction Hamiltonian, $H = H_{\text{hfs}} + H_B$, where

$$H_{\text{hfs}} = A_{\text{hfs}} \mathbf{I} \cdot \mathbf{J} \quad (8.2)$$

$$+ B_{\text{hfs}} \frac{3(\mathbf{I} \cdot \mathbf{J})^2 + \frac{3}{2}(\mathbf{I} \cdot \mathbf{J}) - I(I+1)J(J+1)}{2I(2I-1)J(2J-1)}, \quad (8.3)$$

and

$$H_B = \frac{\mu_B}{\hbar} (g_J J + g_I I) B, \quad (8.4)$$

where A_{hfs} is the magnetic dipole constant, B_{hfs} is the electric quadrupole constant, μ_B is the Bohr magneton, g_I is the nuclear g-factor and g_J is the Landé g-factor [66]. The Breit-Rabi equation provides a notable exception for the ground-state manifold of the D transition in ^{85}Rb and other species, where an analytic expression exist for the energy splittings [66].

Numerically diagonalising and solving for the required magnetic field (165.7G) we obtain the splittings for both the ground and excited hyperfine manifold. Since the ^{85}Rb condensate is formed with the atoms in the $|F = 2, m_F = -2\rangle$ magnetic sub-level, it is possible to determine the resonance frequency of a transition to any of the excited-state levels. Subtracting off the ground-state frequency for the given magnetic field, it is possible to obtain the left part of Figure 8.2. This specifies the resonance frequency of each of the excited-state levels relative to the initial state. Given the magnitude of the magnetic field, the ground state is still in the linear regime where the quantum numbers F and m_F are appropriate quantum numbers. In contrast, the excited states are well into the

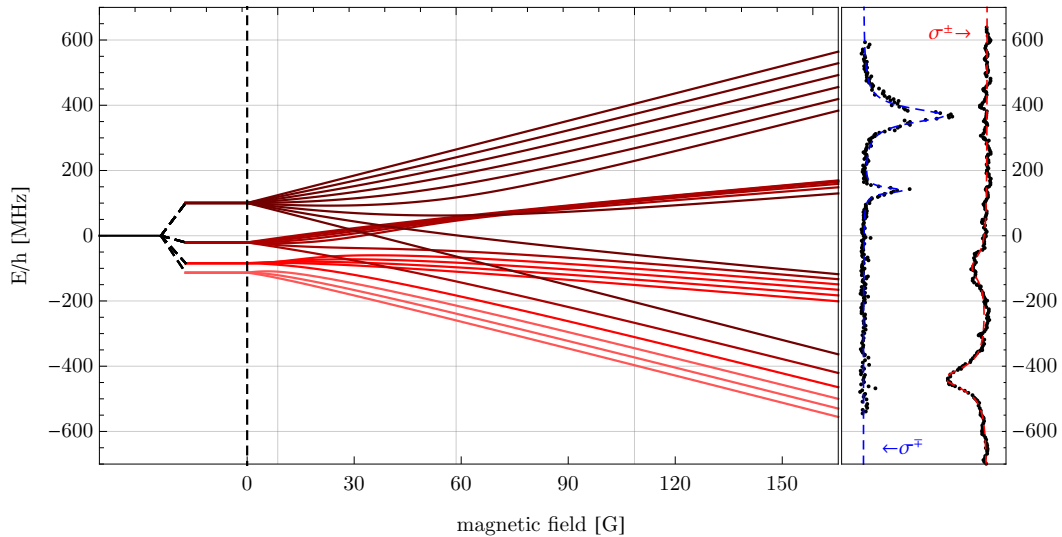


Figure 8.2: Spectroscopic analysis of ^{85}Rb atoms at 165.7G for σ^+ and σ^- -polarised light. The left figure shows the energy level splitting for ^{85}Rb as the magnetic field increases from 0 to 165.7G relative to the magnetically shifted $|F = 2, m_F = -2\rangle$ ground-state level that the atoms initially occupy. The splitting of the ground-state sub-level has also been applied to data, with the remaining shift entirely due to the excited-state splitting. Two major peaks are seen for each orientation of σ -light. Lorentzian fits indicate peaks at $-437.8 \pm 0.8\text{MHz}$, $-98 \pm 3\text{MHz}$, $139.0 \pm 0.7\text{MHz}$ and $368.3 \pm 0.6\text{MHz}$ with uncertainties given as the standard error from the fit. Given the proximity of multiple levels in the vicinity of each peak, it is difficult to determine the specific sub-level corresponding to the transition. The peaks do allow for accurate detuning from resonance for dispersive imaging purposes.

anomalous Zeeman regime where the quantum numbers m_I and m_J are instead appropriate. Given this mix of regimes, the selection rules governing the transition from the ground to excited states are non-trivial.

In order to characterise the allowed transitions, spectroscopy was performed at the required magnetic field with both polarisations of probe light (σ_+ and σ_-). Since the condensate occupies the ground-state magnetic sub-level $F = 2$, $m_F = -2$, the corresponding shift in energy was applied to the data so that the remaining shift is entirely due to the excited-state splitting as shown in Figure 8.2. The signal was obtained by taking a single absorption image at a particular detuning and integrating the signal. This was repeated over a range of detunings. Four peaks were observed with two for each polarisation. Lorentzian fits indicate peaks at -437.8 ± 0.8 MHz (σ_{\pm}), -98 ± 3 MHz (σ_{\pm}), 139.0 ± 0.7 MHz (σ_{\mp}) and 368.3 ± 0.6 MHz (σ_{\mp}) with uncertainties given as the standard error from the fit. The peak at 370 MHz was chosen for use in subsequent dispersive imaging techniques as it provides the largest signal, indicating strong transition strengths. In addition, this transition allows the probe light to be blue-detuned arbitrarily far without interference from other resonances.

8.4 Dark field imaging

The first non-destructive images of a Bose-Einstein condensate came only a year after their first experimental realisation and were obtained using a method called dark field imaging [32, 209]. The method is a variation of a far older technique called Schlieren imaging, described by Toepler in 1864 [210]. The technique is shown schematically in Figure 8.3, where a probe beam is shown to be incident on an atomic sample. The light, which is far-detuned from resonance interacts with the atoms through the refractive index as described in the previous chapter. Given the light is far-detuned from resonance, the majority of the interaction is produced through the real part of the refractive index and corresponds to a phase shift. A lens placed f from the sample focuses the non-interacting light to a point where a dark spot is placed, absorbing the light. In contrast, the light that did interact is collimated by the lens, allowing it to pass around the dark spot before being re-imaged onto a sensor by a second lens.

The signal detected at the sensor is the intensity of light, given by

$$I = \frac{1}{2}c\epsilon_0|E|^2, \quad (8.5)$$

where c is the speed of light, ϵ_0 is the vacuum permittivity and E is the electric field after the interaction. Supposing the electric field of the probe beam is initially E_{probe} and corresponds to a beam with a flat profile that is apertured to be exactly the size of the

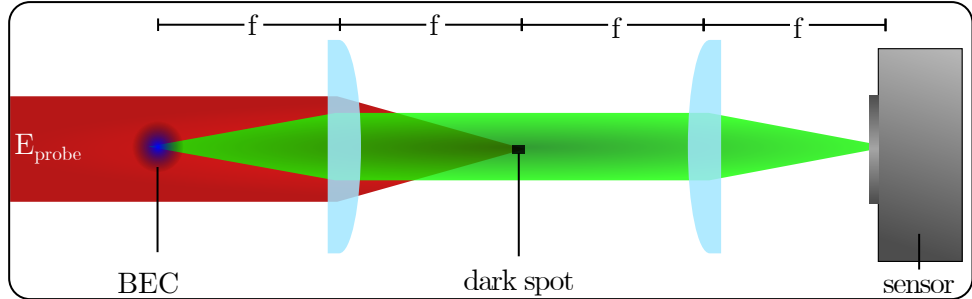


Figure 8.3: Schematic diagram of dark field imaging. The probe light, far-detuned from resonance, is input on an atomic sample. Part of the light interacts with the sample through the refractive index. The light that interacts (green) disperses before being subsequently collimated by a lens placed f from the atoms. The non-interacting light (red) is focused by this lens onto a dark spot which absorbs the light. A second lens collects and re-images the interacted light on a sensor.

sample then, after interaction with the atoms, the electric field is altered such that

$$E = E_{\text{probe}} + E_{\text{atoms}} = E_{\text{probe}} + E_{\text{probe}} \left(t e^{i\phi_{\text{atoms}}} - 1 \right), \quad (8.6)$$

where ϕ_{atoms} and t correspond to the dispersive and absorptive terms respectively. E_{atoms} is defined such that the initial probe field is entirely altered by the interaction.

Ordinarily this field results in the standard absorption signal measuring optical depth. Importantly the intensity is calculated through taking the modulus square of the electric field resulting in the cancellation of any phase signal. Dark field imaging seeks to alter Equation (8.6) to enable measurement of the phase component even after the conversion to intensity. This is achieved by blocking the probe beam after the interaction with the atomic sample. Experimentally this is achieved through clever optical setup (shown in Figure 8.3) allowing only the non-interacting light to be absorbed and removed. Effectively this is equivalent to removing the output probe field in Equation (8.6) resulting in a new expression for the electric field given by

$$E = E_{\text{probe}} \left(t e^{i\phi_{\text{atoms}}} - 1 \right). \quad (8.7)$$

Once again, the sensor measures the absolute value of the field, however, the removal of the probe light now ensures the phase term is still present. The intensity at the sensor is therefore given by

$$I = \frac{1}{2} c \epsilon_0 |E|^2 = I_0 (1 + t^2 - 2t \cos(\phi_{\text{atoms}})), \quad (8.8)$$

where $I_0 = \frac{1}{2} c \epsilon_0 |E_{\text{probe}}|^2$. In the limit that the probe beam is far-detuned from resonance such that the absorption is effectively zero, the transmission $t = 1$. Applying this to the

expression above simplifies the signal to

$$I = 2I_0(1 - \cos(\phi_{\text{atoms}})) . \quad (8.9)$$

Since this technique uses a dark-background, the noise is simply the square-root of the signal, resulting in a signal-to-noise of

$$\text{SNR} = \sqrt{2I_0(1 - \cos(\phi_{\text{atoms}}))} . \quad (8.10)$$

Dark spot imaging results in a signal that is dependent only on the phase acquired through interaction with the atoms, and results in a peak signal of $2I_0$. The derivation of the electric field given in Equation (8.7) is performed through considering the phasors of the interacting and non-interacting light. Though persisting throughout the literature, this approach is only acceptable for small-scale phase objects, with such an approach unacceptable for anything large-scale. In the limit of small shifts in phase due to the atoms, the intensity is found through Taylor expansion, yielding

$$I \approx I_0\phi_{\text{atoms}}^2 . \quad (8.11)$$

The intensity signal is seen to be proportional to the square of the phase shift. This makes inversion of the images somewhat difficult and ensures any background subtraction is problematic. In this limit the signal-to-noise is given by

$$\text{SNR} \approx \phi_{\text{atoms}}\sqrt{I_0} . \quad (8.12)$$

This limit better reflects the analysis provided here. Use beyond small-scale phase objects leads to flawed results. A significantly more rigorous approach is required, and although not provided here is outlined in [211].

The signal is seen to be dependent on the intensity of the probe beam, however this intensity is limited by the amount of destruction deemed tolerable. Additionally, due to the size of the focussed probe beam, the dark spot must be positioned to *microns* making the system experimentally challenging to implement. Since it operates in the dark field limit, detector noise becomes the dominant noise source. A bright field alternative to this system is phase contrast imaging implemented with a phase dot.

8.5 Phase contrast imaging

Extending the previous technique involves using a phase plate to selectively add phase to the non-interacting light to boost the signal-to-noise and allow a bright field operation

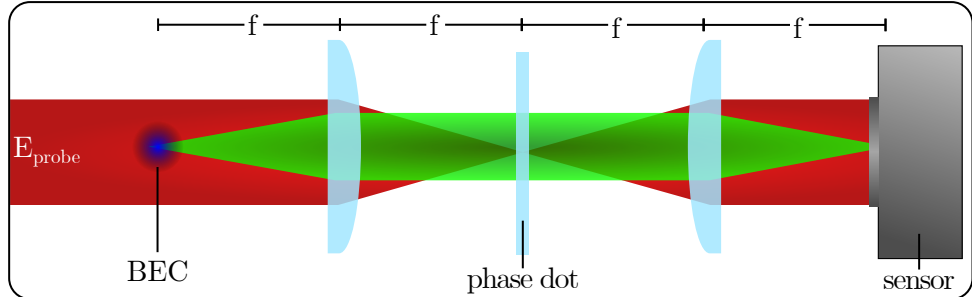


Figure 8.4: Schematic diagram for phase contrast imaging using a phase dot. The probe light is input on an atomic sample where part of the light interacts through the refractive index. The light that interacts (green) disperses and is subsequently collimated by a lens placed f from the atoms. The non-interacting light (red) is focused onto a phase dot; a large aperture plate with a small extrusion designed to apply a phase shift onto the non-interacting beam. A second lens collects and re-images the light on a sensor.

[212, 213]. As illustrated in Figure 8.4, probe light incident on the atomic sample receives a phase shift compared to the non-interacting light. A lens placed f from the sample collimates the dispersed light while focusing the non-interacting light. The non-interacting light is focused to a point f further from the lens where a phase dot is placed. This phase dot consists of an optical flat large enough to pass the full aperture of the beam, with either a small extrusion or intrusion in the centre. This extrusion is manufactured such that the non-interacting light, now focused to a point, acquires a specific phase shift compared to the interacted light. The phase shift is calculated to produce the greatest signal-to-noise. Upon passing through the phase dot, a second lens is used to re-image the signal onto a sensor with both the interacting and non-interacting light now interfering at the detector. This setup results in a phase shift on the interacting light in addition to deliberately adding a phase shift to the non-interacting light as a way of increasing the signal at the camera. By carefully choosing the phase shift applied to the non-interacting light, the total signal can be optimised for a specific sample [213].

Returning to Equation (8.6) obtained in the previous section, now allowing the non-interacting light to acquire a separate phase shift, ϕ_{dot} , from the phase dot, the electric field after the phase dot is given by

$$E = E_{\text{probe}} e^{i\phi_{\text{dot}}} + E_{\text{probe}} \left(t e^{i\phi_{\text{atoms}}} - 1 \right), \quad (8.13)$$

where ϕ_{dot} is the phase acquired by the light after passing through the dot. This value is constant and set during manufacture by the specific width chosen for the phase dot. The intensity incident on the sensor is therefore altered to become

$$I = I_0 (2 + t^2 - 2t \cos(\phi_{\text{atoms}}) + 2t \cos(\phi_{\text{atoms}} - \phi_{\text{dot}}) - 2 \cos(\phi_{\text{dot}})). \quad (8.14)$$

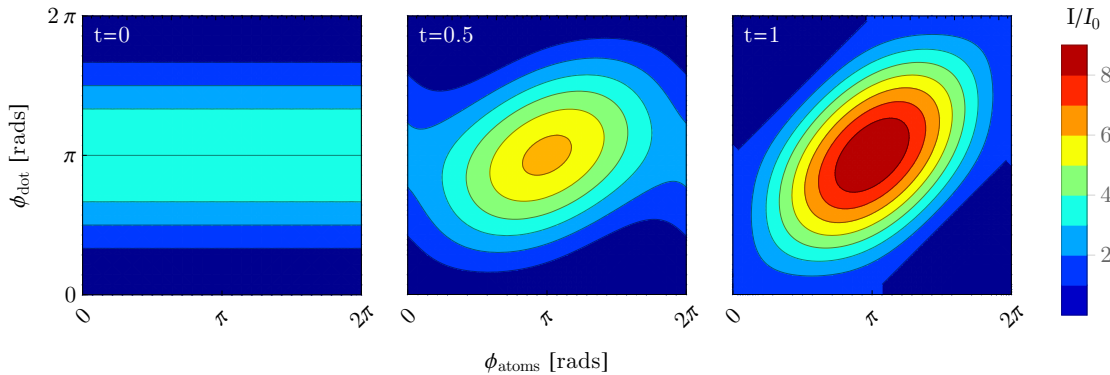


Figure 8.5: Intensity signal at the detector for phase contrast imaging using a phase dot as described in Equation 8.14. As the transmission increases (or alternatively, as the detuning increases to the non-destructive regime) the phase becomes a greater proportion of the signal.

As the system moves from the destructive ($t = 0$) to non-destructive ($t = 1$) regime, the proportion of the signal due to phase changes, as illustrated in Figure 8.5. In reality, the response is much more complex, as the transmission is a function of both detuning, and the spatially-dependent density of the sample.

In the limit of small-scale phase objects, and the simpler case of a phase dot of $\phi_{\text{dot}} = \pi/2$, the intensity simplifies to

$$I \approx I_0(1 + 2\phi_{\text{atoms}}). \quad (8.15)$$

This signal is simpler than the dark spot signal, allowing for convenient background subtraction before inversion. Whilst the signal theoretically achieves a maximum of $5.8I_0$, the size of the phase dot is important and can lead to less than ideal behaviour [214].

Given the phase contrast technique is bright-ground, the noise is larger than that of dark spot imaging. Taking into account the background subtraction and assuming the limit of small phase shifts whilst using a $\pi/2$ dot, the noise is $2\sqrt{I_0}$. The shot noise limited signal-to-noise ratio of phase contrast imaging in the optically thin limit is then

$$\text{SNR} \propto \phi \sqrt{I_0}. \quad (8.16)$$

This signal-to-noise is the same as that of dark spot imaging, but as a result of larger signal and noise, is less susceptible to technical noise.

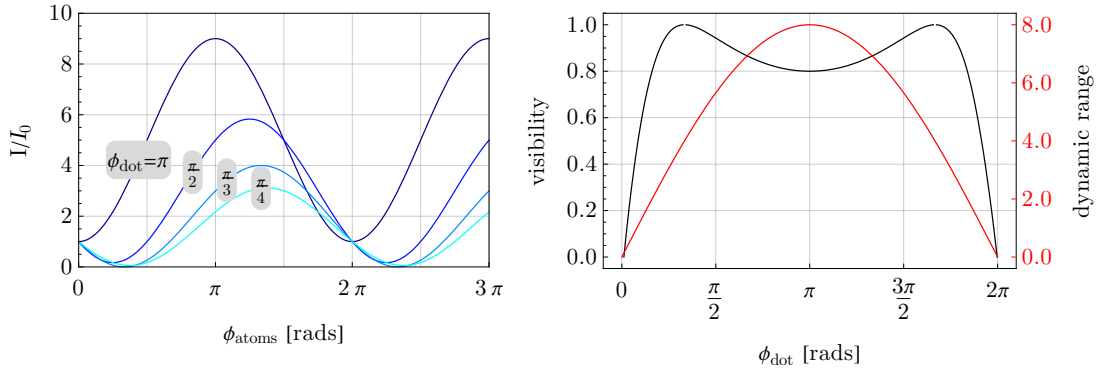


Figure 8.6: Left: The signal at the detector for phase contrast imaging using a phase dot assuming operation in the non-destructive regime. By varying the phase added to the non-interacting beam, the signal may be increased. A π phase dot results in the largest dynamic range, whereas a $\pi/3$ phase dot provides the greatest visibility. Right: The dynamic range and visibility over a full range of phase dot values. The visibility has a peak at $\pm\pi/3$ while the dynamic range has a peak at π .

8.5.1 Phase dot optimisation

Naïvely, one might expect the optimum operating value for the phase dot to be π radians as this would produce the largest contrast, defined as

$$\mathcal{C} = I_{\max} - I_{\min}. \quad (8.17)$$

Although the contrast gives a good measure of the ability to detect a signal, visibility is also an important metric [213], defined as

$$\mathcal{V} = \frac{I_{\max} - I_{\min}}{I_{\max} + I_{\min}}. \quad (8.18)$$

Given this metric, a $\pi/3$ phase plate would be optimal as the signal undergoes a full sweep from the maximum down to zero over the range of phase shifts from the sample. A $\pi/3$ phase plate results in a visibility of unity and a contrast of $4I_0$. The π phase dot results in a visibility of 0.8 and a contrast of $8I_0$. One key disadvantage of the phase dot method is that the phase shift of the dot is constant and set at manufacture. Ideally the applied phase could be dynamic and optimised to the specific system in order to produce maximum signal-to-noise.

8.5.2 Manufacture of dot

The manufacture of the phase dot is an important consideration. The light passing through the phase dot will acquire a phase shift dependent on the refractive index of the mate-

rial. The phase shift is given by

$$\phi = k (n_{\text{ref}} - 1) l, \quad (8.19)$$

where $k = 2\pi/\lambda$ is the wave number of the probe light of wavelength λ , n_{ref} is the refractive index of the material used in the phase dot and l is the thickness of the phase dot. Manufacturing and technical considerations determine whether the phase dot should be a dimple (a thinner section of the plate) or a spot (a thicker section). In order to generate the optimum visibility, as defined by Equation (8.18), the optimum phase shift to apply to the non-interacting light is $\pi/3$ leading to a phase dot thickness of either

$$l = \underbrace{\frac{1}{6} \frac{\lambda}{n_{\text{ref}} - 1}}_{\text{extrusion}} \text{ or } \underbrace{\frac{5}{6} \frac{\lambda}{n_{\text{ref}} - 1}}_{\text{depression}} \quad (8.20)$$

depending on the whether the dot is a dimple or spot.

Poly methyl methacrylate (PMMA) is a relatively cheap and easy to machine material having a refractive index of $n_{\text{ref}} = 1.485$ at a wavelength of 780 nm. Given this material and light focussed by a 1 inch lens of focal length 250 mm, the dot would need to be $\sim 9.5 \mu\text{m}$ in diameter and $\sim 390 \text{ nm}$ thick.

Despite the merits of phase contrast imaging, the typical sizes required for the phase dot and the difficulty of manufacture make the technique appreciably difficult. In addition to manufacturing difficulties, alignment of such a spot also proves to be a non-trivial.

8.6 Polarisation phase contrast imaging

Polarisation phase contrast imaging utilises a magnetic field to polarise the atomic sample and through birefringence generates a rotation in polarisation of the light that passes through the sample compared with the non-interacting light [201, 215, 216]. When the magnetic field is parallel to the imaging beam, the setup is in a Faraday configuration. Although other configurations exist such as the perpendicular setup of a Voight configuration, the following analysis will focus on a Faraday configuration.

The setup required for Faraday rotation imaging is illustrated in Figure 8.7. Although this setup is not the simplest possible configuration, it encapsulates the extra necessary components required to incorporate the system into the existing dual species apparatus. In particular, given the imaging system shares a path with the vertical MOT beam, an initial half-wave plate and liquid crystal wave plate are used in combination to enable fast and robust switching between imaging and MOT optical configurations. In addition, one of the ports of the polarising beam splitter is incident on the MOT retro-reflector.

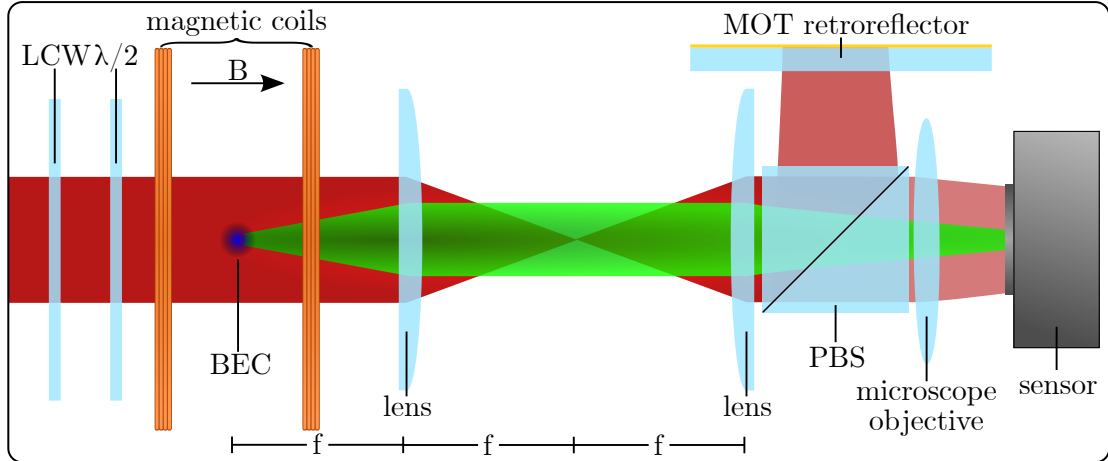


Figure 8.7: Schematic diagram for polarisation phase contrast imaging in the Faraday format. The diagram also includes technical components crucial for implementation in the existing dual-species apparatus. Namely, the imaging shares the same optical path through the atoms as the vertical MOT beam. By combining a half wave plate and a liquid crystal wave plate (LCW), the system can be dynamically switched during the experimental run to accommodate both systems. The reflected port of the polarising beam splitter is used for the MOT retro-reflection mirror limiting use of this port for further imaging information. The magnetic coils polarise the atomic sample with birefringence generating a rotation in the polarisation of the light that passes through the sample relative to the light that does not. This difference can be measured using the polarising beam splitter with both dark and bright-background images possible.

In theory, were the optical setup not sharing the MOT beam line, this port could also be monitored for extra information. The imaging system uses polarised light, directed through a half wave plate and on to a sample that is spin polarised by a magnetic field oriented parallel to the direction of propagation of the light. The light interacts with the sample and, through birefringence, undergoes a rotation of polarisation relative to the non-interacting light. The light then passes through a polarising beam splitter before being imaged onto a sensor. By detecting a change in the intensity of the light at the sensor, information about the sample can be obtained. By rotating the polarisation of the initial light, the system may operate in either a bright or dark-background configuration. The ability to create this polarisation contrast requires much less technical finesse in setup as it does not require the precise alignment of a dark spot or phase dot. The downside is the requirement to operate with a magnetic field, which may not be ideal for all samples or the dynamics being probed.

For the initial analysis, consider purely linear probe light input to the sample, where the polarisation is given as an angle relative to the final beam splitter. The electric field before interaction is, in vector form, then

$$\mathbf{E} = \left\{ \underbrace{E_0 \cos(\theta)}_x, \underbrace{E_0 \sin(\theta)}_y \right\}, \quad (8.21)$$

where the intensity is given by

$$I = \frac{1}{2}c\epsilon_0|\mathbf{E}|^2 = \frac{1}{2}c\epsilon_0|E_0|^2. \quad (8.22)$$

By changing the rotation of this initial polarisation, the amount of light going through each port of the final beam splitter can be changed with the amount of light being detected by the camera being correspondingly altered. Since the quantisation axis is along the direction of propagation, the linearly polarised light interacts with the atoms as a superposition of σ^+ and σ^- circularly polarised light. Transforming the basis of the initial light to the circular basis, we find

$$\mathbf{E} = \frac{1}{\sqrt{2}} \left\{ \underbrace{iE_0(\cos(\theta) - i\sin(\theta))}_{\sigma_+}, \underbrace{iE_0(i\sin(\theta)) - \cos(\theta)}_{\sigma_-} \right\}. \quad (8.23)$$

The light then passes through the atoms and acquires a phase term in the form of a Faraday rotation. In addition to the phase acquired, a certain portion of the incoming photons will be absorbed destructively. Accounting for the phase and transmission, the electric field in the circular polarisation basis is modified producing

$$\mathbf{E} = \frac{1}{\sqrt{2}} \left\{ \underbrace{ie^{i\phi_+}t_+E_0(\cos(\theta) - i\sin(\theta))}_{\sigma_+}, \underbrace{ie^{i\phi_-}t_-E_0(i\sin(\theta)) - \cos(\theta)}_{\sigma_-} \right\}, \quad (8.24)$$

where ϕ_\pm and t_\pm correspond to the phase and transmission respectively that result from interaction with the σ_+ and σ_- components of the light. Given the initial light is linearly polarised, both interaction terms are present. In theory, if the probe light is far-detuned away from all possible transitions, only one of the polarisations will produce significant interaction with the other too far-detuned to result in any phase shift or absorption.

Finally, transforming back to the linear basis to determine the light which passes the beamsplitter and the light which is reflected, we find

$$\mathbf{E} = \frac{1}{2} \left\{ \underbrace{E_0ie^{-i\theta}(t_+e^{i\phi_+} - t_-e^{i(2\theta+\phi_-)})}_x, \underbrace{E_0e^{-i\theta}(t_-e^{i(2\theta+\phi_-)} + t_+e^{i\phi_+})}_y \right\}. \quad (8.25)$$

The light that makes it to the sensor will be one component of this vector, depending on whether the system is set up to detect on the reflected or transmitted port of the beam splitter.

If the system is set up such that in the absence of a sample, all light will be sent to the non-monitored port, then any rotation caused by the introduction of a sample will result in more light on the monitored port. In this regime, and assuming that one of the

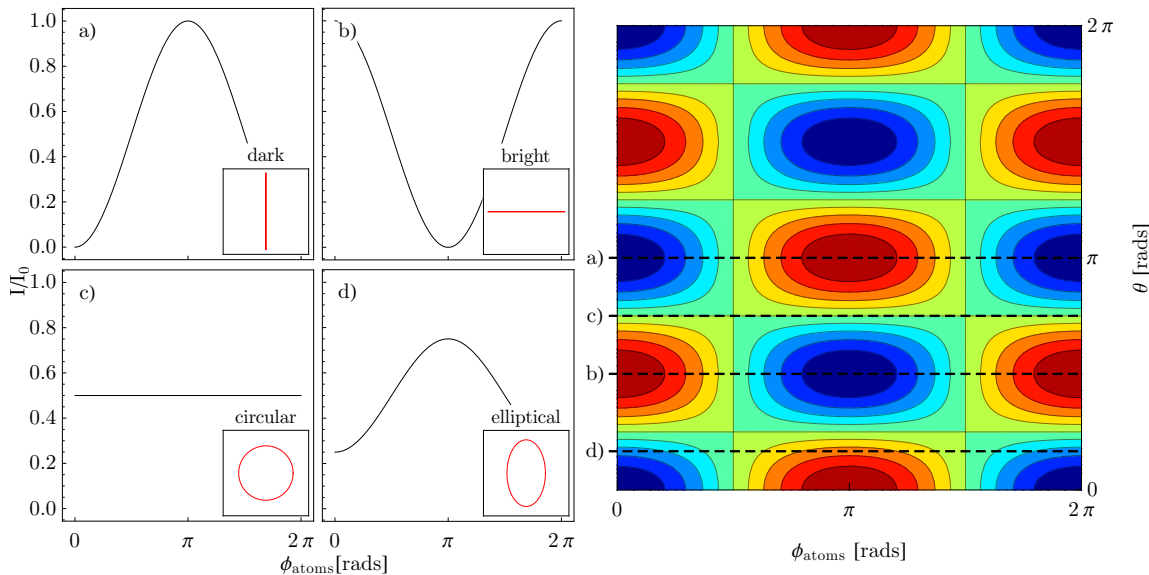


Figure 8.8: The intensity signal as a function of the input polarisation. While *all* polarisations are not represented by the plot, it does illustrate a number of key regimes. In particular, pure circularly polarised light (c) produces no atom-dependent signal. Elliptically polarised light (d) improve upon this, but not as significantly as linearly polarised light (a, b). All linear polarisations produce the same intensity signal, however, the polarisation direction corresponding to a dark background on the sensor will yield the lowest noise of all configurations.

transitions is far enough detuned such that the contribution is negligible ($t_+ = 1$ and $\phi_+ = 0$, for example) then the system yields the same signal as the dark spot technique described in Section 8.4, specifically

$$E = E_0 \left(t e^{i\phi} - 1 \right). \quad (8.26)$$

In contrast to dark spot imaging, the above technique is technically simpler allaying the need for extremely precise alignment of a dark spot in the Fourier plane of the light. In addition, this technique allows for the amount of light reaching the camera to be tuned using only the initial polarisation orientation. Whilst the technique can operate in both dark and bright-ground configurations, a dark-ground setup will result in lower shot-noise. The above derivation began with the assumption of linearly polarised light incident on the sample. It is possible to derive the result for any arbitrary polarisation. Doing so produces the plot seen in Figure 8.8. Of note is that pure circular polarised light (c in Figure 8.8) results in no atom-dependent signal. Linear light (a and b) produces the highest signal with elliptical light (d) producing a diminished signal.

In contrast to dark spot imaging and phase contrast imaging, this technique requires a magnetic field to operate. This introduces the possibility of a second transition contributing to the signal. Although this possibility exists for phase contrast imaging, the additional levels are much further detuned than the magnetic sub-levels exploited for

this technique. Since the signal requires a mixture of σ -polarisations at the atoms, both transitions can contribute to the signal. In most cases we assume that one of the transitions is so far-detuned as to result in negligible contribution.

8.7 Shadowgraph imaging

In the cases of dark field imaging and phase contrast imaging, the precise alignment of optics is tantamount to producing high signal-to-noise dispersive images. Polarisation phase contrast imaging requires a magnetic field to operate, limiting its use in certain applications. Shadowgraph imaging provides a means of generating a dispersive signal with relative ease and no additional optics compared with absorption imaging, allowing both methods to be implemented on the same apparatus. In combination with an optical phase locked loop, the system allows dynamic switching between this dispersive technique and absorption imaging within a single experimental cycle, increasing the applicability and usefulness. The technique itself relies on the spatial scattering of the probe light due to the dispersive term of the refractive index and has been used extensively in other fields such as x-ray tomography where it is called *phase contrast imaging* [217]. Given this name already refers to a different imaging technique used in cold-atom physics, other names such as diffraction contrast imaging have been used. Since the signal is proportional to the second spatial derivative of the density (shown below), the name shadowgraph imaging applies. Shadowgraph imaging, first described by Hooke [202] has been used extensively to image transparent media, and often for imaging heat or pressure waves [218].

The experimental system required to implement the shadowgraph technique is extremely simple. As illustrated in Figure 8.9, probe light is incident on the atomic sample acquiring some attenuation and phase shift. The dense condensate means that the phase shift acts to lens the light, with the focal length extremely close to the sample. A lens placed $2f$ from the sample collects the interacted and non-interacted light and focuses it onto a sensor.

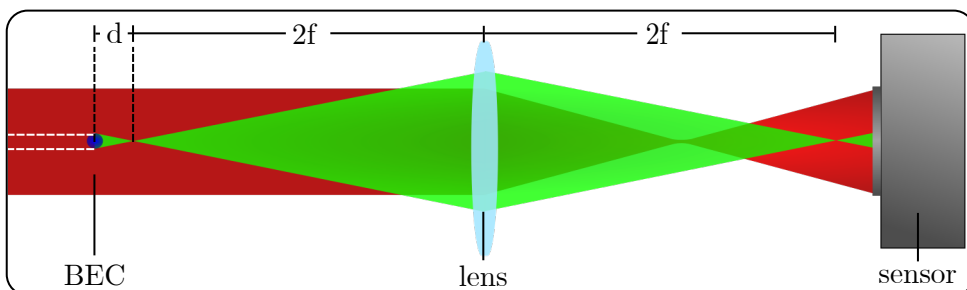


Figure 8.9: Imaging scheme for shadowgraph imaging. Probe light is incident on the atomic sample acquiring some attenuation and phase shift. The dense condensate means that the phase shift acts to lens the light, with the focal length extremely close to the sample. A lens placed $2f$ from the sample collects the interacted and non-interacted light and focuses it onto a sensor.

placed $2f$ from the sample collects the interacted and non-interacted light and focuses it onto a sensor. By re-imaging the effective lens generated by the condensate, a signal can be generated. The signal has been theoretically described in both the near-field and far-field regime using the transport of intensity equation (TIE) and contrast transfer function (CTF) respectively. In the far-field, the CTF approach is used to solve the inverse problem and requires multiple images along the beam propagation direction. Despite this requirement, the technique has been applied to cold atoms [219]. The near-field signal can be re-imaged using a single lens placed at $2f$ or a telescope setup, allowing the TIE approach to be used and the requirement for multiple images relaxed. This approach has previously been used to image a magneto-optical trap [220] with low SNR and high destruction. This research extends the approach to image a Bose-Einstein condensate in-trap in the far-detuned regime, demonstrating no observable heating or atom loss over 100 images. This section begins with a theoretical consideration of shadowgraph imaging, before using a number of experimental examples to demonstrate the capability and utility of the system. This includes dual atomic species imaging, continuous imaging of small ^{85}Rb solitons ($\sim 10^3$ atoms), large ^{87}Rb condensates ($\sim 10^6$ atoms), continuous acquisition of data over the entire experimental duty cycle (images spaced by 100ms), dynamical data acquisition where a sequence of shadowgraph images are followed by a high SNR near-resonant absorption image, and observations of soliton dynamics.

8.7.1 Theoretical signal

As previously described, the refractive index (Equation 7.2) gives rise to an attenuation and dispersion term that affect the probe beam electric field such that

$$E = E_0 T(\mathbf{r}), \quad (8.27)$$

where $T(\mathbf{r})$ is the transmittance function defined by

$$T(\mathbf{r}) = A(\mathbf{r}) e^{i\phi(\mathbf{r})} = e^{B(\mathbf{r})+i\phi(\mathbf{r})}. \quad (8.28)$$

where $B(\mathbf{r})$ and $\phi(\mathbf{r})$ correspond to the absorption and phase shift given by

$$B(\mathbf{r}) = \frac{2\pi}{\lambda} \int \text{Re} \{ n_{\text{ref}}(\mathbf{r}, z) - 1 \} dz, \quad (8.29)$$

$$\phi(\mathbf{r}) = \frac{2\pi}{\lambda} \int \text{Im} \{ n_{\text{ref}}(\mathbf{r}, z) - 1 \} dz, \quad (8.30)$$

respectively, with both components of the refractive index components taken relative to vacuum. The pattern produced by the interaction with the sample is one of Fresnel

diffraction with the transmittance altered according to the Fresnel propagator,

$$P_D(\mathbf{x}) = \frac{1}{i\lambda D} \exp\left(i\frac{\pi}{\lambda D} |\mathbf{x}|^2\right), \quad (8.31)$$

where D denotes the distance of propagation along z . The resultant intensity pattern at D is given by the modulus square of the transmittance propagated with the Fresnel propagator,

$$I_D(\mathbf{x}) = |T(\mathbf{x}) * P_D(\mathbf{x})|^2. \quad (8.32)$$

This propagation becomes simpler when considered in the Fourier domain. Equation 8.31 can be written in Fourier space as

$$\tilde{P}_D(\mathbf{f}) = \exp\left(i\pi\lambda D |\mathbf{f}|^2\right), \quad (8.33)$$

where the Fourier transform is defined as

$$\tilde{g}(\mathbf{f}) = \mathcal{F}\{g(\mathbf{x})\} = \int g(\mathbf{x}) \exp(-i2\pi\mathbf{x} \cdot \mathbf{f}) d\mathbf{x}, \quad (8.34)$$

where $\mathbf{f} = (f_x, f_y)$ being the spatial frequency coordinates. In the Fourier domain, equation 8.32 simplifies and the Fresnel diffraction pattern at the point D becomes

$$\tilde{I}_D(\mathbf{f}) = \int T\left(\mathbf{x} - \frac{\lambda D \mathbf{f}}{2}\right) T^*\left(\mathbf{x} - \frac{\lambda D \mathbf{f}}{2}\right) \exp(-i2\pi\mathbf{x} \cdot \mathbf{f}) d\mathbf{x}. \quad (8.35)$$

Typically, in ultracold atom experiments the sample is formed inside a vacuum chamber, limiting the imaging to the far-field. In this limit the contrast transfer function approach may be used to solve the inverse problem with the process described in detail in [217]. This approach requires multiple images along z in order to determine the phase and is therefore more technically difficult, but has previously been applied to cold atoms [219]. Ideally imaging would occur in the near-field, where the requirement for multiple images is relaxed. This can be achieved by re-imaging the near-field signal using a single re-imaging lens placed at $2f$. The imaging system may then be placed far from the sample and the transport of intensity equation approach used. This approach begins by linearising Equation (8.35) by way of a Taylor expansion of the transmittance function $T(\mathbf{x})$ given by Equation (8.28). The Taylor expansion is performed with respect to D , truncating to first order such that

$$T(\mathbf{x} \pm \lambda D \mathbf{f}/2) \approx T(\mathbf{x}) \pm \frac{1}{2} \lambda D \mathbf{f} \cdot \nabla T(\mathbf{x}). \quad (8.36)$$

This expression may then be substituted into Equation (8.35), with the intensity pattern thus given by

$$I_D(\mathbf{x}) = I_0(\mathbf{x}) - \frac{\lambda D}{2\pi} \nabla [I_0(\mathbf{x}) \nabla \phi(\mathbf{x})]. \quad (8.37)$$

Finally as a result of the approximation of the Taylor expansion and the assumption that D is small, $(I_D(\mathbf{x}) - I_0(\mathbf{x}))/D$ can be approximated as the partial derivative over z such that

$$\nabla [I_0(\mathbf{x}) \nabla \phi(\mathbf{x})] = -\frac{2\pi}{\lambda} \frac{\partial}{\partial z} I_0(\mathbf{x}). \quad (8.38)$$

This expression is known as the transport of intensity equation. Given a particular diffraction pattern, the inverse problem must be solved to relate this to the density of the sample. Many approaches exist for solving the inverse problem including partial differential equation methods [217, 221–225] and Fourier methods [226]. Even in this regime, images at two locations along the propagation direction are required. Further approximation can allow the inverse problem to be solved with images at a single location along the propagation direction. Specifically, in the small D regime, and in the limit of small, flat absorption whereby $t(\mathbf{r}) \approx 1$, $I_0(\mathbf{x})$ can be moved outside the gradient operator such that

$$I_D(\mathbf{x}) = I_0 \left[1 - \frac{\lambda D}{2\pi} \nabla^2 \phi(\mathbf{x}) \right], \quad (8.39)$$

where $I_0 = \frac{1}{2}c\epsilon_0|E_0|^2$. Given this approximation, the phase is simply

$$\phi(\mathbf{x}) = -\frac{2\pi}{\lambda D} \nabla^{-2} \left[\frac{I_D(\mathbf{x})}{I_0(\mathbf{x})} - 1 \right]. \quad (8.40)$$

The key difficulty here is the computation of the inverse Laplacian. This can be performed using Fourier methods whereby

$$\nabla^{-2} = \frac{1}{4\pi^2} \mathcal{F}^{-1} \frac{1}{f_x^2 + f_y^2 + \alpha} \mathcal{F}, \quad (8.41)$$

where $(f_x^2 + f_y^2)^{-1}$ is replaced by zero at the Fourier domain origin with α being a regularisation parameter chosen to fix the singularity that occurs at $f_x = f_y = 0$ [227]. In situations where the inversion is not possible, certain information such as atom number may be lost, while for most non-pathological density distributions positional information can still be obtained as well as relative information.

The condensate effectively lenses the incident light with the optimal signal occurring at the focal point of this lens (d in Figure 8.9). Since the condensate is dense, the effective focal length is short compared to that of the imaging lens. This disparity in the depth of

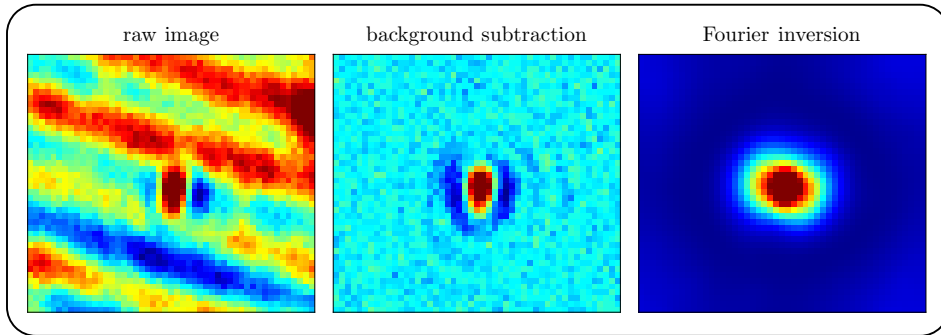


Figure 8.10: The raw image from the camera is shown on the left and is seen to display significant diffraction from various components along the imaging line. Once a background image, taken without the condensate present, is subtracted, these flaws are reduced significantly. A large positive region surrounded by negative rings shows the presence of the condensate. Applying a Fourier method to solve the inverse Laplacian in Equation (8.39) allows the reconstruction of the structure. The technique for inversion is typically extremely sensitive, especially to the size of the region around the structure. In practice using the background subtraction enables significant robust analysis, although direct quantitative analysis of number of atoms and other properties is not possible.

field allows the sensor to be placed in-focus for normal absorption imaging whilst still generating a large shadowgraph signal when the probe beam is heavily detuned. This enables the possibility of using both techniques without any experimental alteration, simply by detuning the probe laser from resonance. Given a method for fast dynamic frequency control of the probe laser, fast switching between imaging methods is possible, introducing the capability of taking a series of continuous non-destructive images followed by a high signal-to-noise absorption image in the same experimental run.

8.7.2 Experimental details and camera plane

To achieve the required detuning of the imaging probe beam, a dedicated external cavity diode laser with optical phase locking loop is used. A master laser locked to an atomic transition using saturated absorption spectroscopy is beat with the probe laser on a 12 GHz fast photo detector. The signal is amplified and divided down such that it can be mixed with a radio-frequency source. The beat lock and feedback is generated using the method described in [228] with the feedback applied on the probe laser using piezo control. The phase lock loop provides a lock with narrow linewidth below 1 Hz and a capture range of 10 MHz enabling swift changes of detuning and dynamic switching between dispersive and absorption imaging.

The probe beam is delivered to the science table by a polarization maintaining fiber where it is combined with the vertical MOT beam, sharing the same optical path through the science cell. This orientation allows for imaging perpendicular to the optical waveguide beam, allowing for non-destructive probing of experiments performed in the wave-

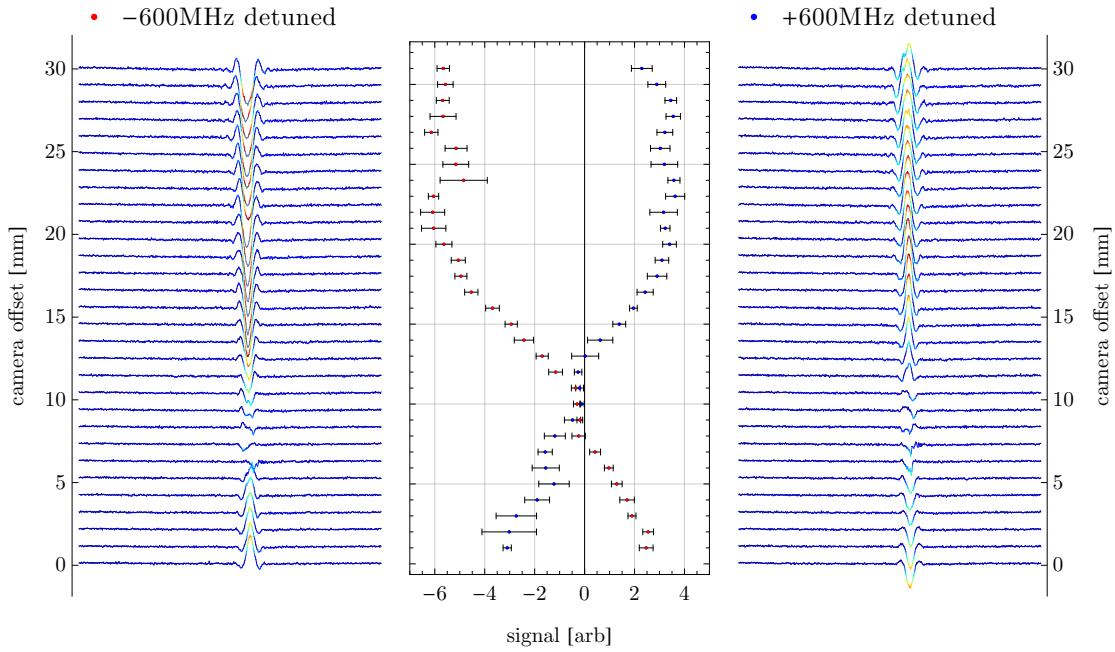
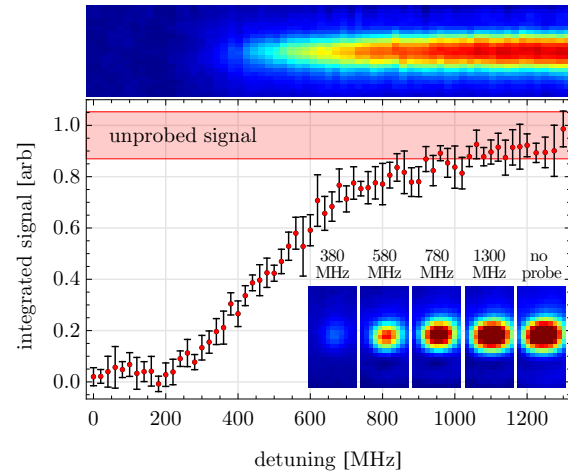


Figure 8.11: Scanning the position of the camera in increments of 1 mm and measuring the signal for each of 10 experimental runs. This is repeated for positive and negative detunings of the same magnitude (600 MHz). The left and right images show a slice through the maximum value in the average image. The signal is seen to be negative and large, move through zero and become positive and increasing. The opposite is seen for the opposite detuning. The centre plot shows this signal as obtained by using a box around the maximum signal and integrating. The mean over 10 experimental runs is obtained along with a standard deviation indicated by the points and error bars respectively. The blue and red points correspond to the probe beam being blue or red-detuned respectively.

uide. Two liquid crystal wave-plates enable dynamic switching of polarization of this optical line, allowing different polarizations of light for the MOT and imaging beams. A dual lens ($f = 10$ cm) telescope allows the near-field signal to be re-imaged far from the vacuum system. Finally a 4 times magnification is achieved using an objective lens with the subsequent signal detected on a CMOS camera (Point Grey GS3-U3-41C6NIR-C). The camera has high quantum efficiency (45% at 780 nm) and is capable of kHz frame rates. The setup enables fast, dynamic imaging that is minimally destructive despite a small and fragile sample and is seen to be robust to extra optics sharing the same path.

Precise alignment of the lens system and camera plane is crucial to success of the system. Slight angular deviations of the optics away from perpendicular to the beam causes large amounts of diffraction that dominate the signal and manifest as repeating rings, necessitating a well aligned optics system. In addition, the placement of the camera plane relative to the optics and condensate is extremely important. Given the shared optics of the dual-species machine, this was demonstrated instead using a separate machine described in detail in [35]. This apparatus allows for greater testing of the shadowgraph

Figure 8.12: Integrated signal from the 22 ms TOF absorption system following 100 dispersive in-trap images spaced 2 ms apart. Maximum destruction occurs at resonance and lessens as the in-trap probe is detuned further. The shaded area indicates one standard deviation either side of the mean integrated signal when the in-trap probe is off. The signal is seen to approach this region as the detuning approaches 1 GHz. Insets show the signal in the TOF absorption image at various detunings from resonance, which at large detuning show negligible difference. Top image shows signal integrated along one direction for each of the measured values of in-trap detuning.



technique as the probe beam path is independent of all other optics. The optical setup for this device is exactly as shown in Figure 8.9, utilising a single lens for imaging. The conclusions apply to the telescope imaging system used in the dual-species machine, albeit with slight modifications. The response of the shadowgraph signal to movement of the camera plane for both a red and blue-detuned probe beam is shown in Figure 8.11. The signal at the camera was recorded over a 30 mm range in steps of 1 mm for both ± 600 MHz detuning from resonance with 10 experimental runs for each step. The signal is seen to be opposite in sign for the opposing directions of detuning, with the signal moving from negative to positive through zero as the camera is scanned along the propagation direction. A slice through the maximum signal is shown in the left and right of Figure 8.11. The point at which the signal is zero corresponds to when the light focussed by the condensate is past the focal point and diverging such that it spatially reflects the flat probe beam without interaction. The negative signal corresponds to when the imaging plane is beyond the focal point and the light is diverging, causing a ‘hole’ in the flat probe beam. A positive signal corresponds to an imaging plane at or close to the focal point of the condensate where all the interacted light has been moved into the centre of the beam. Since there is a large difference between the depth of field of the imaging system and the effective focal length of the condensate, the imaging system may be operated such that it has good dispersive signal while still being in-focus for absorption imaging.

8.7.3 Experimental signal-to-noise and destruction

The imaging system was tested over a range of detunings, time scales and destruction. Using the dual-species apparatus, a small ^{85}Rb ($\sim 10^4$ atoms) condensate was probed through 100 in-trap images over a GHz range of detuning, with each image taken 2 ms apart using an exposure of 100 μs . The condensate was then dropped and imaged after a 22 ms time-of-flight by a separate horizontal absorption system. Equally, the OPLL could

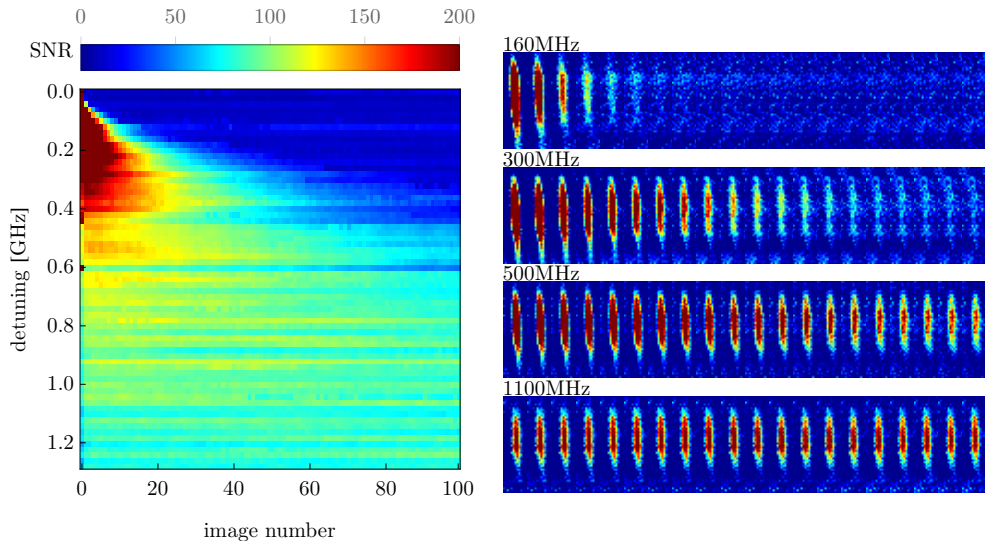
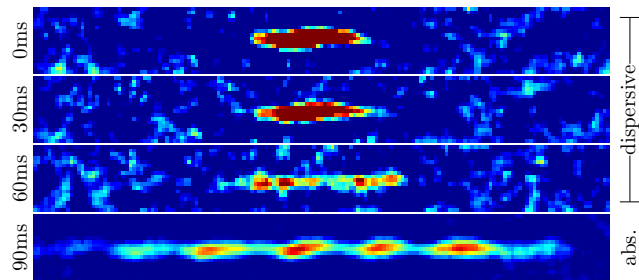


Figure 8.13: The signal-to-noise ratio (SNR) for each of the 100 in-trap images for a range of detunings out to 1.3 GHz. The signal is calculated by integrating an area of pixels around the maximum signal after a Fourier DCT filter is applied and the images have been averaged over 10 sets. The noise is calculated by integrating the same sized area in a part of the image with no signal. The SNR is greatest close to resonance, but decays in very few images as the condensate is destroyed. The SNR falls off as the detuning is increased, however the destruction also decreases, with the SNR remaining constant over all 100 in-trap images for large detunings. It should be noted that due to the shape of the cloud, the edges have the lowest optical depth and therefore the lowest signal. This results in the cloud appearing smaller for larger detunings.

have been used to move the probe detuning on resonance for the final image. Figure 8.12 outlines the change in the condensate as the detuning of the dispersive probe beam is altered. Close to resonance the condensate is completely destroyed. As the detuning increases this destruction decreases. The shaded band at the top of the figure indicates one standard deviation from the mean variation run-to-run with no probe applied. The absorption signal is seen to approach this regime for large detunings with no change in atom number or cloud widths observed after expansion. The inset shows the absorption images for a number of different detunings with the set at 1.3 GHz displaying no qualitative or quantitative difference compared to the situation when no in-trap probing occurs. The top of the figure displays a once integrated signal for each of the measured detunings providing a clearer example of the effect of the in-trap probe detuning on the condensate as measured by the final dropped absorption image.

At large detunings the dropped condensate appears unchanged by the probing. Even this far detuned, the in-trap signal still remains high, as evidenced by the set of images in the right of Figure 8.13, where four 20 image subsets are shown for a range of detunings. A Fourier discrete cosine transform filter has been applied to each image and each has been averaged over a series of 10 runs for each detuning. In application to stochastic processes, such averaging is unavailable, and the signal drops accordingly. Be-

Figure 8.14: Dynamic manipulation of in-trap probe detuning. The 4 images are a subset of 9 in-trap images with the final taken on resonance. The system allows direct observation of a soliton confined to an optical waveguide decaying into a soliton train, a stochastic event with the breakup time and number of components varying run-to-run. Continuous imaging enables observation of individual trajectories of stochastic processes.



yond $\sim 1\text{GHz}$ the signal has negligible decay over the 100 images, and the corresponding dropped cloud closely resembles the cloud with no in-trap probe beam applied. Integrating an area of the in-trap image where no signal is present allows a characterization of the noise. The area of integration is the same for both the signal and the noise. The signal is given by integrating over both spatial dimensions. The noise is calculated by integrating an area of the same size where no signal is present. A second, cumulative integration is performed, with the noise being given by the variance of this result. The resultant SNR is shown in the left of Figure 8.13. The peak signal is close to resonance, however it decays exponentially in time as the condensate is destroyed. As the detuning is increased the signal decreases, but so too does the loss rate due to absorption. Far from resonance, at 1.25GHz , negligible decay occurs and the SNR is ~ 90 and corresponds to near optimal operation in terms of both destruction and signal. At this detuning the SNR for a single experimental run is ~ 32 , being large enough to enable observation and analysis of stochastic processes.

8.7.4 Applications

The shadowgraph imaging technique, with its ease of setup, was implemented on both the dual-species experiment and the gravimeter providing extra capability on both machines. On the dual species machine the continuous imaging enables new regimes of physics to be quantitatively analysed. As a demonstration the technique was applied to a stochastic process called modulational instability, shown in Figure 8.14. This process occurs when a soliton confined to an optical waveguide undergoes stochastic breakup. The soliton is meta-stable, lying on a saddle-point in a stability landscape. Any deviation away from this point causes the soliton to decay into a soliton train. The onset time and number of components in the resultant soliton train varies stochastically preventing single-shot imaging systems from capturing the dynamics. In particular, the onset time is impossible to accurately measure using single-shot destructive techniques. Continuous probing allows these dynamics to be observed and analysed with these results being the subject of a manuscript currently in preparation.

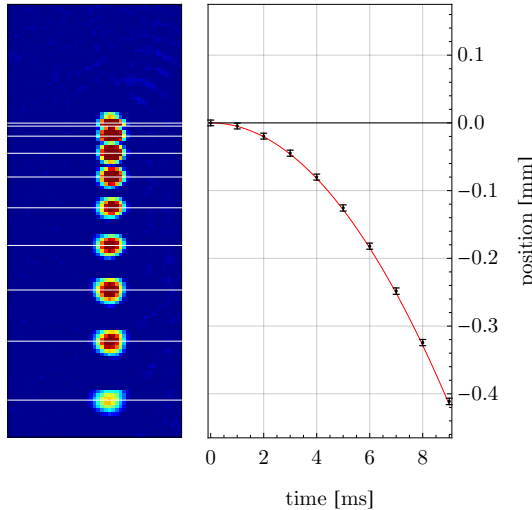


Figure 8.15: Example use of continuous non-destructive imaging. The condensate is imaged in-trap for a number of frames, allowing oscillation frequency to be calculated. The condensate is then released from trap and the acceleration due to gravity observed. By performing this multiple times, a measure of the variation in initial positions and velocities can be acquired. Error bars show one standard deviation about the mean for 20 experimental runs. Position is obtained via a centre of mass calculation. Note: the final image shows lower signal-to-noise due to uneven exposure of the camera, with this section being saturated. The centre-of-mass calculation is unaffected.

The non-destructive imaging also allows for single shot estimation of initial position and velocity of a condensate at release from trap. This would typically require numerous runs and statistical averaging in order to calculate mean values. Non-destructive imaging allows these quantities to be measured each run, potentially facilitating post correction of interferometer measurements based on the result. Figure 8.15 shows an example of such a measurement. The image on the left is an amalgamation of 10 non-destructive images taken immediately after release from trap. The condensate is seen to fall and expand and track out the expected parabolic flight. In order to extract initial velocities and positions, the centre-of-mass was calculated from the image as

$$x_{\text{COM}} = \frac{1}{M} \sum_{i=1}^N m_i x_i, \quad (8.42)$$

$$y_{\text{COM}} = \frac{1}{M} \sum_{i=1}^N m_i y_i, \quad (8.43)$$

where m_i is the value of the pixel at $\{x_i, y_i\}$ and $M = \sum_{i,j=1}^N m_i$ is the total summed value of all pixels. Typically noise can become a dominant factor in centre-of-mass calculations, especially with low signal-to-noise images. For this reason, the centre-of-mass is calculated by providing a limited box around the maximum value and applying a threshold to the data such that all values below a set point are zero. Performing this calculation, it is possible to extract the position of the falling cloud as a function of time. By fitting this data to the standard kinematic equation for an object falling under gravity

$$x(t) = x_0 + v_0 t + \frac{1}{2} g t^2, \quad (8.44)$$

the initial position x_0 , the initial velocity v_0 and the position $x(t)$ at time t and acceleration

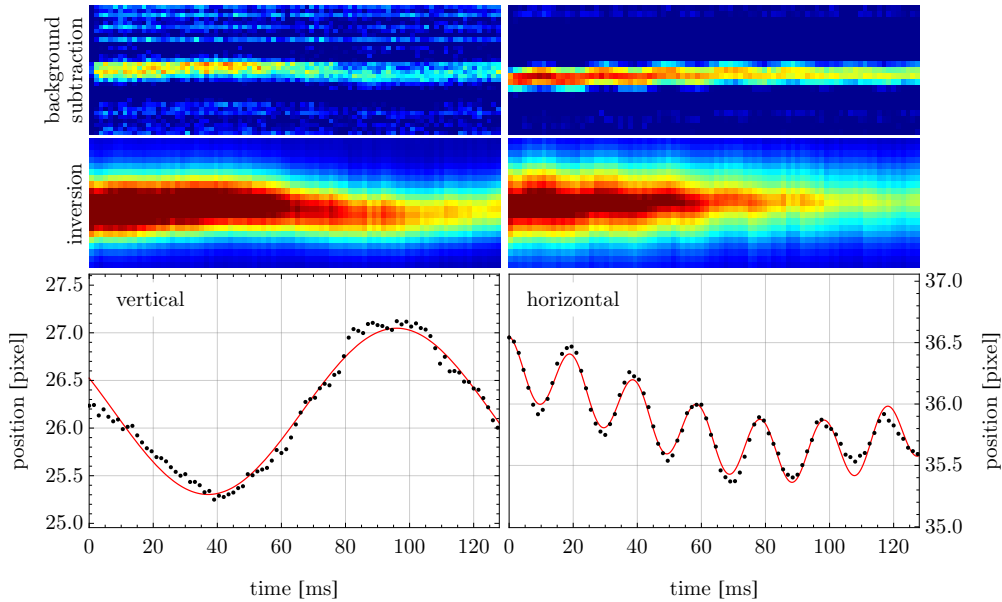


Figure 8.16: An example of continuous imaging used to measure the dipole trap frequencies. A series of 84 in-trap images were obtained each 1.5 ms apart. By calculating the centre of mass for each image, the oscillation in trap can be plotted out. The vertical trap frequency appears to be slower than that of the horizontal, with values of 8.5 ± 0.07 Hz and 50.7 ± 0.1 Hz respectively. The horizontal oscillation also appears to have a slow frequency coupled in with a frequency of $\sim 4.6 \pm 0.3$ Hz. The uncertainty is given by the standard error in the fit. Top two rows display the integration along one axis over time for each of the two axes, with the top row showing a basic background subtraction and the second row showing the result of Fourier technique used to invert the shadowgraph images.

under gravity g can be determined.

An additional benefit of a continuous non-destructive imaging system is a reduction in the amount of time taking data. Figure 8.16 shows the oscillation of a condensate in-trap in a single experimental run. The data was obtained by taking 84 images, exposed for $100\ \mu\text{s}$ every 1.5 ms. By performing a centre-of-mass calculation on each image, a vertical and horizontal position at each point in time may be obtained. This data can be fitted with a sinusoid and the trap frequency extracted. The vertical trap frequency appears to be slower than that of the horizontal, with values of 8.5 ± 0.07 Hz and 50.7 ± 0.1 Hz respectively. The horizontal oscillation also appears to have a low frequency coupled in with a frequency of $\sim 4.6 \pm 0.3$ Hz. The uncertainty is given by the standard error in the fit.

The low cost components, coupled with the high performance and utility of this imaging setup make it a powerful tool for ultracold atom experiments.

Conclusions and outlook

This thesis has presented theoretical and experimental work related to Bose-Einstein condensates in three key areas; a theoretical scheme for precise wavefunction manipulation and generation of solitons, the experimental application of machine learning to the production of a Bose-Einstein condensate, and the development of a robust and experimentally straightforward method for continuous non-destructive imaging.

In Chapters 3 and 4 a protocol was developed for precise one-dimensional control of the density and phase of the macroscopic wavefunction of a Bose-Einstein condensate. A necessary requirement of any wavefunction engineering is that it be capable of writing structures at the finest length scale of the system; the healing length. If this is not achieved, any imprinted phase will only be an approximation of the desired result. Typically optical techniques are diffraction limited to $\sim 1 \mu\text{m}$, larger than the healing length. By exploiting resonance effects, the spatial dependence of the magnetic resonance control scheme is shifted from the wavelength of light to the strength of the magnetic-field gradient. This gradient generates a spatially-dependent resonance which can then be manipulated using radio-frequency radiation to drive adiabatic transfer between internal states which can be used to imprint phase structures directly to the wavefunction. Whilst other techniques exist that are not limited by diffraction they are either slow on the time scale of the condensate dynamics, or they only succeed in generating symmetric structures. The magnetic resonance control scheme is performed many times faster than the healing time of the condensate, and demonstrably capable of generating non-symmetric structures. This was illustrated in Chapter 4 where a quasi-one-dimensional pseudospin-half non-polynomial Schrödinger equation was used to simulate a ^{87}Rb condensate under application of the magnetic resonance control scheme. The precision of the scheme was demonstrated by engineering a single black soliton that remained stationary over the course of five trap periods. Higher order non-linear modes were demonstrated through generation of oscillating double solitons showcasing the control of the scheme through manipulation of the position and trajectories. Although the experimental requirements for these examples were demanding, there are a number of pathways for successful experimental implementation including the use of chip-traps and vector light shifts. Additionally, the salient dynamics utilise adiabatic rapid passage, a technique

known to be robust to experimental flaws such as field inhomogeneities and offsets in frequency.

The results presented in Chapter 4 suggest a pathway for extension of the technique to higher spatial dimensions through the directional modulation of the magnetic-field gradient, analogous to magnetic resonance imaging. This has the potential to allow for exotic topological excitations such as spin knots in the polar order of a quantum fluid [229] to be engineered in a precise and robust way.

In Chapter 6 a machine learning algorithm was developed and implemented on the evaporative cooling stage of the production of a Bose-Einstein condensate with the algorithm converging to a successful set of parameters. The machine learning algorithm, based on Gaussian processes was found to be faster than the well-characterised Nelder-Mead optimisation algorithm. The algorithm can, unlike Nelder-Mead, take into account the uncertainty in a measurement. The appeal of Gaussian processes for experimental optimisation is the ability to feed information about the uncertainty of the measured data, resulting in an algorithm more robust to the noise typically encountered in experimental applications. Furthermore, the algorithm was designed to imitate the scientific method, using a varying internal cost function to determine whether to refine the current model through testing uncertain points, or to test the optimal point in the model. This optimal point is found through a gradient descent method implemented thousands of times in an experimental run allowing the refinement of the optimum much quicker than the time scale of the experimental duty-cycle.

In addition, the model produced by the algorithm can be used in a predictive manner and enable insight into the relationship between controls and experiment. The model is generated using a set of correlation lengths that are used to quantify the sensitivity of each parameter. The choice of correlation length was found to be extremely subtle and nuanced with more intensive versions enabling the classification of the importance of each parameter. It was found that by setting a static correlation length, the algorithm was able to converge faster, but with less information about the landscape. Allowing for a dynamically optimised correlation length, the algorithm was able to identify important and unimportant parameters, enabling guided experimental design in order to eliminate the extraneous parameters.

Extensive discussion has been generated on the topology of optimisation landscapes and the overwhelming disparity between the amount of experiments required for online optimisation compared with a brute force search, with certain landscapes proven to be ‘trap-free’. The work presented in this thesis adds to this discussion with the observation that Nelder-Mead always converged to a set of successful parameters despite being a local solver susceptible to traps in the landscape. Many other applications for machine learning exist in the realm of ultracold atoms with the prospect of providing additional

evidence toward the discussion of quantum optimisation topology.

The cost function used in the optimisation of the evaporative cooling could be augmented to include a measure of the number of atoms, or the time spent on evaporation. By careful design of the cost function, it might be possible to generate larger condensates in a shorter time. Further, atomic species with more complex scattering properties may have non-trivial ‘tricks’ that could be exploited using machine learning to enable cooling where it might otherwise have been problematic. The machine learning algorithm additionally provides a pathway for implementing the magnetic resonance control scheme, allowing direct characterisation of the relationship between the controls and the quality of the outcome. This has the potential to significantly decrease the system identification and analysis overhead when optimizing the experimental parameters.

In Chapter 8, a fast, dynamically tunable system capable of imaging a Bose-Einstein condensate in-trap in the far-detuned regime with negligible destruction was presented and demonstrated no observable heating or atom loss over 100 images. Numerous experimental examples demonstrated the capability and utility of the system. This included simultaneous dual atomic species imaging, continuous imaging of small ^{85}Rb solitons ($\sim 10^3$ atoms), large ^{87}Rb condensates ($\sim 10^6$ atoms), continuous acquisition of data over the entire experimental duty-cycle (images spaced by 100ms), and dynamical data acquisition where a sequence of shadowgraph images are followed by a high SNR near-resonant absorption image. Whilst shown in application to ^{85}Rb and ^{87}Rb , the technique generalises to other atomic species and is shown to be capable of imaging a small sample of only 10^4 atoms up to 100 times with high signal to noise (~ 33 in a single experimental run), negligible decrease in atom number, and no observable heating. With the ability to dynamically change the detuning of the probe beam, the dispersive imaging can be followed by a high signal-to-noise absorption image for accurate analysis. The performance was characterised and a number of applications presented, demonstrating the benefit of such a system to any cold atom experiment.

The combination of continuous non-destructive imaging with machine learning has the potential to enable real-time feedback control of a Bose-Einstein condensate. Much theoretical work has been undertaken using complex quantum field dynamics to model the heating due to measurement back-action and the actual feedback, with results suggesting that feedback control using a non-destructive measurement is possible [104, 230]. Though the theoretical modelling exists, experimental details often obscure the relationship between control and sample. Machine learning could be used to bridge this gap, allowing modulation of trapping potential and inter-particle interactions with the goal of condensation without the number expensive requirement of evaporative cooling.

References

- [1] Bose. *Plancks Gesetz und Lichtquantenhypothese*. Zeitschrift für Physik **26**, 178 (1924). ISSN 0044-3328. DOI: 10.1007/BF01327326. [p 1]
- [2] A. Einstein. *Quantentheorie des einatomigen idealen gases: zweite abhandlung*. Sitzungsber Preuss. Akad. Wiss. **1** (1925). [p 1]
- [3] T. W. Hänsch and A. L. Schawlow. *Cooling of gases by laser radiation*. Optics Communications **13**, 68 (1975). ISSN 0030-4018. DOI: 10.1016/0030-4018(75)90159-5. [p 1]
- [4] S. Chu, L. Hollberg, J. E. Bjorkholm, A. Cable, and A. Ashkin. *Three-dimensional viscous confinement and cooling of atoms by resonance radiation pressure*. Physical Review Letters **55**, 48 (1985). DOI: 10.1103/PhysRevLett.55.48. [p 1]
- [5] W. D. Phillips, J. V. Prodan, and H. J. Metcalf. *Laser cooling and electro-magnetic trapping of neutral atoms*. JOSA B **2**, 1751 (1985). ISSN 1520-8540. DOI: 10.1364/JOSAB.2.001751. [p 1]
- [6] P. D. Lett, R. N. Watts, C. I. Westbrook, W. D. Phillips, P. L. Gould, and H. J. Metcalf. *Observation of Atoms Laser Cooled below the Doppler Limit*. Physical Review Letters **61**, 169 (1988). DOI: 10.1103/PhysRevLett.61.169. [p 1]
- [7] E. L. Raab, M. Prentiss, A. Cable, S. Chu, and D. E. Pritchard. *Trapping of Neutral Sodium Atoms with Radiation Pressure*. Physical Review Letters **59**, 2631 (1987). DOI: 10.1103/PhysRevLett.59.2631. [p 1]
- [8] W. Petrich, M. H. Anderson, J. R. Ensher, and E. A. Cornell. *Stable, Tightly Confining Magnetic Trap for Evaporative Cooling of Neutral Atoms*. Physical Review Letters **74**, 3352 (1995). DOI: 10.1103/PhysRevLett.74.3352. [p 1]
- [9] W. Ketterle and N. J. V. Druten. *Evaporative Cooling of Trapped Atoms*. In B. B. a. H. Walther, ed., *Advances In Atomic, Molecular, and Optical Physics*, volume 37, pages 181–236. Academic Press (1996). DOI: 10.1016/S1049-250X(08)60101-9. [p 1]
- [10] W. D. Phillips. *Nobel Lecture: Laser cooling and trapping of neutral atoms*. Reviews of Modern Physics **70**, 721 (1998). DOI: 10.1103/RevModPhys.70.721. [p 1]

- [11] W. Ketterle. *Nobel lecture: When atoms behave as waves: Bose-Einstein condensation and the atom laser*. *Reviews of Modern Physics* **74**, 1131 (2002). DOI: 10.1103/RevModPhys.74.1131. [p 1]
- [12] E. A. Cornell and C. E. Wieman. *Nobel Lecture: Bose-Einstein condensation in a dilute gas, the first 70 years and some recent experiments*. *Reviews of Modern Physics* **74**, 875 (2002). DOI: 10.1103/RevModPhys.74.875. [p 1]
- [13] C. C. Bradley, C. A. Sackett, J. J. Tollett, and R. G. Hulet. *Evidence of Bose-Einstein Condensation in an Atomic Gas with Attractive Interactions*. *Physical Review Letters* **75**, 1687 (1995). DOI: 10.1103/PhysRevLett.75.1687. [p 1]
- [14] K. B. Davis, M. O. Mewes, M. R. Andrews, N. J. van Druten, D. S. Durfee, D. M. Kurn, and W. Ketterle. *Bose-Einstein Condensation in a Gas of Sodium Atoms*. *Physical Review Letters* **75**, 3969 (1995). DOI: 10.1103/PhysRevLett.75.3969. [p 1]
- [15] G. Modugno, G. Ferrari, G. Roati, R. J. Brecha, A. Simoni, and M. Inguscio. *Bose-Einstein Condensation of Potassium Atoms by Sympathetic Cooling*. *Science* **294**, 1320 (2001). ISSN 0036-8075, 1095-9203. DOI: 10.1126/science.1066687. [p 1]
- [16] T. Kishimoto, J. Kobayashi, K. Noda, K. Aikawa, M. Ueda, and S. Inouye. *Direct evaporative cooling of ^{41}K into a Bose-Einstein condensate*. *Physical Review A* **79**, 031602 (2009). DOI: 10.1103/PhysRevA.79.031602. [p 1]
- [17] S. L. Cornish, N. R. Claussen, J. L. Roberts, E. A. Cornell, and C. E. Wieman. *Stable ^{85}Rb Bose-Einstein Condensates with Widely Tunable Interactions*. *Physical Review Letters* **85**, 1795 (2000). DOI: 10.1103/PhysRevLett.85.1795. [p 1]
- [18] M. H. Anderson, J. R. Ensher, M. R. Matthews, C. E. Wieman, and E. A. Cornell. *Observation of Bose-Einstein Condensation in a Dilute Atomic Vapor*. *Science* **269**, 198 (1995). ISSN 0036-8075, 1095-9203. DOI: 10.1126/science.269.5221.198. [pp 1, 2]
- [19] T. Weber, J. Herbig, M. Mark, H.-C. Nägerl, and R. Grimm. *Bose-Einstein Condensation of Cesium*. *Science* **299**, 232 (2003). ISSN 0036-8075, 1095-9203. DOI: 10.1126/science.1079699. [p 1]
- [20] S. Kraft, F. Vogt, O. Appel, F. Riehle, and U. Sterr. *Bose-Einstein Condensation of Alkaline Earth Atoms: ^{40}Ca* . *Physical Review Letters* **103**, 130401 (2009). DOI: 10.1103/PhysRevLett.103.130401. [p 1]
- [21] S. Stellmer, M. K. Tey, B. Huang, R. Grimm, and F. Schreck. *Bose-Einstein Condensation of Strontium*. *Physical Review Letters* **103**, 200401 (2009). DOI: 10.1103/PhysRevLett.103.200401. [p 1]

- [22] S. Stellmer, M. K. Tey, R. Grimm, and F. Schreck. *Bose-Einstein condensation of ^{86}Sr* . Physical Review A **82**, 041602 (2010). DOI: 10.1103/PhysRevA.82.041602. [p 1]
- [23] P. G. Mickelson, Y. N. Martinez de Escobar, M. Yan, B. J. DeSalvo, and T. C. Killian. *Bose-Einstein condensation of ^{88}Sr through sympathetic cooling with ^{87}Sr* . Physical Review A **81**, 051601 (2010). DOI: 10.1103/PhysRevA.81.051601. [p 1]
- [24] S. Dörscher, A. Thobe, B. Hundt, A. Kochanke, R. L. Targat, P. Windpassinger, C. Becker, and K. Sengstock. *Creation of quantum-degenerate gases of ytterbium in a compact 2d-/3d-magneto-optical trap setup*. Review of Scientific Instruments **84**, 043109 (2013). DOI: 10.1063/1.4802682. [p 1]
- [25] M. Lu, N. Q. Burdick, S. H. Youn, and B. L. Lev. *Strongly Dipolar Bose-Einstein Condensate of Dysprosium*. Physical Review Letters **107**, 190401 (2011). DOI: 10.1103/PhysRevLett.107.190401. [p 1]
- [26] K. Aikawa, A. Frisch, M. Mark, S. Baier, A. Rietzler, R. Grimm, and F. Ferlaino. *Bose-Einstein Condensation of Erbium*. Physical Review Letters **108**, 210401 (2012). DOI: 10.1103/PhysRevLett.108.210401. [p 1]
- [27] A. Griesmaier, J. Werner, S. Hensler, J. Stuhler, and T. Pfau. *Bose-Einstein Condensation of Chromium*. Physical Review Letters **94**, 160401 (2005). DOI: 10.1103/PhysRevLett.94.160401. [p 1]
- [28] D. G. Fried, T. C. Killian, L. Willmann, D. Landhuis, S. C. Moss, D. Kleppner, and T. J. Greytak. *Bose-Einstein Condensation of Atomic Hydrogen*. Physical Review Letters **81**, 3811 (1998). DOI: 10.1103/PhysRevLett.81.3811. [p 2]
- [29] F. Pereira Dos Santos, J. Léonard, J. Wang, C. J. Barrelet, F. Perales, E. Rasel, C. S. Unnikrishnan, M. Leduc, and C. Cohen-Tannoudji. *Bose-Einstein Condensation of Metastable Helium*. Physical Review Letters **86**, 3459 (2001). DOI: 10.1103/PhysRevLett.86.3459. [p 2]
- [30] D. S. Jin, J. R. Ensher, M. R. Matthews, C. E. Wieman, and E. A. Cornell. *Collective Excitations of a Bose-Einstein Condensate in a Dilute Gas*. Physical Review Letters **77**, 420 (1996). DOI: 10.1103/PhysRevLett.77.420. [p 2]
- [31] D. S. Jin, M. R. Matthews, J. R. Ensher, C. E. Wieman, and E. A. Cornell. *Temperature-Dependent Damping and Frequency Shifts in Collective Excitations of a Dilute Bose-Einstein Condensate*. Physical Review Letters **78**, 764 (1997). DOI: 10.1103/PhysRevLett.78.764. [p 2]

- [32] M. R. Andrews, M.-O. Mewes, N. J. v. Druten, D. S. Durfee, D. M. Kurn, and W. Ketterle. *Direct, Nondestructive Observation of a Bose Condensate*. Science **273**, 84 (1996). ISSN 0036-8075, 1095-9203. DOI: 10.1126/science.273.5271.84. [pp 2, 114]
- [33] M. R. Andrews, C. G. Townsend, H.-J. Miesner, D. S. Durfee, D. M. Kurn, and W. Ketterle. *Observation of Interference Between Two Bose Condensates*. Science **275**, 637 (1997). ISSN 0036-8075, 1095-9203. DOI: 10.1126/science.275.5300.637. [p 2]
- [34] N. P. Robins, P. A. Altin, J. E. Debs, and J. D. Close. *Atom lasers: Production, properties and prospects for precision inertial measurement*. Physics Reports **529**, 265 (2013). ISSN 0370-1573. DOI: 10.1016/j.physrep.2013.03.006. [pp 2, 27]
- [35] K. Hardman, P. Everitt, G. McDonald, P. Manju, P. Wigley, M. Sooriyabandara, C. Kuhn, J. Debs, J. Close, and N. Robins. *Simultaneous Precision Gravimetry and Magnetic Gradiometry with a Bose-Einstein Condensate: A High Precision, Quantum Sensor*. Physical Review Letters **117**, 138501 (2016). DOI: 10.1103/PhysRevLett.117.138501. [pp 2, 100, and 129]
- [36] M. W. Jack, M. J. Collett, and D. F. Walls. *Coherent quantum tunneling between two Bose-Einstein condensates*. Physical Review A **54**, R4625 (1996). DOI: 10.1103/PhysRevA.54.R4625. [p 3]
- [37] G. J. Milburn, J. Corney, E. M. Wright, and D. F. Walls. *Quantum dynamics of an atomic Bose-Einstein condensate in a double-well potential*. Physical Review A **55**, 4318 (1997). DOI: 10.1103/PhysRevA.55.4318. [p 3]
- [38] I. Bloch, J. Dalibard, and S. Nascimbène. *Quantum simulations with ultracold quantum gases*. Nature Physics **8**, 267 (2012). ISSN 1745-2473. DOI: 10.1038/nphys2259. [p 3]
- [39] F. Dalfovo, S. Giorgini, L. P. Pitaevskii, and S. Stringari. *Theory of Bose-Einstein condensation in trapped gases*. Reviews of Modern Physics **71**, 463 (1999). DOI: 10.1103/RevModPhys.71.463. [p 3]
- [40] L. P. Pitaevskii. *Vortex lines in an imperfect Bose gas*. Journal of Experimental and Theoretical Physics **13** (1961). [pp 3, 18]
- [41] E. P. Gross. *Hydrodynamics of a Superfluid Condensate*. Journal of Mathematical Physics **4**, 195 (1963). ISSN 0022-2488. DOI: 10.1063/1.1703944. [pp 3, 18]
- [42] S. Inouye, M. R. Andrews, J. Stenger, H.-J. Miesner, D. M. Stamper-Kurn, and W. Ketterle. *Observation of Feshbach resonances in a Bose-Einstein condensate*. Nature **392**, 151 (1998). ISSN 0028-0836. DOI: 10.1038/32354. [p 3]

- [43] E. A. Donley, N. R. Claussen, S. L. Cornish, J. L. Roberts, E. A. Cornell, and C. E. Wieman. *Dynamics of collapsing and exploding Bose–Einstein condensates*. Nature **412**, 295 (2001). ISSN 0028-0836. DOI: 10.1038/35085500. [pp 3, 111]
- [44] K. J. Blow and N. J. Doran. *Multiple dark soliton solutions of the nonlinear Schrödinger equation*. Physics Letters A **107**, 55 (1985). ISSN 0375-9601. DOI: 10.1016/0375-9601(85)90194-X. [pp 3, 22]
- [45] J. Weiner, V. S. Bagnato, S. Zilio, and P. S. Julienne. *Experiments and theory in cold and ultracold collisions*. Reviews of Modern Physics **71**, 1 (1999). DOI: 10.1103/RevModPhys.71.1. [p 3]
- [46] D. J. Frantzeskakis. *Dark solitons in atomic Bose–Einstein condensates: from theory to experiments*. Journal of Physics A: Mathematical and Theoretical **43**, 213001 (2010). ISSN 1751-8121. DOI: 10.1088/1751-8113/43/21/213001. [p 3]
- [47] F. Kh. Abdullaev, A. Gammal, A. M. Kamchatnov, and L. Tomio. *Dynamics of bright matter wave solitons in a bose–einstein condensate*. International Journal of Modern Physics B **19**, 3415 (2005). ISSN 0217-9792. DOI: 10.1142/S0217979205032279. [p 3]
- [48] R. Carretero-González, D. J. Frantzeskakis, and P. G. Kevrekidis. *Nonlinear waves in Bose–Einstein condensates: physical relevance and mathematical techniques*. Nonlinearity **21**, R139 (2008). ISSN 0951-7715. DOI: 10.1088/0951-7715/21/7/R01. [p 3]
- [49] J. Anglin. *Atomic dark solitons: Quantum canaries learn to fly*. Nature Physics **4**, 437 (2008). ISSN 1745-2473. DOI: 10.1038/nphys980. [p 3]
- [50] A. Negretti and C. Henkel. *Enhanced phase sensitivity and soliton formation in an integrated BEC interferometer*. Journal of Physics B: Atomic, Molecular and Optical Physics **37**, L385 (2004). ISSN 0953-4075. DOI: 10.1088/0953-4075/37/23/L02. [p 3]
- [51] G. McDonald, C. Kuhn, K. Hardman, S. Bennetts, P. Everitt, P. Altin, J. Debs, J. Close, and N. Robins. *Bright Solitonic Matter-Wave Interferometer*. Physical Review Letters **113**, 013002 (2014). DOI: 10.1103/PhysRevLett.113.013002. [pp 3, 111]
- [52] J. Denschlag, J. E. Simsarian, D. L. Feder, C. W. Clark, L. A. Collins, J. Cubizolles, L. Deng, E. W. Hagley, K. Helmerson, W. P. Reinhardt, S. L. Rolston, B. I. Schneider, and W. D. Phillips. *Generating Solitons by Phase Engineering of a Bose-Einstein Condensate*. Science **287**, 97 (2000). ISSN 0036-8075, 1095-9203. DOI: 10.1126/science.287.5450.97. [pp 3, 22, 28, and 57]
- [53] A. E. Leanhardt, A. Görlitz, A. P. Chikkatur, D. Kielpinski, Y. Shin, D. E. Pritchard, and W. Ketterle. *Imprinting Vortices in a Bose-Einstein Condensate using Topological*

- Phases.* Physical Review Letters **89**, 190403 (2002). DOI: 10.1103/PhysRevLett.89.190403. [pp 3, 28]
- [54] A. E. Leanhardt, Y. Shin, D. Kielpinski, D. E. Pritchard, and W. Ketterle. *Coreless Vortex Formation in a Spinor Bose-Einstein Condensate.* Physical Review Letters **90**, 140403 (2003). DOI: 10.1103/PhysRevLett.90.140403. [pp 3, 28]
- [55] L. Khaykovich, F. Schreck, G. Ferrari, T. Bourdel, J. Cubizolles, L. D. Carr, Y. Castin, and C. Salomon. *Formation of a Matter-Wave Bright Soliton.* Science **296**, 1290 (2002). ISSN 0036-8075, 1095-9203. DOI: 10.1126/science.1071021. [p 3]
- [56] K. E. Strecker, G. B. Partridge, A. G. Truscott, and R. G. Hulet. *Formation and propagation of matter-wave soliton trains.* Nature **417**, 150 (2002). ISSN 0028-0836. DOI: 10.1038/nature747. [pp 3, 22]
- [57] V. Achilleos, D. Yan, P. G. Kevrekidis, and D. J. Frantzeskakis. *Dark-bright solitons in Bose-Einstein condensates at finite temperatures.* New Journal of Physics **14**, 055006 (2012). ISSN 1367-2630. DOI: 10.1088/1367-2630/14/5/055006. [p 3]
- [58] C. J. Foot. *Atomic physics.* Oxford University Press (2005). ISBN 978-0-19-850695-9. Google-Books-ID: kXYpAQAAQAAJ. [p 7]
- [59] M. O. Scully and M. S. Zubairy. *Quantum Optics.* Cambridge University Press (1997). ISBN 978-0-521-43595-6. Google-Books-ID: 20ISsQCKKmQC. [p 7]
- [60] I. I. Rabi. *Space Quantization in a Gyrating Magnetic Field.* Physical Review **51**, 652 (1937). DOI: 10.1103/PhysRev.51.652. [p 10]
- [61] M. Born and V. Fock. *Beweis des Adiabatensatzes.* Zeitschrift für Physik **51**, 165 (1928). ISSN 0044-3328. DOI: 10.1007/BF01343193. [p 11]
- [62] L. D. Landau. *Zur theorie der energieubertragung. II.* Physics of the Soviet Union **2**, 46 (1932). [p 13]
- [63] E. Majorana. *Atomi orientati in campo magnetico variabile.* Il Nuovo Cimento (1924-1942) **9**, 43 (1932). ISSN 1827-6121. DOI: 10.1007/BF02960953. [p 13]
- [64] E. Stueckelberg. *Theory of inelastic collisions between atoms(Theory of inelastic collisions between atoms, using two simultaneous differential equations).* Helv. Phys. Acta,(Basel) **5**, 369 (1932). [p 13]
- [65] C. Zener. *Non-Adiabatic Crossing of Energy Levels.* Proceedings of the Royal Society of London A: Mathematical, Physical and Engineering Sciences **137**, 696 (1932). ISSN 1364-5021, 1471-2946. DOI: 10.1098/rspa.1932.0165. [p 13]

- [66] Daniel A. Steck. *Rubidium 85 D Line Data*. available online at <http://steck.us/alkalidata>, (revision 2.1.6, 20 September 2013) . [pp 14, 16, 110, and 113]
- [67] A. Landé. *Über den anomalen Zeemaneffekt (Teil I)*. Zeitschrift für Physik **5**, 231 (1921). ISSN 0044-3328. DOI: 10.1007/BF01335014. [p 14]
- [68] F. Paschen and E. Back. *Normale und anomale Zeemaneffekte*. Annalen der Physik **344**, 897 (1912). ISSN 1521-3889. DOI: 10.1002/andp.19123441502. [p 16]
- [69] E. P. Gross. *Structure of a quantized vortex in boson systems*. Il Nuovo Cimento Series 10 **20**, 454 (1961). ISSN 0029-6341, 1827-6121. DOI: 10.1007/BF02731494. [p 18]
- [70] A. J. Leggett. *Bose-Einstein condensation in the alkali gases: Some fundamental concepts*. Reviews of Modern Physics **73**, 307 (2001). DOI: 10.1103/RevModPhys.73.307. [pp 19, 21]
- [71] C. J. Pethick and H. Smith. *Bose-Einstein Condensation in Dilute Gases*. Cambridge University Press (2002). ISBN 978-0-521-66580-3. Google-Books-ID: iBk0G3_5iIQC. [p 21]
- [72] D. D. J. Korteweg and D. G. d. Vries. *XLI. On the change of form of long waves advancing in a rectangular canal, and on a new type of long stationary waves*. Philosophical Magazine Series 5 **39**, 422 (1895). ISSN 1941-5982. DOI: 10.1080/14786449508620739. [p 22]
- [73] J.-l. Ma and F.-t. Ma. *Solitary wave solutions of nonlinear financial markets: data-modeling-concept-practicing*. Frontiers of Physics in China **2**, 368 (2007). ISSN 1673-3487, 1673-3606. DOI: 10.1007/s11467-007-0047-y. [p 22]
- [74] P. Emplit, J. P. Hamaide, F. Reynaud, C. Froehly, and A. Barthelemy. *Picosecond steps and dark pulses through nonlinear single mode fibers*. Optics Communications **62**, 374 (1987). ISSN 0030-4018. DOI: 10.1016/0030-4018(87)90003-4. [p 22]
- [75] D. Krökel, N. J. Halas, G. Giuliani, and D. Grischkowsky. *Dark-Pulse Propagation in Optical Fibers*. Physical Review Letters **60**, 29 (1988). DOI: 10.1103/PhysRevLett.60.29. [p 22]
- [76] G. R. Allan, S. R. Skinner, D. R. Andersen, and A. L. Smirl. *Observation of fundamental dark spatial solitons in semiconductors using picosecond pulses*. Optics Letters **16**, 156 (1991). ISSN 0146-9592, 1539-4794. DOI: 10.1364/OL.16.000156. [p 22]

- [77] G. A. Swartzlander, D. R. Andersen, J. J. Regan, H. Yin, and A. E. Kaplan. *Spatial dark-soliton stripes and grids in self-defocusing materials*. Physical Review Letters **66**, 1583 (1991). DOI: 10.1103/PhysRevLett.66.1583. [p 22]
- [78] B. Denardo, W. Wright, S. Putterman, and A. Larraza. *Observation of a kink soliton on the surface of a liquid*. Physical Review Letters **64**, 1518 (1990). DOI: 10.1103/PhysRevLett.64.1518. [p 22]
- [79] B. Denardo, B. Galvin, A. Greenfield, A. Larraza, S. Putterman, and W. Wright. *Observations of localized structures in nonlinear lattices: Domain walls and kinks*. Physical Review Letters **68**, 1730 (1992). DOI: 10.1103/PhysRevLett.68.1730. [p 22]
- [80] M. Chen, M. A. Tsankov, J. M. Nash, and C. E. Patton. *Microwave magnetic-envelope dark solitons in yttrium iron garnet thin films*. Physical Review Letters **70**, 1707 (1993). DOI: 10.1103/PhysRevLett.70.1707. [p 22]
- [81] R. Heidemann, S. Zhdanov, R. Sütterlin, H. M. Thomas, and G. E. Morfill. *Dissipative Dark Soliton in a Complex Plasma*. Physical Review Letters **102**, 135002 (2009). DOI: 10.1103/PhysRevLett.102.135002. [p 22]
- [82] T. Tsuzuki. *Nonlinear waves in the Pitaevskii-Gross equation*. Journal of Low Temperature Physics **4**, 441 (1971). ISSN 0022-2291, 1573-7357. DOI: 10.1007/BF00628744. [p 22]
- [83] S. Burger, K. Bongs, S. Dettmer, W. Ertmer, K. Sengstock, A. Sanpera, G. V. Shlyapnikov, and M. Lewenstein. *Dark Solitons in Bose-Einstein Condensates*. Physical Review Letters **83**, 5198 (1999). DOI: 10.1103/PhysRevLett.83.5198. [p 22]
- [84] Z. Dutton, M. Budde, C. Slowe, and L. V. Hau. *Observation of Quantum Shock Waves Created with Ultra- Compressed Slow Light Pulses in a Bose-Einstein Condensate*. Science **293**, 663 (2001). ISSN 0036-8075, 1095-9203. DOI: 10.1126/science.1062527. [p 22]
- [85] B. P. Anderson, P. C. Haljan, C. A. Regal, D. L. Feder, L. A. Collins, C. W. Clark, and E. A. Cornell. *Watching Dark Solitons Decay into Vortex Rings in a Bose-Einstein Condensate*. Physical Review Letters **86**, 2926 (2001). DOI: 10.1103/PhysRevLett.86.2926. 339 citations. [pp 22, 28]
- [86] M. Matuszewski, E. Infeld, G. Rowlands, and M. Trippenbach. *Stability analysis of three-dimensional breather solitons in a Bose-Einstein condensate*. Proceedings of the Royal Society of London A: Mathematical, Physical and Engineering Sciences **461**, 3561 (2005). ISSN 1364-5021, 1471-2946. DOI: 10.1098/rspa.2005.1531. [p 22]

- [87] W. B. Cardoso, A. T. Avelar, and D. Bazeia. *Modulation of breathers in cigar-shaped Bose–Einstein condensates.* Physics Letters A **374**, 2640 (2010). ISSN 0375-9601. DOI: 10.1016/j.physleta.2010.04.050. [p 22]
- [88] Y. S. Kivshar, T. J. Alexander, and S. K. Turitsyn. *Nonlinear modes of a macroscopic quantum oscillator.* Physics Letters A **278**, 225 (2001). ISSN 0375-9601. DOI: 10.1016/S0375-9601(00)00774-X. [pp 22, 57]
- [89] G. Theocharis, A. Weller, J. P. Ronzheimer, C. Gross, M. K. Oberthaler, P. G. Kevrekidis, and D. J. Frantzeskakis. *Multiple atomic dark solitons in cigar-shaped Bose–Einstein condensates.* Physical Review A **81**, 063604 (2010). DOI: 10.1103/PhysRevA.81.063604. 30 citations. [p 22]
- [90] S. Stellmer, C. Becker, P. Soltan-Panahi, E.-M. Richter, S. Dörscher, M. Baumert, J. Kronjäger, K. Bongs, and K. Sengstock. *Collisions of Dark Solitons in Elongated Bose–Einstein Condensates.* Physical Review Letters **101**, 120406 (2008). DOI: 10.1103/PhysRevLett.101.120406. [pp 22, 57]
- [91] C. Becker, K. Sengstock, P. Schmelcher, P. G. Kevrekidis, and R. Carretero-González. *Inelastic collisions of solitary waves in anisotropic Bose–Einstein condensates: sling-shot events and expanding collision bubbles.* New Journal of Physics **15**, 113028 (2013). ISSN 1367-2630. DOI: 10.1088/1367-2630/15/11/113028. [pp 22, 57]
- [92] A. Weller, J. P. Ronzheimer, C. Gross, J. Esteve, M. K. Oberthaler, D. J. Frantzeskakis, G. Theocharis, and P. G. Kevrekidis. *Experimental Observation of Oscillating and Interacting Matter Wave Dark Solitons.* Physical Review Letters **101**, 130401 (2008). DOI: 10.1103/PhysRevLett.101.130401. 73 citations. [pp 22, 57]
- [93] E. Hecht. *Optics.* Addison-Wesley (2002). ISBN 978-0-8053-8566-3. Google-Books-ID: 7aG6QgAACAAJ. [p 24]
- [94] N. Goldman, A. Kubasiak, A. Bermudez, P. Gaspard, M. Lewenstein, and M. A. Martin-Delgado. *Non-Abelian Optical Lattices: Anomalous Quantum Hall Effect and Dirac Fermions.* Physical Review Letters **103**, 035301 (2009). DOI: 10.1103/PhysRevLett.103.035301. [p 27]
- [95] J. Simon, W. S. Bakr, R. Ma, M. E. Tai, P. M. Preiss, and M. Greiner. *Quantum simulation of antiferromagnetic spin chains in an optical lattice.* Nature **472**, 307 (2011). ISSN 0028-0836. DOI: 10.1038/nature09994. [p 27]
- [96] J. W. Britton, B. C. Sawyer, A. C. Keith, C.-C. J. Wang, J. K. Freericks, H. Uys, M. J. Biercuk, and J. J. Bollinger. *Engineered two-dimensional Ising interactions in a trapped-*

- ion quantum simulator with hundreds of spins.* Nature **484**, 489 (2012). ISSN 0028-0836. DOI: 10.1038/nature10981. [p 27]
- [97] S. Hild, T. Fukuhara, P. Schauß, J. Zeiher, M. Knap, E. Demler, I. Bloch, and C. Gross. *Far-from-Equilibrium Spin Transport in Heisenberg Quantum Magnets.* Physical Review Letters **113**, 147205 (2014). DOI: 10.1103/PhysRevLett.113.147205. [p 27]
- [98] C. Nayak, S. Simon, A. Stern, M. Freedman, and S. Das Sarma. *Non-Abelian anyons and topological quantum computation.* Reviews of Modern Physics **80**, 1083 (2008). DOI: 10.1103/RevModPhys.80.1083. [p 27]
- [99] A. Stern and N. H. Lindner. *Topological Quantum Computation—From Basic Concepts to First Experiments.* Science **339**, 1179 (2013). ISSN 0036-8075, 1095-9203. DOI: 10.1126/science.1231473. [p 27]
- [100] D.-S. Han, S.-K. Kim, J.-Y. Lee, S. J. Hermsdoerfer, H. Schultheiss, B. Leven, and B. Hillebrands. *Magnetic domain-wall motion by propagating spin waves.* Applied Physics Letters **94**, 112502 (2009). ISSN 0003-6951, 1077-3118. DOI: 10.1063/1.3098409. [p 27]
- [101] X. S. Wang, P. Yan, Y. H. Shen, G. E. W. Bauer, and X. R. Wang. *Domain Wall Propagation through Spin Wave Emission.* Physical Review Letters **109**, 167209 (2012). DOI: 10.1103/PhysRevLett.109.167209. [p 27]
- [102] T. Berrada, S. van Frank, R. Bücker, T. Schumm, J.-F. Schaff, and J. Schmiedmayer. *Integrated Mach–Zehnder interferometer for Bose–Einstein condensates.* Nature Communications **4** (2013). [p 27]
- [103] H. Strobel, W. Muessel, D. Linnemann, T. Zibold, D. B. Hume, L. Pezzè, A. Smerzi, and M. K. Oberthaler. *Fisher information and entanglement of non-Gaussian spin states.* Science **345**, 424 (2014). ISSN 0036-8075, 1095-9203. DOI: 10.1126/science.1250147. [p 27]
- [104] M. R. Hush, S. S. Szigeti, A. R. R. Carvalho, and J. J. Hope. *Controlling spontaneous-emission noise in measurement-based feedback cooling of a Bose–Einstein condensate.* New Journal of Physics **15**, 113060 (2013). ISSN 1367-2630. DOI: 10.1088/1367-2630/15/11/113060. [pp 27, 137]
- [105] L. D. Carr, J. Brand, S. Burger, and A. Sanpera. *Dark-soliton creation in Bose–Einstein condensates.* Physical Review A **63**, 051601 (2001). DOI: 10.1103/PhysRevA.63.051601. 32 citations. [p 27]
- [106] S. Burger, L. D. Carr, P. Öhberg, K. Sengstock, and A. Sanpera. *Generation and interaction of solitons in Bose–Einstein condensates.* Physical Review A **65**, 043611 (2002). DOI: 10.1103/PhysRevA.65.043611. 28 citations. [p 27]

- [107] C. Becker, S. Stellmer, P. Soltan-Panahi, S. Dörscher, M. Baumert, E.-M. Richter, J. Kronjäger, K. Bongs, and K. Sengstock. *Oscillations and interactions of dark and dark–bright solitons in Bose–Einstein condensates*. Nature Physics **4**, 496 (2008). ISSN 1745-2473. DOI: 10.1038/nphys962. [p 28]
- [108] M. F. Andersen, C. Ryu, P. Cladé, V. Natarajan, A. Vaziri, K. Helmerson, and W. D. Phillips. *Quantized Rotation of Atoms from Photons with Orbital Angular Momentum*. Physical Review Letters **97**, 170406 (2006). DOI: 10.1103/PhysRevLett.97.170406. [p 28]
- [109] M. R. Matthews, B. P. Anderson, P. C. Haljan, D. S. Hall, C. E. Wieman, and E. A. Cornell. *Vortices in a Bose–Einstein Condensate*. Physical Review Letters **83**, 2498 (1999). DOI: 10.1103/PhysRevLett.83.2498. [p 28]
- [110] M. A. Bernstein, K. F. King, and X. J. Zhou. *Handbook of MRI Pulse Sequences*. Elsevier (2004). ISBN 978-0-08-053312-4. [p 31]
- [111] M. S. Silver, R. I. Joseph, and D. I. Hoult. *Selective spin inversion in nuclear magnetic resonance and coherent optics through an exact solution of the Bloch–Riccati equation*. Physical Review A **31**, 2753 (1985). DOI: 10.1103/PhysRevA.31.2753. [p 38]
- [112] S. Giorgini, L. Pitaevskii, and S. Stringari. *Theory of ultracold atomic Fermi gases*. Reviews of Modern Physics **80**, 1215 (2008). DOI: 10.1103/RevModPhys.80.1215. [p 45]
- [113] O. Mandel, M. Greiner, A. Widera, T. Rom, T. W. Hänsch, and I. Bloch. *Coherent Transport of Neutral Atoms in Spin-Dependent Optical Lattice Potentials*. Physical Review Letters **91**, 010407 (2003). DOI: 10.1103/PhysRevLett.91.010407. [p 45]
- [114] D. Schrader, I. Dotsenko, M. Khudaverdyan, Y. Miroshnychenko, A. Rauschenbeutel, and D. Meschede. *Neutral Atom Quantum Register*. Physical Review Letters **93**, 150501 (2004). DOI: 10.1103/PhysRevLett.93.150501. [p 45]
- [115] W. Zhang and L. You. *An effective quasi-one-dimensional description of a spin-1 atomic condensate*. Physical Review A **71**, 025603 (2005). DOI: 10.1103/PhysRevA.71.025603. [pp 45, 46]
- [116] H. Godfrin and R. Rapp. *Two-dimensional nuclear magnets*. Advances in Physics **44**, 113 (1995). ISSN 0001-8732. DOI: 10.1080/00018739500101516. [p 45]
- [117] M. L. Chiofalo and M. P. Tosi. *Output from Bose condensates in tunnel arrays: the role of mean-field interactions and of transverse confinement*. Physics Letters A **268**, 406 (2000). ISSN 0375-9601. DOI: 10.1016/S0375-9601(00)00197-3. [p 46]

- [118] L. Salasnich, A. Parola, and L. Reatto. *Effective wave equations for the dynamics of cigar-shaped and disk-shaped Bose condensates*. Physical Review A **65**, 043614 (2002). DOI: 10.1103/PhysRevA.65.043614. [p 46]
- [119] A. Görlitz, J. M. Vogels, A. E. Leanhardt, C. Raman, T. L. Gustavson, J. R. Abo-Shaeer, A. P. Chikkatur, S. Gupta, S. Inouye, T. Rosenband, and W. Ketterle. *Realization of Bose-Einstein Condensates in Lower Dimensions*. Physical Review Letters **87**, 130402 (2001). DOI: 10.1103/PhysRevLett.87.130402. [p 46]
- [120] E. Nicklas, W. Muessel, H. Strobel, P. G. Kevrekidis, and M. K. Oberthaler. *Nonlinear dressed states at the miscibility-immiscibility threshold*. Physical Review A **92**, 053614 (2015). DOI: 10.1103/PhysRevA.92.053614. [p 46]
- [121] M. Egorov, B. Opanchuk, P. Drummond, B. V. Hall, P. Hannaford, and A. I. Sidorov. *Measurement of s-wave scattering lengths in a two-component Bose-Einstein condensate*. Physical Review A **87**, 053614 (2013). DOI: 10.1103/PhysRevA.87.053614. [p 46]
- [122] G. R. Dennis, J. J. Hope, and M. T. Johnsson. *XMDS2: Fast, scalable simulation of coupled stochastic partial differential equations*. Computer Physics Communications **184**, 201 (2013). ISSN 0010-4655. DOI: 10.1016/j.cpc.2012.08.016. [p 48]
- [123] M. L. Chiofalo, S. Succi, and M. P. Tosi. *Ground state of trapped interacting Bose-Einstein condensates by an explicit imaginary-time algorithm*. Physical Review E **62**, 7438 (2000). DOI: 10.1103/PhysRevE.62.7438. [p 48]
- [124] R. Grimm, M. Weidemuller, and Y. B. Ovchinnikov. *Optical dipole traps for neutral atoms*. Advances in Atomic Molecular and Optical Physics page 95 (1999). Advances in Atomic, Molecular and Optical Physics Vol. 42, 95-170 (2000). [p 50]
- [125] T. Isoshima, K. Machida, and T. Ohmi. *Spin-domain formation in spinor Bose-Einstein condensation*. Physical Review A **60**, 4857 (1999). DOI: 10.1103/PhysRevA.60.4857. [p 55]
- [126] S. Watabe, Y. Kato, and Y. Ohashi. *Excitation transport through a domain wall in a Bose-Einstein condensate*. Physical Review A **86**, 023622 (2012). DOI: 10.1103/PhysRevA.86.023622. [p 55]
- [127] M. Garwood and L. Delabarre. *The Return of the Frequency Sweep: Designing Adiabatic Pulses for Contemporary NMR*. Journal of Magnetic Resonance **153**, 155 (2001). ISSN 1090-7807. DOI: 10.1006/jmre.2001.2340. [p 56]
- [128] Y. A. Tesiram. *Implementation Equations for HSn RF Pulses*. Journal of magnetic resonance (San Diego, Calif. : 1997) **204**, 333 (2010). ISSN 1090-7807. DOI: 10.1016/j.jmr.2010.02.022. [p 56]

- [129] P. B. Blakie, A. S. Bradley, M. J. Davis, R. J. Ballagh, and C. W. Gardiner. *Dynamics and statistical mechanics of ultra-cold Bose gases using c-field techniques*. Advances in Physics **57**, 363 (2008). ISSN 0001-8732. DOI: 10.1080/00018730802564254. [p 56]
- [130] W. Hänsel, P. Hommelhoff, T. W. Hänsch, and J. Reichel. *Bose-Einstein condensation on a microelectronic chip*. Nature **413**, 498 (2001). ISSN 0028-0836. DOI: 10.1038/35097032. [p 56]
- [131] J. R. Gardner, M. L. Marable, G. R. Welch, and J. E. Thomas. *Suboptical wavelength position measurement of moving atoms using optical fields*. Physical Review Letters **70**, 3404 (1993). DOI: 10.1103/PhysRevLett.70.3404. [p 56]
- [132] C. Y. Park, H. Noh, C. M. Lee, and D. Cho. *Measurement of the Zeeman-like ac Stark shift*. Physical Review A **63**, 032512 (2001). DOI: 10.1103/PhysRevA.63.032512. [p 56]
- [133] R. J. C. Spreeuw, C. Gerz, L. S. Goldner, W. D. Phillips, S. L. Rolston, C. I. Westbrook, M. W. Reynolds, and I. F. Silvera. *Demonstration of neutral atom trapping with microwaves*. Physical Review Letters **72**, 3162 (1994). DOI: 10.1103/PhysRevLett.72.3162. [p 56]
- [134] P. G. Kevrekidis, V. V. Konotop, A. Rodriguez, and D. J. Frantzeskakis. *Dynamic generation of matter solitons from linear states via time-dependent scattering lengths*. Journal of Physics B: Atomic, Molecular and Optical Physics **38**, 1173 (2005). ISSN 0953-4075. DOI: 10.1088/0953-4075/38/8/008. [p 57]
- [135] S. Wright. *The roles of mutation, inbreeding, crossbreeding, and selection in evolution*. In *26th International Congress on Genetics*, volume 1, pages 356–366 (1932). [p 62]
- [136] M. T. Heath. *Scientific Computing: An Introductory Survey*. McGraw-Hill (2005). ISBN 978-0-07-124489-3. [p 62]
- [137] D. E. Kirk. *Optimal Control Theory: An Introduction*. Dover Publications (2004). ISBN 978-0-486-43484-1. [p 65]
- [138] J.-S. Li, J. Ruths, and D. Stefanatos. *A pseudospectral method for optimal control of open quantum systems*. The Journal of Chemical Physics **131**, 164110 (2009). ISSN 0021-9606, 1089-7690. DOI: 10.1063/1.3253796. [p 65]
- [139] R. S. Judson and H. Rabitz. *Teaching lasers to control molecules*. Physical Review Letters **68**, 1500 (1992). DOI: 10.1103/PhysRevLett.68.1500. [pp 66, 77, and 90]
- [140] W. S. Warren, H. Rabitz, and M. Dahleh. *Coherent Control of Quantum Dynamics: The Dream Is Alive*. Science **259**, 1581 (1993). ISSN 0036-8075, 1095-9203. DOI: 10.1126/science.259.5101.1581. [pp 66, 77]

- [141] B. Amstrup, G. J. Toth, G. Szabo, H. Rabitz, and A. Loerincz. *Genetic Algorithm with Migration on Topology Conserving Maps for Optimal Control of Quantum Systems*. *The Journal of Physical Chemistry* **99**, 5206 (1995). ISSN 0022-3654. DOI: 10.1021/j100014a048. [pp 66, 77]
- [142] J. Dods, D. Gruner, and P. Brumer. *A genetic algorithm approach to fitting polyatomic spectra via geometry shifts*. *Chemical Physics Letters* **261**, 612 (1996). ISSN 0009-2614. DOI: 10.1016/0009-2614(96)01009-3. [pp 66, 77]
- [143] T. Baumert, T. Brixner, V. Seyfried, M. Strehle, and G. Gerber. *Femtosecond pulse shaping by an evolutionary algorithm with feedback*. *Applied Physics B* **65**, 779 (1997). ISSN 0946-2171, 1432-0649. DOI: 10.1007/s003400050346. [pp 66, 77, and 90]
- [144] B. J. Pearson, J. L. White, T. C. Weinacht, and P. H. Bucksbaum. *Coherent control using adaptive learning algorithms*. *Physical Review A* **63**, 063412 (2001). DOI: 10.1103/PhysRevA.63.063412. [pp 66, 77]
- [145] D. Zeidler, S. Frey, K.-L. Kompa, and M. Motzkus. *Evolutionary algorithms and their application to optimal control studies*. *Physical Review A* **64**, 023420 (2001). DOI: 10.1103/PhysRevA.64.023420. [pp 66, 77]
- [146] I. Walmsley and H. Rabitz. *Quantum physics under control*. *Physics Today* **56**, 43 (2003). ISSN 0031-9228, 1945-0699. DOI: 10.1063/1.1611352. [pp 66, 77]
- [147] W. Rohringer, R. Bücker, S. Manz, T. Betz, C. Koller, M. Göbel, A. Perrin, J. Schmiedmayer, and T. Schumm. *Stochastic optimization of a cold atom experiment using a genetic algorithm*. *Applied Physics Letters* **93**, 264101 (2008). ISSN 0003-6951, 1077-3118. DOI: 10.1063/1.3058756. [pp 66, 77]
- [148] M. Tsubouchi and T. Momose. *Rovibrational wave-packet manipulation using shaped midinfrared femtosecond pulses toward quantum computation: Optimization of pulse shape by a genetic algorithm*. *Physical Review A* **77**, 052326 (2008). DOI: 10.1103/PhysRevA.77.052326. [pp 66, 77]
- [149] W. Rohringer, D. Fischer, J. Schmiedmayer, M. Trupke, and T. Schumm. *Stochastic optimization of Bose-Einstein condensation using a genetic algorithm*. INTECH Open Access Publisher (2011). [pp 66, 77]
- [150] G. Heinze, C. Hubrich, and T. Halfmann. *Stopped Light and Image Storage by Electromagnetically Induced Transparency up to the Regime of One Minute*. *Physical Review Letters* **111**, 033601 (2013). DOI: 10.1103/PhysRevLett.111.033601. [pp 66, 77]

- [151] P. T. Starkey, C. J. Billington, S. P. Johnstone, M. Jasperse, K. Helmerson, L. D. Turner, and R. P. Anderson. *A scripted control system for autonomous hardware-timed experiments*. Review of Scientific Instruments **84**, 085111 (2013). ISSN 0034-6748, 1089-7623. DOI: 10.1063/1.4817213. [pp 66, 77]
- [152] I. Geisel, K. Cordes, J. Mahnke, S. Jöllenbeck, J. Ostermann, J. Arlt, W. Ertmer, and C. Klempt. *Evolutionary optimization of an experimental apparatus*. Applied Physics Letters **102**, 214105 (2013). ISSN 0003-6951, 1077-3118. DOI: 10.1063/1.4808213. [pp 66, 77]
- [153] W. Spendley, G. R. Hext, and F. R. Himsorth. *Sequential Application of Simplex Designs in Optimisation and Evolutionary Operation*. Technometrics **4**, 441 (1962). ISSN 0040-1706. DOI: 10.2307/1266283. [p 66]
- [154] J. A. Nelder and R. Mead. *A Simplex Method for Function Minimization*. The Computer Journal **7**, 308 (1965). ISSN 0010-4620, 1460-2067. DOI: 10.1093/comjnl/7.4.308. [p 66]
- [155] J. Kelly, R. Barends, B. Campbell, Y. Chen, Z. Chen, B. Chiaro, A. Dunsworth, A. Fowler, I.-C. Hoi, E. Jeffrey, A. Megrant, J. Mutus, C. Neill, P. O’Malley, C. Quintana, P. Roushan, D. Sank, A. Vainsencher, J. Wenner, T. White, A. Cleland, and J. M. Martinis. *Optimal Quantum Control Using Randomized Benchmarking*. Physical Review Letters **112**, 240504 (2014). DOI: 10.1103/PhysRevLett.112.240504. [pp 67, 77, and 90]
- [156] A. Krizhevsky, I. Sutskever, and G. E. Hinton. *Imagenet classification with deep convolutional neural networks*. In *Advances in neural information processing systems*, pages 1097–1105 (2012). [p 70]
- [157] Y. Lecun, L. Bottou, Y. Bengio, and P. Haffner. *Gradient-based learning applied to document recognition*. Proceedings of the IEEE **86**, 2278 (1998). ISSN 0018-9219. DOI: 10.1109/5.726791. [p 70]
- [158] M. Bojarski, D. Del Testa, D. Dworakowski, B. Firner, B. Flepp, P. Goyal, L. D. Jackel, M. Monfort, U. Muller, J. Zhang, X. Zhang, J. Zhao, and K. Zieba. *End to End Learning for Self-Driving Cars*. arXiv:1604.07316 [cs] (2016). ArXiv: 1604.07316. [p 70]
- [159] D. Silver, A. Huang, C. J. Maddison, A. Guez, L. Sifre, G. van den Driessche, J. Schrittwieser, I. Antonoglou, V. Panneershelvam, M. Lanctot, S. Dieleman, D. Grewe, J. Nham, N. Kalchbrenner, I. Sutskever, T. Lillicrap, M. Leach,

- K. Kavukcuoglu, T. Graepel, and D. Hassabis. *Mastering the game of Go with deep neural networks and tree search*. Nature **529**, 484 (2016). ISSN 0028-0836. DOI: 10.1038/nature16961. [p 70]
- [160] C. M. S. Nambakhsh, J. Yuan, K. Punithakumar, A. Goela, M. Rajchl, T. M. Peters, and I. B. Ayed. *Left ventricle segmentation in MRI via convex relaxed distribution matching*. Medical Image Analysis **17**, 1010 (2013). ISSN 1361-8415. DOI: 10.1016/j.media.2013.05.002. [p 70]
- [161] T. J. W. Dawes, A. de Marvao, W. Shi, T. Fletcher, G. M. J. Watson, J. Wharton, C. J. Rhodes, L. S. G. E. Howard, J. S. R. Gibbs, D. Rueckert, S. A. Cook, M. R. Wilkins, and D. P. O'Regan. *Machine Learning of Three-dimensional Right Ventricular Motion Enables Outcome Prediction in Pulmonary Hypertension: A Cardiac MR Imaging Study*. Radiology page 161315 (2017). ISSN 0033-8419. DOI: 10.1148/radiol.2016161315. [p 70]
- [162] C. E. Rasmussen and C. K. I. Williams. *Gaussian Processes for Machine Learning*. The MIT Press (2006). ISBN 0-262-18253-X. [pp 73, 77]
- [163] R. B. Gramacy and N. G. Polson. *Particle Learning of Gaussian Process Models for Sequential Design and Optimization*. Journal of Computational and Graphical Statistics **20**, 102 (2011). ISSN 1061-8600. DOI: 10.1198/jcgs.2010.09171. [pp 74, 77, and 88]
- [164] A. R. Conn, N. I. M. Gould, and P. L. Toint. *Trust Region Methods*. Society for Industrial and Applied Mathematics (2000). ISBN 978-0-89871-460-9. [p 75]
- [165] Y.-x. Yuan. *A review of trust region algorithms for optimization*. In *ICIAM*, volume 99, pages 271–282 (2000). [p 75]
- [166] J. Roslund and H. Rabitz. *Gradient algorithm applied to laboratory quantum control*. Physical Review A **79**, 053417 (2009). DOI: 10.1103/PhysRevA.79.053417. [p 77]
- [167] D. Egger and F. Wilhelm. *Adaptive Hybrid Optimal Quantum Control for Imprecisely Characterized Systems*. Physical Review Letters **112**, 240503 (2014). DOI: 10.1103/PhysRevLett.112.240503. [p 77]
- [168] S. Seo, M. Wallat, T. Graepel, and K. Obermayer. *Gaussian process regression: active data selection and test point rejection*. In *IJCNN 2000, Proceedings of the IEEE-INNS-ENNS International Joint Conference on Neural Networks, 2000*, volume 3, pages 241–246 vol.3 (2000). DOI: 10.1109/IJCNN.2000.861310. [p 77]
- [169] L. Csató and M. Opper. *Sparse On-line Gaussian Processes*. Neural Comput. **14**, 641 (2002). ISSN 0899-7667. DOI: 10.1162/089976602317250933. [p 77]

- [170] M. P. Deisenroth, C. E. Rasmussen, and J. Peters. *Gaussian process dynamic programming*. Neurocomputing **72**, 1508 (2009). ISSN 0925-2312. DOI: 10.1016/j.neucom.2008.12.019. [p 77]
- [171] D. Nguyen-Tuong and J. Peters. *Local Gaussian process regression for real-time model-based robot control*. In *2008 IEEE/RSJ International Conference on Intelligent Robots and Systems*, pages 380–385 (2008). DOI: 10.1109/IROS.2008.4650850. [p 77]
- [172] D. Nguyen-tuong, J. R. Peters, and M. Seeger. *Local Gaussian Process Regression for Real Time Online Model Learning*. In D. Koller, D. Schuurmans, Y. Bengio, and L. Bottou, eds., *Advances in Neural Information Processing Systems 21*, pages 1193–1200. Curran Associates, Inc. (2009). [p 77]
- [173] A. Ranganathan, M.-H. Yang, and J. Ho. *Online Sparse Gaussian Process Regression and Its Applications*. IEEE Transactions on Image Processing **20**, 391 (2011). ISSN 1057-7149. DOI: 10.1109/TIP.2010.2066984. [p 77]
- [174] J. Yu. *Online quality prediction of nonlinear and non-Gaussian chemical processes with shifting dynamics using finite mixture model based Gaussian process regression approach*. Chemical Engineering Science **82**, 22 (2012). ISSN 0009-2509. DOI: 10.1016/j.ces.2012.07.018. [p 77]
- [175] X. LI, H. SU, and J. CHU. *Multiple Model Soft Sensor Based on Affinity Propagation, Gaussian Process and Bayesian Committee Machine*. Chinese Journal of Chemical Engineering **17**, 95 (2009). ISSN 1004-9541. DOI: 10.1016/S1004-9541(09)60039-2. [p 77]
- [176] P. Gao, A. Honkela, M. Rattray, and N. D. Lawrence. *Gaussian process modelling of latent chemical species: applications to inferring transcription factor activities*. Bioinformatics **24**, i70 (2008). ISSN 1367-4803, 1460-2059. DOI: 10.1093/bioinformatics/btn278. [p 77]
- [177] K. B. Davis, M.-O. Mewes, M. A. Joffe, M. R. Andrews, and W. Ketterle. *Evaporative Cooling of Sodium Atoms*. Physical Review Letters **74**, 5202 (1995). DOI: 10.1103/PhysRevLett.74.5202. [p 78]
- [178] H. Wu and C. J. Foot. *Direct simulation of evaporative cooling*. Journal of Physics B: Atomic, Molecular and Optical Physics **29**, L321 (1996). ISSN 0953-4075. DOI: 10.1088/0953-4075/29/8/003. [p 78]
- [179] A. J. Olson, R. J. Niffenegger, and Y. P. Chen. *Optimizing the efficiency of evaporative cooling in optical dipole traps*. Physical Review A **87**, 053613 (2013). DOI: 10.1103/PhysRevA.87.053613. [p 78]

- [180] C. A. Sackett, C. C. Bradley, and R. G. Hulet. *Optimization of evaporative cooling*. Physical Review A **55**, 3797 (1997). DOI: 10.1103/PhysRevA.55.3797. [p 78]
- [181] T. Shobu, H. Yamaoka, H. Imai, A. Morinaga, and M. Yamashita. *Optimized evaporative cooling for sodium Bose-Einstein condensation against three-body loss*. Physical Review A **84**, 033626 (2011). DOI: 10.1103/PhysRevA.84.033626. [p 78]
- [182] P. A. Altin, G. R. Dennis, G. D. McDonald, D. Döring, J. E. Debs, J. D. Close, C. M. Savage, and N. P. Robins. *Collapse and three-body loss in a ^{85}Rb Bose-Einstein condensate*. Physical Review A **84**, 033632 (2011). DOI: 10.1103/PhysRevA.84.033632. [pp 78, 111]
- [183] C. C. N. Kuhn, G. D. McDonald, K. S. Hardman, S. Bennetts, P. J. Everitt, P. A. Altin, J. E. Debs, J. D. Close, and N. P. Robins. *A Bose-condensed, simultaneous dual-species Mach-Zehnder atom interferometer*. New Journal of Physics **16**, 073035 (2014). ISSN 1367-2630. DOI: 10.1088/1367-2630/16/7/073035. [pp 79, 111]
- [184] C. G. Townsend, N. H. Edwards, C. J. Cooper, K. P. Zetie, C. J. Foot, A. M. Steane, P. Sriftgiser, H. Perrin, and J. Dalibard. *Phase-space density in the magneto-optical trap*. Physical Review A **52**, 1423 (1995). DOI: 10.1103/PhysRevA.52.1423. [p 81]
- [185] H. A. Rabitz, M. M. Hsieh, and C. M. Rosenthal. *Quantum Optimally Controlled Transition Landscapes*. Science **303**, 1998 (2004). ISSN 0036-8075, 1095-9203. DOI: 10.1126/science.1093649. [p 89]
- [186] R. Chakrabarti and H. Rabitz. *Quantum control landscapes*. International Reviews in Physical Chemistry **26**, 671 (2007). ISSN 0144-235X. DOI: 10.1080/01442350701633300. [p 89]
- [187] R. Wu, H. Rabitz, and M. Hsieh. *Characterization of the critical submanifolds in quantum ensemble control landscapes*. Journal of Physics A: Mathematical and Theoretical **41**, 015006 (2008). ISSN 1751-8121. DOI: 10.1088/1751-8113/41/1/015006. [p 89]
- [188] R. Wu, A. Pechen, H. Rabitz, M. Hsieh, and B. Tsou. *Control landscapes for observable preparation with open quantum systems*. Journal of Mathematical Physics **49**, 022108 (2008). ISSN 0022-2488, 1089-7658. DOI: 10.1063/1.2883738. [p 89]
- [189] M. Hsieh, R. Wu, C. Rosenthal, and H. Rabitz. *Topological and statistical properties of quantum control transition landscapes*. Journal of Physics B: Atomic, Molecular and Optical Physics **41**, 074020 (2008). ISSN 0953-4075. DOI: 10.1088/0953-4075/41/7/074020. [p 89]

- [190] T.-S. Ho, J. Dominy, and H. Rabitz. *Landscape of unitary transformations in controlled quantum dynamics*. Physical Review A **79**, 013422 (2009). DOI: 10.1103/PhysRevA.79.013422. [p 89]
- [191] A. N. Pechen and D. J. Tannor. *Are there Traps in Quantum Control Landscapes?* Physical Review Letters **106**, 120402 (2011). DOI: 10.1103/PhysRevLett.106.120402. [p 89]
- [192] H. Rabitz, T.-S. Ho, R. Long, R. Wu, and C. Brif. *Comment on “Are There Traps in Quantum Control Landscapes?”*. Physical Review Letters **108**, 198901 (2012). DOI: 10.1103/PhysRevLett.108.198901. [p 89]
- [193] A. N. Pechen and D. J. Tannor. *Pechen and Tannor Reply*. Physical Review Letters **108**, 198902 (2012). DOI: 10.1103/PhysRevLett.108.198902. [p 89]
- [194] M. Hush. *M-LOOP - Machine-learning online optimization package* (2016). <https://github.com/michaelhush/M-LOOP>. [p 90]
- [195] F. Pedregosa, G. Varoquaux, A. Gramfort, V. Michel, B. Thirion, O. Grisel, M. Blondel, P. Prettenhofer, R. Weiss, V. Dubourg, J. Vanderplas, A. Passos, D. Cournapeau, M. Brucher, M. Perrot, and E. Duchesnay. *Scikit-learn: Machine Learning in Python*. Journal of Machine Learning Research **12**, 2825 (2011). [p 90]
- [196] H. J. Metcalf and P. van der Straten. *Laser cooling and trapping*. Graduate texts in contemporary physics. Springer, corrected edition (1999). ISBN 0387987282, 9780387987286, 0387987479. [p 98]
- [197] G. C. Bjorklund, M. D. Levenson, W. Lenth, and C. Ortiz. *Frequency modulation (FM) spectroscopy*. Applied Physics B **32**, 145 (1983). ISSN 0946-2171, 1432-0649. DOI: 10.1007/BF00688820. [p 103]
- [198] K. S. Hardman, P. B. Wigley, P. J. Everitt, P. Manju, C. C. N. Kuhn, and N. P. Robins. *Time-of-flight detection of ultra-cold atoms using resonant frequency modulation imaging*. Optics Letters **41**, 2505 (2016). ISSN 0146-9592, 1539-4794. DOI: 10.1364/OL.41.002505. [p 103]
- [199] C. C. Bradley, C. A. Sackett, and R. G. Hulet. *Analysis of in situ images of Bose-Einstein condensates of lithium*. Physical Review A **55**, 3951 (1997). DOI: 10.1103/PhysRevA.55.3951. [p 109]
- [200] C. C. Bradley, C. A. Sackett, and R. G. Hulet. *Bose-Einstein Condensation of Lithium: Observation of Limited Condensate Number*. Physical Review Letters **78**, 985 (1997). DOI: 10.1103/PhysRevLett.78.985. [p 109]

- [201] M. Gajdacz, P. L. Pedersen, T. Mørch, A. J. Hilliard, J. Arlt, and J. F. Sherson. *Non-destructive Faraday imaging of dynamically controlled ultracold atoms*. Review of Scientific Instruments **84**, 083105 (2013). ISSN 0034-6748, 1089-7623. DOI: 10.1063/1.4818913. [pp 109, 120]
- [202] R. Hooke. *Of a New Property in the Air*. In *Micrographia*, pages 217–219. London (1665). [pp 109, 124]
- [203] F. Zernike. *Phase contrast, a new method for the microscopic observation of transparent objects*. Physica **9**, 686 (1942). ISSN 0031-8914. DOI: 10.1016/S0031-8914(42)80035-X. [p 109]
- [204] R. Grimm, M. Weidemüller, and Y. B. Ovchinnikov. *Optical Dipole Traps for Neutral Atoms*. In B. B. a. H. Walther, ed., *Advances In Atomic, Molecular, and Optical Physics*, volume 42, pages 95–170. Academic Press (2000). [p 110]
- [205] J. H. V. Nguyen, P. Dyke, D. Luo, B. A. Malomed, and R. G. Hulet. *Collisions of matter-wave solitons*. Nature Physics **10**, 918 (2014). ISSN 1745-2473. DOI: 10.1038/nphys3135. [p 111]
- [206] H. Saito and M. Ueda. *Intermittent Implosion and Pattern Formation of Trapped Bose-Einstein Condensates with an Attractive Interaction*. Physical Review Letters **86**, 1406 (2001). DOI: 10.1103/PhysRevLett.86.1406. [p 111]
- [207] H. Saito and M. Ueda. *Power laws and collapsing dynamics of a trapped Bose-Einstein condensate with attractive interactions*. Physical Review A **63**, 043601 (2001). DOI: 10.1103/PhysRevA.63.043601. [p 111]
- [208] J. L. Roberts, J. P. Burke, N. R. Claussen, S. L. Cornish, E. A. Donley, and C. E. Wieman. *Improved characterization of elastic scattering near a Feshbach resonance in ^{85}Rb* . Physical Review A **64**, 024702 (2001). DOI: 10.1103/PhysRevA.64.024702. [p 111]
- [209] A. Reinhard, J.-F. Riou, L. A. Zundel, and D. S. Weiss. *Dark-ground imaging of high optical thickness atom clouds*. Optics Communications **324**, 30 (2014). ISSN 0030-4018. DOI: 10.1016/j.optcom.2014.02.070. [p 114]
- [210] A. J. I. Toepler and A. Witting. *Beobachtungen nach einer neuen optischen methode*. M. Cohen & sohn, Bonn (1864). [p 114]
- [211] J. Glückstad and P. C. Mogensen. *Optimal phase contrast in common-path interferometry*. Applied Optics **40**, 268 (2001). ISSN 1539-4522. DOI: 10.1364/AO.40.000268. [p 116]

- [212] M. R. Andrews, D. M. Kurn, H.-J. Miesner, D. S. Durfee, C. G. Townsend, S. Inouye, and W. Ketterle. *Propagation of Sound in a Bose-Einstein Condensate*. Physical Review Letters **79**, 553 (1997). DOI: 10.1103/PhysRevLett.79.553. [p 117]
- [213] R. Meppelink, R. A. Rozendaal, S. B. Koller, J. M. Vogels, and P. van der Straten. *Thermodynamics of Bose-Einstein-condensed clouds using phase-contrast imaging*. Physical Review A **81**, 053632 (2010). DOI: 10.1103/PhysRevA.81.053632. [pp 117, 119]
- [214] C. S. Anderson. *Fringe visibility, irradiance, and accuracy in common path interferometers for visualization of phase disturbances*. Applied Optics **34**, 7474 (1995). ISSN 1539-4522. DOI: 10.1364/AO.34.007474. [p 118]
- [215] J. M. Higbie, L. E. Sadler, S. Inouye, A. P. Chikkatur, S. R. Leslie, K. L. Moore, V. Savalli, and D. M. Stamper-Kurn. *Direct Nondestructive Imaging of Magnetization in a Spin-1 Bose-Einstein Gas*. Physical Review Letters **95**, 050401 (2005). DOI: 10.1103/PhysRevLett.95.050401. [p 120]
- [216] S. Franke-Arnold, M. Arndt, and A. Zeilinger. *Magneto-optical effects with cold lithium atoms*. Journal of Physics B: Atomic, Molecular and Optical Physics **34**, 2527 (2001). ISSN 0953-4075. DOI: 10.1088/0953-4075/34/12/316. [p 120]
- [217] M. Langer, P. Cloetens, J.-P. Guigay, and F. Peyrin. *Quantitative comparison of direct phase retrieval algorithms in in-line phase tomography*. Medical Physics **35**, 4556 (2008). ISSN 0094-2405. DOI: 10.1118/1.2975224. [pp 124, 126, and 127]
- [218] G. S. Settles. *Schlieren and Shadowgraph Techniques: Visualizing Phenomena in Transparent Media*. Experimental Fluid Mechanics. Springer-Verlag Berlin Heidelberg, 1 edition (2001). ISBN 978-3-642-63034-7, 978-3-642-56640-0. [p 124]
- [219] L. D. Turner, K. F. E. M. Domen, and R. E. Scholten. *Diffraction-contrast imaging of cold atoms*. Physical Review A **72**, 031403 (2005). DOI: 10.1103/PhysRevA.72.031403. [pp 125, 126]
- [220] L. D. Turner, K. P. Weber, D. Paganin, and R. E. Scholten. *Off-resonant defocus-contrast imaging of cold atoms*. Optics Letters **29**, 232 (2004). ISSN 0146-9592, 1539-4794. DOI: 10.1364/OL.29.000232. [p 125]
- [221] L. J. Allen and M. P. Oxley. *Phase retrieval from series of images obtained by defocus variation*. Optics Communications **199**, 65 (2001). ISSN 0030-4018. DOI: 10.1016/S0030-4018(01)01556-5. [p 127]
- [222] T. E. Gureyev, C. Raven, A. Snigirev, I. Snigireva, and S. W. Wilkins. *Hard x-ray quantitative non-interferometric phase-contrast microscopy*. Journal of Physics D: Applied Physics **32**, 563 (1999). ISSN 0022-3727. DOI: 10.1088/0022-3727/32/5/010. [p 127]

- [223] T. E. Gureyev and K. A. Nugent. *Rapid quantitative phase imaging using the transport of intensity equation*. Optics Communications **133**, 339 (1997). ISSN 0030-4018. DOI: 10.1016/S0030-4018(96)00454-3. [p 127]
- [224] T. E. Gureyev and K. A. Nugent. *Phase retrieval with the transport-of-intensity equation II Orthogonal series solution for nonuniform illumination*. Journal of the Optical Society of America A **13**, 1670 (1996). ISSN 1084-7529, 1520-8532. DOI: 10.1364/JOSAA.13.001670. [p 127]
- [225] M. R. Teague. *Deterministic phase retrieval: a Green's function solution*. Journal of the Optical Society of America **73**, 1434 (1983). ISSN 0030-3941. DOI: 10.1364/JOSA.73.001434. [p 127]
- [226] D. Paganin and K. A. Nugent. *Noninterferometric Phase Imaging with Partially Coherent Light*. Physical Review Letters **80**, 2586 (1998). DOI: 10.1103/PhysRevLett.80.2586. [p 127]
- [227] A. Groso, R. Abela, and M. Stampanoni. *Implementation of a fast method for high resolution phase contrast tomography*. Optics Express **14**, 8103 (2006). ISSN 1094-4087. DOI: 10.1364/OE.14.008103. [p 127]
- [228] C. Wei, S. Yan, A. Jia, Y. Luo, Q. Hu, and Z. Li. *Compact phase-lock loop for external cavity diode lasers*. Chinese Optics Letters **14**, 051403 (2016). [p 128]
- [229] Y. Kawaguchi, M. Nitta, and M. Ueda. *Knots in a Spinor Bose-Einstein Condensate*. Physical Review Letters **100**, 180403 (2008). DOI: 10.1103/PhysRevLett.100.180403. [p 136]
- [230] M. R. Hush, A. R. R. Carvalho, and J. J. Hope. *Number-phase Wigner representation for scalable stochastic simulations of controlled quantum systems*. Physical Review A **85**, 023607 (2012). DOI: 10.1103/PhysRevA.85.023607. [p 137]